

**Conductively Filled Poly(methyl methacrylate) Composites;
Manufacture and Testing Processes for EMI Shielding Effectiveness**

Jonathan R. Smuga

A thesis submitted in partial fulfilment of the requirements of Edinburgh
Napier University, for the award of Doctor of Philosophy

June 2012

Abstract

Electromagnetic interference (EMI) is an escalating concern in the modern electronic climate. As such it has become a critical area to consider when designing and packaging electronics. With the growing volume of electronic devices available and with processor frequencies increasing, the electromagnetic environment is becoming ever more congested. The need for adequate EMI shielding has become an essential consideration.

The desire for high performance combined with reductions in size, weight and manufacturing cost suggests that polymers should be ideal materials for parts such as electronic housings. Unfortunately polymers generally do not provide shielding from electromagnetic waves.

The research detailed in this thesis investigates the manufacture and testing of conductively filled poly(methyl methacrylate) (PMMA) composites. Samples of PMMA resin and various electrically conductive filler materials were manufactured. The processing methods, electrical properties and electromagnetic behaviour were all investigated. Composite polymer coatings were printed with a K-Control Coater and evaluated for surface resistivity and EMI shielding effectiveness. Samples were produced with a range of filler materials including nickel, carbon, copper/aluminium and silver coated glass spheres. Shielding effectiveness values of approximately 70 dB were obtained for coatings of PMMA filled with silver coated hollow glass microspheres.

Attempts were made to produce an alternative filler material by electroless nickel plating of expanded graphite powder. Successful plating was achieved using conventional methods of surface sensitisation of the graphite. This however resulted in

agglomerations of the powder and a loss of the desired physical properties. Alternative thermal surface treatments proved to be unsuccessful in activating the graphite surface with no nickel deposition occurring.

Furthermore, electroless nickel plating techniques were successfully utilised in the development of an alternative manufacturing process for producing electrically conductive PMMA composites which contained a reduced metallic content, in relation to a more traditional production technique. Plaques were manufactured by compression moulding of nickel plated PMMA granules. These were compared against samples manufactured with nickel powder mixed in a Brabender Plasti-Corder. The electroless plating method produced samples that outperformed the comparative method and were shown to contain a reduced metallic content. Shielding effectiveness of the electroless plated granule samples achieved approximately 34 dB compared to a maximum of only 2.5 dB for the Brabender compounded samples.

Outwith these areas of empirical testing a computer model was produced to simulate the electromagnetic shielding behaviour of composite materials using Comsol Multiphysics. This model appears to successfully simulate the waveguide testing apparatus. However the theoretical conductivity values as calculated from effective media theory resulted in disproportionate shielding effectiveness values obtained.

Further research into the electroless plated and compression moulded PMMA composites would be beneficial in order to fully optimise the process. Equally the theoretical model would require further investigating and validating before more accurate simulations could be achieved.

Acknowledgements

I would initially like to thank Silberline for all their contributions throughout this research. Additional thanks to Microsphere Technologies for the sample materials provided.

Sincere thanks go to my supervisor, Dr Mike Barker and my secondary supervisors, Mr Alan Davidson and Dr John Sharp for all their expertise, assistance and support throughout.

I am also grateful to Mr Bill Brownlee, Mr Derek Cogle and Mrs Lynn Chalmers for all their time and assistance during my testing in their respective laboratories.

Declaration

I hereby declare that the work presented in this thesis was solely carried out by myself at Edinburgh Napier University, except where due acknowledgment is made, and that it has not been submitted for any other degree.

.....

Jonathan R. Smuga (candidate)

.....

Date

Contents

Abstract	i
Acknowledgements	iii
Declaration	iv
Contents	v
List of Figures	x
List of Tables.....	xv
Glossary of Symbols	xvi
1 Introduction	1
1.1 Electromagnetic Interference Issues	2
1.2 Aims and Objectives.....	5
1.3 Silberline.....	6
2 Literature Review.....	7
2.1 Traditional Approach to Shielding	7
2.2 Metallising Processes.....	8
2.2.1 Electroless Plating.....	8
2.2.2 Evaporation Coating.....	8
2.2.3 Sputter Coating	9
2.2.4 Metallic Conformal Coating	9
2.3 General Electrical Conduction.....	10
2.4 Conduction Mechanisms.....	11
2.5 Atomic Structure.....	12
2.6 Quantum Hopping and Tunnelling	16
2.7 Magnetic Properties	17
2.8 Inherently Conductive Polymers	18
2.9 Conjugated Chain Polymers	18

2.9.1	Polyacetylene	19
2.9.2	Polyaniline	20
2.9.3	Polythiophene.....	21
2.9.4	Poly(3, 4-ethylenedioxythiophene) (PEDOT)	23
2.9.5	Charge Transfer Complexes.....	23
2.9.6	Organometallics	24
3	Electronically Conductive Polymer Composites	25
3.1	Conductive Composite Manufacture	25
3.2	Percolation	25
3.3	Percolation Theory.....	26
3.3.1	Random Resistor Networks	27
3.4	Poly(methyl methacrylate) Matrix.....	29
3.5	Filler Properties.....	30
3.6	Packing Factors.....	32
3.7	Filler Materials.....	33
3.8	Substrate Induced Coagulation	34
3.9	Nanomaterials	35
3.10	Carbon Nanotubes.....	36
3.10.1	Carbon Nanotube Polymer Composites.....	39
3.11	Graphene Sheets	41
3.12	Metallic Nanowires.....	42
3.13	Commercially Available Materials.....	43
4	Electromagnetism.....	45
4.1	Nature of Electromagnetic Waves	45
4.2	Maxwell's Theory.....	46
4.2.1	Maxwell's 1 st Equation	46
4.2.2	Maxwell's 2 nd Equation.....	46

4.2.3	Maxwell's 3 rd Equation	47
4.2.4	Maxwell's 4 th Equation	48
4.3	Shielding Theory.....	49
4.4	Shielding Requirements.....	55
4.5	Effective Conductivity.....	57
4.6	Effective Permittivity.....	59
4.7	Skin Depth	61
4.8	Network Analyser Analysis.....	62
4.9	Measurement Process	63
4.9.1	S - Parameters	64
4.10	Return Loss (Reflection/Impedance Mismatch).....	66
4.11	Transmission Lines and Impedance.....	66
4.12	Transmission Line Insertion Loss.....	67
5	Methodology	68
5.1	Sample Preparation.....	68
5.2	Filler Volume.....	68
5.3	Material Mixing	69
5.4	Printing of Coatings.....	69
5.5	Microsphere Technologies.....	71
5.6	Compression Moulded PMMA-Nickel Composite Plaque Manufacture	72
5.6.1	Brabender Plasti-Corder.....	73
5.6.2	Electroless Nickel Plating	74
5.7	Plaque Sample Density Measurements.....	79
5.8	Scanning Electron Microscopy and Elemental Energy Dispersive X-ray (EDX) Analysis.....	80
5.9	Surface Resistivity Testing	80
5.10	EMI Shielding Testing.....	83

5.11	Dual Dipole Antenna Method.....	84
5.12	Dual Horn Antenna Method	85
5.13	Waveguide Attenuation Method.....	87
5.14	Comsol Multiphysics Modelling	88
6	Results and Discussion.....	92
6.1	Initial Resistivity Measurements	92
6.1.1	Carbonaceous Samples.....	95
6.1.2	Carbon and Nickel Samples	96
6.1.3	Surface Resistance Variations.....	98
6.2	LCR Surface Resistivity Results	99
6.2.1	Silberline Samples.....	100
6.2.2	Microsphere Technology Samples.....	111
7	EMI Attenuation Results.....	129
7.1	Dipole Test.....	129
7.2	Horn Antennas Results	130
7.2.1	Attenuation Measurements	131
7.3	Waveguide EMI Attenuation Results	135
7.3.1	Silberline Samples.....	136
7.3.2	Expanded Graphite.....	137
7.3.3	Microsphere.....	139
7.3.4	Result Fluctuations - Normalisation and TRL Calibration	141
8	Investigation of Additional Processes	143
8.1	Electroless Plating of Expanded Graphite	143
8.2	Brabender Compounded PMMA-Nickel Compared Against Electroless Nickel Plated PMMA	149
8.3	Shielding Effectiveness.....	153
8.4	Comsol Multiphysics Modelling	156

8.4.1	Model Parameters.....	157
9	Conclusion	163
10	Suggestions for Future Work	165
11	References	166
12	Appendix A – Institute of Circuit Technology Publication	178
13	Appendix B – Resistivity Measurements.....	179
14	Appendix C – Waveguide EMI Measurements	180
15	Appendix D – Comsol Multiphysics Model Report	181

List of Figures

Figure 1.1, RF Spectrum

Figure 1.2, False Pulse Generation

Figure 2.1, Crystal Structure of Metals

Figure 2.2, Atomic Structure

Figure 2.3, Band Model of Conduction

Figure 2.4, Electron Transfer Between Sites Separated by Potential Energy Barrier

Figure 2.5, Polyacetylene Structure

Figure 2.6, Polyaniline Structure

Figure 2.7, Yanamoto and Lin/Dudek Routes of Polythiophene Synthesis

Figure 2.8, Sugimoto and Yoshima Route for Polythiophene Synthesis

Figure 2.9, Manufacture of Organometallic Networks

Figure 3.1, Percolation Curve

Figure 3.2, Lattice Percolation

Figure 3.3, PMMA Repeating Unit

Figure 3.4, Schematic of Constriction Resistance

Figure 3.5, Packing Arrangement

Figure 3.6, Expanded Graphite Production

Figure 3.7, Nanotube Structure Types and Vector System

Figure 4.1, Electromagnetic Waveform

Figure 4.2, Mechanisms of Shielding

Figure 4.3, Near and Far Field Regions

Figure 4.4, NSA Specifications for EMI Shielding of Enclosures

Figure 4.5, Skin Depth versus Frequency

Figure 4.6, Network Analysis Process

Figure 4.7, S-Parameters

Figure 4.8, Determination of S-Parameters

Figure 5.1, K-Control Printing Process

Figure 5.2, Composite Curing Behaviour

Figure 5.3, Glass Microsphere Production Process

Figure 5.4, Brabender Mixer Measuring Head

Figure 5.5, Deposition Rate with Time

Figure 5.6, Temperature Dependent Deposition Rate

Figure 5.7, Surface Resistivity Test Jig

Figure 5.8, Surface Resistivity Applications

Figure 5.9, Horn Antennas Apparatus

Figure 5.10, Initial CAD and Meshed Q-Band Model

Figure 5.11, Meshed Q-Band Model

Figure 6.1, SEM Micrographs of HCA-1 Nickel Flake

Figure 6.2, SEM Micrographs of 525 Regular Grade Nickel

Figure 6.3, SEM Micrographs of 525 Low Density Nickel Powder

Figure 6.4, SEM Micrographs of Sil-Shield Silver Coated Glass

Figure 6.5, Surface Resistivity of Carbon for Spectroscopy and HSAG 100 Samples

Figure 6.6, Surface Resistivity of Expanded Graphite Samples

Figure 6.7, Schematic Diagram of a Three Phase Composite

Figure 6.8, Surface Resistivity of Expanded Graphite Samples with Additional Nickel

Figure 6.9, SEM Micrograph of GA180 Particles

Figure 6.10, EDXA Spectrum GA 180

Figure 6.11, Surface Resistivity of GA 180

Figure 6.12, SEM Micrograph of GA 182 Particles

Figure 6.13, EDXA Spectrum GA 182

Figure 6.14, Surface Resistivity of GA 182

Figure 6.15, SEM Micrograph of GA 184 Particles

Figure 6.16, EDXA Spectrum GA 184

Figure 6.17, Surface Resistivity of GA 184

Figure 6.18, SEM Micrograph of GA186 Particles

Figure 6.19, EDXA Spectrum GA 186

Figure 6.20, Surface Resistivity of GA 186

Figure 6.21, SEM Micrograph of L1-1837 Flakes

Figure 6.22, EDXA Spectrum L1-1837

Figure 6.23, Resistivity Measurements of L1-1837

Figure 6.24, SEM Micrograph of L-60 Silver Coated Microsphere

Figure 6.25, Surface Resistivity Measurements of L-60

Figure 6.26, SEM Micrograph of X-10 Silver Coated Particles

Figure 6.27, Surface Resistivity Measurements of X-10

Figure 6.28, SEM Micrograph of M-18 Silver Coated Microspheres

Figure 6.29, Surface Resistivity Measurements of M-18

Figure 6.30, SEM Micrograph of B55-LX Silver Coated Microspheres

Figure 6.31, Resistivity Measurements of B55-LX Microspheres

Figure 6.32, SEM Micrograph of SSB005 Silver Coated Microspheres

Figure 6.33, Resistivity Measurements of SSB005 Microsphere Samples

Figure 6.34, SEM Micrograph of SSB006 Silver Coated Microspheres

Figure 6.35, Resistivity Measurements of SSB006 Microspheres

Figure 6.36, SEM Micrograph of SSB007 Silver Coated Microspheres

Figure 6.37, Resistivity Measurements of SSB007 Microspheres

Figure 6.38, SEM Micrograph of SSB008 Silver Coated Microspheres

Figure 6.39, Resistivity Measurements of SSB008 Microspheres

Figure 6.40, SEM Micrograph of SSB011 Silver Coated Cenospheres

Figure 6.41, Resistivity Measurements of SSB011 Cenospheres

Figure 6.42, SEM Micrograph of SSB012 Silver Coated Cenospheres

Figure 6.43, Resistivity Measurements of SSB012 Cenospheres

Figure 6.44, SEM Micrograph of SSB013 Silver Coated Cenospheres

Figure 6.45, Resistivity Measurements of SSB013 Cenospheres

Figure 7.1, Dipole Antenna Attenuation

Figure 7.2, Attenuation Measurement of Expanded Graphite

Figure 7.3, Attenuation Measurement of 525 Regular Grade Nickel

Figure 7.4, Attenuation Measurement of 50% Expanded Graphite and 525 Low Density Nickel

Figure 7.5, Attenuation Measurement of Expanded Graphite and HCA-1 Nickel Flake

Figure 7.6, Attenuation Measurement of Expanded Graphite and 525 Regular Grade

Figure 7.7, Attenuation Measurements of Silberline Samples

Figure 7.8, S-Band Waveguide Attenuation Measurements of Silberline GA180

Figure 7.9, X-Band Waveguide Attenuation Measurements of Silberline GA180

Figure 7.10, Q-Band Waveguide Attenuation Measurements of Silberline GA180

Figure 7.11, S-Band Waveguide Attenuation Measurements of Expanded Graphite

Figure 7.12, X-Band Waveguide Attenuation Measurements of Expanded Graphite

Figure 7.13, Q-Band Waveguide Attenuation Measurements of Expanded Graphite

Figure 7.14, S-Band Waveguide Attenuation Measurements of SSB005 Microspheres

Figure 7.15, X-Band Waveguide Attenuation Measurements of SSB005 Microspheres

Figure 7.16, Q-Band Waveguide Attenuation Measurements of SSB005 Microspheres

Figure 7.17, Calibration Procedures Comparison

Figure 8.1, SEM Micrograph Virgin Expanded Graphite

Figure 8.2, EDX Analysis of Virgin Expanded Graphite

Figure 8.3, SEM Micrograph of Heat Treated Expanded Graphite

Figure 8.4, EDX Analysis of Heat Treated Expanded Graphite

Figure 8.5, SEM Micrograph of Heat Treated Expanded Graphite after Nickel Plating Bath

Figure 8.6, EDX Analysis of Heat Treated Expanded Graphite after Nickel Plating Bath

Figure 8.7, SEM Micrograph of Electroless Nickel Plated Expanded Graphite

Figure 8.8, Expanded Graphite after Standard Nickel Plating Bath

Figure 8.9, PMMA Granule Dimensions

Figure 8.10, S-Band Attenuation Measurements of Brabender Compounded Samples

Figure 8.11, S-Band Attenuation of Electroless Nickel Plated PMMA Samples

Figure 8.12, S-Band Attenuation of Electroless Nickel Plated Ground PMMA Samples

Figure 8.13, Model Navigator

Figure 8.14, Material Boundary Conditions

Figure 8.15, Comsol Simulation Indicating Electric Field Strength

Figure 8.16, Simulated Attenuation Values of Nickel/PMMA Composite

Figure 8.17, Simulated Attenuation Values of Graphite/PMMA Composite

List of Tables

Table 1 - Relative Conductivities

Table 2 - Mechanical Properties of Engineering Fibres

Table 3 - Transport Properties

Table 4 - 2 Port S - Parameters

Table 5 - Density and Resistivities with Phosphorus Content

Table 6 - Waveguide Information

Table 7 - Typical Shielding Requirements of Electronic Devices

Table 8 - Initial Resistivity Test Results

Table 9 - Carbonaceous Powder Properties

Table 10 - Variation of Resistivity with Pressure Applied

Table 11 - Orientation of Surface Resistivity Measurement - 525 Regular Grade Nickel

Table 12 - Orientation of Surface Resistivity Measurement – 50% Expanded Graphite
with Additional 525 Regular Grade Nickel

Table 13 - Elemental Analysis of GA180

Table 14 - Elemental Analysis of GA182

Table 15 - Elemental Analysis of GA184

Table 16 - Elemental Analysis of GA186

Table 17 - Elemental Analysis of L1-1837

Table 18 - Properties of Microsphere Samples

Table 19 - Density and Dielectric Properties of Plaques Produced

Table 20 - Effective Conductivities of Composites

Glossary of Symbols

A	Area
α_R	Reflection Loss
α_A	Absorption Loss
α_{IR}	Internal Reflection Loss
B	Magnetic Induction
C	Capacitance
C_o	Capacitance in Vacuum
D	Dissipation Factor
δ	Skin Depth
E	Electric Field Strength
ε	Permittivity (Dielectric Constant)
ε_o	Permittivity of Free Space
ε_r	Relative Permittivity
Γ	Reflection Coefficient
η_o	Characteristic Impedance in a Vacuum
H	Magnetic Field Strength
I	Current
J	Current Density
k_o	Wave Number of Free Space
l	Length
λ	Wavelength
M	Magnetisation, Mass
m	Magnetic Moment

μ	Permeability, Drift Mobility
μ_o	Permeability of Free Space
μ_r	Relative Permeability
ω	Angular Frequency
P	Power
q	Charge
R	Resistance
R_c	Constriction Resistance
r	Radius
ρ	Density
ρ_{apparent}	Apparent Density
ρ_s	Surface Resistivity
ρ_p	Reflected Power
ρ_v	Reflected Voltage
σ	Conductivity
t	Critical Exponent of Conductivity
τ	Torque, Transmission Coefficient
V	Voltage
V_1	Volume Fraction of Matrix
V_2	Volume Fraction of Filler
Z	Impedance
Z_m	Intrinsic Impedance
Z_{pw}	Plane Wave Impedance

1 Introduction

Electromagnetic radiation is a combination of electronic and magnetic energy that spans the frequency spectrum with varying properties and applications. As can be seen in Figure 1 these range from low energy (large wavelength) radio waves through to high energy (very short wavelength) gamma radiation. The scope of this investigation will be to examine electromagnetic waves within the microwave region, predominantly in the ultra high frequency and super high frequency ranges, for interference issues and to examine the potential role for polymeric composites as suitable shielding solutions. Electromagnetic studies have been one of electrical engineering's original and fundamental subject matters and are still as valid as ever today. Growth in modern electronic devices has ensured that electromagnetic waves have become more ubiquitous than ever ^[1]. Alongside traditional electromagnetic emitting devices such as radios and television, the current trend towards wireless devices has seen the collective signals combine and create an ever more congested electromagnetic environment ^[2]. With processing speeds, frequencies and functionality of such devices regularly increasing, this electromagnetic environment is only set to become more saturated and consequently the need for shielding will also increase ^[3-4].

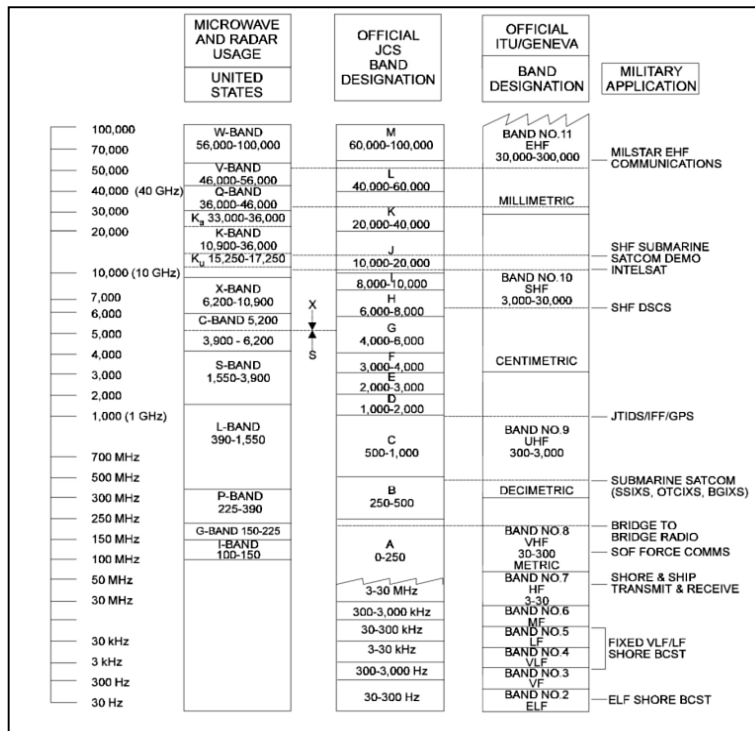


Figure 1.1, RF Spectrum [2]

1.1 Electromagnetic Interference Issues

Electromagnetic interference (EMI) controlling methods are varied and largely dependent on the type of EMI and constraints within the emitting product or device itself. There are two main types of EMI to investigate - those consisting of conducted interference, and those of radiated interference;

- With conducted radiation the EMI is conducted through cabling and circuitry. This kind of problem is best solved through electromagnetic (EM) filtering and designing devices with EM in mind [5-6]. However this is beyond the scope of this investigation and is not something that will be considered here.

- Radiated emissions are more random and require that devices are shielded from EM waves penetrating into susceptible components, and from internally generated emissions escaping and potentially creating interference problems elsewhere [7]. This can be achieved through encasing the device in a shielding housing. This provides a barrier that is impenetrable to EM waves. Shielding materials generally require high electrical conductivity. However in the case of composite materials, full electrical connectivity is not always required for shielding, although it will significantly aid the shielding effectiveness [8].

EMI problems range from equipment damage, erratic responses, and general malfunction. Many of these are caused by false signals being introduced to the system as can be seen in Figure 2, where a false pulse is generated due to an induced electromagnetic disturbance. In this example the device would be operating under normal conditions until a disturbance is induced into the signal, which in turn is detected by the device as an intended pulse. This could then be taken as a command resulting in an erratic response from the system.

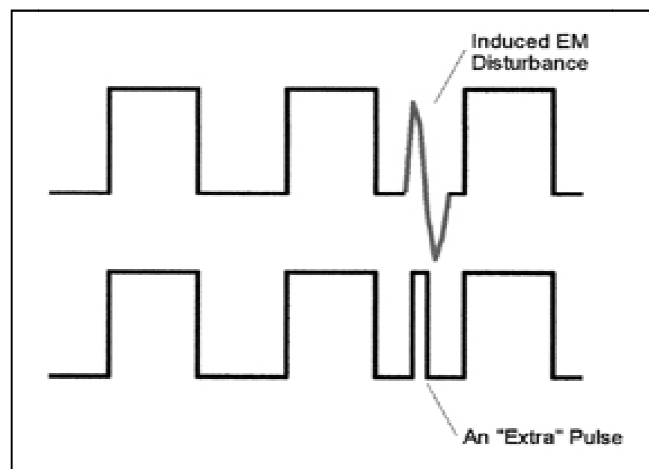


Figure 1.2, False Pulse Generation [9]

Electromagnetic emissions are waves generated and transmitted through the operation of a device and although these will not always cause operational interference they have the potential to reach a certain critical level where they will. Once the critical level is reached these emissions are classed as EMI. Examples of these forms of interference are;

- Parasitic emissions
- Intentional emissions, integral process for many devices
- Electrostatic discharges (ESD)

Parasitic emissions are the resultant electromagnetic fields that are generated as a by-product of a devices normal operation ^[10]. Although electromagnetic compatibility (EMC) regulations have been introduced in an attempt to control the level of emissions generated by such devices, the levels that are actually emitted are often much larger than predicted and designed for. A variety of conditions, including testing methods, the installation process, long cabling and often simply that shielding covers are not being utilised, can all influence the level of EMI emissions when operational. Parasitic emissions being unintentional and generally quite randomly generated are very unpredictable. This makes it more important to control them at the source through adequate design, shielding and correct operations ^[11].

Intentional radiation of electromagnetic waves is also a very important area to consider. Much of the electromagnetic environment comprises signals from electronic components ranging from mobile communication devices, to radio and TV broadcasting. These all operate at differing frequencies with different energy levels. The accumulation of all these signals alongside the parasitic emissions make up the background noise

levels that surrounds us all on a daily basis and have to be accounted for when investigating EMI problems.

1.2 Aims and Objectives

The aim of this research is to develop suitable manufacturing processes and testing procedures for electrically conductive polymer composite materials for use within the electronics industry as suitable shielding for electromagnetic interference applications. It is imperative that the manufacture and test regime is relevant to commercial applications while being sufficiently rigorous to provide reproducible and comparable results. The project has been undertaken in collaboration with an industrial partner Silberline with the aim of producing an ink, paint or solid plastic suitable for housing or coating electronic shielding enclosures. Silberline's assistance has involved providing filler materials, manufacturing equipment and relevant industrial knowledge.

Research will focus on the following key areas;

- Development of screen printable composite materials and test sample production methods.
- Investigation and comparison of filler material properties and the resultant composite characteristics.
- Comparison of alternative materials and production methods for conductive polymer composites.
- Development of a suitable procedure for electronic and electromagnetic shielding effectiveness testing.

- Simulation of the electromagnetic shielding behaviour in Comsol Multiphysics.

1.3 Silberline

Silberline was founded in 1945 to manufacture and supply effect pigments for the paint, industrial coating and polymer industry. Focusing their product range mainly on aluminium and aluminium alloys, they manufacture a range of pigments with varying visual properties. Although highly focused on the effect pigments industry and providing improved aesthetics, they developed an interest in the possibility of functionalising their pigments. This project will investigate filler materials for sample manufacturing and testing provided by Silberline alongside other commercially available materials.

2 Literature Review

2.1 Traditional Approach to Shielding

Common methods of shielding involve housing the device within a conductive barrier of sheet metal or wire mesh that dissipates the energy safely away. This process follows Faraday's cage principle which states that within an enclosed conductive area no electrical field will be present, and equally the opposite is true that no EM field will escape an enclosed conductive area. This effect occurs due to the application of Gauss's law where all excess positive or negative charge in a conductor will reside on the surface. Due to the ability of the charge to move within this conductor, the free charges redistribute themselves nearly instantaneously until each charge is under zero net force. Therefore the electrostatic field inside a charged conductor and away from the surface is zero ^[12-13]. Solid metal sheeting is rarely a viable option as metals are expensive and the limitations of size, weight, shape and manufacturing processing render them unsuitable for many modern applications. Foil covers can also be utilised as shielding blankets but can be subject to apertures along the seams which can then act as a transmitting slot antenna, exacerbating the interference ^[14]. Polymers on the other hand, are relatively inexpensive and can be easily processed into complex shapes that can provide lightweight housings. Unfortunately, polymers are generally highly insulative materials that provide little or no barrier to EM waves. As a result, conductivity modification to the polymer is required to enable shielding behaviour. This could be in the form of metallising a preformed polymer through a variety of methods including electroless plating, chemical vapour deposition and vacuum deposition amongst others ^[15-16]. These will all provide a good EMI shield but the overall operation can be costly as there are

many different stages and materials required. Other alternatives include modifying the polymer chemistry to allow for conduction within the polymer structure. This has its own limitations which will be further discussed later in the investigation.

2.2 Metallising Processes

2.2.1 Electroless Plating

Electroless (or autocatalytic) plating involves chemically bonding metallic ions onto the surface of a substrate without the need for a conductive substrate or electrical currents. The deposition is highly uniform and allows for complex shapes to be plated. However it can be relatively slow and can also be expensive due to the chemicals and multiple process stages required. The nature of the process provides double sided plating with high conductivity and effective shielding for low material deposition ^[17-18].

2.2.2 Evaporation Coating

The coating material is vaporised inside a high vacuum chamber and deposited onto the substrate surface as it condenses. This vaporisation can be achieved through resistive heating, cathode arc, electron beam bombardment, or by laser. Being a line of sight process, the complexity of the work piece that can be plated is limited and sizes are restricted by chamber dimensions. However in certain commercial processes large scale vacuum chambers, of up to 20 m², have been constructed. In operations of this scale, continuous or semi-continuous reel to reel processing is common. This involves a flexible substrate that is passed from reel to reel over a ceramic crucible, known as a

boat, containing the metal being vaporised. This vapour then condenses on the substrate as it passes over. Rigid substrates such as glass can be metallised in a similar semi-continuous process. The quality of coating is dependent on a high level of vacuum, as any vapour can contaminate the deposited metal. This results in a loss of adhesion, conductivity and appearance quality^[19].

2.2.3 Sputter Coating

Another form of vacuum deposition is the sputter coating process. Unlike evaporation, sputter coating is a momentum transfer process where ionised gas becomes attracted to the negative surface of a material, bombarding it and dislodging the surface atoms before depositing them back onto a substrate. This process can transfer a small volume of metallic material from a high purity metal known as a “target”, resulting in very thin and uniform coatings often only micrometers thick. In general sputtering is limited to coating of small objects, due to the line of sight nature and the restrictive dimensions of the vacuum chamber. Larger scale commercial sputtering is utilised for the metallising of glass sheets using an inline sputtering system that incorporates an arrangement of locks, pre-treatment chamber, sputter chamber and venting chamber^[20].

2.2.4 Metallic Conformal Coating

A novel processing technique known as metallic conformal coating has been developed that robotically sprays atomised low melting point metals or metal alloys onto the desired substrate. Unlike traditional thermal spray coatings, which deposit metals at high temperatures and often highly oxidised, metallic conformal coating is suitable for

coating polymers. The molten metal flows, flattens and cools almost instantly and without the thermal mass required to be detrimental to thin-walled plastic substrates ^[21]. Mechanical interlocking with the substrate surface ensures strong adhesion but once again being a line of sight process, although more flexible than vacuum processes, this will limit the complexity of substrate suitable.

2.3 General Electrical Conduction

In order to study the mode of conduction within a material, it is important to investigate the process of mobility within the atomic structure of such materials.

Electronic conduction involves the mobility of electrons or holes within a material's atomic structure. Holes are empty electron vacancies of equal positive charge that allow for a free electron to move into such a hole. Therefore, as the electron moves in one direction the hole moves the opposite way thus allowing electronic conduction throughout the material. The conductivity of a material is governed by the basic equation;

$$\sigma = q n \mu \quad (1)$$

Where σ = Conductivity, q = charge, n = concentration and μ = Drift mobility.

The drift mobility (μ) is a measurement of the ease that a charged body can pass through a material when under the influence of an external applied electrical field and is expressed as the velocity per unit field ($\text{m}^2\text{V}^{-1}\text{s}^{-1}$). ^[22]

2.4 Conduction Mechanisms

Electrical conductivity is defined as the quantity of electrical charge that is transferred per unit of time over a unit of cross sectional area under a unit potential difference gradient;

$$\sigma = \frac{\left(\frac{dq}{dt}\right)}{A\left(\frac{dV}{dx}\right)} \quad (2)$$

Ohms law describes an equivalent definition as the ratio of the current density to electric field;

$$\sigma = \frac{J}{E} \quad (3)$$

When a non-conducting material is subjected to an electric field it becomes electrically polarised. This relationship between the level of polarisation and the electrical field it has been influenced by, is known as the materials permittivity or dielectric constant ϵ .

$$\epsilon = \epsilon_0 + \frac{P}{E} = \epsilon_0 \left(1 + \frac{P}{\epsilon_0 E}\right) = \epsilon \epsilon_r \quad (4)$$

Where P is the polarisation density, ϵ_0 is the permittivity of free space and ϵ_r is the relative permittivity or dielectric constant.

Therefore this dielectric constant is a measure of how much energy is stored within a dielectric material per unit electric field. It also affects the speed that an electromagnetic wave can travel within a material ^[5]. This value can be calculated directly by measuring the capacitance of a material in relation to the capacitance of a vacuum of the same dimension as the sample;

$$\epsilon_r = \frac{C}{C_0} \quad (5)$$

2.5 Atomic Structure

Solid materials comprise atomic cores arranged in various repeating structures. The easiest to describe are crystalline structures; these consist of regular periodic structures of atoms in a defined arrangement known as the crystal lattice. These lattice structures are all repeating structures that share boundary atoms with neighbouring lattices making up a solid material. The arrangement of the atoms is what defines the lattice type. These different arrangements can result in seven main classes of lattice structure. Although some variety within each type is also possible. These seven classes are cubic, orthorhombic, tetragonal, monoclinic, triclinic, rhombohedral and hexagonal (Figure 2.1).

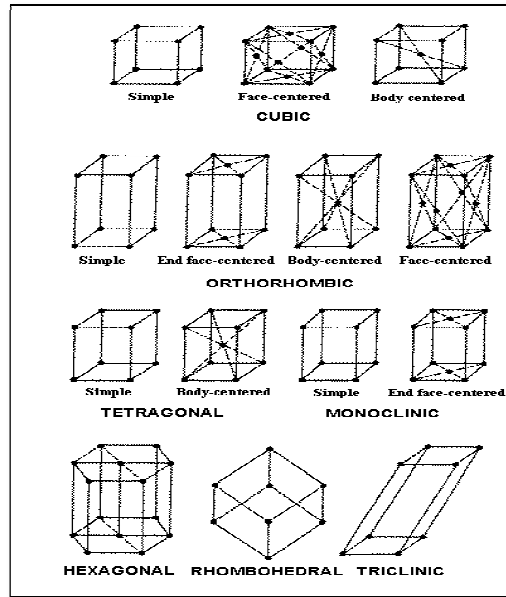
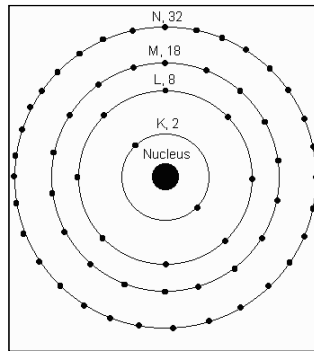


Figure 2.1, Crystal Structure of Metals ^[23]

The atomic structures of such lattices are often described as a combination of the positively charged ionic lattice surrounded by negative electrons. These separate components will affect material properties independently and “since all electrons are identical it can be shown that the differences in electronic properties are due more to the ions and their lattice symmetry than to the electrons themselves” ^[23].

The atomic structure of atoms has been described as a nucleus of neutrons and protons with orbiting electrons. These electrons are theorised to be grouped in several energy levels or bands, as can be seen in Figure 2.2 ^[24]. As the atom grows in size the extra electrons form new energy bands. It is the outermost band which influences the ease of electron transport.



(Figure 2.2 Atomic Structure [25])

When close enough to a neighbouring atom, these orbiting electrons can form bonds due to the orbitals overlapping. For example, when two hydrogen atoms pair, both the 1s-electron orbitals overlap and form two new σ electronic orbitals. In the case of crystalline solids, these divided energy levels form two continuous energy bands known as the valence and conduction bands (Figure 2.3), which are separated by a band called a forbidden zone free of electrons sites. For significant conduction to occur electrons are required to be in the higher electron bands where the charge-carrier mobilities are high [26].

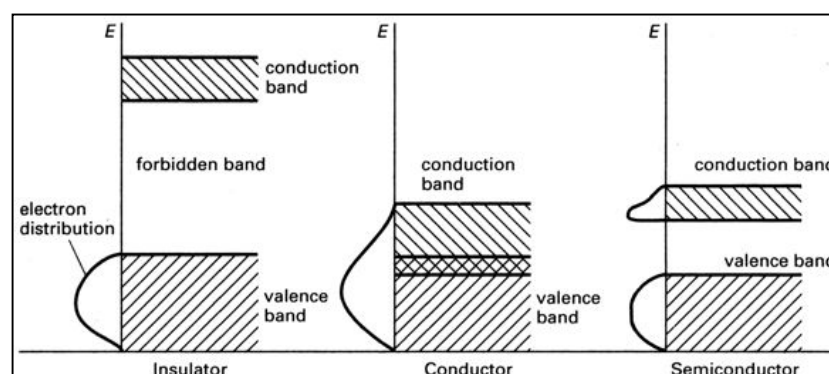


Figure 2.3, Band Model of Conduction

In good conductors the valence and conduction bands are said to overlap, i.e. requiring no extra energy to allow the electron transfer to occur. In the case of semi conductors

this energy gap is small enough to require only a small input of energy, which allows the electrons to be excited into the conduction band providing conduction.

Typical band gaps are 0 eV for metals, 0.5 – 5.0 eV for semiconductors and greater than 5.0 eV for insulators.

Intrinsic semi conductors are materials which naturally have small enough band gaps to require only a minimal input of thermal energy to stimulate electron transfer between valance and conduction bands. Materials such as germanium, band gap 0.7 eV, and silicon, 1.1 eV, are both intrinsically semiconducting but still have relatively high resistivities of 50 ohm/cm and 2×10^5 ohm/cm respectively ^[27]. Such resistivity can be greatly reduced via doping to create extrinsic semiconductors. One method of doping is to add minute quantities of a donor element with a higher valence, such as arsenic, into the crystalline lattice. This results in additional electrons being only loosely bound into the structure and at temperatures close to room temperature the bonds are broken. The electrons are now available for conduction. This type of semiconductor is known as n-type (negative).

Similarly if the dopant is of a lower valence, such as boron, it is known as an acceptor. The addition of it into the crystalline structure results in a bond unfilled which is then in turn filled from a neighbouring electron creating a free hole within the structure. This is type of semiconductor is known as p-type (positive).

2.6 Quantum Hopping and Tunnelling

As disorder within the lattice increases, the mobility is lowered and electronic energy states become increasingly more localised. In the band gap model these new energy states can be created within the previous forbidden zone. The process of electron hopping or tunnelling is the ability of electrons to cross the forbidden zone. Conduction may occur under sufficient thermal energy by an electron hopping the energy barrier. Electrons can tunnel through such a barrier even when they do not have sufficient kinetic energy to hop it (Figure 2.4). “If two electrodes are separated by a sufficiently thin insulating film current can flow between them by means of the tunnel effect. It is known that at low voltages this current is ohmic”^[28] .

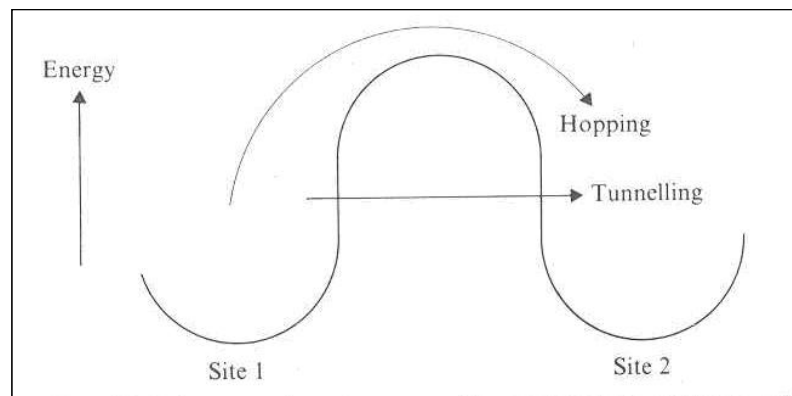


Figure 2.4, Electron Transfer Between Sites Separated by Potential Energy Barrier^[22]

2.7 Magnetic Properties

Magnetisation is classed as the magnetic moment “ m ” of a material per unit volume under the action of a magnet. The magnetic moment is therefore the highest torque value “ τ_m ” imparted onto a material when subjected to a magnetic field in free space, divided by the magnetic field “ H ”;

$$m = \frac{\tau_m}{\mu_0 H} \quad (6)$$

Where μ_0 is the permeability of free space, and the magnetisation is therefore;

$$M = \frac{m}{V} \quad (7)$$

Magnetic susceptibility “ X ” is a material property relating to the ratio of magnetisation with the magnetic field strength;

$$X = \frac{M}{H} \quad (8)$$

Similarly the magnetic permeability of a material is the ratio of the magnetic induction “ B ” to the magnetic field strength;

$$\mu = \frac{B}{H} \quad (9)$$

Magnetic induction is given by;

$$B = \mu_0(H + M) \quad (10)$$

Therefore, this gives the relationship between the susceptibility and the permeability;

$$\mu = \mu_0(X + 1) = \mu_0\mu_r \quad (11)$$

2.8 Inherently Conductive Polymers

Polymers that are conductive as a result of their structure are known as inherently conductive polymers (ICP). They can be synthesised for a specific structure or to contain dopants to allow electron transfer.

2.9 Conjugated Chain Polymers

One solution can be achieved through modification to the polymer structure to allow the transfer of electrons along a chain structure known as a conjugated chain polymer. These involve chemically unsaturated polymers that have a backbone chain structure of alternating single and double bonded atoms. The simplest form is polyacetylene (Figure 2.5). This structure allows for each carbon atom to be bonded with only one other kind of atom (in this case a hydrogen) and leaves one electron free from each carbon atom. These overlap and can create what is known as a delocalised molecular π -orbital. "If π -orbital overlap extends throughout a very long chain, the discrete set of molecular

electronic states may be expected to merge into a half full valence band, giving metallic-like conduction within the molecular chain” [22].

Historically the main drawback in utilising many of these polymers is that they have tended to require high crystallinity and stereoregularity for good conductivity often leaving them impractical to produce, especially while maintaining conductivity. However recent developments in the field have seen this situation change.

2.9.1 Polyacetylene

Polyacetylene was instrumental in the development of many conducting polymers with the initial fundamental research on doped polyacetylene leading to the three professors involved sharing the 2000 Nobel Prize in chemistry [29]. Although early research predicted that pure polyacetylene could exhibit metallic like conduction, these polymers were discovered to be intrinsically semi-conducting. Shirakawa et al. discovered in the early 1970's that synthesis of polyacetylene was achievable from acetylene in the presence of a Zeigler catalyst. This research group also showed it was possible to thermally control the synthesis producing a full trans-polyacetylene structure which was stable at room temperatures. However this was found to be only semiconductive [30]. It was subsequently proven that through the halogen doping of semi-conductive trans-polyacetylene, conductivity could be increased by 7 orders of magnitude into a metallic like conduction state [31]. As Figure 2.5 shows polyacetylene is theoretically the most basic conjugated structure but in practice, disorder generally limits its electrical conductivity and therefore has seen little commercial development.

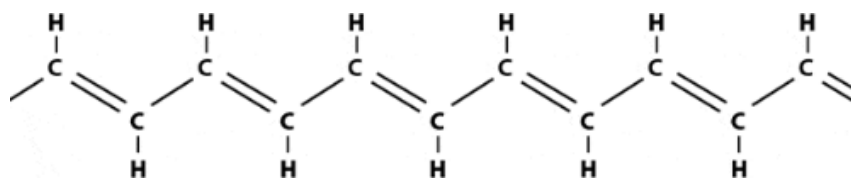


Figure 2.5, Polyacetylene, ^[32]

The field of ICP's was still an area of continual interest and in the 1980's Heeger and MacDiarmid successfully developed electrochemical doping methods which opened the door to advances in conductive polymers and further new applications.

2.9.2 Polyaniline

Polyaniline can be synthesised via two varying methods. This approach can be either oxidation or by protonation of the base emeraldine structure through an acid treatment (Figure 2.6) ^[33-34]. Both chemical and electrochemical oxidation treatments have been shown to be successful at producing conductive polyaniline and it was utilising functionalised acids to protonate and convert polyaniline into a conductive form which enabled Cao et. al. to produce a processable polymer soluble in organic solvents ^[35]. The functionalised acid also aided compatibility with non-polar and weakly polar organic liquids and polymers which enabled polyaniline polyblends to be formulated ^[36].

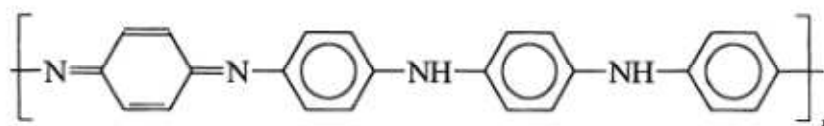


Figure 2.6, Polyaniline ^[34]

More recently polyaniline has been shown to combine well with functionalised graphene, an oxidation process that improves the wettability of graphene, to exhibit good conductivities and shielding characteristics. Zhang et al. demonstrated that by combining nano fibres of polyaniline with graphene oxide that composites with conductivities reaching 231.3 S/m were achievable ^[37]. Similarly, Basavaraja et al. were successful in producing composite sheets of polyaniline and gold nano particles which achieved a shielding effectiveness of 45-69 dB. When the addition of graphene oxide was also included into the composite an excellent shielding effectiveness of 90-120 dB was achieved. Considering the graphene oxide alone only provided 20-33 dB of attenuation it was surmised that the addition of graphene oxide must greatly enhance the interaction between the polyaniline and gold nano particles ^[38].

2.9.3 Polythiophene

Polythiophene was developed using the electropolymerisation technique that had previously been utilised in the earlier discovery of the aromatic conductive polymer polypyrrole. Polypyrrole can be easily synthesised in the doped state from suitable electrolyte and conductive electrodes. Although polythiophene is slightly more difficult to oxidise it produces a more stable polymer. Initially, this synthesis was carried out by either the Yanamoto route or the Lin and Dudek route. Both methods are metal catalysed condensation reactions that use magnesium and tetrahydrofuran. They vary slightly with the different metallic additions utilised in the reaction, as can be seen in Figure 2.7 ^[39-40].

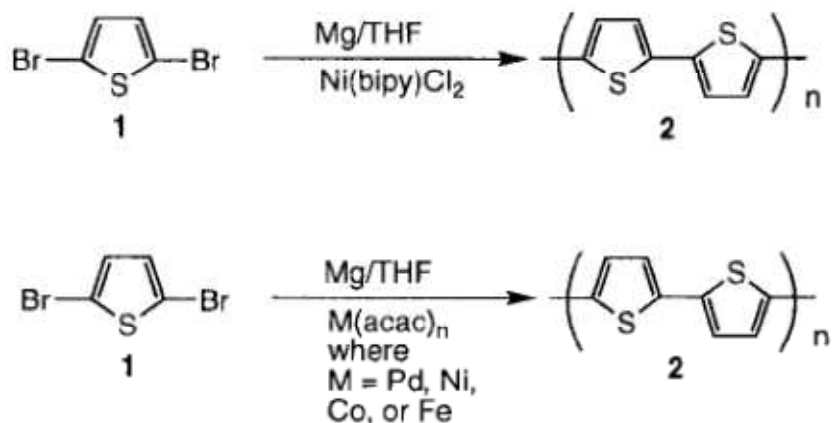


Figure 2.7, Yanamoto and Lin/Dudek Routes of Polythiophene Synthesis ^[41]

The two methods both form insoluble low molecular weight polythiophene with approximately 1-3% magnesium remnant within the polymer ^[41]. Another common approach is to polymerise thiophene at room temperature with a ferric chloride oxidant in chloroform as developed by Sugimoto and Yoshima (Figure 2.8) ^[42]. Karim et al. have utilised this approach to combine carbon nanotubes during in situ polymerisation to produce a composite which increased the conductivity of polythiophene from 1.67×10^6 (S/cm) to 0.41 (S/cm) ^[43].



Figure 2.8, Sugimoto and Yoshima Route for Polythiophene Synthesis ^[41]

2.9.4 Poly(3, 4-ethylenedioxythiophene) (PEDOT)

PEDOT is synthesised via a deprotonation polymerisation process from the monomer EDOT. Although inherently conductive the PEDOT polymer was of limited practical use due to its insolubility. This limitation was overcome when Bayer AG developed a soluble compound of PEDOT and poly(styrene sulfonic acid) (PSS) ^[44-45]. This ensured that PEDOT became a commercial success and has been utilised by AGFA as a transparent heavy metal free antistatic coating for their photographic film and has also been used in printed circuit board (PCB) fabrication.

2.9.5 Charge Transfer Complexes

Charge transfer complexes are a class of organic compound similar to radical ion systems that exhibit high electrical conductivity. These can be incorporated into polymers and still retain the majority of their electrical properties. These charge transfer complexes are formed through a donor molecule with low ionisation potential partially transferring electrons to another acceptor molecule with high electron affinity. Charge transfer complexes form into a rigid stacked crystalline structure giving a brittle, highly anisotropic material with conduction being the greatest along the stacked layers ^[46]. In the 1990's, demand in microelectronics packaging saw chemical companies such as Ciba-Geigy develop polymer film coated for antistatic applications using charge transfer salts in a polymer matrix ^[47].

2.9.6 Organometallics

Molecules that contain metal-carbon bonds are known as organometallics and can exhibit electrical properties similar to the metals contained within them. These organometallic groups can be incorporated into polymer structures and impart some electrical properties to the chain as a whole. This effect has been explained by the possible mechanism where the “metal d-orbitals may overlap with the π -orbitals of the organic structure and thereby extend electron delocalisation along a molecule”. This process has gathered recent interest with the development of conducting/semi-conducting polymers for applications such as corrosion control to light emitting diodes. Figure 2.9 shows two methods of manufacturing conjugated organometallic networks prepared by (a) ligand-exchange reaction and (b) polymerisation of pre-fabricated complex ^[22,48-49].

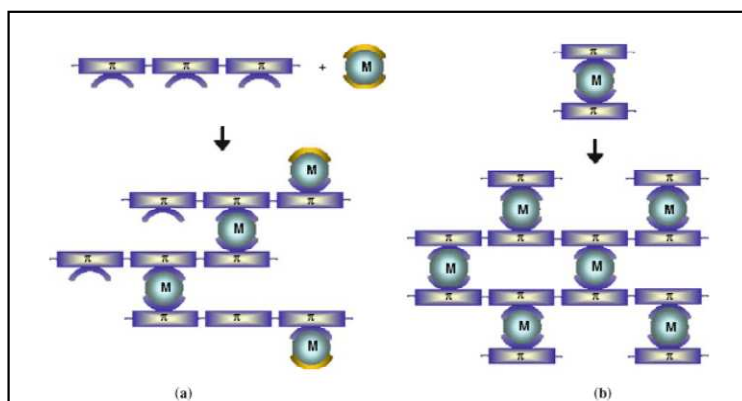


Figure 2.9, Manufacture of Organometallic Networks^[49]

3 Electronically Conductive Polymer Composites

3.1 Conductive Composite Manufacture

Conductive polymer composites can be manufactured through a variety of techniques depending on the properties of the polymer, the reinforcement and also the required properties of the final composite. The limitations on certain reinforcements such as long fibre and pre-fabricated mesh restrict them to manufacturing processes such as hand layup, prepregging^[50] or continuous processes such as pultrusion^[51]. Prepregging is where an intermediate composite is manufactured by pre-impregnated fibrous reinforcement with polymer resin. This then can undergo a final process to bind and form the near-finished product. Pultrusion is a continuous process where fibrous reinforcement is guided through a polymer resin impregnation stage before being drawn through a heated die. This forms and cures the composite into a uniform cross-sectional continuous product.

The less restrictive nature of particulate reinforcement allows for most standard polymer processing techniques to be utilised. This additional functionality improves the range of products and applications that are feasible.

3.2 Percolation

When manufacturing a conductive polymer composite by filling an insulative matrix with conductive fillers, the matrix gradually becomes less resistive as the volume of filler increases. This trend continues until the filler volume reaches a level where the

resistance rapidly drops (Figure 3.1). This is known as percolation threshold or critical volume. This resistance drop continues until a limit is reached and the reduction in resistance slows down again. At this stage conductive networks have been formed. Once percolation has been reached the addition of further fillers is unlikely to give any significant improvement to the conductivity but may be likely to have a detrimental impact on the mechanical properties of the composite [52-57].

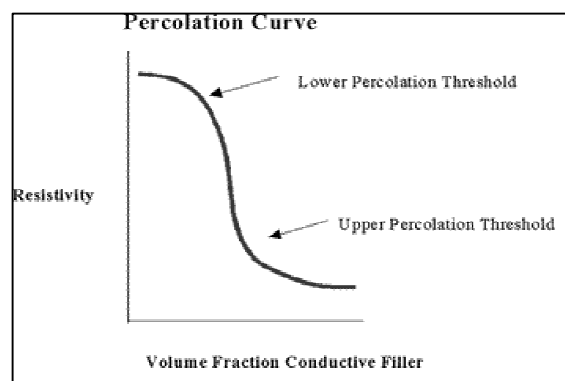


Figure 3.1, Percolation Curve

Percolation threshold values vary depending upon the filler and matrix properties. Typically the filler material is the heaviest and most costly aspect to a composite, therefore reduction in the percolation threshold value will optimise the amounts of filler required. Previous research shows that percolation thresholds are highly dependent on the filler particle shape and their distribution within the matrix [58].

3.3 Percolation Theory

Percolation theory is a statistical means of describing properties and behaviour of porous media, diffusion systems and conductive composites. Here the focus will be on the conductivity of composite materials and how the loading levels of conductive fillers

affect the overall system. These are known here as random resistor networks and are described as a grid system with sites that are either occupied by a conductor or remain empty and therefore insulating. This approach then models the system as the conductor sites are increased and positioned at random within the grid, therefore increasing the potential for conductive chains to form, until most sites are full and the material is effectively a perfect conductor ^[59-60].

3.3.1 Random Resistor Networks

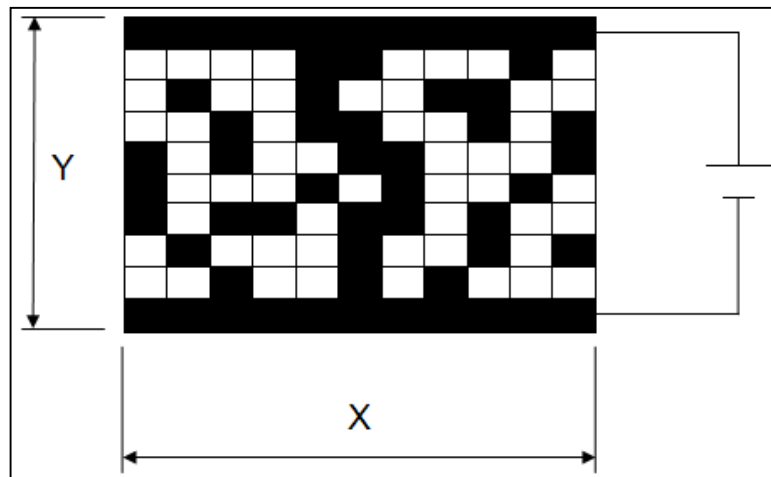


Figure 3.2, Lattice Percolation

For the example shown in Figure 3.2 the empty sites are treated as insulators, the shaded sites as conductors and current is only allowed to flow between sites that share a complete border. With a voltage being applied across the complete rows at the top and the bottom, and with a sufficiently large complete grid, the conductance of a sample would be proportional to the width X and inversely proportional to the height Y.

For grids that are large and do not have enough sites filled to create a path through, then the sample will have no conductivity, therefore loading volume V is far less than the

critical volume V_c (the volume required to create sufficient networks within the grid). On the other hand when V is 100% the grid's conductivity will equal that of the material filling the sites. If it is assumed that the conductivity is a single unit then;

$$\sigma_{V=100\%} = V_{V=100\%} = 1 \quad (12)$$

This is saying that for one unit voltage applied the grid will carry 1 unit current when filled with an ideal conductor. The relationship suggests that it will be proportional across the volume range greater than V_c . However experiments have proven this is not entirely correct and that the conductivity will not follow the same path when plotted against V , although in theory it should have the same V_c and conductivity at $V_{100\%}$. This is due to the fact that as the network is filling up, the conductivity only increases when a network is fully formed and therefore many semi complete networks can exist. These are known as dead ends and will be included in the volume fraction but not yet contributing to the overall conductivity.

To account for this, the power law relationship was developed by Kirkpatrick ^[60] for simple cubic resistor networks;

$$\sigma \propto (V - V_c)^t \quad (13)$$

Where t is the critical exponent of conductivity, this critical exponent has been extensively studied and is generally in the predicted region of 1.7-2.0 ^[61-63].

Above the percolation threshold the relationship changes to;

$$\sigma \propto (V_c - V)^t \quad (14)$$

3.4 Poly(methyl methacrylate) Matrix

The purpose of the matrix is to bind the conductive fillers together into a functional network. This can then be applied as a coating or formed into complex shapes that otherwise may not be suitable for manufacture out of metal.

Poly(methyl methacrylate) PMMA is a linear acrylic polymer, and was first developed c.1930 by both R.Hill ^[64] and D Bauer ^[65] independently (Figure 3.3). This discovery stemmed from the earlier development of methyl methacrylate which was being developed as a soft surface coating material. When polymerised they discovered it formed a transparent, stiff plastic that does not splinter upon shattering; ideal properties for use as aircraft windscreens.

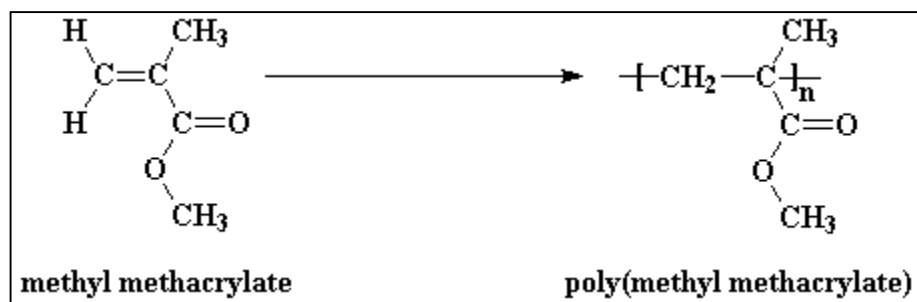


Figure 3.3, PMMA Repeating Unit ^[66]

Methyl methacrylate can be polymerised relatively simply by either bulk polymerisation or through suspension polymerisation depending on the application of the final polymer.

Bulk polymerisation is suitable for producing sheets and rods of PMMA as it involves preparing a prepolymer from the MMA monomer. This is done by removing any inhibitors through a mixing and heat treatment process. The resulting resin can be cast and further heat treated to polymerise within the moulds, into the final product. Solution polymerisation is more suitable for applications such as extrusion or injection moulding as it can produce a lower molecular weight polymer with improved flow properties ^[66]. The properties of poly(methyl methacrylate) (PMMA), such as its processability, transparency, weather resistance, good mechanical properties and low water absorption lend themselves well to a matrix although these come at a cost with its high volume resistivity ($1 \times 10^{13} \Omega\text{m}$) and poor solvent resistance.

3.5 Filler Properties

The filler characteristics are the most significant properties within such polymer composites. They are the foundation for the conduction mechanism within it. As such they will be the area where this research is primarily focused.

There has been significant previous research into conductive fillers within various forms of composite ^[67-70] and the fundamentals of this are transferable to this study. Much of the previous research has focused on the particle material, size and shape as the means of significant improvement of the conductivity and therefore electromagnetic properties. In general it is accepted that through utilising particles of high conductivity and high aspect ratio, a conductive network will form more successfully and at a lower percolation thresholds. The particle shape or aspect ratio is the key property dictating threshold values. Therefore by increasing the aspect ratios of filler, the contact area of

particles also increases. This is shown best by looking at the lowest possible aspect ratio spherical particles compared to high aspect ratio flakes. The point contact between spheres restricts the amount of current that can flow and is known as the constriction resistance. This is demonstrated in Figure 3.4.

This constriction resistance can be estimated by the equation;

$$R_c = \frac{\Omega}{2a} \quad (15)$$

Where;

Ω = Bulk resistance of the filler material

a = Contact spot radius

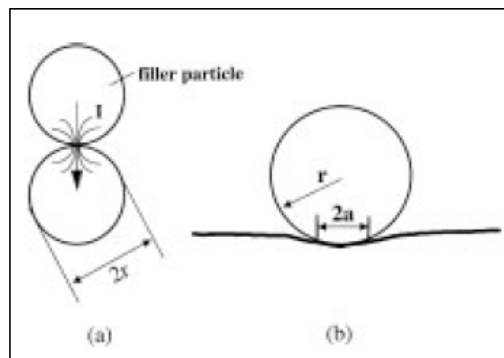


Figure 3.4, Schematic of Constriction Resistance ^[71]

“This constriction resistance is the resistance value to consider when examining composite resistance as long as the contact spot radius is considerably smaller than the radius of the particles, otherwise the bulk resistance of the filler material should be considered” ^[71].

3.6 Packing Factors

The order or packing arrangements that filler materials will form within the composite has a great bearing on many of the final materials properties. As can be seen in Figure 3.5, the two materials are of equal particle mass but different shape and therefore the packing arrangement is different. Thus this elongation of the particles aids the formation of contact networks more easily and ultimately will percolate at a lower volume.

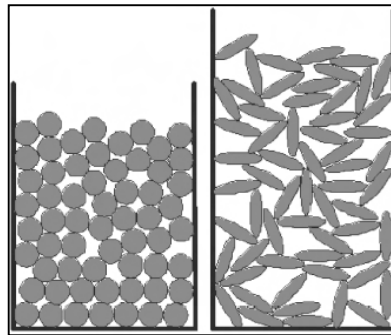


Figure 3.5, Packing Arrangement

Filler morphology can have more effect than just how easily or how much contact is made between particles. As described by D Bloor et al. ^[72], where they found that by using careful polymer/metal mixing methods the small and sharp protrusions present on the filler materials were preserved. By retaining such features they observed significant electron tunnelling behaviour. This was attributed to the fillers' sharp surface points acting in a similar manner to the tips in a scanning tunnelling microscopy. "The electric field strength at these tips is very large and results in field assisted tunnelling" ^[72].

3.7 Filler Materials

The variety of commonly available filler materials is large and they are generally chosen according to the required conductivity and associated cost. For applications where only electrostatic dissipation is a concern, then often carbon powder or carbon fibres will be sufficient but for other applications that require higher conductivity, then metallic fillers may be required. The range of material conductivities can be seen in Table 1.

Table 1 - Relative Conductivities ^[17]

**Electrical Conductivities of Materials
Relative to Copper**

Copper – 1.00
Silver – 1.05
Gold – 0.70
Aluminium – 0.61
Magnesium – 0.38
Zinc – 0.29
Brass – 0.26
Nickel – 0.20
Iron – 0.17
Tin – 0.15
Steel – 0.10
Lead – 0.08
Stainless Steel – 0.02
Graphite – 0.001

Common commercial fillers which are available are often pure metals or alloys of silver, nickel, stainless steel, copper, aluminium, tin, and carbon. One material worthy of note is graphite. Given that it is known to exhibit anisotropic conduction along its layered structure it does not instantly seem like a good material for a randomly orientated network that ideally requires isotropic conduction. What is unusual about graphite is that it can be chemically and thermally expanded. This exfoliates the layers and randomises the structure, forming a very low density material. It is formed by taking natural crystalline graphite and treating it with acids then rapidly heating it to

temperatures in the region of 1000°C (Figure 3.6). This process expands the weaker interlayer van der Waals bonds, which then allow the individual layers to collapse and support their surroundings. This allows for the expansion to remain after heating. This process can expand the graphite to between 100-300% of its volume and therefore should allow for very low percolation values. [73-78]

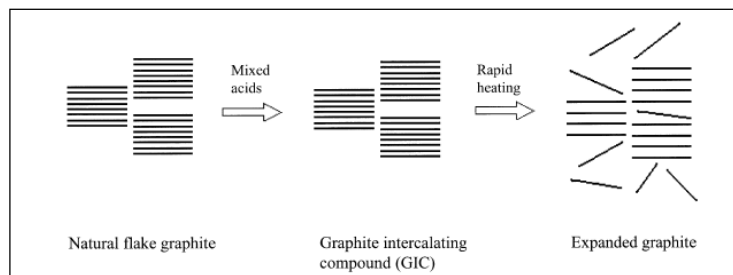


Figure 3.6, Expanded Graphite Production^[74]

3.8 Substrate Induced Coagulation

One alternative method of producing conductive polymer composites uses a surface coating technique known as substrate induced coagulation, where instead of conventionally filling a polymer matrix with conductive additives, non-conducting polymer particles are coated with a fine layer of conductive material through an aqueous dip coating process. The process is based on the interaction of a surface conditioner that is adsorbed alongside an additional conductive dispersion of fine particles onto the substrate surface. These coated particles are then compression moulded creating a network of the highly conductive coating material at a relatively low material volume. The process relies on compression at the correct temperature and pressure so as to allow for full agglomeration without melting the polymer substrate. Pre-coating of the polymer particles creates a network within the compressed sample at far lower

percolation than standard mixed composite as the conductive coatings will be in contact throughout the moulding process. Although this method is attractive in principle it is restrictive due to the pre-manufacture preparation and the limitations within the compression process that have to be rigorously controlled in order to optimise the network formation of the fine powders ^[79]. It does however suggest possibilities of producing conductive polymer composites following a more robust particle coating process such as electroless plating.

3.9 Nanomaterials

Since the discovery in 1985 of new stable ordered carbon structures known as Buckminster Fullerenes ^[80], the interest in carbon nanomaterials has rapidly expanded ^[81-84]. Further advances were made by Sumio Iijima in 1991 ^[85-87], where production of high quality nanotubes based on these fullerene structures opened the door to much of the recent developments that have many applications in composite materials. Utilising the unique properties of such nano-scale fillers, composites have been developed which have been shown to exhibit conductivity at highly reduced percolation thresholds. Additional desirable and beneficial properties such as flexibility or transparency are often also feasible. These had previously been unachievable with traditional fillers used in the manufacture of conductive polymer composites. As well as carbon nanotubes there is a range of other nanomaterials suitable for conductive applications including graphene, metallic nanowires and nano particles. Utilisation of these materials encompasses a variety of approaches and techniques for developing such nano-scale composites.

3.10 Carbon Nanotubes

Carbon nanomaterials have become increasingly popular for multiple applications due to their conductivity, aspect ratio and specific strength. Initially the development of these enclosed carbon structures known as Fullerenes began with the most common form Buckminster Fullerene (C_{60}), a spherical carbon structure containing 60 atoms all linked in hexagonal and pentagonal rings, also known as buckyballs. Additionally many other similar structures with varying numbers of carbon atoms have been discovered. Sheets of C_{60} are inherently semi-conducting and through the bonding of alkali metal cations onto the surface their conductivity can be increased into a metallic state. These have even been found to be superconducting at $-243\text{ }^{\circ}\text{C}$ with Rhodium cations^[88].

Following on from C_{60} , carbon nanotubes were developed. Through processes such as arc evaporation, catalytically grown and laser ablation, tubes of coiled layers of a graphite structure (known as graphene sheets) can be synthesised forming nano-scale tubes^[89-91]. The ends of these tubes are often capped with a half C_{60} dome type structures. Diameters of these tubes can be as small as 0.5 nm for single walled nano tubes and generally 3-30 nm for multiwalled nanotubes, although nanotubes as small as 4 angstroms wide have been measured at the core of a multiwall carbon nanotubes^[92]. Nanotubes can reach micrometers in length giving a very high aspect ratio material. They also have a theoretical tensile strength in the region of 300 GPa^[93] although published data on tensile strength has been found to differ significantly^[94-96]. The variations in these results are partly due to the nature of the non-standard testing methods implemented with some tests performed on single nanotubes within scanning electron microscope (SEM) chambers and others tests performed on bundled rope

specimens. There is also an inconsistency in the cross sectional area values applied to the calculations of tensile strength, with some authors measuring the total occupied cross section and others taking the smaller van der Waals areas. However it is clear that the specific strength of nanotubes is significantly higher than is achievable with conventional materials such as steel (Table 2).

Table 2 - Mechanical Properties of Engineering Fibres ^[97]

Fibre Material	Specific Density	E (TPa)	Strength (GPa)
Carbon Nanotube	1.3 - 2	1	10 - 60
Steel	7.8	0.2	4.1
Carbon Fibre - PAN	1.7 - 2	0.2 - 0.6	1.7 - 5
Carbon Fibre - Pitch	2 - 2.2	0.4 - 0.96	2.2 - 3.3
Glass	2.5	0.07 / 0.08	2.4 / 4.5
Kevlar 49	1.4	0.13	3.6 - 4.1

Nano tube structure types are often characterised by the angle of the coiled sheet into three main forms known as chiral, zigzag and armchair. These varying structures can be defined and referred to by a vector system (m, n) as seen in Figure 3.7.

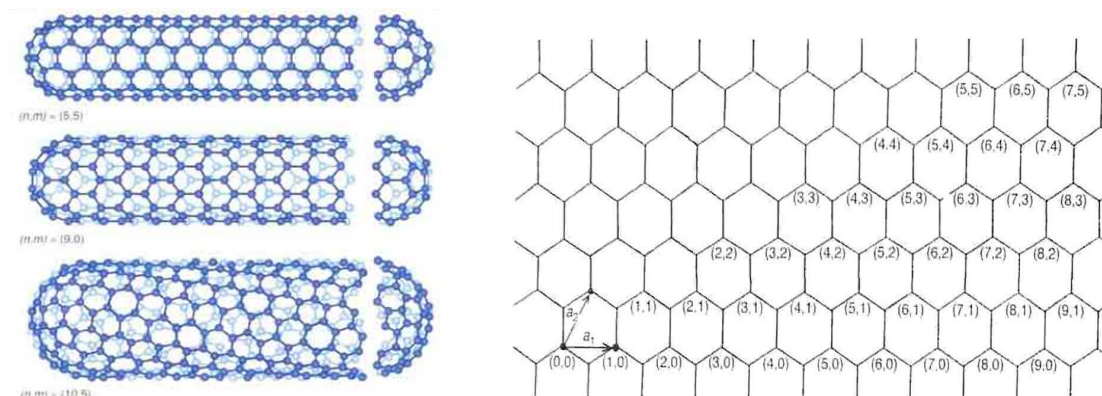


Figure 3.7, Nanotube Structure Types and Vector System ^[97]

These nanotubes can be single walled, double or multi walled where multiple graphene layers are coiled together. Each of these permutations has different properties and applications as the packing structure will determine the density and conductivity of the nanotubes.

The carbon-carbon bonds within armchair structures allow metallic type conduction where the structures of zigzag and chiral types give rise to a semi conducting state. Unlike many other structures where minute defects have great effects on the overall properties, carbon nanotubes can be synthesised to give a unique structural uniformity and therefore achieve values of conductivity, strength and thermal conductivity very close to the theoretical values. Typical values are given in Table 3.

Table 3 - Transport Properties ^[97]

Material	Thermal Conductivity (W/m.k)	Electrical Conductivity (S/m)
Carbon Nanotubes	> 3000	$10^6 - 10^7$
Copper	400	6×10^7
Carbon Fibre - Pitch	1000	$2 - 8.5 \times 10^6$
Carbon Fibre - PAN	8 - 105	$6.5 - 14 \times 10^6$

As previously mentioned, synthesis can be achieved through various methods including arc evaporation method, catalytically grown and laser ablated. Arc evaporation involves passing a current of approximately 50 A between two graphite electrodes in an inert helium atmosphere. This is sufficient to vaporise the graphite and re-deposit onto the cathode. Within the deposited graphite are multiwalled carbon nanotubes. Single walled tubes can also be synthesised by doping the anode with metals such as cobalt or nickel.

Catalytically grown nanotubes follow a chemical vapour deposition process to decompose a hydrocarbon gas over a transition metal. Already a well established

procedure to grow carbon fibres and filaments, it was shown in 1993 that multiwalled nanotubes could be grown by decomposing acetylene over iron particles. Further experimental work on the process utilising higher reaction temperature and replacing the acetylene with carbon monoxide or methane was successful in producing single walled nanotubes.

Laser ablation nanotubes are synthesised by pulsing an Nd-YAG laser into a 1200 °C heated argon atmosphere and directed onto a graphite and metallic target. All contained inside a sealed flow tube where the vaporised carbonaceous gas then condenses onto a cooled collector outside of the furnace area.

Each of these methods of production has its advantages, with the arc evaporation method probably producing the highest quality of nanotube. Catalytic growth and laser ablation methods are able to produce higher volumes than by evaporation and are also demonstrating a continual improvement in quality ^[98].

3.10.1 Carbon Nanotube Polymer Composites

Carbon nanotube polymer composites have been shown to be quite varied in potential applications from structural reinforcement, field emission displays, electrochemical/electromechanical devices, electronic materials and can even have biological applications ^[99-102].

Electronic applications are one of the primary commercial interests of nanotube polymer composite due to the high aspect ratio of nanotube fillers very low percolation

levels required ^[103-104]. Some manufactured pre-mixed blends of polymers with nanotube additions are available from companies such as Nanocyl and RTP. This low percolation threshold allows for functionalised composites which can retain certain aspects of the matrix polymer such as its mechanical properties, processability and aesthetics. Recent research in the field has seen Shrivastava et al. develop bulk polymerised polystyrene/multiwall nanotube composites with conductivity observed at a percolation threshold measured as low as 0.08% Wt ^[105]. Low percolation values of 0.12% Wt have also been reported by Jurewicz et al. in composites of carbon nanotubes and latex where by formulating the composite near to the glass transition temperature a segregated and ordered network was formed through the matrix. This was found to percolate at a threshold of almost 4 times lower than the equivalent random distribution of the same materials. This provided a reproducible method of manufacturing conductive and stretchable thin films with improved transparency ^[106]. A different approach to producing stretchable conductive composites has been reported by Yongjin et al. where a conductive nanotube composite layer was coated onto the surface of an elastomeric substrate. Higher loading levels of 20% Wt were utilised to provide good levels of conductivity that did not drop off significantly when under large levels of strain compared to the equivalent bulk nanocomposite ^[107]. EMI shielding studies of both single wall and multiwall nanotube composites have achieved shielding effectiveness values in the region of 20-28 dB although they have required high loading levels of up to 40% Wt ^[108-110]. This level of shielding is low in comparison to micro sized fillers, however the reduction in weight is significant.

3.11 Graphene Sheets

As discussed previously, carbon nanotubes are essentially monolayers of carbon atoms bonded into a hexagonal structure which exist as coiled tubes. These monolayer sheets are known as graphene and have unique properties in their own right. Consequently since its discovery there has been a surge of interest in graphene with the Nobel Prize in Physics 2010 being awarded to Andre Geim and Konstantin Novoselov for “ground breaking experiments regarding the two-dimensional material graphene”^[111]. They had managed to isolate and characterise these graphene sheets via a handcrafted technique that used adhesive tape to separate out an individual layer^[112].

Graphene sheets have been found to be one of the strongest materials ever measured. They exhibit a large electron capacity which allows electron transport without considerable scattering or resistance and can sustain current densities 6 times that of copper^[113-114]. These properties have made graphene a highly desirable research topic.

Incorporating graphene into polymer composites has been shown to be slightly problematic as fillers of such small scale have a tendency to agglomerate. In the case of graphene this can result in the restacking into graphitic layers due to van der Waals forces. Additionally pure graphene exhibits poor wettability characteristics which further hinders good dispersion within a polymer matrix^[115]. One solution to this is to synthesise graphene through an exfoliation process of graphite oxide powder. By oxidising graphite powder with nitric acid and sulphuric acid with potassium chlorate and then rapidly heating the mixture, exfoliated sheets of graphene can be obtained in relative bulk quantities. This form of graphene is termed oxidised or functionalised

graphene. It comprises sheets that are a few layers thick with remnant oxygen containing groups still present. This functionalised form has a higher surface energy and more of an affinity for polar solvents and polymers thus improving its dispersion properties ^[116].

Stankovich et al. demonstrated a good dispersion of graphene nanosheets within a polystyrene matrix reporting percolation threshold values in the region of 0.1% Wt. The same researchers further demonstrated this dispersion of functionalised graphene in a PMMA matrix finding the filler to be comparable to single walled carbon nanotubes ^[117-118]. Similar to carbon nanotubes, graphene nanosheets demonstrate potential in conductive transparent film applications. Tein et al. showed that by using a two stage process to form graphene nanosheets with an addition of silver nanoparticles to prevent the restacking, a transparent conductive film could be deposited onto a polyethylene terephthalate (PET) substrate ^[119].

3.12 Metallic Nanowires

Metallic nanowires can be produced through processes that involve the casting of solid nanoscale metallic fibres within nano pores or nanotubes. This can be achieved through wet chemistry, electron beam lithography and electrochemical growth ^[120]. Wet chemistry has been demonstrated as an accessible production route with examples of silver nanowires having been grown onto substrates via chemical reduction processes ^[121]. A similar method has been proposed as a suitable cost effective and greener alternative material in photovoltaic panel manufacture ^[122]. Silver nanowires have also been successfully produced through casting within peptide nanotubes where the silver

was chemically reduced inside the nanotube before enzyme degradation of the nanotube mould ^[123]. Low percolation composites of silver and copper nanowires in a polystyrene matrix have been reported by Gelves et al. where the nanowires were produced through electrodeposition into a porous alumina template. Percolation thresholds of 0.50-0.75 % Wt and 0.25-0.75 % Wt were reported for the silver and copper respectively. This more rapid percolation transition of the silver has been attributed to the lower aspect ratio and the reduction in surface oxidation ^[124].

3.13 Commercially Available Materials

There are various conductive polymer products commercially available with applications ranging from sprayable coating, flexible gaskets, conductive tapes and conductive adhesives. Parker is one of the largest manufacturers of such products and through their Chomerics division offer a variety of materials for a range of applications. Branded under the moniker “Cho-Shield”, they comprise formulations of acrylic, epoxy or polyurethane with fillers such as silver, nickel and copper. These are designed specifically for anti-static and electromagnetic shielding coatings ^[125-128]. Other similar commercial products include MG Chemicals “Super-Shield”, an acrylic nickel paint that is suitable for dip, brush or spray applications ^[129]. Creative Materials offer a silver filled epoxy ink “117-48” with improved abrasion resistance. intended for electromagnetic shielding as well as for printing thin conductive circuit lines ^[130]. As well as metallic particle based products, companies such as Ceno Technologies supply coated silver cenospheres and microspheres as conductive fillers ^[131].

In addition to coating applications, conductive elastomeric composites are commonly available. Kemtron is a company that specialise in EMC solutions. They produce a range of gaskets, o-rings and extruded parts made from silicone or fluoroelastomers. These are filled with either nickel, nickel coated graphite, silver coated aluminium or silver coated copper ^[132]. Similar products are also available from Speciality Silicone Products such as SSP547-65 a silver coated copper filled silicone elastomer, which can be supplied in fully cured sheet form or in compound for moulding applications ^[133].

4 Electromagnetism

4.1 Nature of Electromagnetic Waves

Electromagnetic waves are waves of electric (E) and magnetic (H) fields that consist of a definite wavelength and frequency (Figure 4.1). These are what define the wave and its characteristics, for example, visible light, radio waves and microwaves ^[134]. All electronic devices will generate associated electromagnetic fields, with the voltage creating the electric field and the current creating the magnetic field ^[135]. These fields in turn will induce voltages and currents in any conductive media encountered. This is the principle of antennas within televisions and mobile phones. It can also be very undesirable and cause problems, as previously indicated, within electronics systems i.e. electromagnetic interference. These signal interferences often cause unintended operation of equipment or sensors by mistaking the induced disturbance for an intended signal.

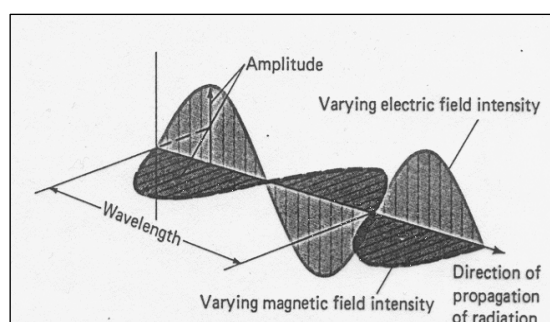


Figure 4.1, Electromagnetic Waveform

4.2 Maxwell's Theory

James Clerk Maxwell (1831-1879) was a Scottish born physicist and mathematician who managed to describe mathematically theories on magnetic and electrical charge distributions. Through these concepts he created a series of equations and developed a new term, the displacement factor. These equations would become synonymous with his name. Maxwell's equations express the varied existence of electricity, magnetism, their collaborative effects and behaviour ^[136-137].

4.2.1 Maxwell's 1st Equation

(Taken from Gauss's law for electric fields)

$$\int \vec{E} \cdot d\vec{A} = \frac{q}{\epsilon_0} \quad (16)$$

Maxwell's first equation represents the electric field strength from a closed surface. It models the surface as very small areas ($d\vec{A}$) which can be treated as if they were flat surfaces. The area vector ($d\vec{A}$) is the value of this area and will point outwards and perpendicular from the contained volume.

4.2.2 Maxwell's 2nd Equation

(The related formula for magnetic fields)

$$\int \vec{H} \cdot d\vec{A} = 0 \quad (17)$$

The second of Maxwell's equations is an equivalent equation to explain the magnetic field over a closed surface that has no magnetic sources within it. This is often visually described as the force lines of magnetic flux flow. As there are no magnetic sources present these lines always join themselves in closed loops indicating that the net flux is always zero.

4.2.3 Maxwell's 3rd Equation

(The electrostatic case)

The simplified form of the third equation is:

$$\oint \vec{E} \cdot d\vec{l} = 0 \quad (18)$$

By neglecting Faradays law of induction that states "if a closed circuit has a changing magnetic field through it, a circulating current will arise" ^[12] this in turn indicated a non-zero voltage within the circuit. The complete form of the third equation is:

$$\oint_c \vec{E} \cdot d\vec{l} = - \frac{d}{dt} \int_s \vec{H} \cdot d\vec{s} \quad (19)$$

Here the integral on the right hand side spans the area of the circuit on the left hand side and this induced current will generate a magnetic field that opposes any external field variations. This gives us two equal and opposite integrals on either side of the circuit and is true for any closed path spanning the circuit.

4.2.4 Maxwell's 4th Equation

(The magnetostatic case)

The magnetostatic version of the previous equations is taken from Ampere's law which states:

$$\oint \vec{H} \cdot d\vec{l} = \mu_o \quad (20)$$

The currents that are evaluated here are ones that pass through the span of the circuit. Again by deciding on the directions of these currents the opposite values can be subtracted to give the resultant total across the whole circuit.

Maxwell realised that this equation was not always a valid one since it did not account for any changing fields and therefore he introduced his "displacement current term". By thinking about the situation as a capacitor inserted into an infinite length of wire with a steady state current, the circuit will be uniform everywhere except at the capacitor plates where charges will be building up and dissipating.

The evaluation of the circular path about the wire moving away from the capacitor Ampere's law ^[138] gives a magnetic field of:

$$H = \frac{\mu_o I}{2\pi r} \quad (21)$$

However, with the capacitor plates being close enough together that a charging up of the plates can be observed, a change in electric field occurs without any current crossing the

surface. The total electric flux can be measured by the electric field lines from the charge on one plate flowing to the other. The electric flux is then given by:

$$\int \vec{E} \cdot d\vec{A} = \frac{q}{\epsilon_0} \quad (22)$$

The wire current is the rate of change of the charge, therefore:

$$I = \frac{dq}{dt} \quad (23)$$

By combining these two equations together:

$$I = \frac{d}{dt} (\epsilon_0 \int \vec{E} \cdot d\vec{A}) \quad (24)$$

Then by substituting this term into Ampere's law, Maxwell's 4th equation is stated as:

$$\oint \vec{H} \cdot d\vec{l} = \mu_0 (I + \frac{d}{dt} (\epsilon_0 \int \vec{E} \cdot d\vec{A})) \quad (25)$$

4.3 Shielding Theory

As a wave comes into contact with a barrier surface there are three possible mechanisms of interaction;

The wave passes through the barrier.

The wave is absorbed by the surface and its energy is dissipated.

The wave is reflected by the surface.

In practice a combination of all three mechanisms are present during wave barrier interaction ^[139-141]. If the assumption that an ideal shield is a metallic barrier between the source and the receiver, then as the EM waves penetrate the barrier they will encounter the intrinsic impedance of the metal. This intrinsic impedance ‘ Z_m ’ is the resistance to AC currents within the material at given frequencies. In metals this is given by;

$$Z_m = \sqrt{\left(\frac{\omega\mu_0}{2\sigma}\right)}(1 - j) \quad (26)$$

Where j is an imaginary constant.

Therefore whenever the conductivity is not zero, the intrinsic impedance is a complex number indicating a phase difference between the electric and magnetic fields present. Due to the high level of conduction in most metals this intrinsic impedance value, at the frequencies considered here, will be relatively low.

With the basic principles of shielding behaviour resulting from the interaction mechanisms of the wave penetrating the barrier shield, the process of these interactions should be investigated. This includes the reflection loss, the absorption loss and the internal reflection loss ^[142].

Reflection occurs at the barrier's surface when there is impedance mismatch i.e. high impedance signal and low impedance (high conductivity shield). Of the remainder of the signal that transmits through the initial surface, some will become absorbed and dissipated and some will become internally reflected at the outer surface. All of the remaining signal will transmit through (Figure 4.2). It is this attenuation of signal strength in relation to the transmitted EM wave that determines how effectively a barrier shield performs.

The total shielding effectiveness is often expressed as;

$$SE \text{ (dB)} = \alpha_R + \alpha_A + \alpha_{IR} \quad (27)$$

Where;

α_R = Reflection losses from initial contact surface (dB)

α_A = Absorption losses inside the barrier (dB)

α_{IR} = Internal reflection losses from within the barrier (dB)

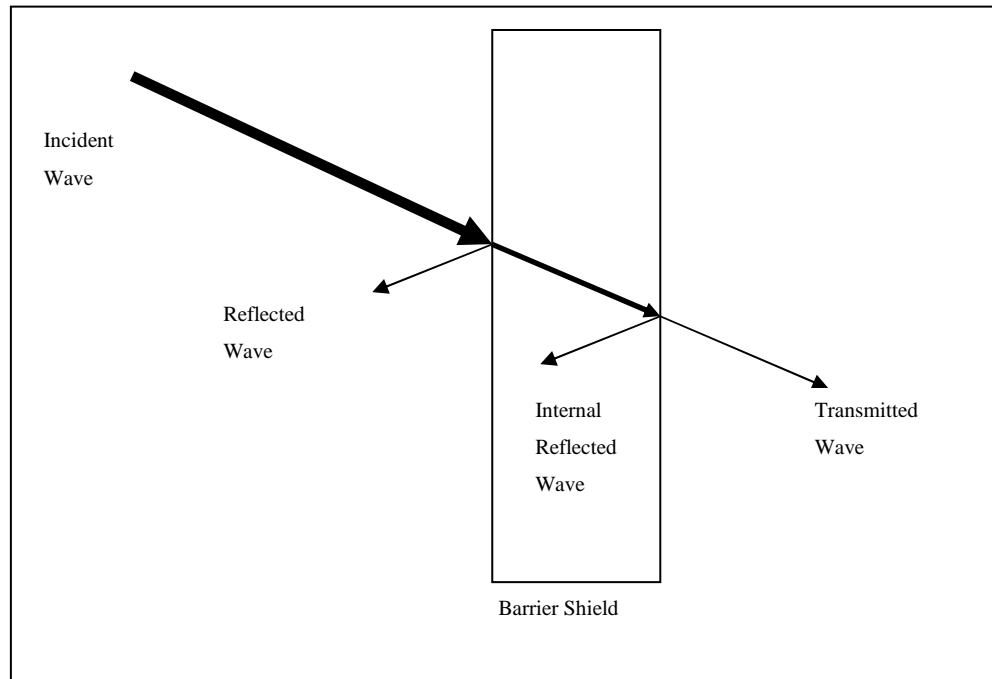


Figure 4.2, Mechanisms of Shielding

Although shielding theory and shielding in practice will vary quite significantly, the basic principles are addressed to gain a good understanding of the mechanisms involved. The distance away from a radiating source will determine the nature of the wave itself. This is due to the EM wave being composed of two components, the electric “E” field and the magnetic “H” field. Within the region close to the transmitter the wave will consist of a dominant component either E or H, while the other is less prominent. This is known as the near field region. The impedance of the near field signal is given by the ratio of the two components;

$$Z = \frac{|\vec{E}|}{|\vec{H}|} \quad (28)$$

After a certain distance 'r' from the source, the two components merge at mid point with standard impedance (Figure 4.3). This distance depends on the wavelength of the signal and is given by; $r > \frac{d^2}{2\lambda}$ when the source diameter (d) is greater than half a wavelength, or by $r > \frac{\lambda}{2\pi}$ when the diameter is significantly less than a wavelength.

Waves beyond this distance are known as plane waves with impedance;

$$Z_{PW} = \sqrt{\frac{j\omega\mu}{\sigma + j\omega\epsilon}} \quad (29)$$

Due to the wave travelling in air (free space), where $\omega\epsilon_0 \gg \sigma$, this can be reduced to;

$$Z_{PW} = \eta_0 = \sqrt{\frac{\mu_0}{\epsilon_0}} = 120\pi\Omega \quad (30)$$

$$\approx 377\Omega$$

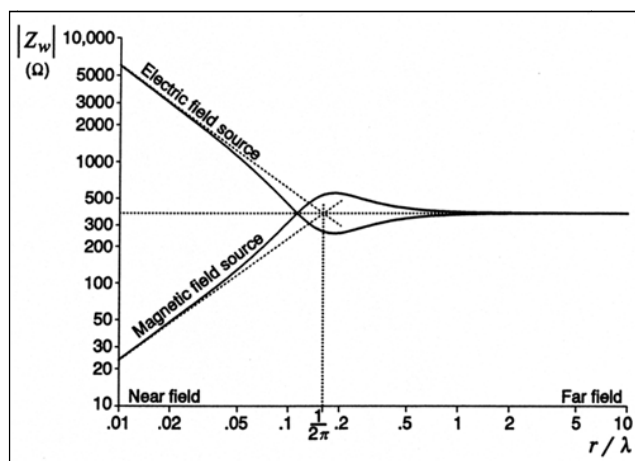


Figure 4.3, Near and Far Field Regions^[143]

Within the near field region the impedance of the E and H fields can be estimated by assuming the source to be a small dipole antenna;

$$Z_E = \frac{\eta_0 \lambda_0}{2\pi r} \gg \eta_0 \quad (31)$$

$$Z_E = \frac{\eta_0 2\pi r}{\lambda_0} \ll \eta_0 \quad (32)$$

“Near field have high variations with impedance giving highly electric components and highly magnetic components with the electric ones having high impedance and the magnetic ones having low impedance therefore requiring different methods of shielding. Electric waves reflect while magnetic absorb ^[144].

The shielding effectiveness of the signals can be measured by taking the power ratio of an unshielded signal to a shielded one.

For plane waves;

$$SE = 10 \log_{10} \frac{P_{Unshielded}}{P_{Shielded}} \quad (33)$$

For electric field waves;

$$SE = 20 \log_{10} \frac{E_{Unshielded}}{E_{Shielded}} \quad (34)$$

For magnetic field waves;

$$SE = 20 \log_{10} \frac{H_{Unshielded}}{H_{Shielded}} \quad (35)$$

Different applications will require different levels of each shielding mechanism to satisfy the desired outcome. For example radar systems rely on the target object being visible to electromagnetic waves to detect their position or velocity. Therefore small boats use radar reflection devices to increase the size of their echo helping to increase their radar visibility to other boats in the vicinity^[145]. On the other hand military applications can require the exact opposite such as stealth technology. Where the radar signal must be controlled to minimise reflectance and therefore disguise the radar signature ^[146]. For this to be achievable, it requires a combination of good design to avoid shapes that are detectable to radar along with a coating of radar absorbent material. This is usually a highly ferrite loaded paint to absorb and dissipate the magnetic field of the radar waves.

4.4 Shielding Requirements

Defining shielding requirements is not a straight forward process as the criteria for meeting guidelines and conforming to EMC regulations are very broad and generally loosely defined. EMC is often defined by statements such as “the ability of an equipment or system to function satisfactorily in its electromagnetic environment without introducing intolerable electromagnetic disturbances to anything in that environment” ^[147]. Categorising a defined level of dB that will provide suitable shielding is more difficult. As electromagnetic emissions are often a design consideration throughout the development and manufacture of devices, the exact level of shielding can vary significantly. However for some applications such as shielded enclosures, defined shielding requirements are specified. As shown in Figure 4.4, the

National Security Association specification for shielded enclosures - NSA 73-2a ^[148], requires shielding greater than 100 dB for plane waves above frequencies of 10 kHz

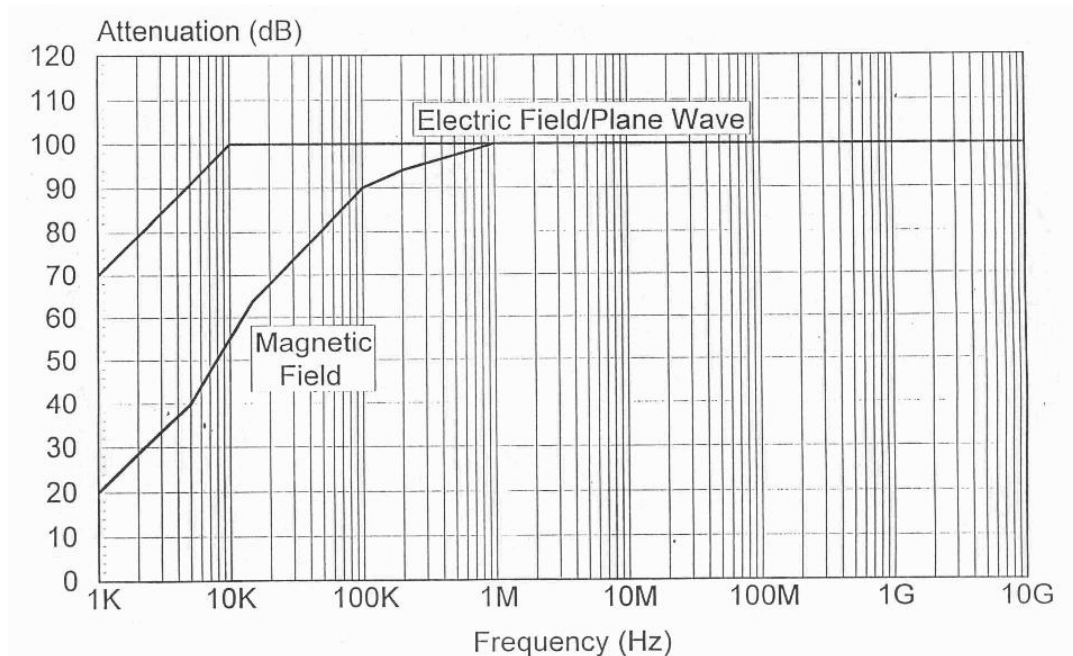


Figure 4.4, NSA Specifications for EMI Shielding of Enclosures

As the application of the shield will influence the required shielding effectiveness, it has been stated that for RF shielding enclosures practical shielding can range from low level 30 dB requirements to very high level shielding of 120 dB ^[149];

- Low level shielding of 30-50 dB can be satisfactory when low frequency, predominantly magnetic waves are to be attenuated.
- Medium level shielding of 50-80 dB can be satisfactory when only moderate shielding is required or a sufficiently large control zone surrounds the enclosure.

- High level shielding of 100 dB is required when a large safety margin is required. This can increase to a required minimum of 120dB when sensitive equipment is required to be shielded.

One study was undertaken by GE plastics to quantify the shielding required for portable electronic devices ^[150]. A large focus was placed on the effect that early considerations to shielding in the design process has on reducing the likelihood of a product failing EMC testing while also reducing overall costs. After designing in and utilising techniques to suppress electromagnetic emissions at circuit board level, the approximate shielding requirements for various classes of applications were determined. Table 4 details these values ^[150].

Table 4 - Typical Shielding Requirements of Electronic Devices ^[150]

Application	Shielding Required (dB)
Notebook Computer	15-20
Desktop Computer	15-20
Mobile Phone	70-90
Cable Tap	70-90
Workstation/Server	30-40

4.5 Effective Conductivity

Composite material properties can often be estimated through the rule of mixtures which accounts for the volume of each material and the related characteristics of each component within the composite. This is often used to estimate mechanical properties such as density or elastic behaviour but is less useful for electrical properties unless the phases within the composite have similar properties to each other. Therefore, in this case the conductivity can be estimated through the following equations ^[151-154];

$$\sigma = V_1\sigma_1 + V_2\sigma_2 \quad (36)$$

“V” is the dimensionless volume fraction of the phases within the composite. $V_1+V_2=1$ with subscript 1 denoting the properties of the matrix and subscript 2 denoting the filler. This relationship does not hold up well. As the differences in conductivity between the phases increases, the relationship between the volume fraction and conductivity becomes far more of a non linear relationship. Models using effective media theory have been developed to account for these relationships as developed by Garnett ^[155] and later further refined for use with conductivity calculations by Bruggeman ^[156], where by assuming that a spherical or ellipsoidal conductive inclusion is uniformly embedded within a single phase matrix the effective media theory gives ^[157];

$$V_1 \frac{\sigma_1 - \sigma_{eff}}{\sigma_1 + 2\sigma_{eff}} + V_2 \frac{\sigma_2 - \sigma_{eff}}{\sigma_2 + 2\sigma_{eff}} = 0 \quad (37)$$

This expression is still limited to small conductivity variations between phases and due to the assumption that the effective media is uniform throughout the composite, this fails to describe insulator/conductor composites near or above percolation threshold, V_c , as networks will have formed within the insulator.

Below percolation the conductive inclusions can be considered fully isolated and therefore $\sigma_{eff} = 0$, but once $V_2 \geq V_c$ the effective conductivity will tend towards that of the conductive filler as more and more networks are formed within. Effective media theory gives an expression for the effective conductivity above percolation by taking the percolation value to be $V_c=1/3$:

$$\sigma_{eff} = \sigma_2 \left(\frac{V_2 - \frac{1}{3}}{1 - \frac{1}{3}} \right) \quad (38)$$

Although this method has been shown to produce inaccurate results when verified through experimental procedures, it can be improved by taking the values for the percolation threshold from the percolation theory.

Therefore:

$$\sigma_{eff} = 0, \text{ for } V_2 < V_c \quad (39)$$

$$\sigma_{eff} = \sigma_2 \left(\frac{V_2 - V_c}{1 - V_c} \right)^t, \text{ for } V_2 \geq V_c \quad (40)$$

Where, t is the critical exponent of the system and has been predicted to equal 2.0^[59]. Unfortunately, the percolation threshold is less predictable and is highly dependent on the filler properties and processing methods.

4.6 Effective Permittivity

The effective permittivity of two phase mixtures has been studied in previous research and models relating to different phase dimensions are explained below^[158-159];

Following Maxwell Garnett approximations for effective media with circular inclusions in two dimensions, the effective permittivity is given as;

$$\varepsilon_{eff} = \varepsilon_m + 2V_2 \varepsilon_m \left(\frac{\varepsilon_i - \varepsilon_m}{\varepsilon_i + \varepsilon_m - V_2(\varepsilon_i - \varepsilon_m)} \right) \quad (41)$$

Where the filler is regarded as " ε_i " within a homogeneous matrix " ε_m " and the filler occupies a volume fraction " V_2 ".

The Bruggeman formula is another popular method of determining the effective permittivity and is used often in remote sensing studies under other names;

$$(1 - V_2) \frac{\varepsilon_m - \varepsilon_{eff}}{\varepsilon_m + \varepsilon_{eff}} + V_2 \frac{\varepsilon_i - \varepsilon_{eff}}{\varepsilon_i + \varepsilon_{eff}} = 0 \quad (42)$$

These theories correspond to mixtures of different insulating materials and have been proven to be reliable up to certain limits known as Wiener bounds ^[160],

$$\varepsilon_{eff,max} = V_2 \varepsilon_i + (1 - V_2) \varepsilon_m \quad (43)$$

$$\varepsilon_{eff,min} = \frac{\varepsilon_i \varepsilon_m}{f \varepsilon_m + (1 - V_2) \varepsilon_i} \quad (44)$$

No single theory predicts the effective values across the larger range of volume fractions but they should fall within the limits set here. Due to the nature of this study into conductive composites containing a metallic phase, it is not possible to predict the effective permittivity of the composite due to the conductive fillers having infinite permittivity. Alternatively, it may be possible to calculate these values from transmission line theory measuring the reflected impedance during the experimental

process. On this basis, only the effective media theory for conductivity would be utilised during the modelling process.

4.7 Skin Depth

The skin depth is a phenomenon of alternating current electrical behaviour within materials where the majority of the current density is focused towards the surface of the material. Below the skin depth there is still current flowing, but at a significantly reduced density. This depth, where the current density is at a maximum, is dependent on the frequency of the induced current (ω), the magnetic permeability (μ) and the conductivity (σ). The higher the product of these variables, the smaller the skin depth will be. In practice it is the frequency of EM wave and the magnetic permeability of the material that affects the skin depth most significantly. As can be seen in Figure 4.5, copper, aluminium and gold all have similar skin depths while nickel is considerably smaller due to its increased magnetic permeability. Likewise the reduced permeability of carbon and graphite results in an increased skin depth.

$$\delta = \sqrt{\frac{2}{\mu\sigma\omega}} \quad (45)$$

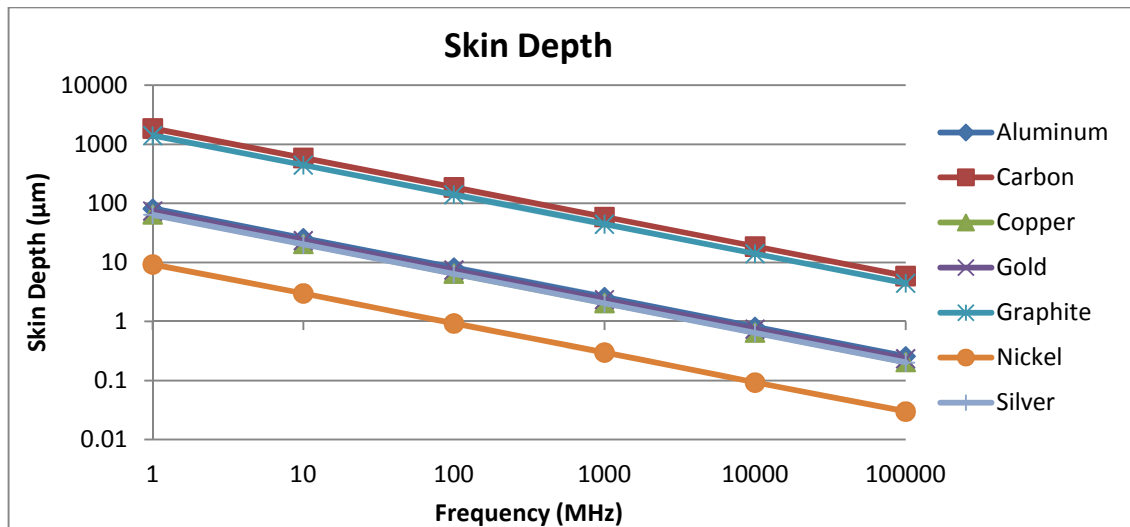


Figure 4.5, Skin Depth versus Frequency

This principle allows for conductors to be tailored keeping material usage to a minimum. With many suitable metals being more expensive and often quite dense, a core can be used to reduce weight while still retaining the majority of electrical properties. This issue is not a consideration with DC current as the full cross-section of the work piece becomes one conductor path, therefore resistance can increase greatly with significant reduction of cross-sectional area.

4.8 Network Analyser Analysis

“Network analysing is the characterising of a device, component or circuit by measuring and comparing the signal applied to the device with the signal coming out of the device”^[161]. Dating back into the 1950’s, network analysis referred to the electrical circuits which at that time were known as electrical networks and are used to characterise RF and microwave devices, components, circuitry, sub assemblies and systems^[162]. By testing the individual components of a system before they are combined into the more complex finished article, this allows any issues or failings to be located and rectified

early (pre-testing) and more easily, therefore saving further testing, troubleshooting and costs at a later stage of development.

4.9 Measurement Process

Network analysers themselves are devices that can measure or calculate electrical parameters over wide frequency ranges. The basics of measuring through network analysis stems from the analyser measuring and comparing the magnitude and phase of a signal transmitted through and reflected from a device relative to the incident signal initially generated (Figure 4.6) ^[163-164].

$$\frac{\textit{Reflected Signal}}{\textit{Incident Signal}} \textit{ and } \frac{\textit{Transmitted Signal}}{\textit{Incident Signal}}$$

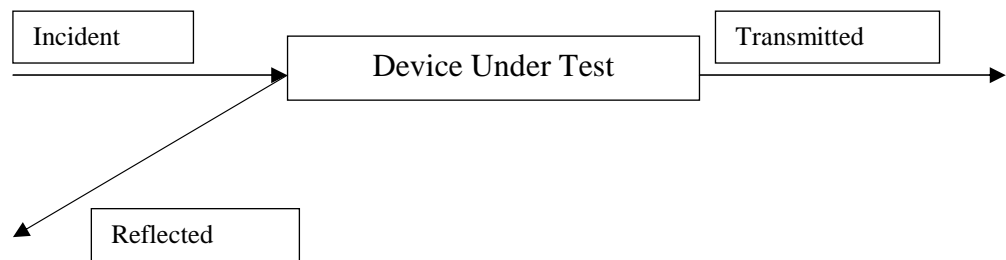


Figure 4.6, Network Analysis Process

The analyser achieves this usually through a two port set up with a reference receiver. This allows a signal to be generated from port one and transmitted through a device before being received in port two. While measuring this transmitted signal the analyser can also measure from port one into the device and back again to port one therefore

measuring the reflected signal value (Figure 4.7). By taking reference from the initially generated incident signal the analyser can calculate the relative amplitudes and phase. This is known as forward characteristics of the device and by reversing the direction of the signal and going from port two into port one or back into port two the reverse characteristics can be measured.

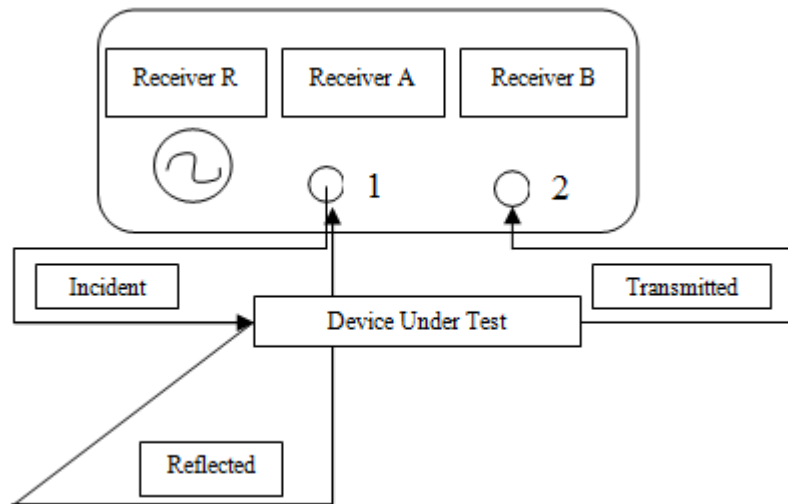


Figure 4.7, S Parameters

4.9.1 S - Parameters

These measurements are also known as S - parameters where the designation numbering refers first to where a signal is intended for, and then secondly to where it originated from.

The S parameters for a two port analyser are listed in Table 5;

Table 5 – 2 Port S - Parameters

S_{11}	Reflection measurement from port 1 returned to port 1
S_{21}	Transmitted measurement from port 1 to port 2
S_{22}	Reflection measurement from port 2 returned to port 2
S_{12}	Transmitted measurement from port 2 to port 1

S parameters do not use voltage and current relationships to calculate values but instead use the relationship between the transmission and reflection of wave terms. By using line theory, wave quantities and characteristic wave impedances (Figure 4.8) these S - parameters can be determined, assuming the device under test does not have fluctuating impedance and/or mismatched power generators. This allows the S - parameters to be determined only by the circuit, device and the measurement setup.

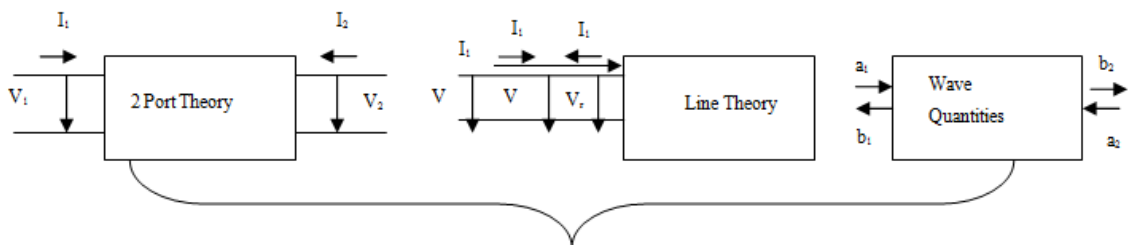


Figure 4.8, Determination of S-Parameters

The main quantities that are required to be calculated from the S - parameters are the transmission and reflections coefficients. These are obtained from wave amplitudes and can form the basis for many other determinable quantities.

4.10 Return Loss (Reflection/Impedance Mismatch)

Reflection occurs when a wave encounters a change in the characteristic impedance, known as a mismatch. This produces an opposing backwards travelling wave that interacts with the forward travelling one creating a standing wave. In most situations the incident wave will partially transmit, partially absorb and partially reflect. Therefore the ratio of reflected wave voltages (V_{\max} and V_{\min}) can be measured to determine the reflection coefficient and is known as the voltage square wave ratio (VSWR). The reflection coefficient can then be calculated from the VSWR through the formula;

$$VSWR = \left| \frac{V_{\max}}{V_{\min}} \right| \quad (46)$$

$$\text{Reflection Coefficient } (\Gamma) = \left| \frac{VSWR-1}{VSWR+1} \right| \quad (47)$$

$$\text{Return loss (dB)} = 20 \log \Gamma \quad (48)$$

4.11 Transmission Lines and Impedance

Transmission lines are essentially a means for directing or transporting a signal within a controlled environment. For example coaxial cables and waveguides are both transmission lines. Transmission line theory describes an ideal transmission line as a series of distributed inductors and capacitors that transfer the signal from the source to the device with as little transformation or loss of power as possible. Although described as inductors and capacitors, the line is not inductive or capacitive as all reactances are cancelled out. The main factor that incurs losses within a transmission line is the

impedance losses. These are related to the characteristic impedance of the transmission line which is the AC resistance at a given frequency and relates to the voltage and current of the travelling waves within the line.

4.12 Transmission Line Insertion Loss

In order to calculate the amount of signal that is lost through a device or shielding material, the ratio of transmitted signal to incident signal with and without the device under test in place need to be measured.

$$\text{Insertion Loss (dB)} = -10 \log_{10} \left| \frac{P_{\text{Transmitted}}}{P_{\text{Incident}}} \right| \quad (49)$$

$$\text{Insertion Loss (dB)} = -10 \log_{10} \left| \frac{V_{\text{Transmitted}}}{V_{\text{Incident}}} \right|^2 \quad (50)$$

$$\text{Insertion Loss (dB)} = -20 \log_{10} \tau \quad (51)$$

Where τ is the transmission coefficient; $\frac{V_{\text{Transmitted}}}{V_{\text{Incident}}}$

5 Methodology

5.1 Sample Preparation

Standard sample preparation was performed using standard laboratory equipment and hand mixing procedures. The filler materials were measured following the standard test method described in ASTM D1895 ^[165] into required volumes by first measuring their apparent density, the weight per unit volume of a material, including voids that exist. This is measured by weighing a known volume of powder and dividing it by the volume therefore giving the apparent density.

$$\rho_{\text{apparent}} = \frac{M}{V} \quad (52)$$

The apparent density is then used to weigh the correct volume of powder required for each sample.

5.2 Filler Volume

Where possible, volume percentages were used for loading calculations in preference to weight percentages. This was felt to give a more accurate representation of the material interaction and their percolation behaviour patterns. Filler volumes were increased in regular intervals of 5 or 10% with percolation usually expected between the 30-50% filler range. The chosen volumes were generally dictated by the availability of the filler materials. Where possible smaller increases in volumes were preferred as this would give a more detailed transition through the upper and lower percolation thresholds.

5.3 Material Mixing

The materials were measured out and mixed by hand in a beaker with an ethyl acetate solvent.

First the correct volume of filler powder would be placed into a beaker and mixed with a small amount of ethyl acetate (3-5 cm³) to remove any agglomerations and hopefully create a paste (if a paste was formed it indicated that the powder went into solution easily). This paste was then mixed with 10 cm³ of solvent based poly(methyl methacrylate) PMMA resin (Coates Lorilleux 10180VSH Acrylic Medium). These materials were then well mixed by hand stirring. This mixing process was sufficient to disperse fully the filler within the acrylic medium while at the same time not being too excessive which may have resulted in a loss of particle contact. Mechanical stirring and ultrasonic mixing methods were also trialled but neither resulted in improving the technique.

5.4 Printing of Coatings

To begin with, samples were manufactured using an AMI Presco semi-automated screen printer. This printing device is normally operated using a masking screen over the substrate to print detailed patterns or to achieve a more uniform particle distribution when deposited onto a substrate. The screen was not deemed necessary and most likely would have been detrimental as it would likely restrict particle interaction. Instead the printer was operated as an automated spreader which produced samples with dimension 150 mm x 75 mm. However as well as the small area that could be printed, this method

had other drawbacks including a complex set-up and adjustment routine that made controlling the print thickness difficult and resulted in a loss of repeatability. The labour intensive cleaning required also reduced the volume of samples that could be produced.

After this initial method was deemed unsuitable, a K-Control Coater was obtained that facilitated in producing semi-automated prints. K-Control Coaters are devices commonly used within the paint industry to provide repeatable test prints when comparing new formulations. The wire wound rods are automatically drawn down over the surface of the substrate producing a uniform coating. These rods are locked into the moving head and held down onto the substrate with weighted arms. The pre-mixed acrylic/ filler solution is then poured evenly ahead of the rod before it is drawn down across the surface of the substrate, leaving an even layer behind, (Figure 5.1). This was then left flat to reflow into one uniform sheet before being transferred into an 80°C oven to cure for 10 minutes. These curing parameters were chosen as sufficient time and temperature to evaporate off the solvents from the acrylic resins without adversely affecting the substrate. Figure 5.2, indicates how the evaporation of the solvents during curing will further aid particle to particle contact.

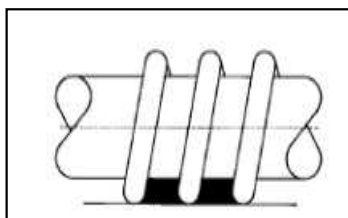
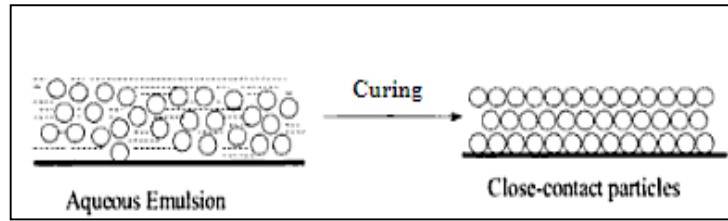


Figure 5.1 K-Control Printing Process



(Figure 5.2, Curing Behaviour ^[166])

This K-Control Coater allowed the printing of test samples at almost A4 size with a range of coating thicknesses and a degree of repeatability that was not possible with any other method available.

5.5 Microsphere Technologies

An additional industrial collaboration with Microsphere Technology, a local company that specialised in producing metallic coated glass microspheres, was formed. This partnership facilitated a broadening of the investigation to evaluate the manufacture and testing of lightweight electrically conductive polymer composites consisting of silver coated hollow glass microspheres. Manufactured through a novel silver electroless plating procedure, very lightweight conductive fillers were manufactured. Microspheres being hollow have low particle density given in the region of 0.5g/cm^3 . When compared to that of silver or nickel, 10.5 g/cm^3 and 8.9 g/cm^3 respectively, the potential weight reduction is evident. We investigated the manufacture and electrical testing of such lightweight fillers and also examined the performance characteristics for EMI shielding.

Uniform hollow glass microspheres are commonly manufactured by adding a sulphur compound blowing agent, commonly sodium sulphate, to a borosilicate glass mixture known as frit. By passing this frit through a flame heat treatment the gases are rapidly

expanded within the molten glass forming bubbles. These then solidify into the microspheres themselves that are then blown by the flame into a collection tube (Figure 5.3). This method of production can be rigorously controlled allowing for high uniformity and dimensional tailoring of the spheres.

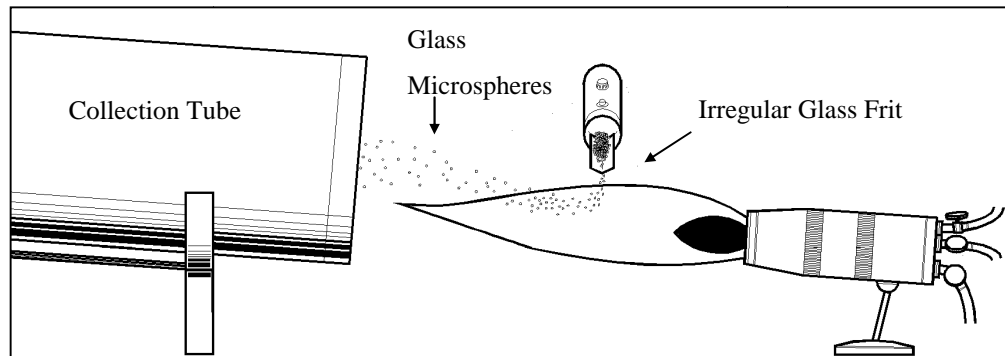


Figure 5.3, Glass Microsphere Production Process

There are also naturally occurring hollow glass spheres that are formed either as a by-product within the fly ash from coal fired power stations or extracted from volcanic ash, often classed as cenospheres. Formed as a by-product, they can be cost effective and more environmentally beneficial but there is less control over the particle size and surface morphology.

5.6 Compression Moulded PMMA-Nickel Composite Plaque Manufacture

The aim of this section is to investigate an alternative method of producing conductive polymer composite plaques and form a comparison with a more commonplace mixing method of production. The goal was to analyse whether an equivalent EMI shielding performance was achievable at reduced metallic content within the polymer composite. The manufacturing methods compared are nickel flake filled acrylic plaques that have

been manufactured through Brabender Plasti-Corder compounding before being compression moulded into a 2 mm thick plaque. The comparison will be made against identical plaques compression moulding from the same PMMA granules which have been electroless plated with a thin nickel coating prior to compression. Testing of the resultant samples for electrical properties and electromagnetic shielding performance will subsequently be undertaken.

As discussed previously, it is a common process to fill insulative polymer matrices with conductive fillers to generate electrical conduction whilst allowing the polymer to retain most of its properties and processability. This approach can be perfectly adequate although potentially wasteful. An increase in the required thickness of polymer also results in a large volume increase of fillers necessary. This is typically in the region of over 30% volume to achieve conduction in filled two phase composites. By utilising the ability of the electroless plating process to produce very thin and uniform coatings, the PMMA granule can be pre-plated and compression moulded into a plaque. Through this process it is foreseen that an internal nickel network could be retained throughout the composite and therefore provide conductivity at a significantly reduced metallic content.

5.6.1 Brabender Plasti-Corder

A Brabender compounder is a high shear double arm polymer mixing device that allows for accurate compounding of fillers into a polymer matrix. The device consists of a heated chamber with two “three wing” parallel shaft mixing blades turning in opposite directions downwards into the chamber between the blades (Figure 5.4). The operating temperature is chosen to be within the polymer’s softening region but controlled to limit

degradation. The mixing chamber shown in Figure 5.4 shows where the polymer granules are fed into the mixer via the small hopper and ram. These are then processed until the polymer is softened and begins to flow within the chamber. Once the polymer granules have begun to amalgamate the filler can be then be fed into the mixer. This is then left to mix fully for a few minutes until a homogenous blend has formed ^[167].

Removal of the combined polymer/ filler is done while chamber and blades are still warm to aid full removal of the material. The recovered material is in a form that requires a final processing stage to achieve the desired form. Compression moulding was deemed a suitable method of forming the finished test plaque.



Figure 5.4, Brabender Mixer Measuring Head

5.6.2 Electroless Nickel Plating

Since the initial discovery over a century and a half ago that nickel and phosphorus were highly reactive when heated together ^[168-169], there has been some resurgence in the subject as it was rediscovered that metallic coatings could be deposited from a

solution containing nickel and hypophosphite ^[170]. Unlike electroplating, no electricity is required.

Nickel phosphorus plating has seen a significant amount of development since the 1950's and has grown into a commonly utilised process. Product Finishing Magazine Online estimates that 55% of electroless nickel is applied for protective coatings, such as wear and corrosion resistance ^[171-173]. These wear resistant coatings have also been further developed with nickel often being co-deposited along with additional particulate reinforcements. These reinforcements can be hard such as tungsten, boron, silicon carbide, alumina or diamond. Alternatively they could be lubricating soft materials such as polytetrafluoroethylene (PTFE) ^[174-176]. Another common application of high phosphorus electroless nickel has been as an under layer for magnetic coatings in memory disk manufacture ^[177].

The electroless plating process is an auto-catalytic chemical reduction process which uniformly deposits nickel onto the surface of a substrate. This substrate requires to be catalytically activated before being immersed within a nickel and sodium hypophosphite solution and raised to a required reaction temperature. The reducing agent releases hydrogen before oxidising therefore generating a negative charge upon the substrate which acts as the catalyst and attracts the nickel ions from the solution.

A number of metals are inherently active allowing for the reduction reaction to begin spontaneously. These metals include iron, cobalt, palladium and nickel. This results in all newly formed nickel layers also acting as a catalyst hence the auto-catalytic reaction. This also allows the plating process to continue until the desired coating thickness has

been deposited or the solution concentration of the bath is reduced sufficiently. As can be seen in Figure 25, the plating rate drops off as the bath is depleted although the concentration can be replenished when required.

The principal chemical reactions during the final plating bath are;



As this process requires the substrate to be sensitised and catalytically activated, a 4 stage pre-treatment procedure is followed. This involves immersing the substrate into the following baths - the initial preparation is a Cuprolite X96 (2-aminoethanol) bath (supplied by Alfachimici, Italy) for cleaning and sensitising, a short bath at 20°C for 2 minutes being all that is required. Stage 2 is a pre-catalyst (stannous chloride anhydrous) bath where it is heated to 35°C for 5 minutes. Stage 3 is the catalyst (acidified stannous chloride anhydrous) activation bath. The final surface preparation stage (Niplast AT 78) is a 1%-5% hydrochloric acid based bath for 3-4 minutes.

Once activated, the substrate can be immersed in a nickel rich plating solution, (Slotonip 1850, Shloetter Co. Ltd.). This is the most temperature critical stage. As catalytic processes, such as electroless nickel plating, require a certain input of energy to react, heat is applied to maintain optimum plating conditions. The relationship between temperature and plating rate follow exponential growth. In some cases the rate

of nickel deposited can almost double for every 10°C increase. Therefore too low a temperature and there will be insufficient energy within the system to initiate plating. Too high a temperature and an excess of nickel is released from the solution resulting in nickel falling out and not depositing onto the substrate. Plating is optimised between 87°C - 91°C.

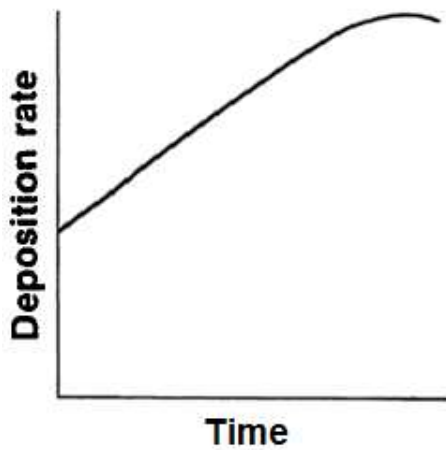


Figure 5.5, Deposition Rate with Time

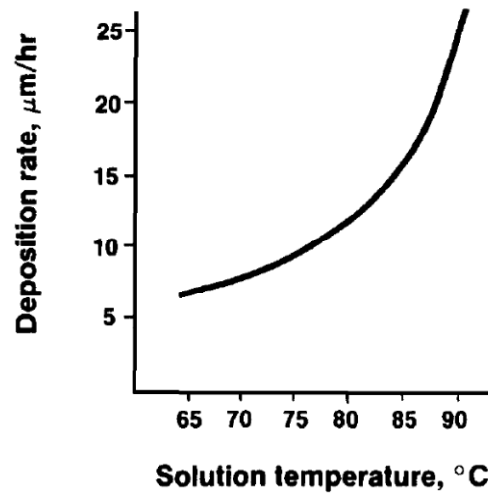


Figure 5.6, Temperature Dependent Deposition Rate ^[168]

Electroless nickel is generally divided into three categories dependent on the phosphorus content deposited alongside the nickel; 1% - 5% is classed as low phosphorus or hard nickel plating as deposited coatings can be up to 60 Rockwell C, therefore providing excellent wear resistance. Low phosphorus coatings have a microcrystalline structure with grain size in the nano-meter range. Ferromagnetism is also evident.

Medium phosphorus contains 6% - 10%: this additional phosphorus content aids the efficiency of the plating bath while still providing a bright and reasonably hard coating

and retaining good corrosion protection. Medium phosphorus coatings are considered amorphous and only slightly ferromagnetic.

Once the phosphorus content reaches over 11% it is classed as high phosphorus nickel. Coatings of this grade are amorphous and highly corrosion resistant with low porosity. They are also non-magnetic.

As the phosphorus content increases, the conductivity of the coating is reduced. This has been attributed predominantly to the relative volume fraction of nickel decreasing as the phosphorus alloy is increased. Additional factors such as a lack of crystal structure have been shown to also affect the conductivity. Increased conductivity has been demonstrated after age hardening heat treatment processes to electroless nickel. It has been shown that the amorphous structure can recrystallise and precipitate phosphorus out of the solid solution as Ni₃P intermetallics. This results in a reduction of phosphorus within the crystal structure and therefore reduces the resistivity [178].

Table 6 provides values for electrical resistivity of electroless nickel at various phosphorus contents.

Table 6 - Density and Resistivities with Phosphorus Content [168]

Phosphorus Content (%)	Density (g/cm³)	Resistivity (μΩ/cm)
1-3%	8.6	30
5-7%	8.3	50-70
8-9%	8.1	70-90
> 10%	< 8.0	< 110

Further plating of gold onto electroless nickel is common within the printed circuit board industry. Known as electroless nickel / immersion gold (ENIG) it is a galvanic displacement deposition technique that can deposit a thin layer of gold ($\approx 0.05 \mu\text{m}$) onto the surface of a nickel coating ^[179]. This gold layer provides corrosion protection and improves the wettability of the surface thus improving the solderability. As the nickel substrate is less noble than gold when immersed in a gold solution, the immediate surface of nickel is depleted and instantaneously replaced with a thin layer of gold. Unlike the electroless nickel process immersion gold is a self extinguishing process. The plating rate is governed by the electro-potential of the galvanic couple and can result in an excessively high reaction rate which produces porous and poorly bonded deposits. In the case of plating electroless nickel the addition of phosphorus reduces this reaction rate and improves the density and bonding of the deposited gold. The utilisation of high phosphorus nickel as a substrate has shown to have additional benefits for flexible circuitry. Not only is the gold adherence improved but the nickel substrate is more ductile resulting in less cracking ^[180].

5.7 Plaque Sample Density Measurements

Density of the compression moulded plaques would be measured through the Archimedes buoyancy method;

$$\rho = \frac{M_{in\ air}}{M_{in\ air} - M_{in\ water}} \quad (57)$$

This method is based on the principle that the mass difference when measured in air and in water will always be equal to the volume of water displaced by the sample, as for

water $1\text{cm}^3 = 1\text{ ml} = 1\text{ g}$. The equation then follows the standard description of density where the mass is divided by the volume.

5.8 Scanning Electron Microscopy and Elemental Energy Dispersive X-ray (EDX) Analysis

Scanning electron microscopy was performed using two different SEM's. One was a Cambridge Stereoscan 90 and the other was a Tescan Vega LHM integrated with a Thermo Scientific Noran System 7 Microanalyser for EDX analysis.

EDX analysis is a detection system that when used in conjunction with an SEM can determine a material's elemental composition. The material's surface is bombarded by a high energy electron beam which in turn stimulates electrons from lower energy shells into higher energy bands. Electrons are then replaced into the vacant site of the original energy band. This results in an emission of energy in the form of x-rays. Since each element has a unique set of energy bands, the corresponding x-ray emissions are also of unique energies. By matching the peaks detected at certain energy levels the elemental composition of a material can be identified.

5.9 Surface Resistivity Testing

Surface resistivity is a material property describing the electrical resistance of a set area of the material's surface. It can be measured through placing flat plate electrodes onto the material surface. The simplest is the parallel plate electrode configuration described in the standard method ASTM D257 ^[181], which involves measuring the resistance between two parallel copper electrodes over a known area (Figure 5.7). In theory the

length and configuration of these electrodes can vary as “the surface resistance measurement depends on both the material and the geometry of the electrodes used in the measurement.”^[182]. By keeping it a square area direct readings can be taken from the device.

This testing apparatus was initially set up with a 9 volt ohmmeter to measure the resistivity. Although a practical solution due to its portability and ease of use, the limitations of measuring insulating or highly conducting materials resulted in a more accurate method being required. The replacement was a Wayne Kerr precision component analyser 6425, a far more precise measurement technique that also allowed testing of each sample at a variety of frequencies.

In order to differentiate between the resistance and the resistivity of a material’s surface, the unit for surface resistivity, taken over a square area, is expressed as ohms/square rather than simply ohms.

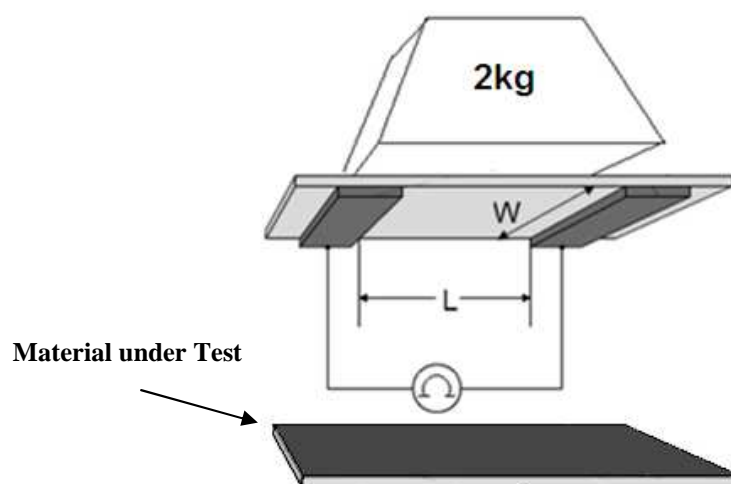


Figure 5.7, Surface Resistivity Test Jig

The surface resistivity is measured by;

$$\rho_s = R \times \frac{W}{L} \quad (58)$$

Where;

ρ_s = Surface resistivity (ohm/square)

R = Resistance measured (ohm)

W = Test width (m)

L = Test length (m)

The pressure applied to the test rig when measuring surface resistivity affects the results obtained as any variation in pressure will alter the contact between the probes and the material under test. A 2 kg mass was chosen to be applied as a constant force in order to maintain test reproducibility. Another version of this test is the concentric ring probe which has the advantage of giving a resistivity reading eliminating the directionality of the parallel probe test.

This directionality was investigated during an undergraduate degree project and found to exhibit minimal variation between horizontal and vertical measurements taken ^[183]. The results of this study will be discussed later in this thesis.

The potential applications of conductive materials are commonly determined by the level of resistivity achieved, as can be seen in Figure 5.8. Materials that are less resistive than plastics are capable of dissipating static charges. This kind of material is used

within areas where any level of static discharge could have a damaging effect or where static build up attracts contaminants. An example of this would be in clean rooms, where it is necessary to reduce the contamination of sensitive equipment or where any static discharge could damage sensitive components such as in the semi-conductor manufacturing industry. Clothes and floorings are made from conducting materials that are able to dissipate static build up. This alleviates the risk of discharge and reduces contamination attraction. In order to become fully conductive, the level of resistivity must be low enough to allow larger current flows. The same is true for EMI shielding materials where the material has to dissipate the electronic component of the wave. Therefore at lower resistivities this is achievable faster.

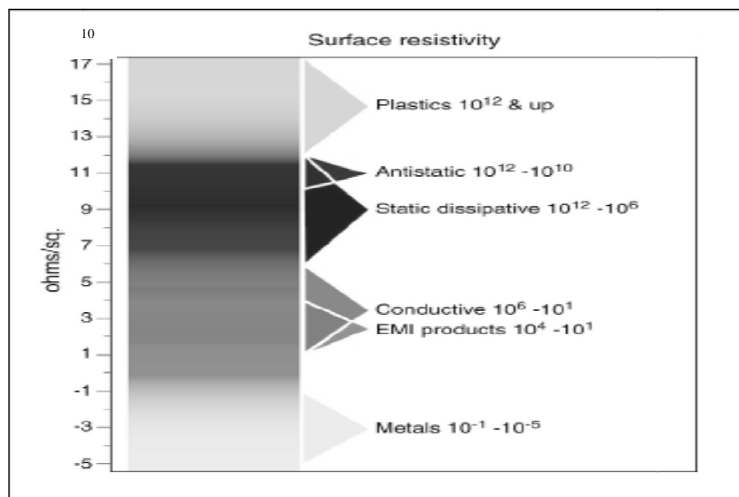


Figure 5.8, Surface Resistivity Applications ^[184]

5.10 EMI Shielding Testing

EMI test set up was designed to accurately test the attenuation of the composite coating through transmitting a signal to a receiver and comparing the signal strength at the receiver. From knowing the received signal strength through the uncoated polyester

sheet substrate and by comparing the signal received through the coated one, the attenuation attributable to only the coating could be determined.

5.11 Dual Dipole Antenna Method

This test is very similar to MIL-STD-285 ^[185], which involves two dipole or loop antennas separated by a barrier shield and the shielding effectiveness is measured by the attenuation of signal strength with the barrier in place. Tests were performed within a small chamber containing two dipole antennas connected to a 300 MHz – 3 GHz network analyser. The samples were positioned around the transmitting antenna as a semi circular barrier aiming to reduce the scattered waves from reaching the receiver. The inside of the chamber was lined with high frequency absorbing anechoic foam to limit scattered waves reaching the receiver.

This test method was limited in its ability to provide comparable results over an applicable frequency range. Due to the small size of the test chamber, waves in far field were also unable to be measured. These restrictions were the result of the dipole antennas effectively being tuned to one distinct frequency which provided a limited frequency range. Dipole antennas also transmit a toroidal shaped field which was not ideal for shielding analysis as the wave scattering within the chamber would be significant. Another method of generating more directional waves would give clearer and more accurate attenuation results. Although this initial set up helped to develop the sample production and measuring techniques, further more accurate testing methods would be required.

5.12 Dual Horn Antenna Method

Due to the limitations within the previous test method, it was decided that a dual horn antenna test procedure would suit the testing better. Two horn antennas, one connected to a signal generator and one connected to a network analyser, were arranged within a shielded chamber (Figure 5.9). The signal strength without a shield would be measured and the strength with a test sample in place then measured. The difference between these results would give the attenuation due to the shield. A horn antenna is a waveguide with a flared open aperture at one end. This aids the gain, transmission and reception of waves. Horn antennas allow for good directionality of wave propagation and therefore with correct positioning of test samples accurate repeatable results are achievable. Using this set up it is possible to measure the overall attenuation and the reflection loss. Therefore it is possible to get a measurement for the internal losses, absorption and internal reflections, giving a more complete picture of the shielding mechanisms.

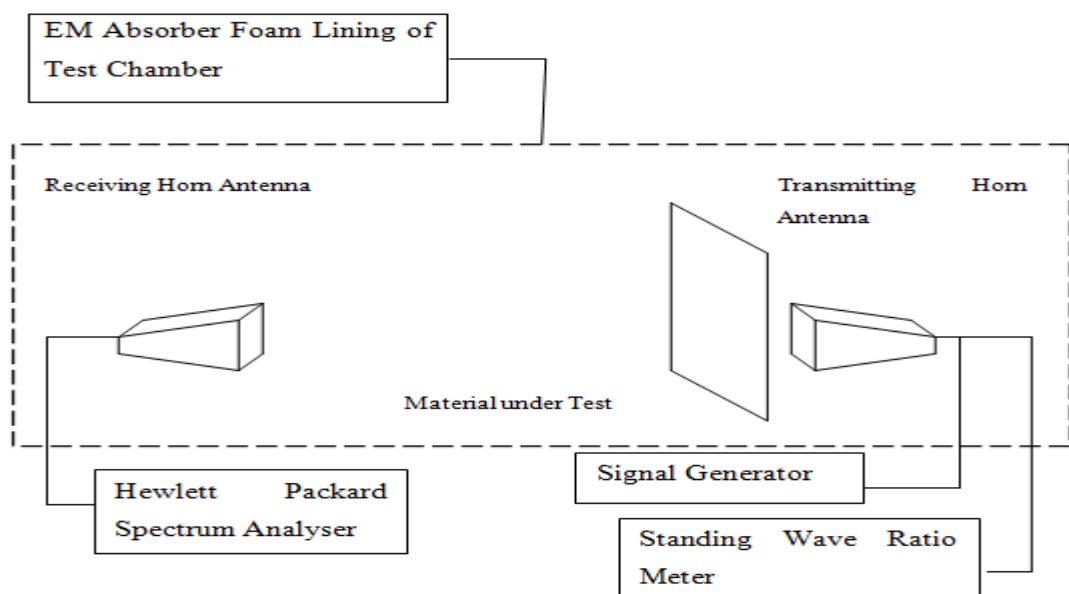


Figure 5.9, Horn Antennas Apparatus

The signal was generated by a Marconi Instruments Signal Source 6158A with a frequency range of 8.2 – 12.4 GHz (X-Band). This was transmitted through a shielding barrier placed directly in front of either the transmitting horn or receiving horn depending on the measurement required. A reference decibel level of received signal is measured on the spectrum analyser before a shield is in place and an attenuated level is measured after. The difference between readings is taken to be the attenuation due to the shield.

Reflection measurements are obtained by taking the power of the standing wave ratio (PSWR) that is reflected back into the transmission horn antenna and converting it to the voltage standing wave ratio (VSWR). The reflection ratios are expressed by;

$$PSWR = \frac{Peak\ Value}{Min\ Value} \quad (59)$$

$$VSWR = \sqrt{PSWR} \quad (60)$$

$$\rho_v = \frac{VSWR-1}{VSWR+1} \quad (61)$$

$$\rho = [\rho_v]^2 \quad (62)$$

Where ρ_v and ρ_p are the reflected voltage and power ratios respectively.

5.13 Waveguide Attenuation Method

A guided wave is simply a means of transporting wave energy from one source to another. These are commonplace within various electronic devices and they range in types from simple microstrip conductors and coaxial cables to optical fibres. Although coaxial lines are probably the most commonly used and most practical method of guiding waves, they are limited at higher frequencies due to the potential of additional wave propagation modes developing. To counter this, dimensions must be reduced accordingly, therefore increasing the attenuation and manufacturing costs.

A more suitable solution for the test regime was to utilise hollow rectangular metal waveguides coupled together and then transmit a signal through a test piece clamped between them. This technique is based on ASTM – D4935 ^[186]. The test set-up detailed in the standard uses an expanded coaxial connection with an annulus test piece inside that is connected to a network analyser and the S-parameters are measured through the sample. By replacing the expanded coaxial connection with a range of rectangular waveguides, it was possible to test at a large range of high frequencies whilst only requiring a variation to the dimensions of the waveguide. This method can allow practical testing capabilities from 1 – 100 GHz in a highly controllable environment. The facilities available were limited in range up to 40 GHz.

Table 7 – Waveguide Information

Band Designation (UK Designation)	Electronics Industry Association Designation	Internal Dimensions (mm)	Frequency Range (GHz)
S - Band	WR284	72.0 x 34.0	2.6 – 3.95
X – Band	WR90	23.0 x 10.0	8.2 – 12.4
Q – Band	WR28	7.1 x 3.6	26.5 – 40

By placing a test material between two waveguide sections the free space can be eliminated and therefore any attenuation in the signal strength can be attributed to that of the material under test. The frequencies chosen for the tests are given in Table 7. These are commonly used frequency bands with many commercial and military applications.

The process utilised the waveguides as a means to measure the transmitted S_{21} parameter through the material tested. By connecting them up to a Rhode Schwartz ZVA 40 network analyser and following suitable calibration and normalising procedures, it was possible to sweep across the full range of frequencies for each waveguide rather than the laborious task of alternating frequency with every test. Test results were then exported to a spreadsheet for formatting and analysis.

5.14 Comsol Multiphysics Modelling

Computer generated simulations were modelled through Comsol Multiphysics, a simulation package that is designed to be able to model and couple varying physics tasks. In this research the three dimensional RF and electromagnetic wave module was sufficient to model a waveguide and shielding media.

To begin with, three dimensional CAD models were created and specific internal faces were allocated with certain tasks and boundary conditions. These included the transmitting and receiving ports, magnetic and electrical boundary conditions and the properties of the material under test (Figure 5.10).

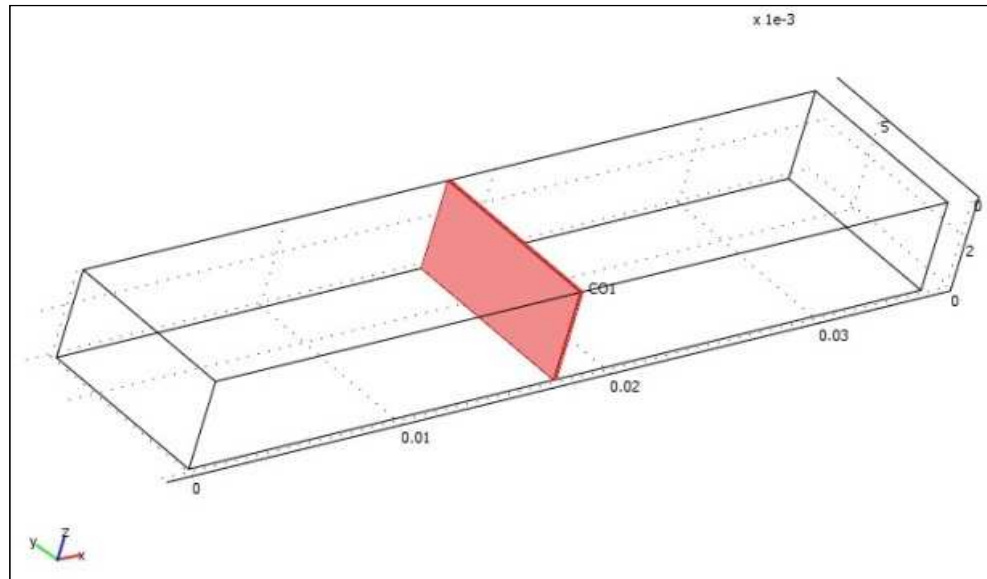


Figure 5.10, Initial Q-Band CAD Model

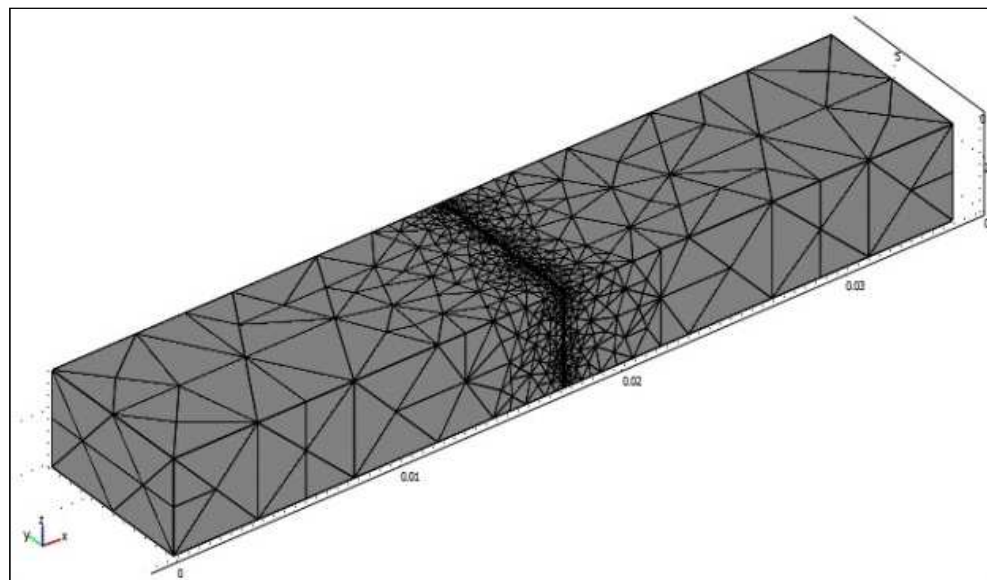


Figure 5.11, Meshed Q-Band Model

The pre-defined vector elements equations of the RF module were sufficient to generate the simulations required, although the material properties of the composite shielding material would have to be defined independently. There was no scope to model particulate reinforced composites within the geometry of the software and any attempts

to do so resulted in creating a model with an excessive amount of elements and therefore a model that was too demanding to solve with the resources available.

The governing partial differential equations, derived from Maxwell-Ampere and Faraday's laws, and utilised by Comsol for describing the wave behaviour are given as;

$$\nabla \times (\mu_r^{-1} \nabla \times E) - k_0^2 \epsilon_{rc} E = 0 \quad (63)$$

$$\nabla \times (\epsilon_{rc}^{-1} \nabla \times H) - k_0^2 \mu_r H = 0 \quad (64)$$

Where:

E is the vector field intensity vector,

H is the magnetic field intensity vector,

μ_r is the environment's relative permeability

ϵ_{rc} is the environment's complex permittivity.

k_0 is the wave number of the free environment and is defined by;

$$k_0 = \omega \sqrt{\epsilon_0 \mu_0} = \frac{\omega}{c_0} \quad (65)$$

Therefore for the model established, relevant material properties were determined from Effective Media Theory which takes into account the individual constituents of the composite to equal a bulk value for material as a whole. This approach to estimating material properties is used often in materials science, although it is more suitable for determining properties that vary linearly with volume fraction. With electronic and

magnetic properties following a percolation curve, it was yet to be established whether this model would be successful in predicting the composite materials electromagnetic shielding behaviour.

6 Results and Discussion

6.1 Initial Resistivity Measurements

As a method of quality control, initial measurements were taken using the surface resistivity jig connected to a 9 volt ohmmeter. This provided instant clarification regarding whether or not a sample was conducting and therefore percolated. It also quantified when the upper percolation threshold had been reached and therefore further loading volumes were not required. Although rudimentary with limitations in accuracy at high and low conductivities, this set-up provided initial results before more accurate measurement routines were established.

The initial samples were manufactured at 45% volume as this was assumed to be sufficient to surpass percolation and would give a fair comparison with the commercially available silver filled epoxy from Loctite.

Two of the initial Silberline particle batches tested (Tin coated iron and Cup 21) were of significantly large particle size and therefore did not mix well into solution with the PMMA resin. This in turn had a major impact when printing as the large particles would sink and agglomerate before a uniform print could be drawn. The final prints were therefore of a grainy appearance and non-conducting. The remaining pigment (AB1) produced well mixed and uniform prints but they were still non-conducting. Table 8 details the results of these initial tests.

Table 8 – Initial Resistivity Test Results

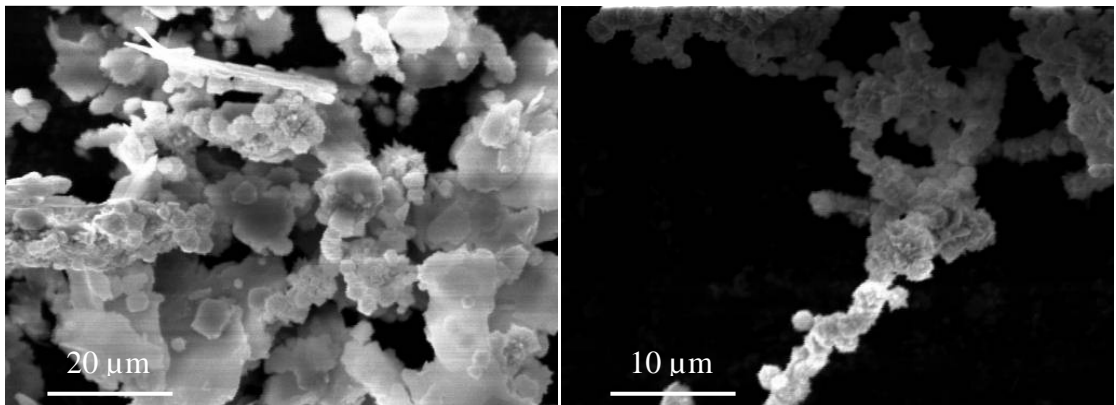
Filler material	Filler content	Particle Size (mm)	Surface Resistivity (Ω/square)
Silberline - Tin Coated Iron	45%	0.330	Non Conducting
Silberline - Copper Pigment AB1	45%	0.004	Non Conducting
Silberline - Cup 21 Copper Paste	45%	0.013	Non Conducting
HCA-1 Nickel Flake	45%	0.010	303.5
525 Nickel	45%	0.004	Non Conducting
525 Nickel (Low Density)	45%	0.004	Non Conducting
Sil-Shield Silver Coated Glass	45%	0.020-0.060	Non Conducting
Loctite - Silver Epoxy (Neat)	40-60%	0.003	1.5
Loctite - Silver Epoxy (Thinned)	40-60%	0.003	12.3

The Novamet filler powders;

- Novamet HCA-1 nickel - A thin flake powder with a high aspect ratio. Given as almost 20 to 1 in the material data sheet ^[187]. An SEM micrograph of these flakes can be seen in Figure 6.1.
- Novamet 525 regular grade and low density grade nickel – These are fine powders that have been produced through heat treated nickel carbonyl giving filamentary type particles ^[188]. SEM micrographs of these powders can be seen in Figures 6.2 and 6.3.
- Sil-Shield silver coated solid glass spheres. An SEM micrograph of these particles can be seen in Figure 6.4.

These fillers all mixed well and produced uniform prints, although only the flake powder (HCA-1) formed a conductive network. The slightly larger particle size and high aspect ratio of the HCA-1 flakes have likely been a factor as to why conduction was observed. As the printed samples are relatively thin it is also possible the flake

shape particles could have an affinity to align within the acrylic therefore further increasing the contact area between individual flakes. The Sil-Shield silver coated glass spheres also failed to percolate at this volume. With the Sil-shield particles being spherical it is assumed that the percolation threshold will be raised and follow a more rapid transition from insulator to conductor.



(Figures 6.1 and 6.2, SEM Micrographs of HCA-1 Nickel Flake and 525 Regular Grade Nickel)

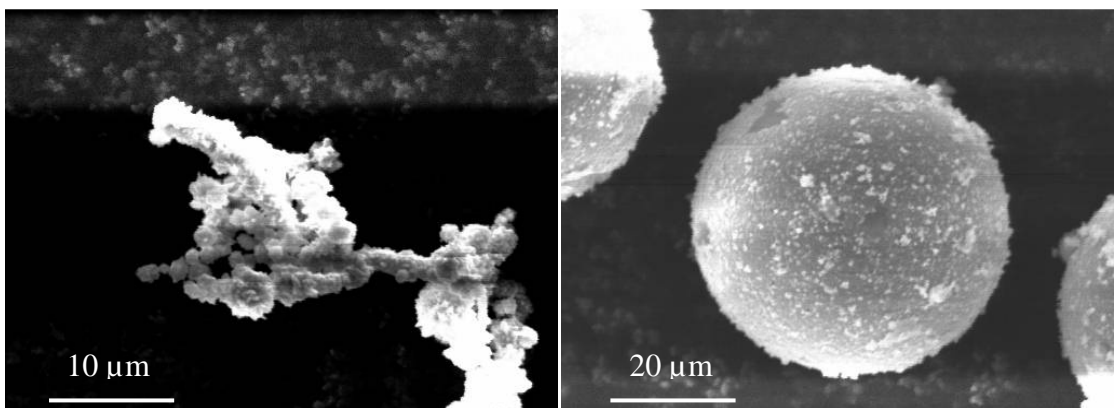


(Figure 6.3 and 6.4, SEM Micrographs of 525 Low Density Nickel Powder and Sil-Shield Silver Coated Glass)

6.1.1 Carbonaceous Samples

The carbon materials tested included a high surface area graphite powder, Timrex HSAG 100, a carbon black powder for spectroscopy and an expanded graphite powder from SGL carbon. Table 9 details the particle properties of these fillers.

Table 9 Carbonaceous Powder Properties

Filler Type	Particle Size (μm)	Apparent Density (g/cm^3)
HSAG 100	13.2	0.4
Carbon for Spectroscopy	35.7	0.69
Expanded Graphite	5.0	0.098

As can be seen in Figure 6.5, the spectroscopy carbon and the Timrex HSAG100 both showed classical percolation behaviour where the higher resistivity values dropped consistently until an upper percolation threshold was reached. This occurred at around 40% for both samples. The resultant resistivity reached for HSAG 100 was measured as approximately 1.5×10^4 ohm/ square whereas the carbon for spectroscopy reached a resistivity as low as 454 ohm/ square.

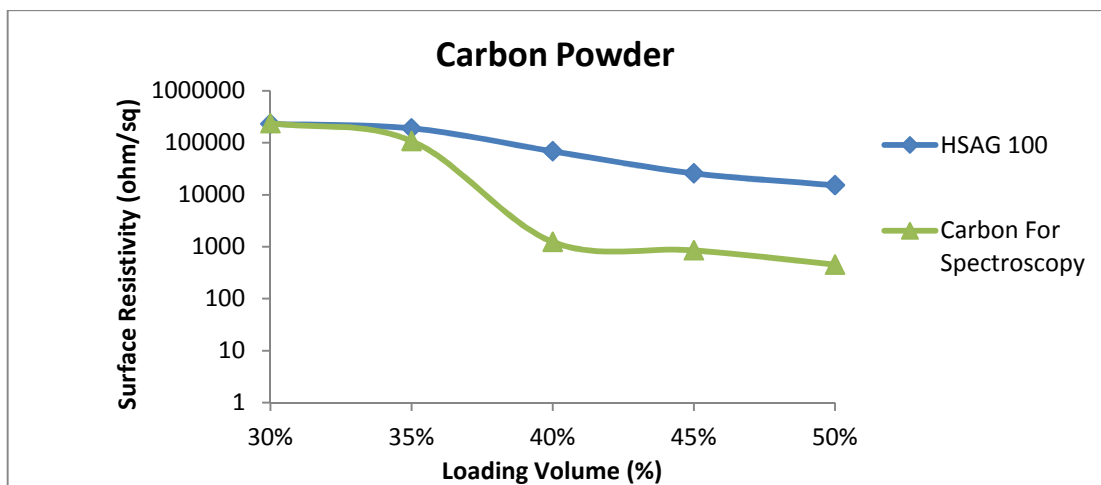


Figure 6.5, Surface Resistivity of Carbon for Spectroscopy and HSAG 100 Sample

Results in Figure 6.6 indicate that for the expanded graphite samples percolation was observed between 30-45% volume loading where the resistivity dropped to approximately 4.5×10^3 ohm/ square. This value further decreased as loading was incrementally increased reaching a minimum surface resistivity of 566 ohm/ square at a loading of 90% volume. The primary advantage to using expanded graphite over the other carbonaceous fillers is its low powder density. This results in making it a very lightweight and cost effective filler material.

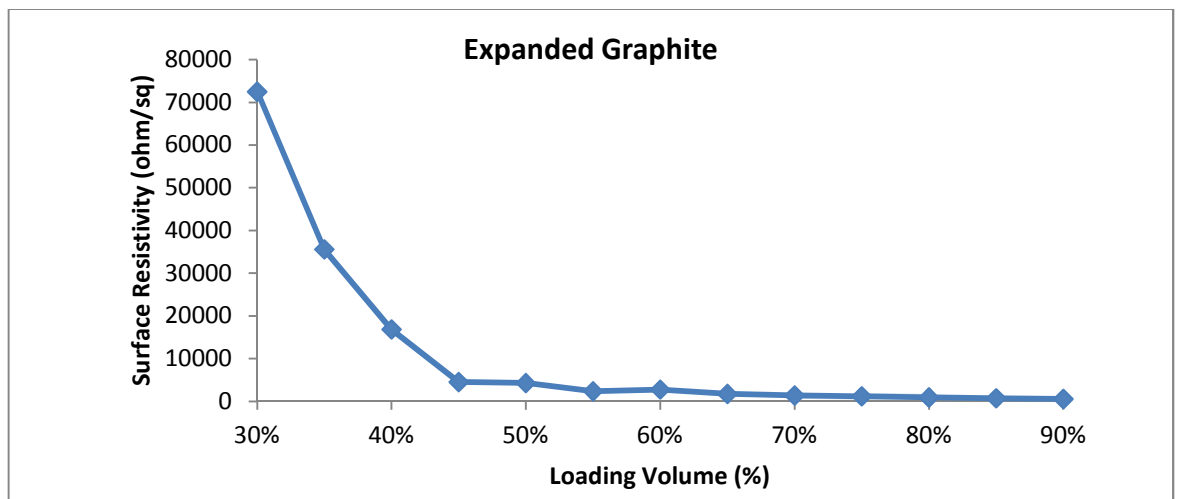


Figure 6.6, Surface Resistivity of Expanded Graphite Samples

6.1.2 Carbon and Nickel Samples

It was thought that by loading the matrix with expanded graphite the bulk resistance could be reduced before adding additional conductive particles and creating a 3 phase composite (Figure 6.7). HCA-1 and 525 regular powders were chosen to be the additional filler as these were both commercially available and had demonstrated an ability to print successfully. It was theorised that the percolation threshold of the additional filler may be reduced resulting in a lower volume metallic filler required. The

hypothesis was that the expanded graphite may bridge the insulating gaps between metallic particles. If successful a reduction in nickel content and therefore cost may be achievable. As can be seen from Figure 6.8, the results show that the addition of expanded graphite only lowered the resistivity until the normal percolation threshold of the nickel was met. Upon reaching this volume the nickel then followed its normal percolation trend gaining no benefits from the expanded graphite's presence.

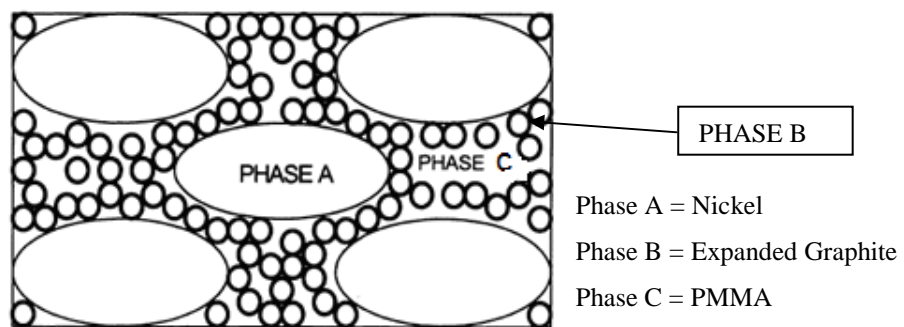


Figure 6.7, Schematic Diagram of a Three Phase Composite

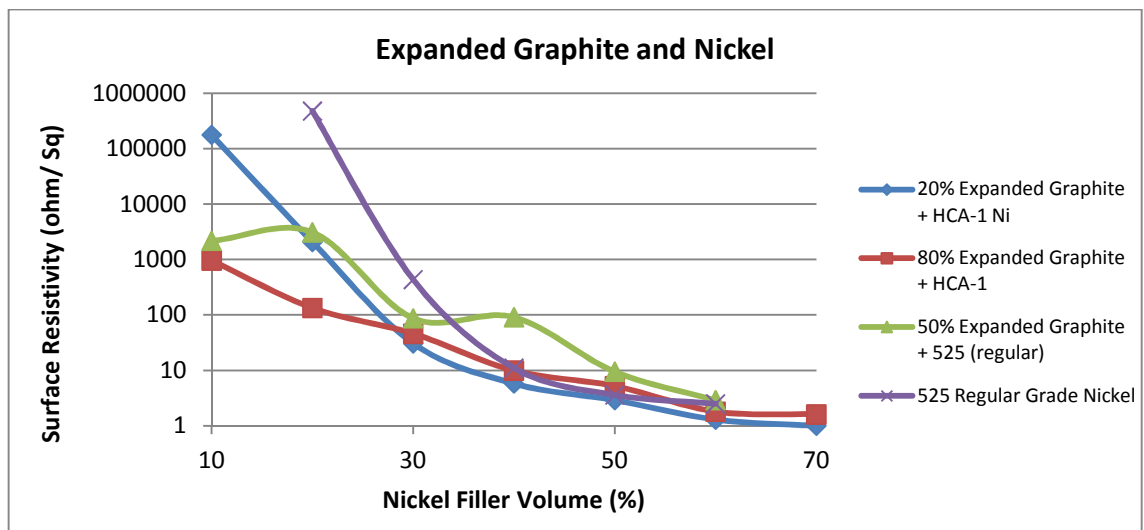


Figure 6.8, Surface Resistivity of Expanded Graphite Samples with Additional Nickel

6.1.3 Surface Resistance Variations

Additional studies were undertaken which investigated the effect that variables in the measurement technique had upon the surface resistivity. The variation in pressure applied to the test and the directionality of the test were both investigated.

It was clear during measurements of the surface resistivity that the loading applied to the test jig influenced the results obtained. This variation was observed by taking multiple surface resistivity measurements of a set of HCA-1 nickel filled samples with an incrementally increasing mass placed on top of the test jig. As can be seen in Table 10, a general trend is observed where the resistivity measured tends to lower as the mass is increased. The largest variations are noted between 0.5 kg and 2 kg, whereupon with the additional further masses the effect was less apparent.

Table 10 - Variation of Resistivity with Load Applied

Filler Volume (%)	Surface Resistivity (Ω /sq)									
	0.5 kg	1.0 kg	1.5 kg	2.0 kg	2.5 kg	3.0 kg	3.5 kg	4.0 kg	4.5 kg	5.0 kg
10	-	-	-	-	-	-	-	-	-	-
20	-	-	-	-	-	-	-	-	-	-
30	3.9 M	91.0 k	74.7 k	45.1 k	44.6 k	44.3 k	43.1 k	45.4 k	44.7 k	41.1 k
40	33.9	30.5	28.8	28.1	27.8	27.4	27.5	27.2	26.8	26.1
50	7.3	6.0	5.9	5.5	5.4	5.4	5.4	5.3	5.3	5.2
60	4.8	4.1	3.8	3.3	3.3	3.4	3.3	3.3	3.2	3.2

It was thought that the K-Control Coater printing process may preferentially align particles more in one direction than the other. This would create a less homogeneous composite and result in a more conductive sample when measured longitudinally compared to transverse measurements. As part of an undergraduate degree project, measurements were made on two sets of samples. These compared the resistivities obtained when measured transverse to the printing direction and longitudinal with the

printing direction. Tables 11 and 12 indicate that the resistivities measured do not demonstrate any significant variation with the orientation of the measuring jig ^[183].

Table 11 - Orientation of Surface Resistivity Measurement - 525 Regular Grade Nickel

Filler Volume (%)	Transverse Resistivity (Ω /sq)	Longitudinal Resistivity (Ω /sq)
10	N/C	N/C
20	N/C	N/C
30	15000	16300
40	720	800
50	11	8.2
60	4.8	4.4

Table 12 - Orientation of Surface Resistivity Measurement – 50% Expanded Graphite with Additional 525 Regular Grade Nickel

Filler Volume (%)	Transverse Resistivity (Ω /sq)	Longitudinal Resistivity (Ω /sq)
10	4600	4800
20	4100	4200
30	593	523
40	550	600
50	25	23
60	4	4

6.2 LCR Surface Resistivity Results

Surface resistivity measurements were also made at varying frequencies. The K-Control coated prints that had been previously produced were retested on a Wayne Kerr Precision Component Analyser 6425. Surface resistivity was measured using the standard test jig while following the procedure described in the analyser manual ^[189]. Samples were placed face up on a flat surface and the measurement rig placed on top of a uniform area of print. A 2 kg mass was then applied to the rig and the electrodes connected to the analyser. The analysis was carried out at varying frequencies and the resistivities were measured across the full range of sample loadings.

6.2.1 Silberline Samples

Following on from the initial pigments tested, Silberline provided an alternative range of samples, designated GA 180, GA 182, GA 184 and GA 186. SEM examinations and EDX analysis revealed these newer samples were copper based alloys and had been ball milled into a disc shape known as “silver dollar” particles.

Due to the limited volume of material available within each batch it was decided to produce samples that would most likely encompass the percolation threshold. This resulted in only three samples of each pigment being produced at loadings of 30%, 40% and 50%.

Initial sample manufacture indicated that the most likely to demonstrate conductivity was manufactured from pigment GA 180. This pigment mixed well and on initial DC surface resistivity checks demonstrated a degree of conductivity apparent, albeit the samples were still highly resistive. On this basis Silberline later produced a further batch of material with a similar composition, designated L1-1837.

GA 180

GA 180 is of a lustrous gold coloured appearance and as can be seen in the SEM micrograph in Figure 6.9, contains a range of particle sizes of approximately 3-25 μm . These particles also have a relatively high aspect ratio having been milled flat into their disc shape.

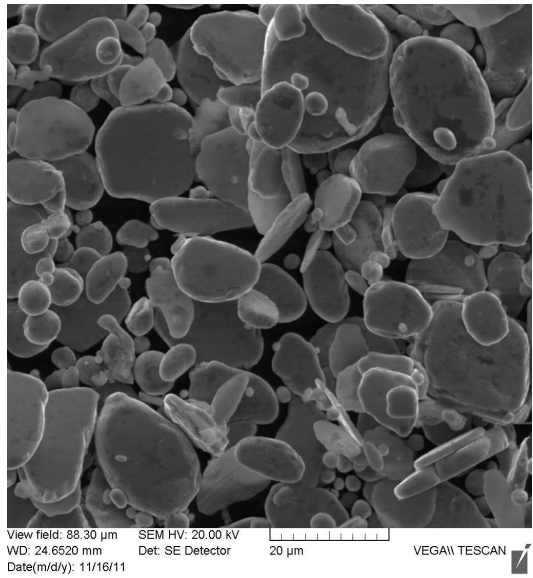


Figure 6.9, SEM Micrograph of GA180 Particles

EDX Analysis established the particles comprise only copper and aluminium alloyed together. Figure 6.10 and Table 13 provides the spectrum and details of the elemental chemical analysis obtained.

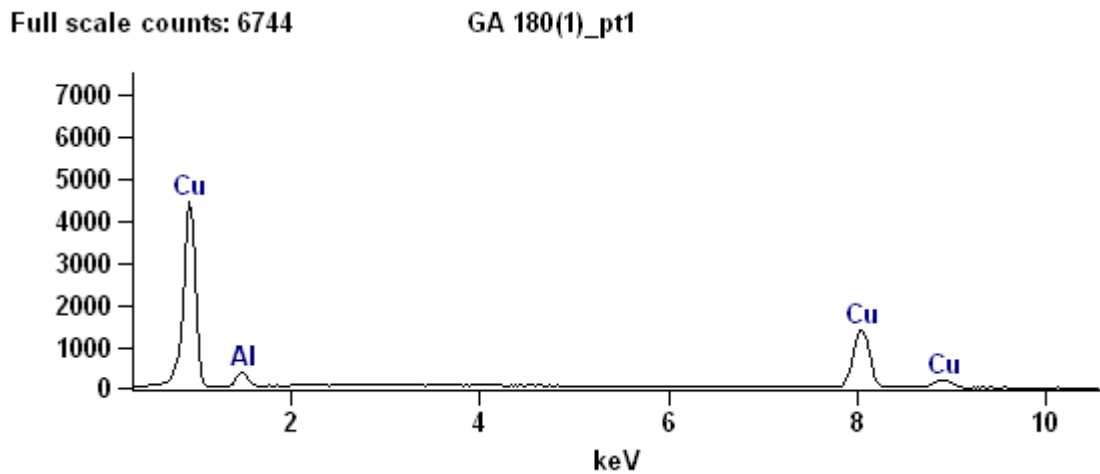


Figure 6.10, EDXA Spectrum GA 180

Table 13 Elemental Analysis of GA180 (wt%)

Material	Elemental Analysis	
	Al	Cu
GA 180	5.91	94.09

Although initial DC resistivity checks revealed some conductivity, further surface resistivity tests at various frequencies found no evidence of any percolation to be apparent. Figure 6.11 provides the results obtained.

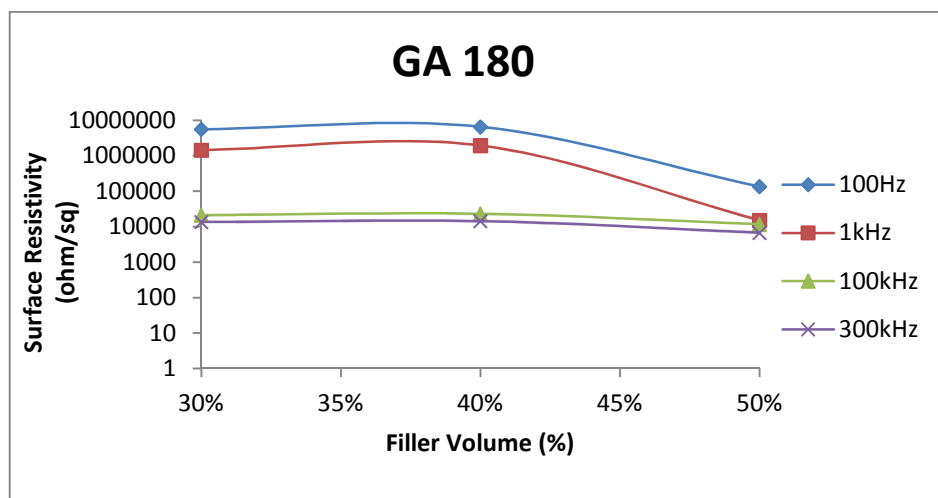


Figure 6.11, Surface Resistivity of GA 180

GA 182

GA 182 is of a pale tarnished gold appearance and as can be seen in the SEM micrograph Figure 6.12, contains a range of larger particle sizes of approximately 5-30 μm . These particles are a mixture of relatively high aspect ratio particles and others which are more cuboidal in appearance.

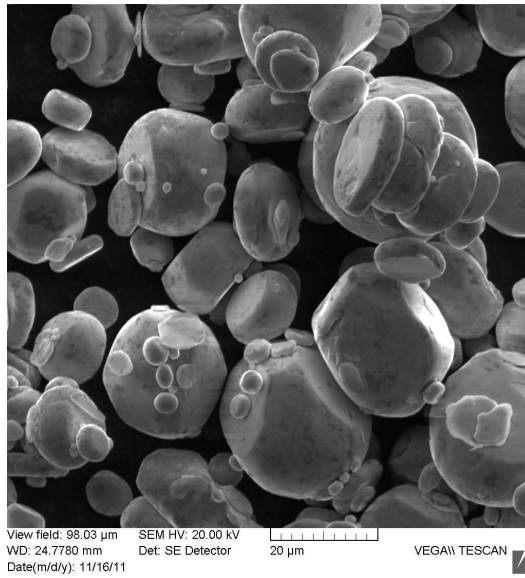


Figure 6.12, SEM Micrograph of GA 182 Particles

EDX Analysis established the particles comprise a copper, aluminium and nickel alloy. Figure 6.13 and Table 14 provides the spectrum and details of the elemental chemical analysis obtained.

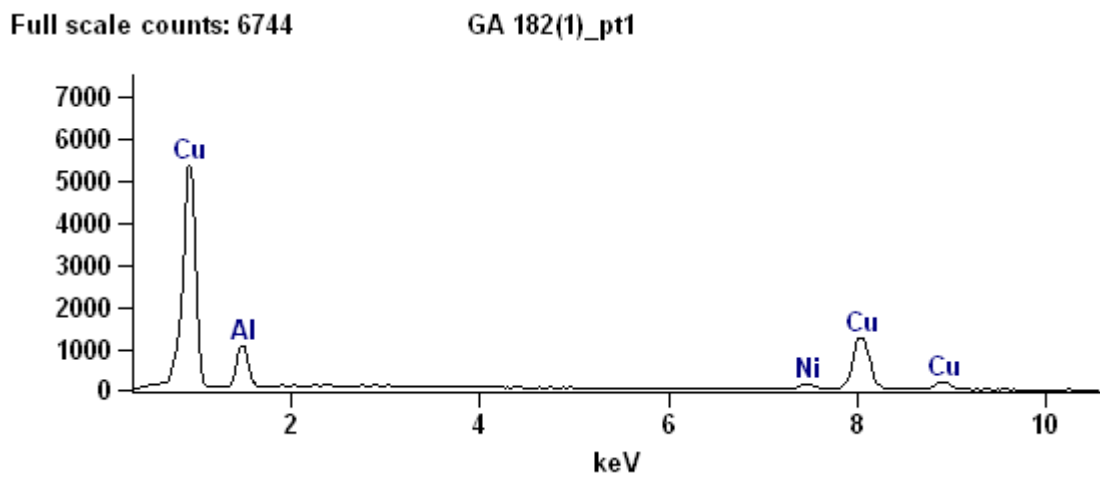


Figure 6.13, EDXA Spectrum GA 182

Table 14 - Elemental Analysis of GA182

Material	Elemental Analysis (wt%)		
	Al	Ni	Cu
GA 182	5.91	4.94	94.09

Surface resistivity testing at various frequencies revealed no evidence of any reduction in resistivity or percolation apparent. Figure 6.14 details the results obtained.

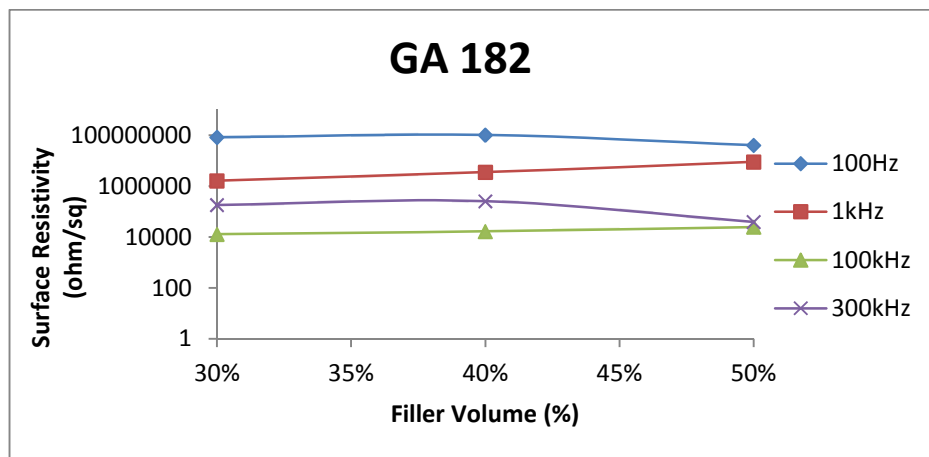


Figure 6.14, Surface Resistivity of GA 182

GA 184

GA 184 is also of a pale tarnished gold appearance and as can be seen in the SEM micrograph Figure 6.15, contains a range of particle sizes of approximately 5-35 μm . These particles are a mixture of slightly lower aspect ratio and some thin high aspect ratio discs.

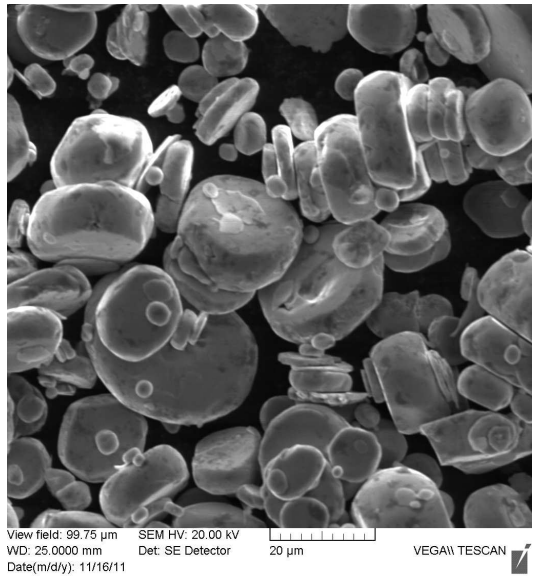


Figure 6.15, SEM Micrograph of GA 184 Particles

EDX Analysis established the GA 184 particles comprise a copper aluminium and nickel alloy, with a slightly higher level of aluminium and a slightly lower level of nickel than GA182. Figure 6.16 and Table 15 provides the spectrum and details of the elemental chemical analysis obtained.

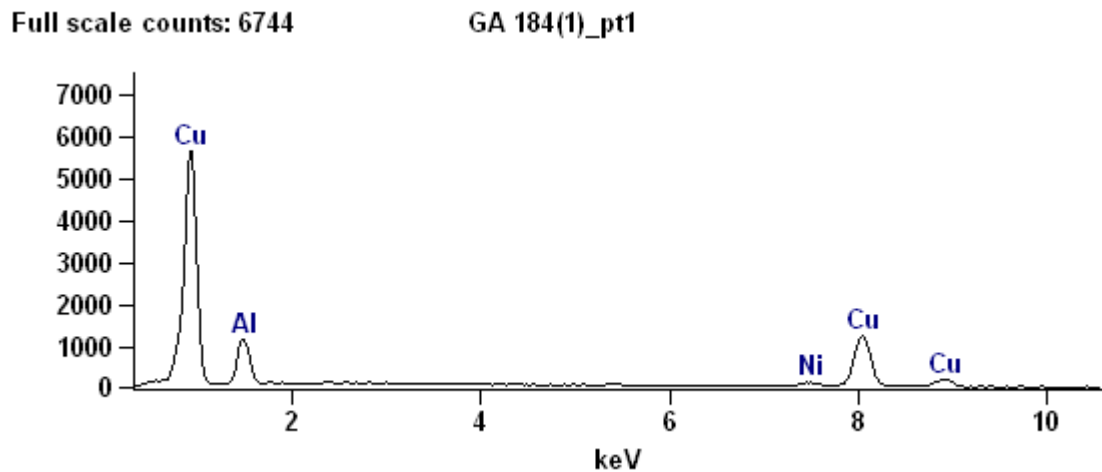


Figure 6.16, EDXA Spectrum GA 184

Table 15 - Elemental Analysis of GA184

Material	Elemental Analysis (wt%)		
	Al	Ni	Cu
GA 184	17.30	3.78	78.92

Surface resistivity testing at various frequencies revealed no evidence of any reduction in resistivity or percolation apparent. Figure 6.17 provides the results obtained.

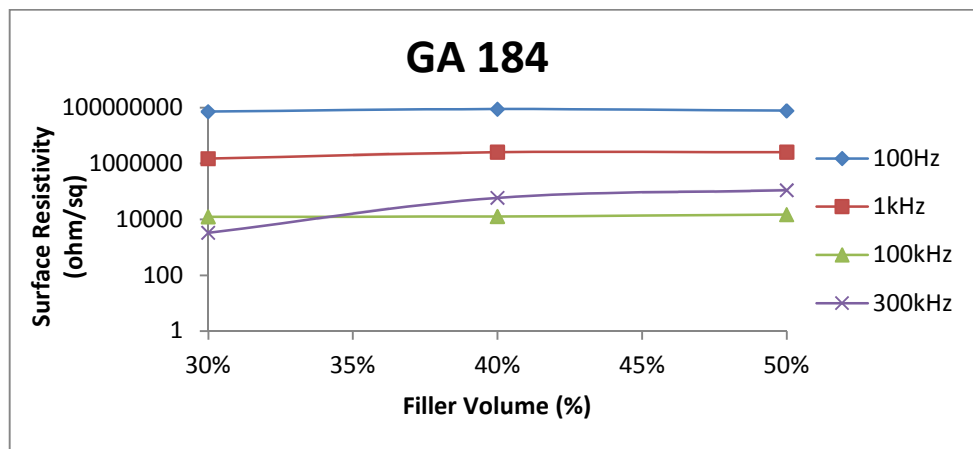


Figure 6.17, Surface Resistivity of GA 184

GA 186

GA 186 is of a reddish brown appearance and as can be seen in the SEM micrograph Figure 6.18, contains a range of larger particle sizes of approximately 7-35 μm . These particles appear to be a mixture of slightly thicker discs.

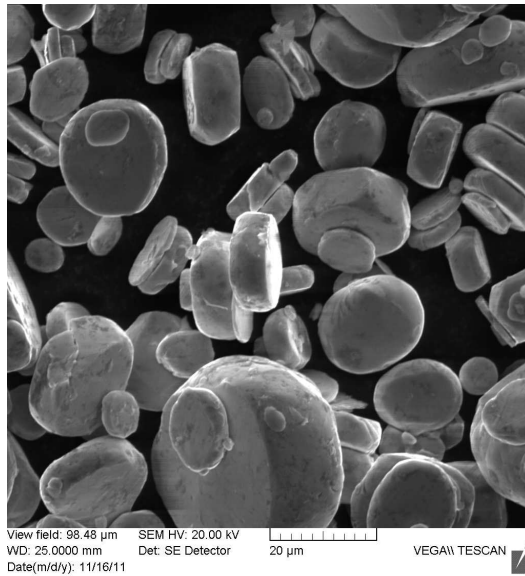


Figure 6.18, SEM Micrograph of GA186 Particles

EDX Analysis established the GA 186 particles comprise a copper aluminium and nickel alloy although, oxygen was also detected. This is most likely attributable to oxidation of the particle surfaces. Figure 6.19 and Table 16 provides the spectrum and details of the elemental chemical analysis obtained.

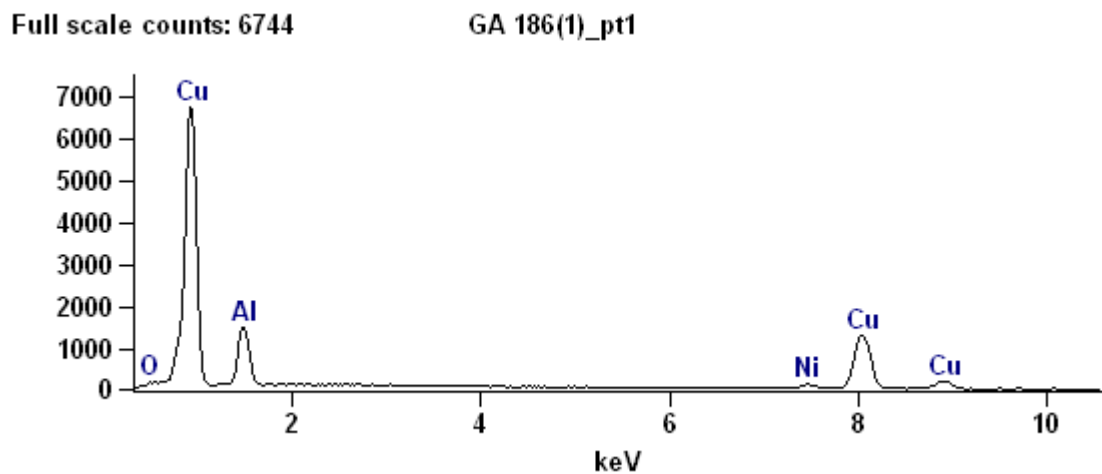


Figure 6.19, EDXA Spectrum GA 186

Table 16 - Elemental Analysis of GA186

Material	Elemental Analysis (wt%)			
	O	Al	Ni	Cu
GA 186	1.05	17.80	3.11	78.04

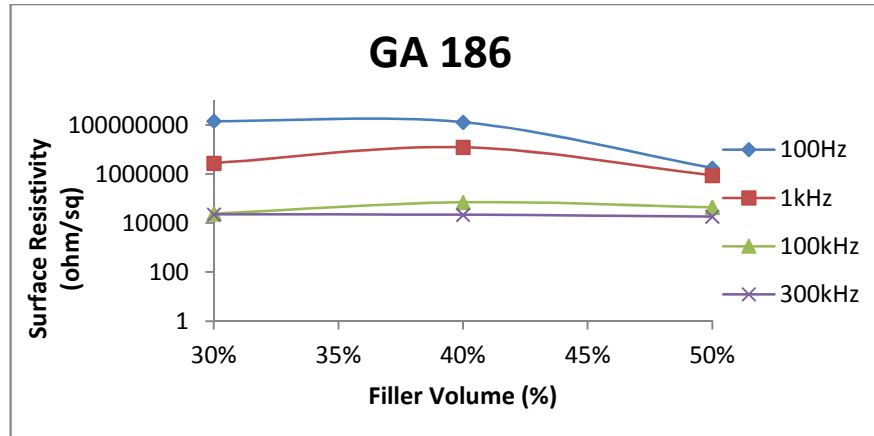


Figure 6.20, Surface Resistivity of GA 186

L1-1837

L1-1837 is of a dark gold coloured appearance and was supplied in a solvent binder creating an agglomerated paste. The solvent was removed with ethyl acetate and filtered in a Buchner funnel. SEM examination revealed the particles were of a much thinner flake type with a more ragged edge to them, known as “cornflake type”. These can be seen in the SEM micrograph, Figure 6.21. The particle size range is approximately 3-25 μm . These flakes also have a relatively high aspect ratio.

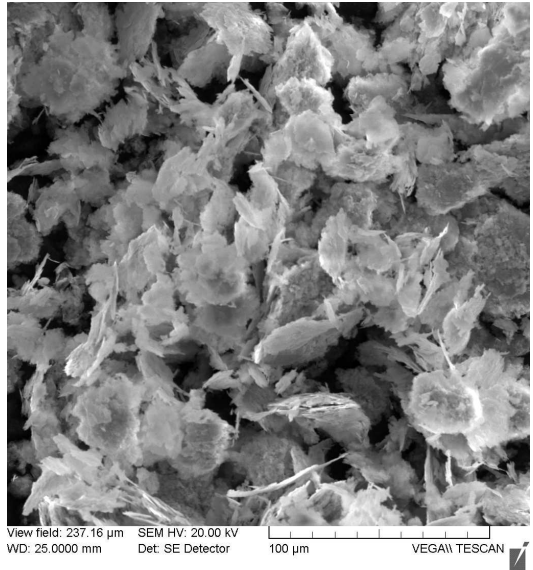


Figure 6.21, SEM Micrograph of L1-1837 Flakes

EDX Analysis established the particles comprise of a copper and aluminium alloy with a significant oxygen detection also noted. This again is likely to be the result of oxidation of the particles. Figure 6.22 and Table 17 provides the spectrum and details of the elemental chemical analysis obtained.

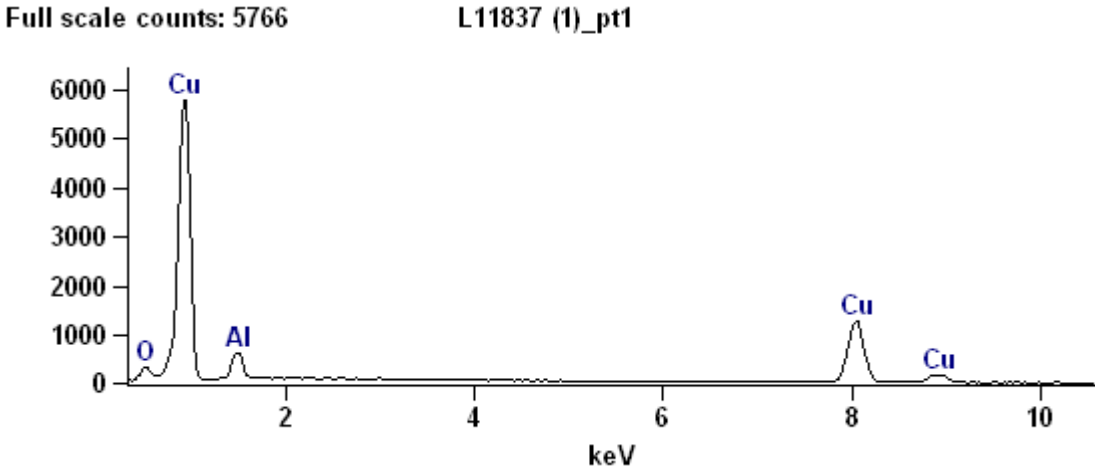


Figure 6.22, EDXA Spectrum L1-1837

Table 17 - Elemental Analysis of L1-1837 (wt%)

Material	Elemental Analysis (wt%)		
	O	Al	Cu
L1-1837	5.67	9.59	84.73

The larger volume of sample material provided allowed for a more exhaustive range of test samples to be produced. These initially ranged from 20% to 70% volume. Checks on these samples revealed that still no notable conduction was occurring. Samples were then produced with increased loading volume up to 200% to investigate the effect very high loading would have on the composite. Again no percolation behaviour or conduction was evident.

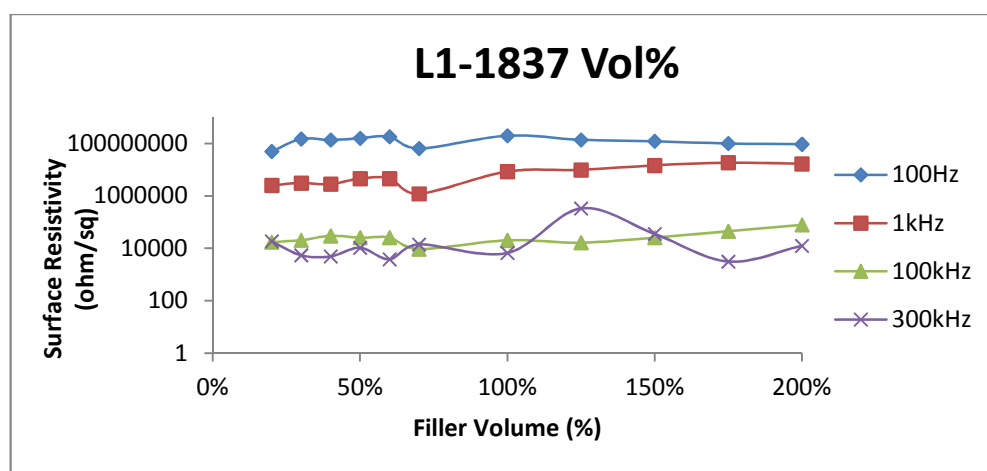


Figure 6.23, Resistivity Measurements of L1-1837

Summary

From the results obtained it can be seen that all of these samples demonstrate high resistivity with very little evidence of percolation behaviour patterns. There is a small drop in resistivity between 40% - 50% loading on samples GA-180 and GA-186 at lower frequencies. This is not significant enough to be seen as evidence of percolation

thresholds. It should also be noted that the differing testing frequencies did affect the resistivity of the overall sample. However, they do not appear to influence the percolation of the particles in these samples as the resistivity was consistent across the range of loading. This variation of resistivity is likely to be caused by the skin effect and the frequency variable reactive component of the impedance. As the frequency increases this reactance term is reduced.

6.2.2 Microsphere Technology Samples

Microsphere technology provided batches of silver coated microspheres and cenospheres. Following the established standard method of production, a range of samples were prepared and tested. These particles were of varying sphere types with different densities and size range as shown in Table 18. The test samples were produced with various loading levels and printed on the K-Control coated before being testing for surface resistivity at 100 Hz, 1000 Hz, 100 kHz and 300 kHz using the LCR meter.

Table 18 - Properties of Microsphere Samples

Sample Reference	Sample Type	Density (g/cm³)	Particle Size Range (µm)
L - 60	Microsphere	0.23	39 – 98
X - 10	Expanded Volcanic Ash	0.39	53 - 105
M - 18	Microsphere	0.72	5 - 30
B – 55 LX	Microsphere	0.55	34 - 72
SSB005	Microsphere	0.57	10 - 30
SSB006	Microsphere	0.45	10 – 45
SSB007	Microsphere	0.21	25 – 80
SSB008	Microsphere	0.26	25 - 70
SSB011	Cenosphere	1.78	5 - 30
SSB012	Cenosphere	0.78	10 – 45
SSB013	Cenosphere	0.77	10 - 45

All values provided by Microsphere Technology.

L-60

L-60 is a silver coated hollow glass microsphere of a light tan appearance. With a density of 0.23 g/cm^3 they are very lightweight. As can be seen in the SEM micrograph in Figure 6.24 they comprise highly uniform spheres.

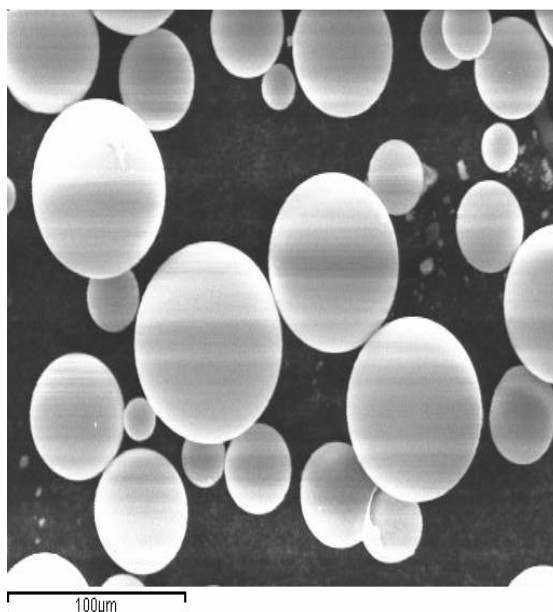


Figure 6.24, SEM Micrograph of L-60 Silver Coated Microsphere

Surface resistivity measurements revealed a rapid drop in resistivity within the 10% to 30% loading volume range that continues to reduce slightly up to the 50% maximum loading (Figure 6.25). The sample appears to have reached the percolation threshold by this 30% value. Resistivity obtained at this loading was measured in the region of 4 ohm/square for all frequencies tested and dropped further to just over 1 ohm/square at 50% loading.

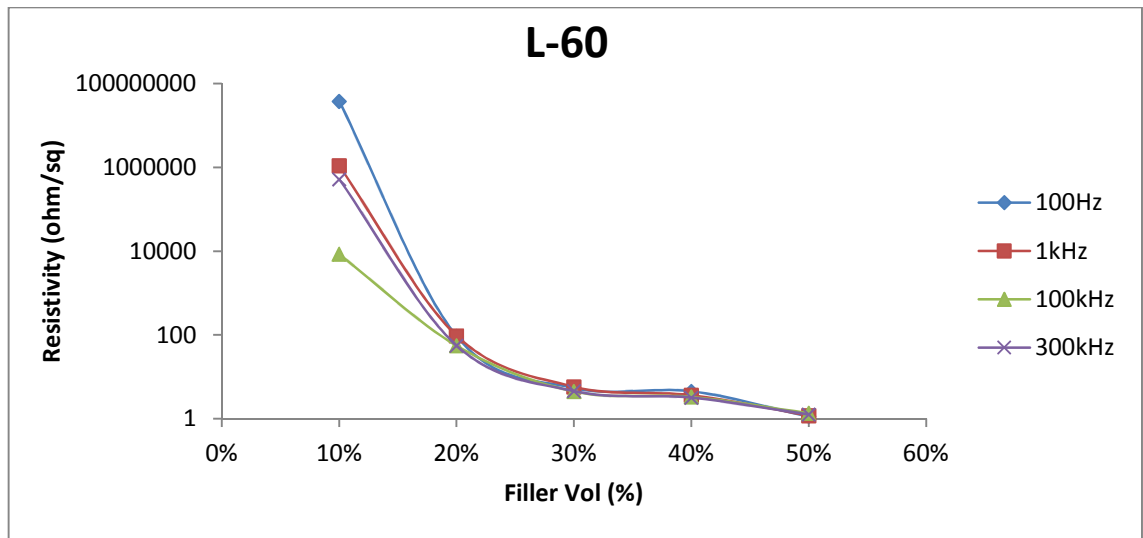


Figure 6.25, Surface Resistivity Measurements of L-60

X-10

X-10 particles are silver coated cenospheres produced from expanded volcanic ash. They have a light grey appearance and with a density of 0.39g/cm^3 they are also very lightweight. As can be seen in the SEM micrograph in Figure 6.26, they comprise uneven oval shaped particles with a nodular surface texture evident.

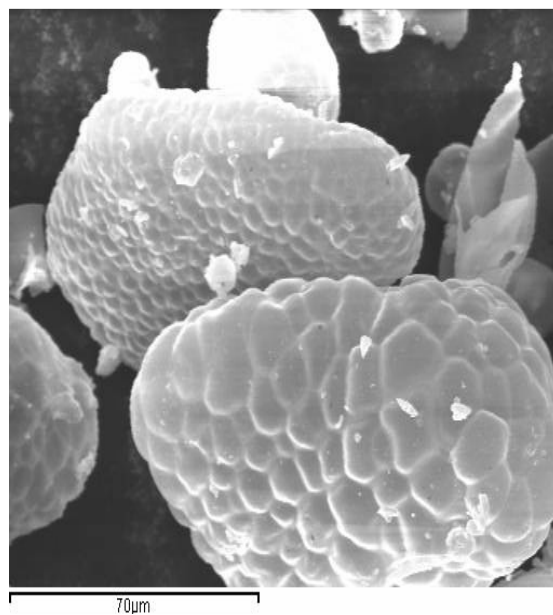


Figure 6.26, SEM Micrograph of X-10 Silver Coated Particles

Surface resistivity measurements revealed a rapid drop in resistivity within the 10% to 20% loading volume range which again continues to reduce slightly up to the 50% maximum loading (Figure 6.27). The samples appear to have percolated between the 20% and 30% values. Resistivity obtained at 30% was measured in the region of 4.5 ohm/square for all frequencies tested and dropped further to just around 2 ohm/square at 50% loading.

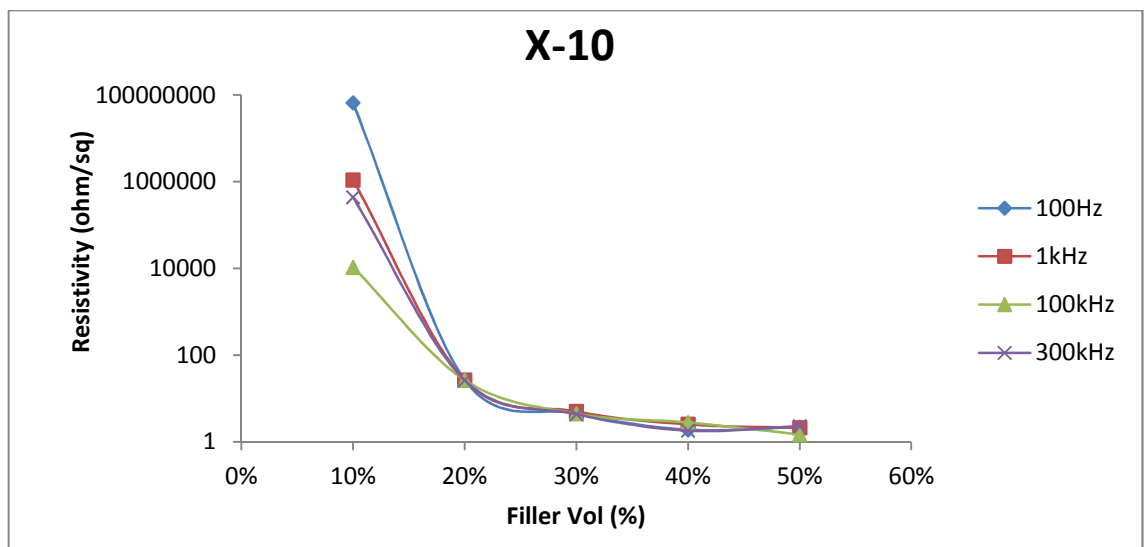


Figure 6.27, Surface Resistivity Measurements of X-10

M-18

M-18 particles are silver coated hollow glass microspheres of a light grey appearance. Although, in relation to the other microspheres tested, with a slightly increased density of 0.72 g/cm³, they are still a lightweight material. As can be seen in the SEM micrograph in Figure 6.28 they comprise highly uniform spheres of a reduced particle size.

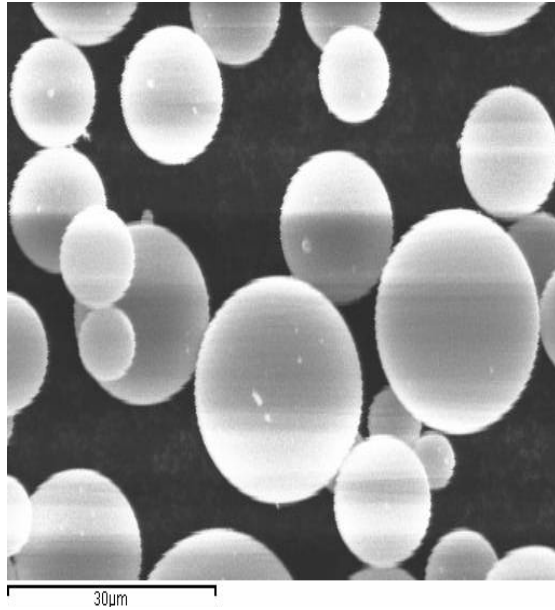


Figure 6.28, SEM Micrograph of M-18 Silver Coated Microspheres

Following the trend of the previous samples M-18 appears to percolate at a low threshold in the region of 20% loading volume. However as also seen previously the resistivity continues to drop with the increasing loading volumes (Figure 6.29). Resistivities of around 1.5 ohm/square were obtained at only 20% loading volume which dropped to around 0.2 ohm/square by 50% loading volume.

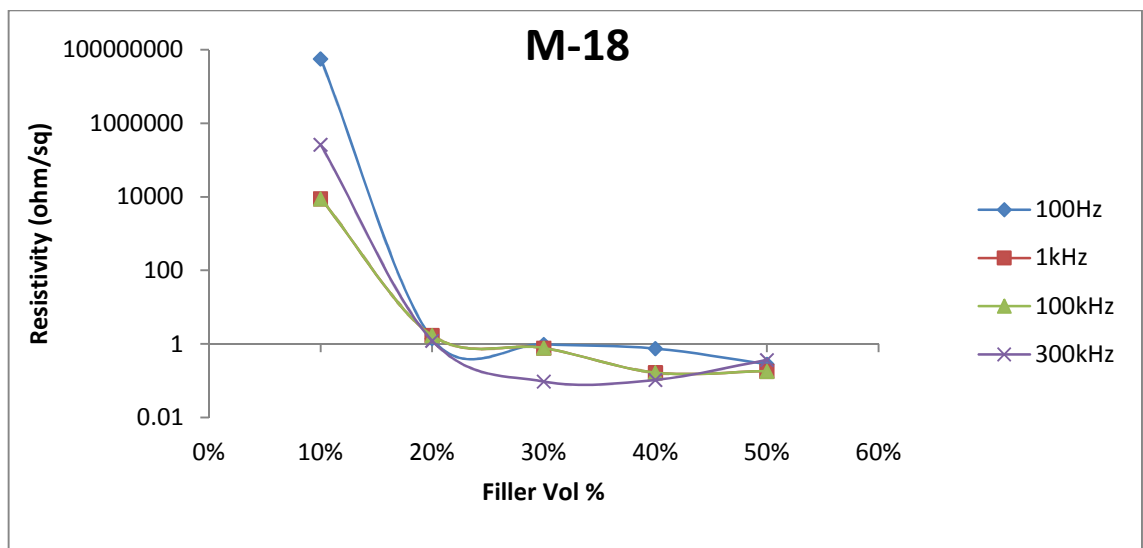


Figure 6.29, Surface Resistivity Measurements of M-18

B55-LX

B55-LX particles are silver coated hollow aluminosilicate glass microspheres with a tan appearance. They have a density of 0.55 g/cm^3 which again results in a lightweight material. As can be seen in the SEM micrograph in Figure 6.30, they comprise highly uniform spheres with a slightly coarser surface.

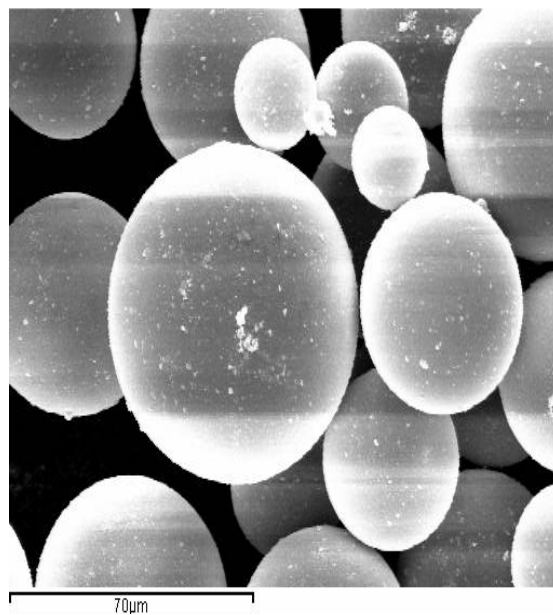


Figure 6.30, SEM Micrograph of B55-LX Silver Coated Microspheres

Again following the trend, a rapid drop in resistivity is noted between the 10% and 30% loading volume range (Figure 6.31). The sample appears to have percolated by this 30% value with resistivities of around 2.5 ohm/ square obtained. These only dropped slightly, reaching around 1.5 ohm/square at 50% loading.

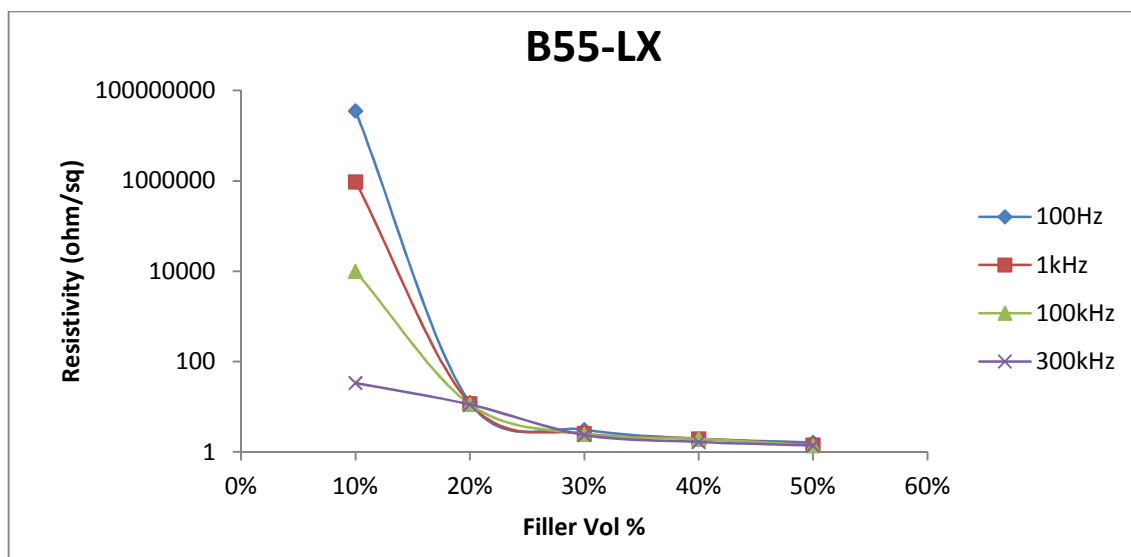


Figure 6.31, Resistivity Measurements of B55-LX Microspheres

The excellent results obtained for the M-18 samples encouraged Microsphere Technologies to produce an additional range of samples which were based around similar characteristics. Four samples of this range, denoted SSB005 – SSB008, were of the same glass type and with similar dimensions although the silver content was varied. A further three samples SSB011-SSB0013 were manufactured from natural cenospheres particles.

SSB005

Similar to the M-18 particles, SSB005 are silver coated hollow glass microspheres of a light grey appearance. They have a slightly lower density of 0.57 g/cm^3 . As can be seen in the SEM micrograph in Figure 6.32, they comprise highly uniform spheres of a small particle size.

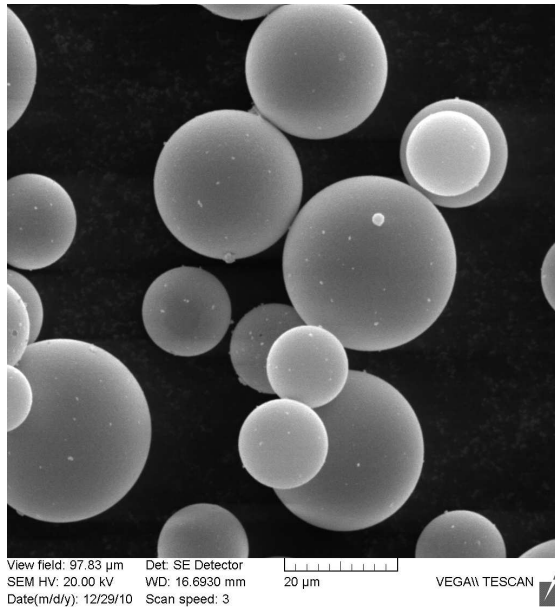


Figure 6.32, SEM Micrograph of SSB005 Silver Coated Microspheres

The range of loadings was increased slightly to include a 5% volume sample and continue up to 60% loading volume. As the previous results indicated a low percolation threshold, it was decided to include extra samples to ensure that the full percolation curve was observed. The results indicate that percolation was again reached between 20% and 30% loading volumes with resistivities of around 0.2 ohm/ square being observed at 30% (Figure 6.33).

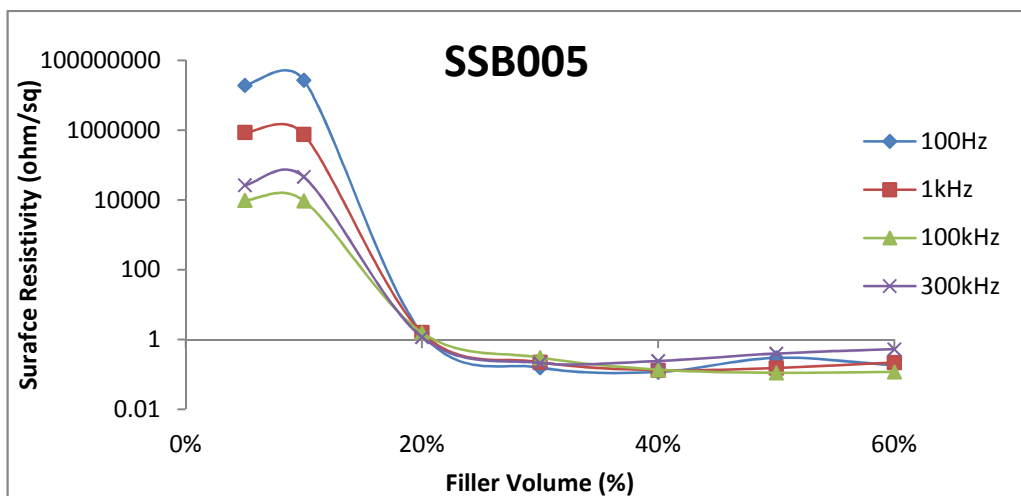


Figure 6.33, Resistivity Measurements of SSB005 Microsphere Samples

SSB006

SSB006 particles were very similar to SSB005 although with a slightly larger particle size range and reduction in density to 0.45 g/cm^3 . An SEM micrograph of the particles can be seen in Figure 6.34.

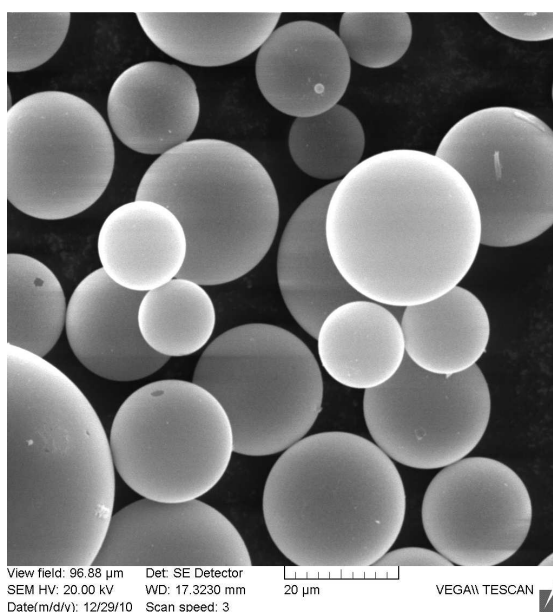


Figure 6.34, SEM Micrograph of SSB006 Silver Coated Microspheres

Again similar to SSB005, the results indicate that percolation was reached between 20% and 30% loading volumes with resistivities of around 0.3 ohm/ square being observed at 30% loading volume (Figure 6.35).

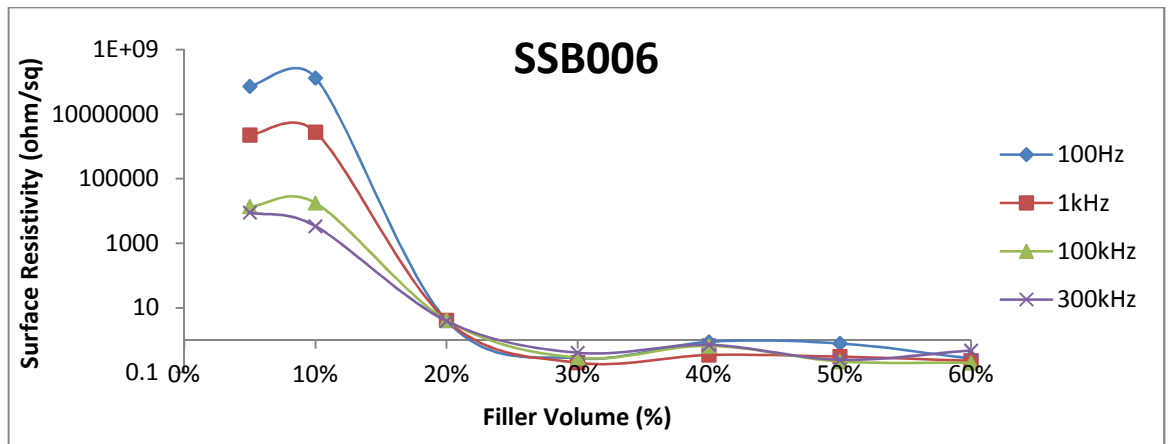


Figure 6.35, Resistivity Measurements of SSB006 Microspheres

SSB007

SSB007 are silver coated hollow glass microspheres of a grey appearance. These particles have a larger particle size range and low density of 0.21 g/cm^3 . As can be seen in the SEM micrograph in Figure 6.36, they comprise highly uniform spheres of a small particle size. Some fractured spheres are present - this may be a consequence of such a low density particle.

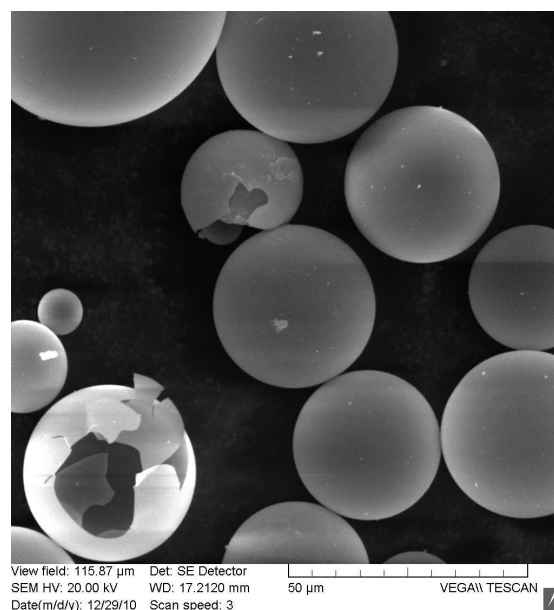


Figure 6.36, SEM Micrograph of SSB007 Silver Coated Microspheres

Percolation again appears to occur in the region of 30% loading volume. However a further notable reduction in the resistivity is observed between 50% and 60% volume loadings. The resistivities measured at 30% are around 17 ohm/square and when fully percolated at 50% this value decreases to around 2 ohm/square (Figure 6.37).

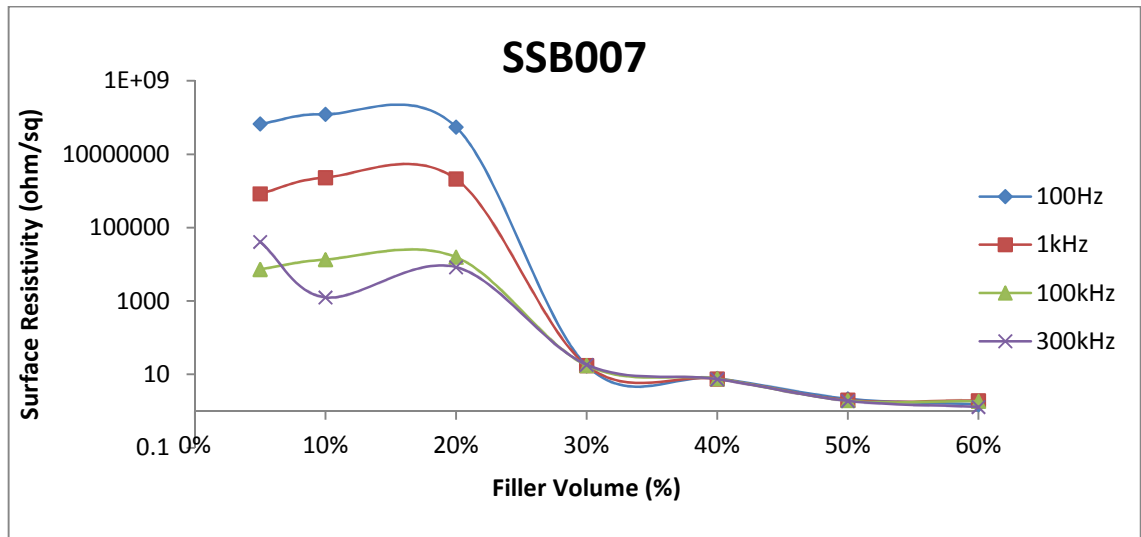


Figure 6.37, Resistivity Measurements of SSB007 Microspheres

SSB008

SSB008 are very similar to the SSB007 particles. These particles have a tighter particle size range and slightly higher density of 0.26 g/cm^3 . As can be seen in the SEM micrograph in Figure 6.38, they comprise highly uniform spheres of a small particle size. Again some fractured spheres were noted.

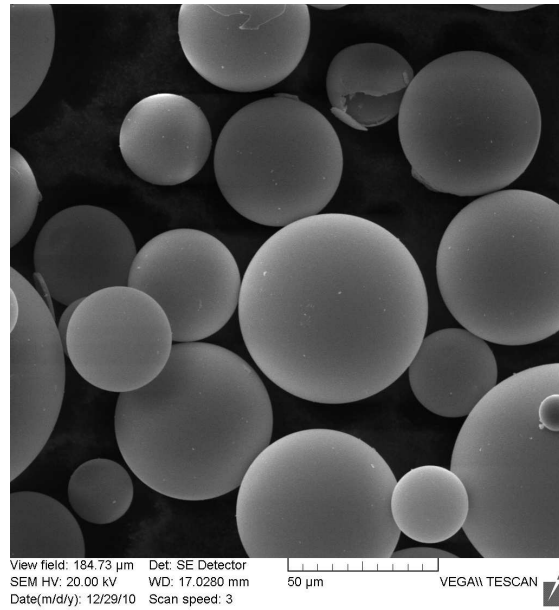


Figure 6.38, SEM Micrograph of SSB008 Silver Coated Microspheres

Again following the same behaviour as SSB007, percolation appears to occur in the region of 30% loading volume and again a further reduction in the resistivity is observed between 50% and 60% volume loadings. The resistivities measured at 30% are however lower at around 3 ohm/ square and once fully percolated at 50% the value decreases to around 0.15 ohm/square (Figure 6.39).

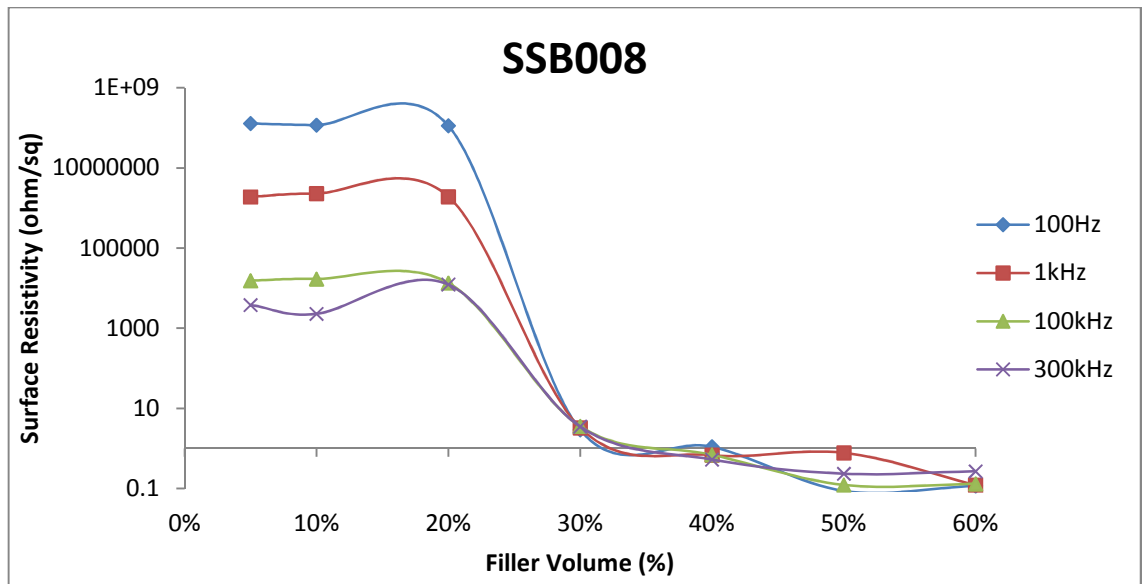


Figure 6.39, Resistivity Measurements of SSB008 Microspheres

SSB011

SSB011 are silver coated cenospheres of a light tan appearance. These particles are naturally occurring spheres that are subsequently silver coated. They have a small particle size and are of higher density than most of the comparable particles at 1.78 g/cm³. As can be seen in the SEM micrograph in Figure 6.40, they comprise uniform spheres with additional less uniform particles also included.

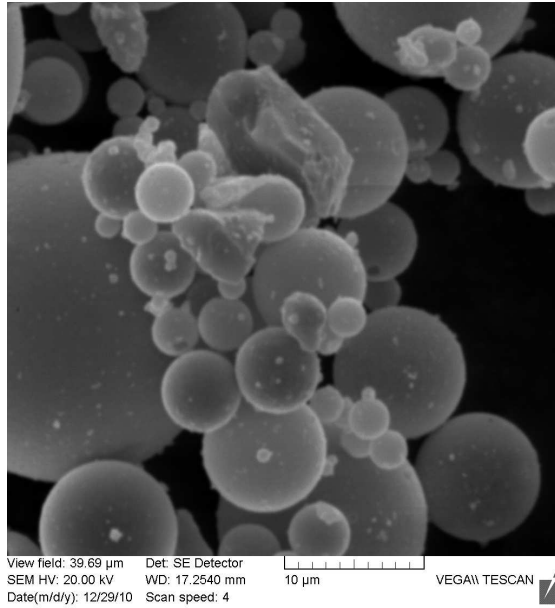


Figure 6.40, SEM Micrograph of SSB011 Silver Coated Cenospheres

Surface resistivity measurements indicate a very low percolation threshold between 10% and 20% loading volumes. The values obtained at 20% are around 0.1 ohm/ square and remain at this level with all additional loading (Figure 6.41).

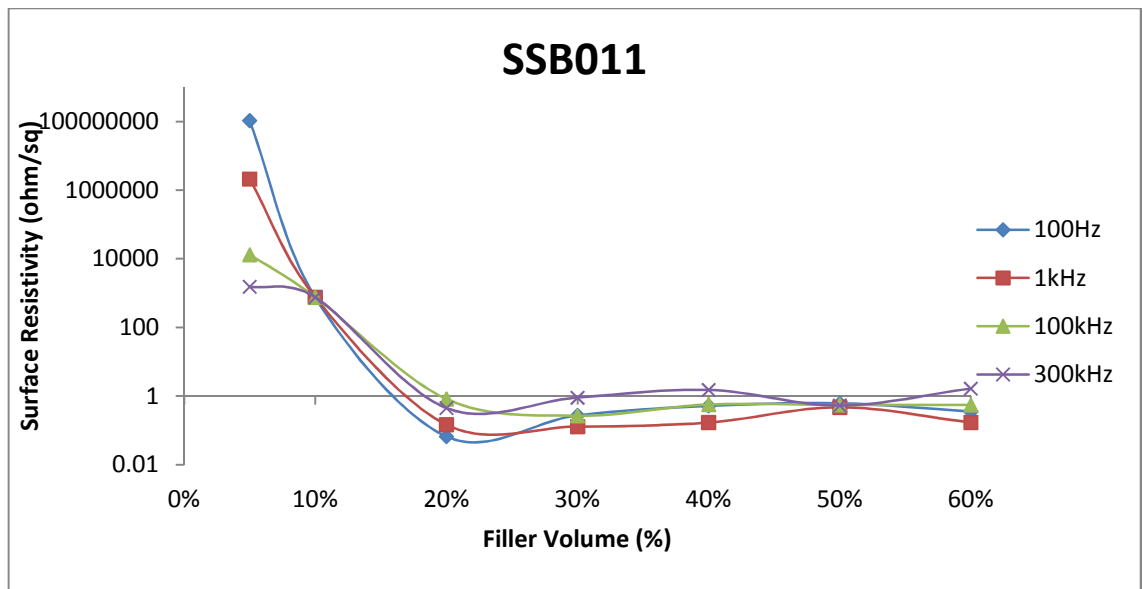


Figure 6.41, Resistivity Measurements of SSB011 Cenospheres

SSB012

SSB012 are also natural cenospheres of a light tan appearance. They have a slightly larger particle size and are of lower density than SSB011 at 0.71 g/cm^3 . As can be seen in the SEM micrograph in Figure 6.42, they comprise uniform spheres with additional less uniform particles also included.

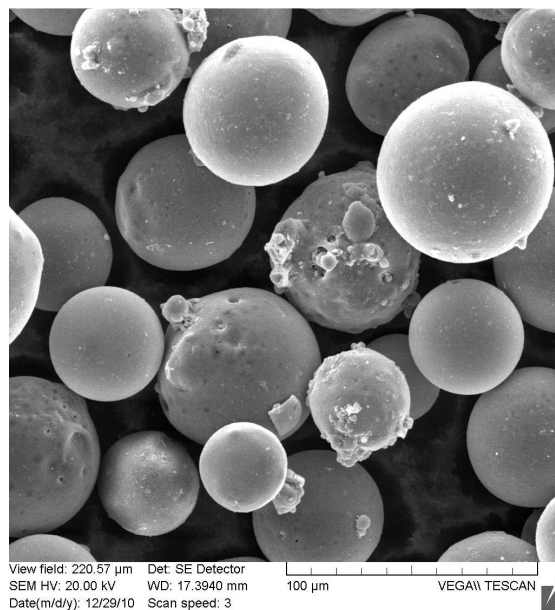


Figure 6.42, SEM Micrograph of SSB012 Silver Coated Cenospheres

Surface resistivity measurements indicate SSB012 behaves similarly to the majority of the microsphere samples, initially percolating at about 30% loading and continuing to reduce in surface resistivity until 50% loading. The values obtained at 30% are around 11 ohm/ square reducing to around 2ohm/ square at 50% loading (Figure 6.43).

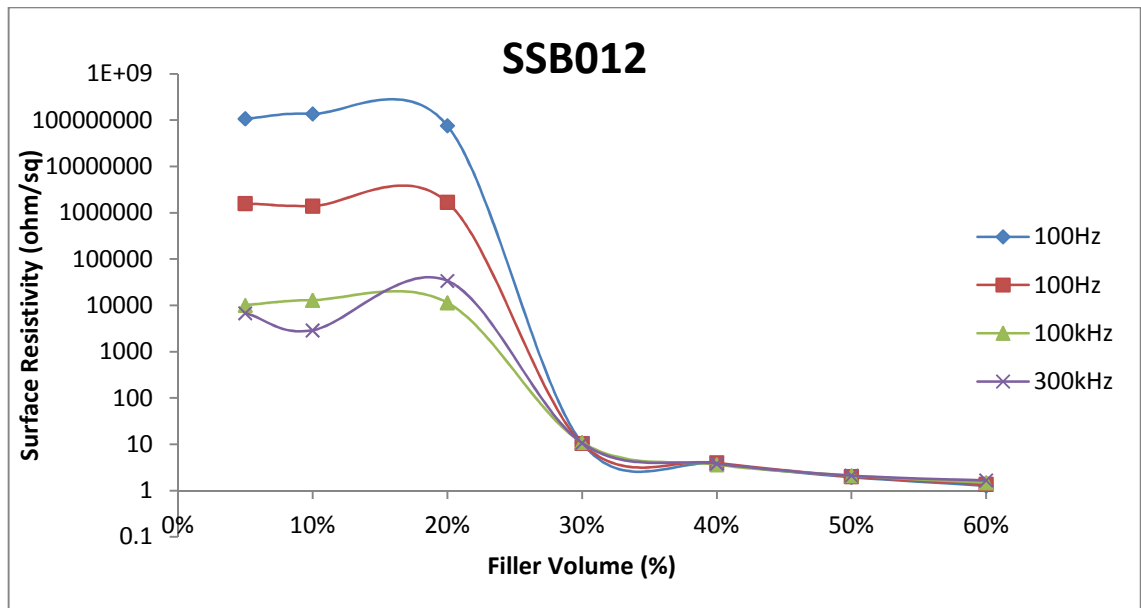


Figure 6.43, Resistivity Measurements of SSB012 Cenospheres

SSB013

SSB013 are again natural cenospheres of a light tan appearance. They share very similar properties to SSB012 although they have a density of 0.77 g/cm^3 . As can be seen in the SEM micrograph in Figure 6.44, they comprise uniform spheres with additional less uniform particles evident.

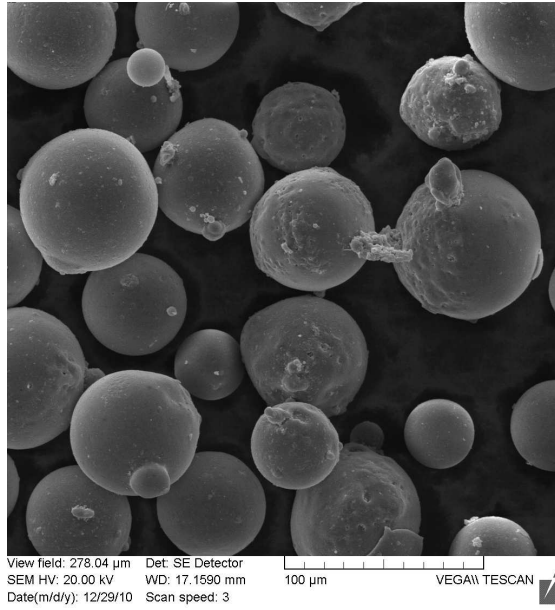


Figure 6.44, SEM Micrograph of SSB013 Silver Coated Cenospheres

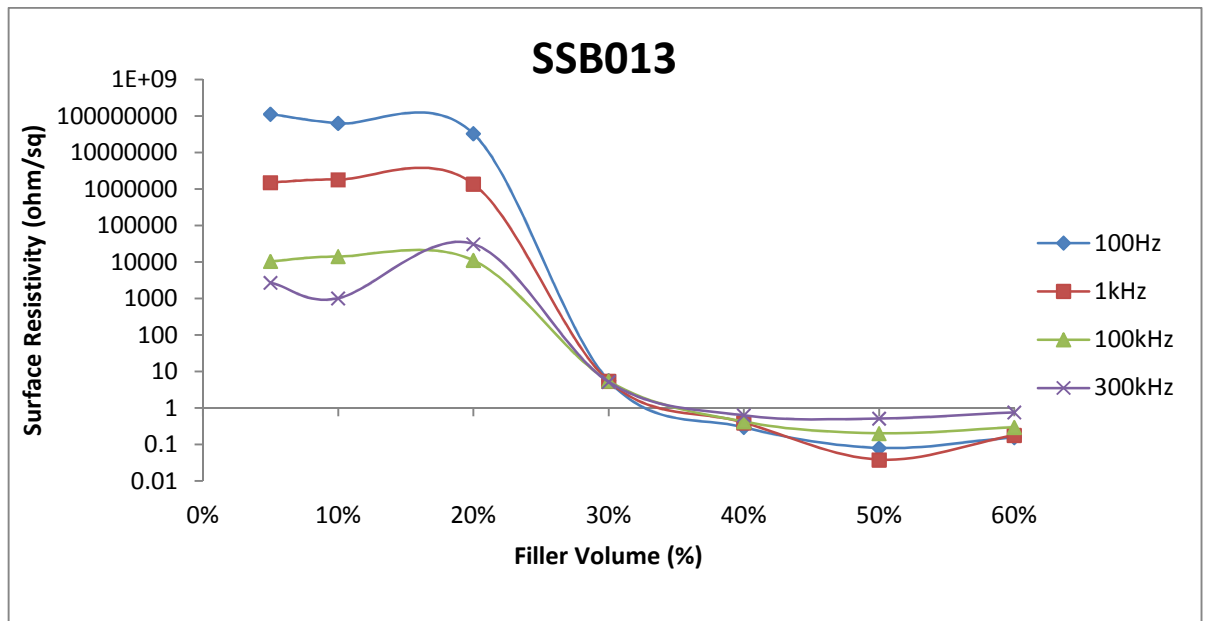


Figure 6.45, Resistivity Measurements of SSB013 Cenospheres

Again SSB013 behaves similarly to the other samples although initially percolating at a slightly higher loading between 30% and 40% loading. The values obtained at 40% are

around 0.4 ohm/ square and remain in this region through the higher loading levels (Figure 6.45).

Summary

The results observed from the surface resistivity testing of Microsphere Technology's samples indicated that the majority of samples followed a common trend of percolation behaviour. Almost all the samples demonstrated percolation between 20% and 30% loading volumes although the level of resistivity reached varied between samples. Exceptions to this trend were samples M-18, SSB005 and SSB011 that percolated in the region of 20% loading reaching resistivities in the region of 0.2 ohm/ square once fully percolated.

Conversely, some samples only exhibited resistivities in the region of 2 ohm/ square when fully percolated. These tended to be the larger particle size samples. It is likely that as a result of fewer particles per unit area, a reduced number of connected network paths are available. Therefore a slight increase in resistivity is observed.

Surface resistivity results obtained for all additional materials tested following this technique can be found in Appendix B.

7 EMI Attenuation Results

7.1 Dipole Test

Initial shielding measurements were made using a two dipole antennas set up contained within a small shielded chamber. The dimensions of the antennas available limited the test frequency to 2.1 GHz. This was the frequency the dipoles were tuned to and therefore provided the strongest signal strength.

Figure 7.1 provides the shielding effectiveness measured using this apparatus. These results have been plotted alongside the corresponding surface resistivity of each sample demonstrating the relationship between resistivity and shielding effectiveness. In general, it can be seen that the lower the surface resistivity the more the signal is attenuated. However this is not the case when comparing the silver filled epoxy with the three nickel powder filled samples. All the nickel samples demonstrate a higher surface resistivity while still providing a higher level of shielding effectiveness. The higher magnetic permeability of nickel than silver combined with good conductivity results in a higher level of shielding being achieved.

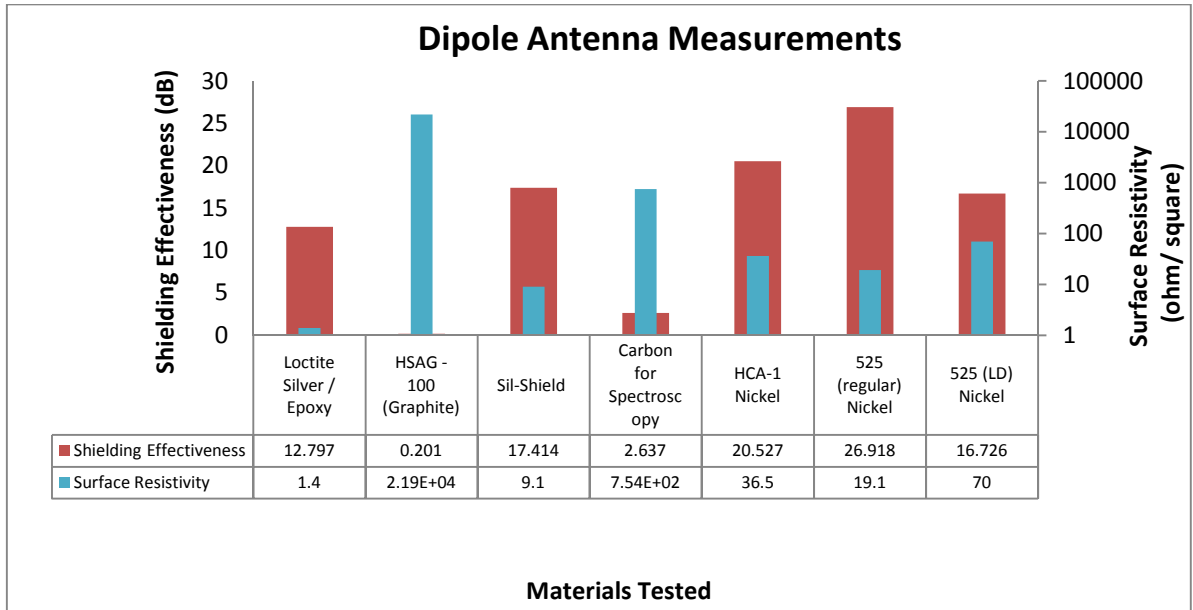


Figure 7.1, Dipole Antenna Attenuation

After performing this small batch of tests, the limitations of the small test chamber and basic antennas set-up became apparent. The inability to easily vary the test frequency and restrictive nature of the small chamber resulted in a new, more appropriate test regime being required.

7.2 Horn Antennas Results

Subsequent measurements were made using horn antennas and an analog power meter to measure the transmitted signal power. By taking the unshielded and shielded signal power measurements, the power ratio could be determined therefore the attenuation could be calculated;

$$Power Ratio_{Receiver} = \frac{Unshielded\ Signal\ Strength}{Shielded\ Signal\ Strength}$$

$$Attenuation\ (dB) = -10\log_{10}Power\ Ratio$$

After a period of time this power meter was replaced with a spectrum analyser. This allowed direct decibel readings to be taken. Therefore an unshielded value and a shielded value would be measured and the attenuation would be the difference. All testing was performed with a 9 GHz signal.

7.2.1 Attenuation Measurements

Expanded Graphite and Nickel Composites

Samples were produced comprising nickel powder, expanded graphite and various combinations of both combined. Figures 7.2 and 7.3 provide the results for the samples made with these fillers alone. It can be seen that the levels of shielding recorded are significantly larger for the nickel samples than for the expanded graphite with a maximum attenuation of 38 dB obtained compared to 4 dB with the graphite. However it was still to be seen whether combinations of both fillers would have an effect on the attenuation levels obtainable.

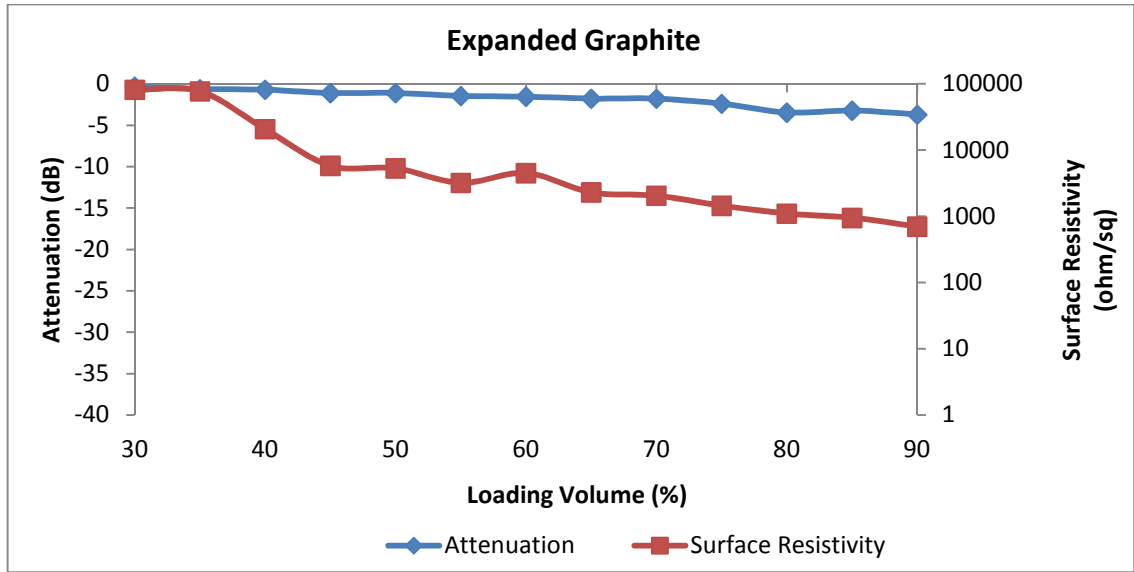


Figure 7.2, Attenuation Measurement of Expanded Graphite

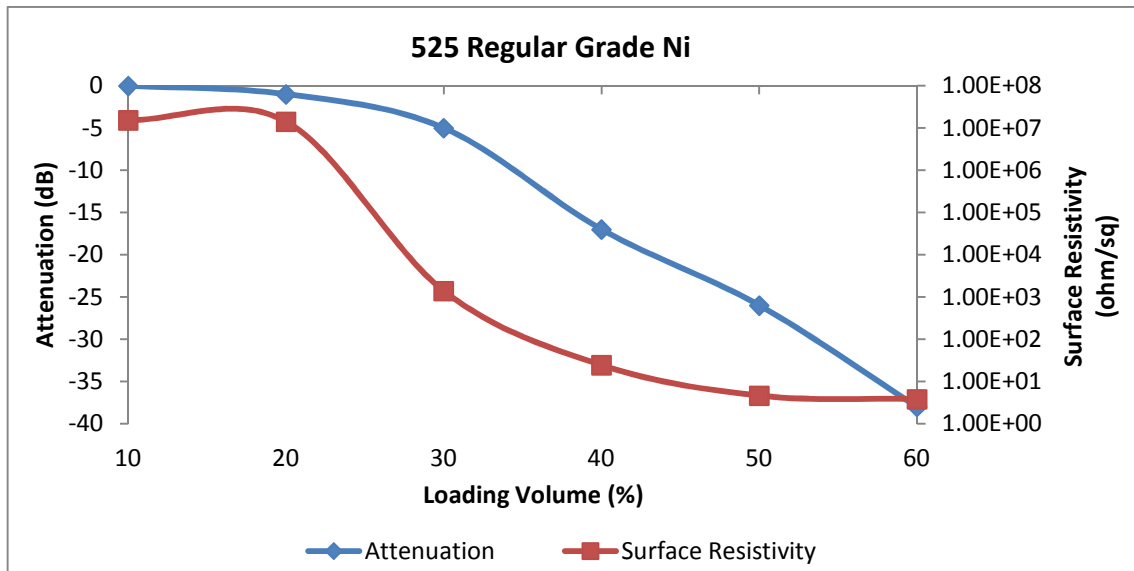


Figure 7.3, Attenuation Measurement of 525 Regular Grade Nickel

Figures 7.4 and 7.5 examined the possibility that highly loaded expanded graphite samples could have an improved shielding performance from a small addition of nickel fillers. These results indicate that the addition of either 525 low density nickel powder or HCA-1 nickel flake impart little additional shielding performance to samples of expanded graphite that were already loaded above the critical percolation threshold. The

addition of 25% 525 low density nickel to a 50% loaded graphite sample achieved an attenuation of 5 dB while the addition of 25% HCA-1 flakes to an 80% loaded graphite sample attenuated just over 9 dB. These were not considered to be an improvement to the nickel samples without additional graphite.

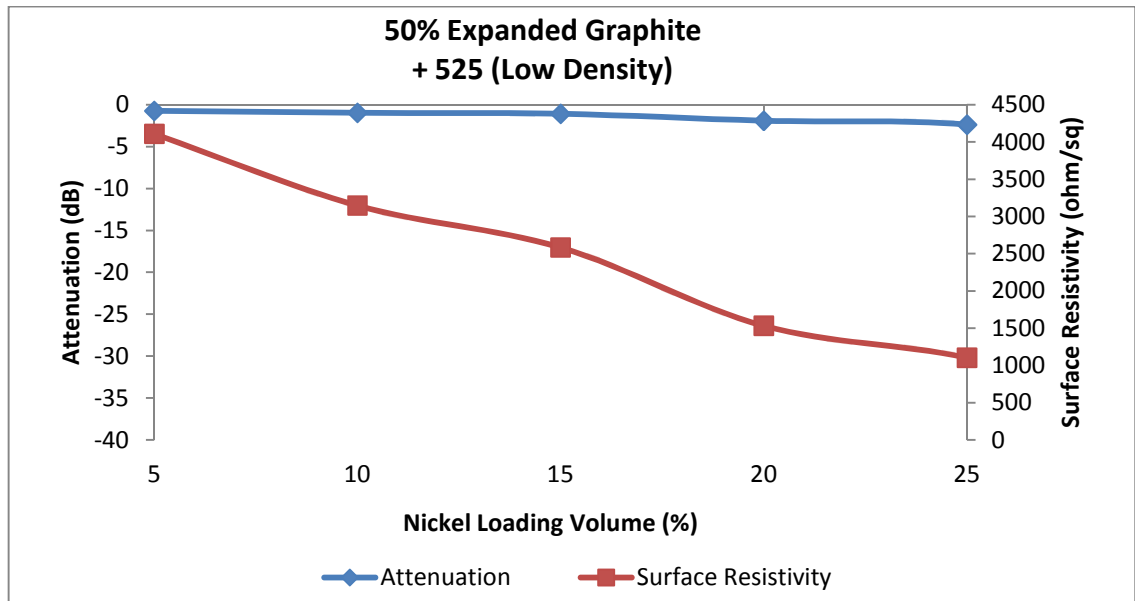


Figure 7.4, Attenuation Measurement of 50% Expanded Graphite and 525 Low Density Nickel

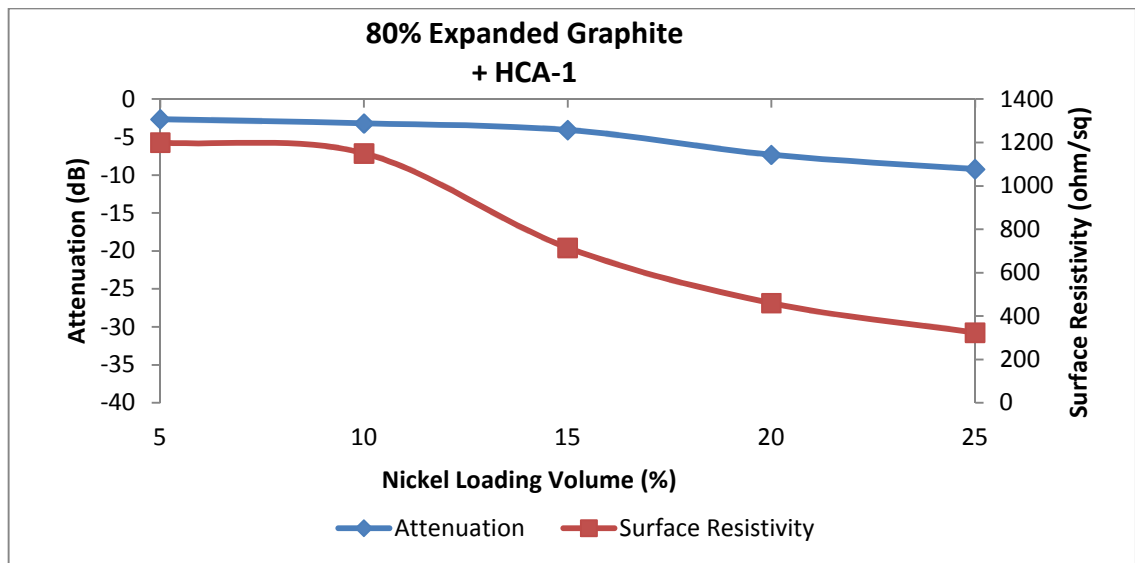


Figure 7.5, Attenuation Measurement of Expanded Graphite and HCA-1 Nickel Flake

It was again shown to be the case in Figure 7.6, where the 525 regular grade nickel loading reaches 60% volume within a matrix of PMMA and 50% expanded graphite. It can be seen that the percolation transition still occurs between 20% - 30% nickel volume and achieves a maximum attenuation of 38 dB. These results are equal to the 525 regular grade samples produced without any graphite addition.

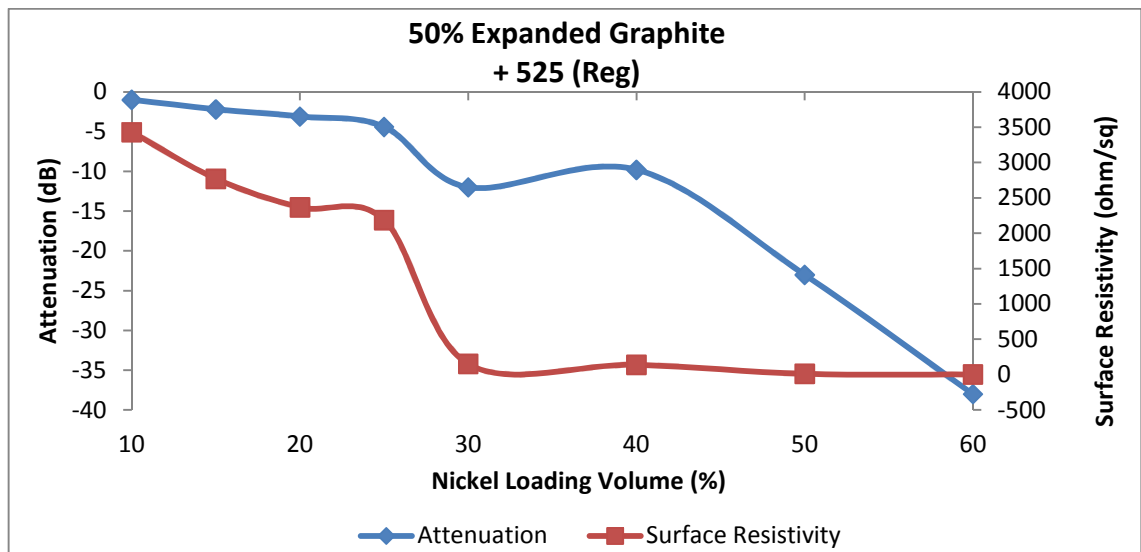


Figure 7.6, Attenuation Measurement of Expanded Graphite and 525 Regular Grade

The nickel based samples proved to be far superior to the graphite samples. The previous trend continued where the expanded graphite, although percolated, provides very little shielding until the nickel levels reach percolation. After which the nickel network becomes the dominant shielding mechanism.

The level of shielding achieved with the nickel filled samples reached approximately 35-40 dB and compares well to that of a similar commercially available material, Super Shield from MG Chemicals. Super Shield is available as a nickel filled acrylic spray with a shielding effectiveness in the range of 25 – 45 dB (for comparable test frequencies) ^[129]. However the samples do not compare quite as favourably with another

range of acrylic/nickel materials produced by Parker Chomerics. Cho-Shield 2044 and Cho-Shield 4916 are brush on or sprayable composites that have quoted attenuation values of 60-70 dB and 40-50 dB respectively.

Silberline Alloy Samples

The Silberline samples produced from the GA range of samples were also tested in the horn antennas set up. Of the four samples tested GA180 was clearly the most conductive. It also provided the highest attenuation of 10.2 dB at a 50% volume loading (Figure 7.7).

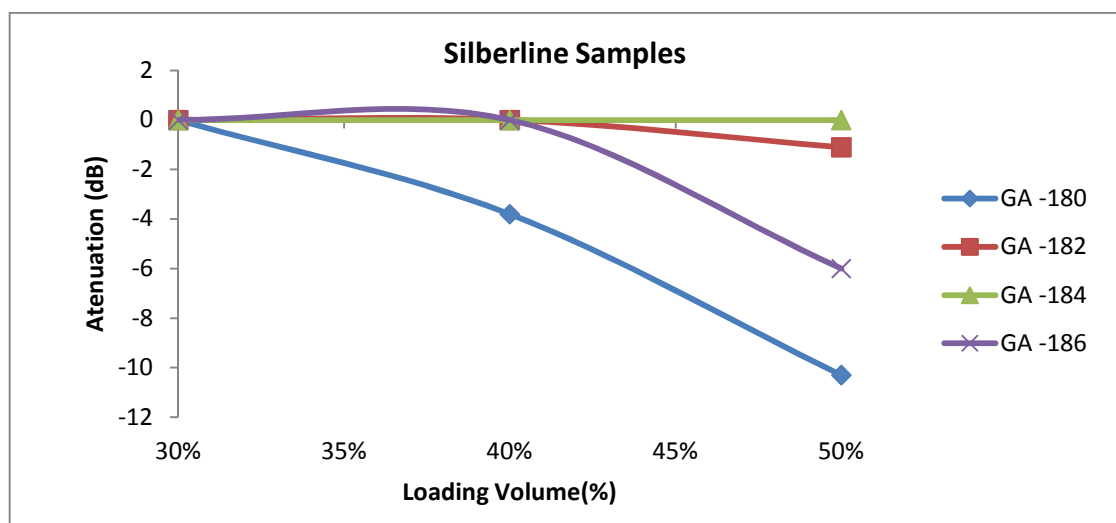


Figure 7.7, Attenuation Measurements of Silberline Samples

7.3 Waveguide EMI Attenuation Results

Following the waveguide technique described previously, a large range of samples were tested over the S-Band, X-Band and Q-Band frequency ranges. The samples were carefully placed at the aperture of the two open ends of the wave guides and clamped in

place to create as little deviation as possible between the two sections of wave guide. A two port normalising calibration procedure was utilised. This standardised the measured attenuation to zero before any shield was inserted into the waveguide. This procedure also allows direct S_{21} parameter readings to be taken. Attenuation is then measured in dB.

7.3.1 Silberline Samples

Figures 7.8 – 7.10 show the attenuation values reached by Silberline GA180 samples. In the S-Band and X-Band range, maximum values in the region of 4 dB were measured and in the Q-Band an increase to about 15 dB was measured. These figures are in keeping with the low values of surface resistivity measured previously, where a slight decrease in resistivity was also noted in the higher frequency range. This increased high frequency conductivity is in keeping with the predicted behaviour. It has been stated that the attenuation loss through a shield is directly proportional to the wave frequency as well as the conductivity and permeability of the shielding material ^[139]. This effect has also been previously simulated in random resistor networks ^[190].

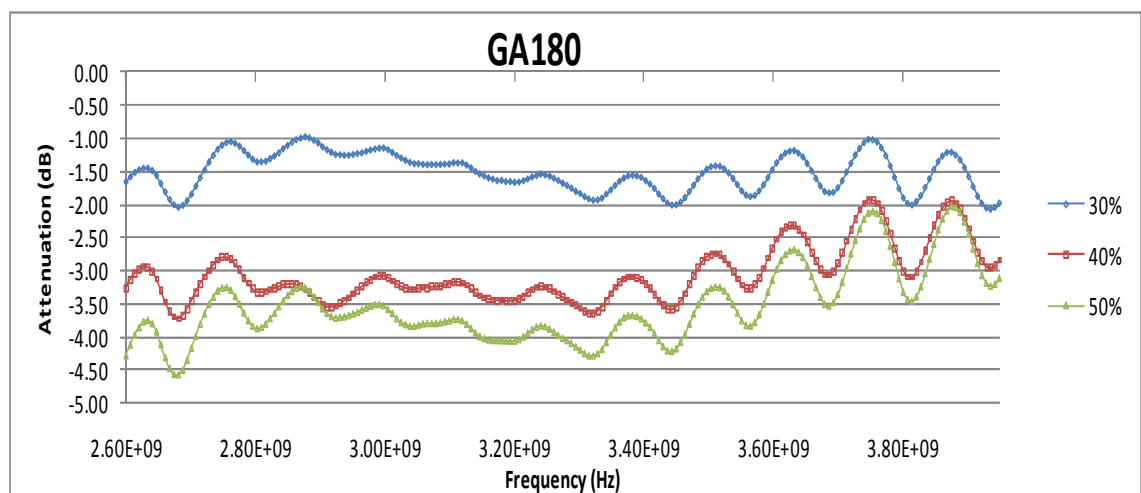


Figure 7.8, S-Band Waveguide Attenuation Measurements of Silberline GA180

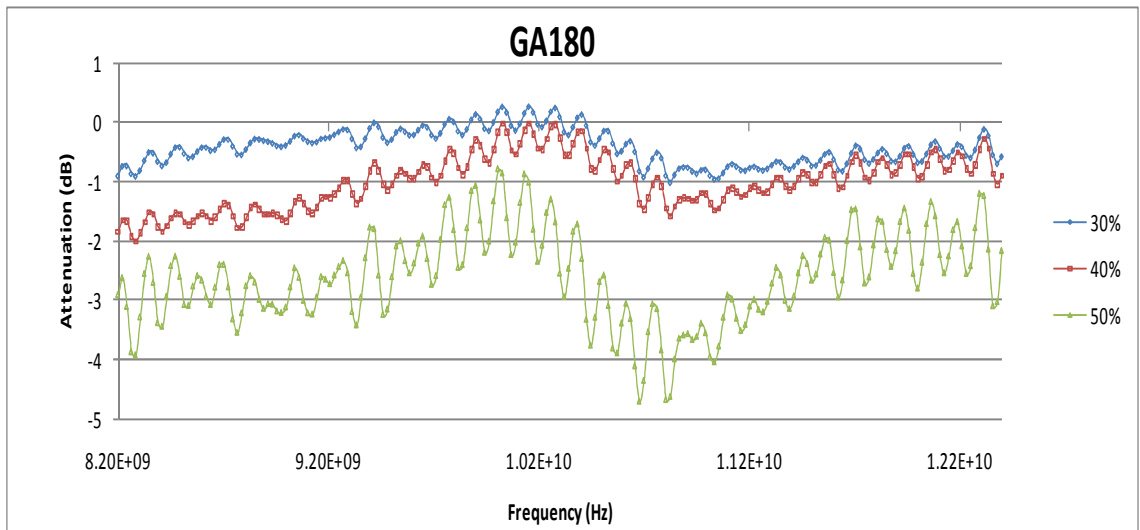


Figure 7.9, X-Band Waveguide Attenuation Measurements of Silberline GA180

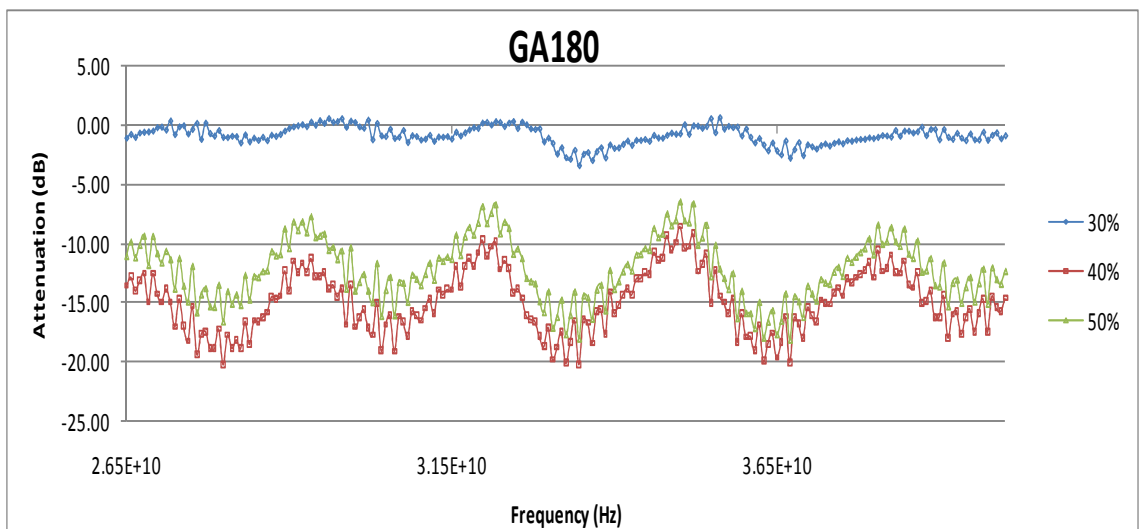


Figure 7.10, Q-Band Waveguide Attenuation Measurements of Silberline GA180

7.3.2 Expanded Graphite

The expanded graphite samples tested here in Figures 7.11 – 7.13 again follow the trend of exhibiting higher attenuation at higher frequencies. It was observed in the S-Band and X-Band frequency range, that the attenuation was in the region of only 1.5 dB. This increases to an average attenuation of around 4 – 5 dB in the Q-Band range. It can be

seen from these results that significant fluctuations are apparent, especially in the high frequency results. This appears to be more prominent as the loading levels are increased. These fluctuations will be discussed further in section 7.3.4.

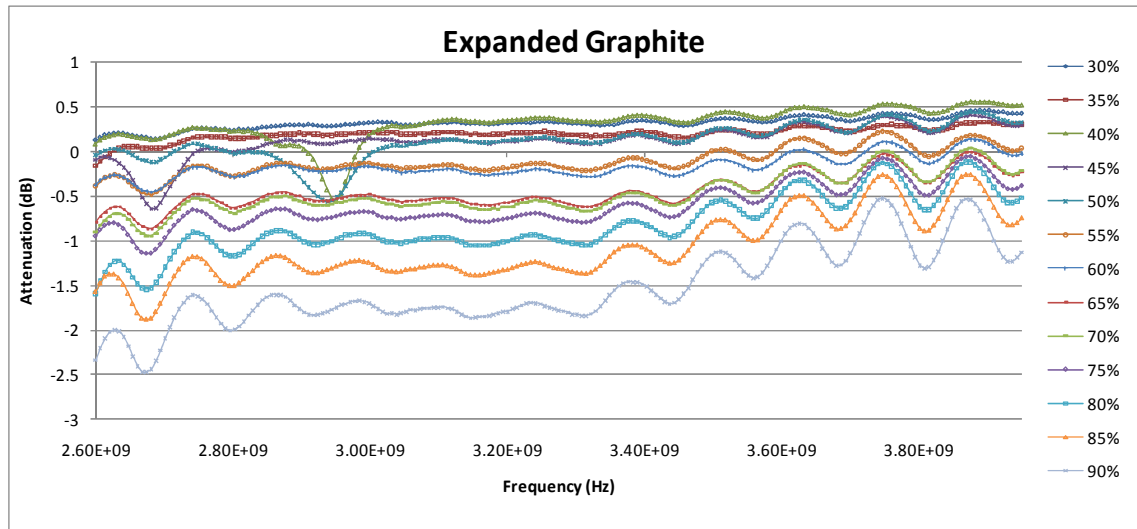


Figure 7.11, S-Band Waveguide Attenuation Measurements of Expanded Graphite

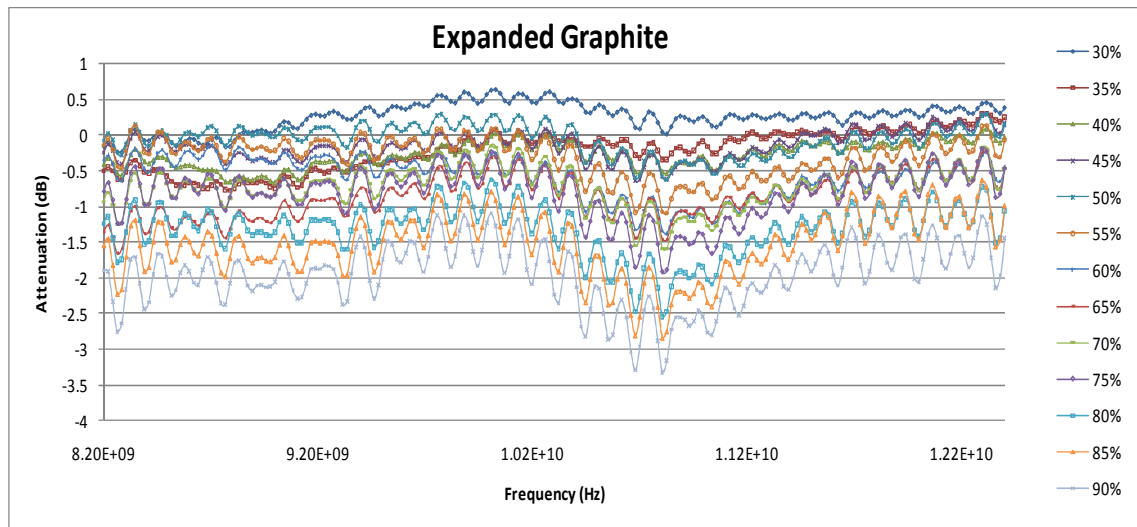


Figure 7.12, X-Band Waveguide Attenuation Measurements of Expanded Graphite

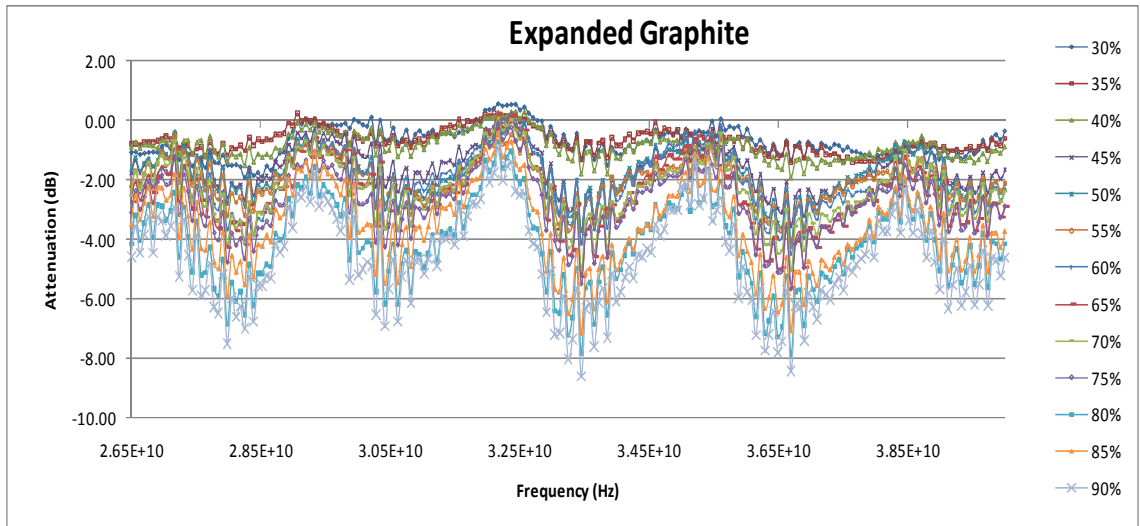


Figure 7.13, Q-Band Waveguide Attenuation Measurements of Expanded Graphite

7.3.3 Microsphere

Figures 7.14 – 7.16 show the shielding effectiveness values achieved by the SSB005 silver coated glass microspheres. In the S-Band range a shielding effectiveness of between 55-60 dB was measured. This improves to 65-70 dB in the X-Band and further to 70-80 dB in the Q-Band although again quite rippled results are apparent.

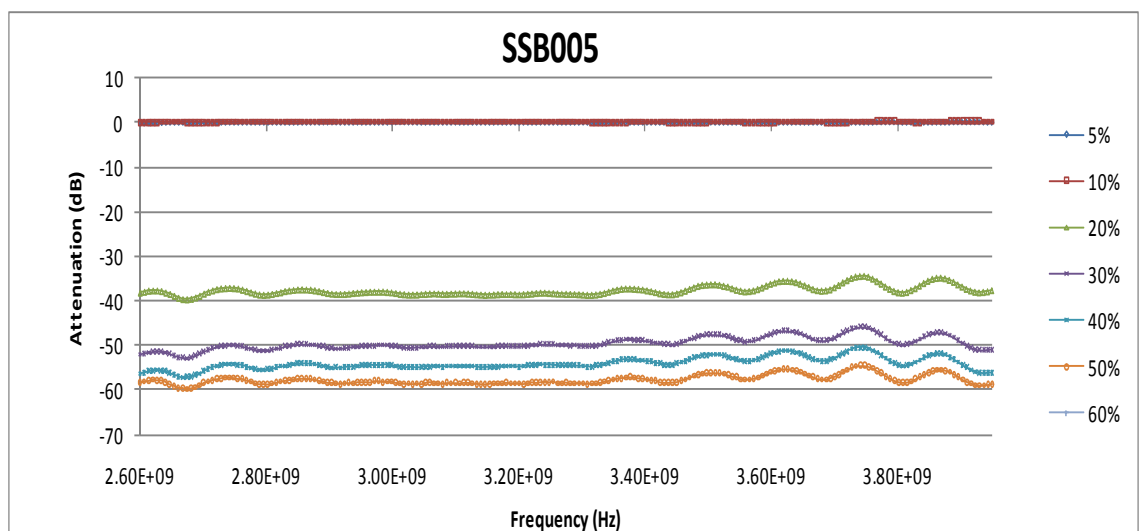


Figure 7.14, S-Band Waveguide Attenuation Measurements of SSB005 Microspheres

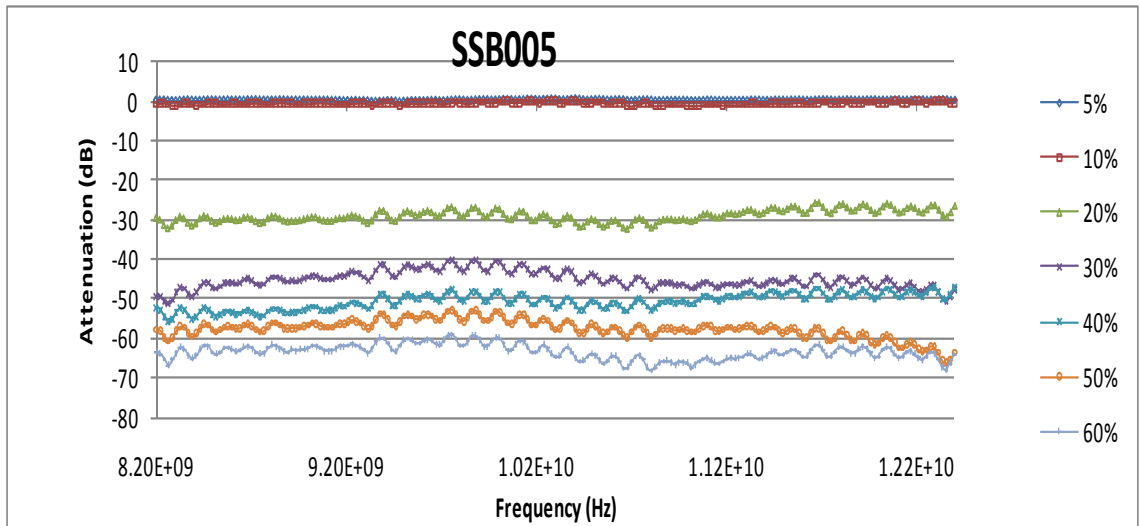


Figure 7.15, X-Band Waveguide Attenuation Measurements of SSB005 Microspheres

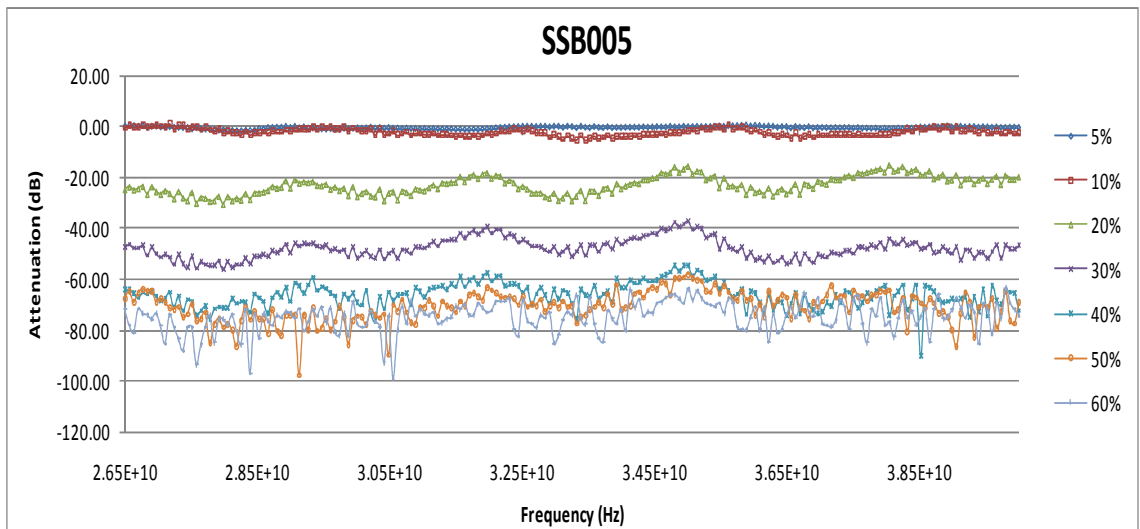


Figure 7.16, Q-Band Waveguide Attenuation Measurements of SSB005 Microspheres

These results demonstrate the advantages that silver coated hollow glass spheres have on the shielding effectiveness. For a relatively small volume of metal a high level of shielding effectiveness, ranging from 55–80 dB, has been achieved. These results compare favourably with the shielding effectiveness values quoted for similar commercial material. For example, Ceno Technologies offer silver coated cenospheres with an advertised shielding effectiveness of 60 dB at 100 MHz to 25 GHz ^[131].

The shielding effectiveness results detailed here indicate only a small proportion of the variety of attenuation levels measured. Over a large selection of materials tested the dependency on conductivity and frequency remains consistent with all samples achieving higher shielding effectiveness as the test frequency is increased.

All additional test results are provided in Appendix C.

7.3.4 Result Fluctuations - Normalisation and TRL Calibration

The fluctuations noted in the network analyser results can be attributed in part to the calibration procedure undertaken prior to testing. It has been shown that improved calibration techniques, such as transmission-reflection-line (TRL) calibration, can reduce the levels of these fluctuations. However at the time of the sample testing during this study, no calibration kits were available.

The normalisation procedure undertaken for calibration takes into account only the attenuation of the signal and not the test port matching. Due to this test port mismatch, when transmission measurements are being made on samples with a different match coefficient, ripples are usually found in the results. Some variation will still be apparent even after calibration as any small mismatch at the test ports will result in multiple reflections being produced. This imparts errors in the measurements giving this ripple effect ^[163].

Subsequently TRL calibration kits have since been purchased by Edinburgh Napier University. The difference between the normalised result and TRL calibrated result in a

test sample measured at Q-Band frequencies can be seen in Figure 7.17. The fluctuations have been reduced from variation of around 12 dB to only around 3 dB.

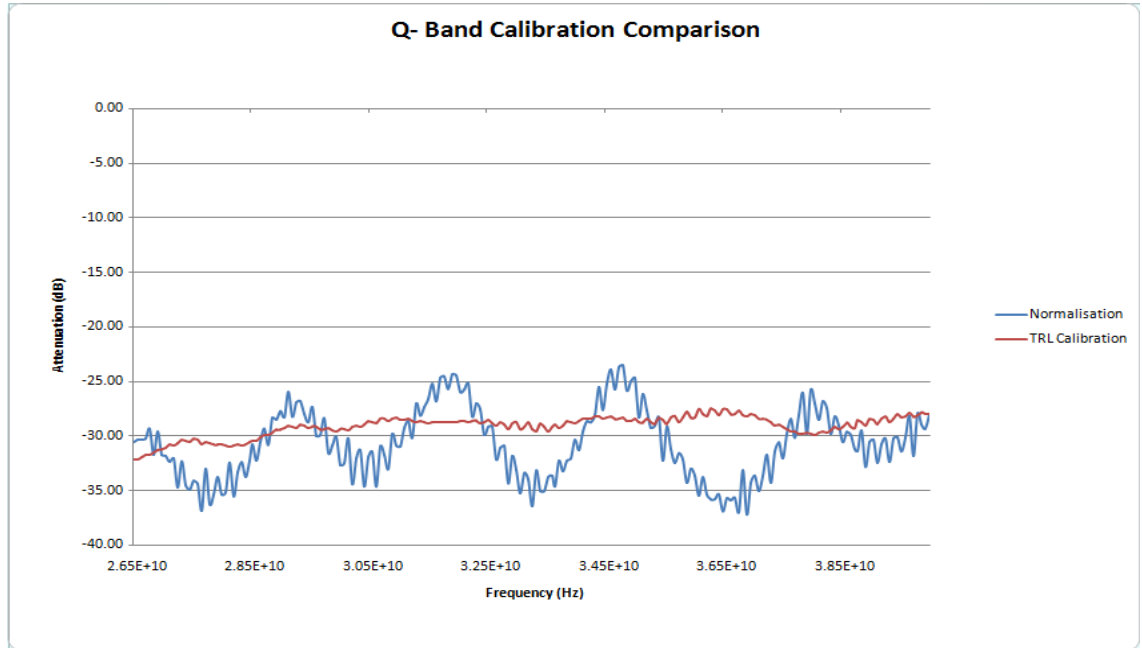


Figure 7.17, Calibration Procedures Comparison

The TRL technique uses a line with corresponding characteristic impedance as its reference instead of a fixed match. As it is possible to more accurately manufacture the characteristic impedance of an air line than a fixed match, a better test port match is achieved.

8 Investigation of Additional Processes

8.1 Electroless Plating of Expanded Graphite

The potential to utilise expanded graphite's lightweight and low percolation threshold properties within conductive composites remains a possibility. It has been shown that the limit of graphite's conductivity is too low to produce significant EMI shielding attenuation alone. The use of expanded graphite alongside nickel powder fillers also failed to produce significant improvements to that of nickel/PMMA alone. One other possible method of improving the conductivity of graphite was to electroless plate a nickel coating onto the surface of the particles. It was surmised that if it was possible to coat the expanded graphite in such a manner that retained the expanded structure, then it may be possible to obtain a highly conductive yet still high volume powder.

Following the electroless plating process as described previously, batches of expanded graphite powder were processed through the sensitising and activation baths. It became evident that this process was flawed and less suitable for a powder of such nature. Due to its random and disordered open structure of graphite layers, expanded graphite is highly susceptible to interlocking and therefore agglomerating together. In fact many interesting applications exploit this mechanical interlocking ability to produce products formed into graphite sheets.

The wet stages of sensitising and activation all required the powder to be rinsed, filtered and dried before the following stage could be performed. This all required filtering through a Buchner funnel then dried in a warm oven before removing the powder from

the filter paper. This process was repeated over all the remaining stages. After each stage it was clear that the powder was agglomerating more each time and even if successfully plated, it would be likely the unique properties of the expanded graphite structure would be lost.

One solution was thought to have been found when it was realised that previous research ^[191] had found by introducing graphite powder into a furnace at 380°C for one hour it was possible to remove any adsorbed gases from the graphite's surface. This therefore improved the wettability and activated it for plating. Although the previous research had been performed on much larger non-expanded graphite particles, there was no reason to foresee any problems for this application.

Small quantities of expanded graphite were subsequently placed within a crucible and heated inside a rapid heat box furnace to the recommended 380°C. They were then held at temperature for one hour. Upon removal the graphite was stored at vacuum to prevent the re-adsorption of any gases. Plating was then attempted following the standard conditions of the nickel-phosphorus plating process. The agglomerated particles from the conventional pre-treatment processing were also plated following identical conditions. The resulting powders were examined in a scanning electron microscope for examination of the particle morphology and EDX analysis. Figures 8.1 and 8.2 show the structure and the resulting EDX analysis spectrum of expanded graphite in the virgin condition. As can be seen here the flakes of graphite are uncontaminated with only carbon being detected.

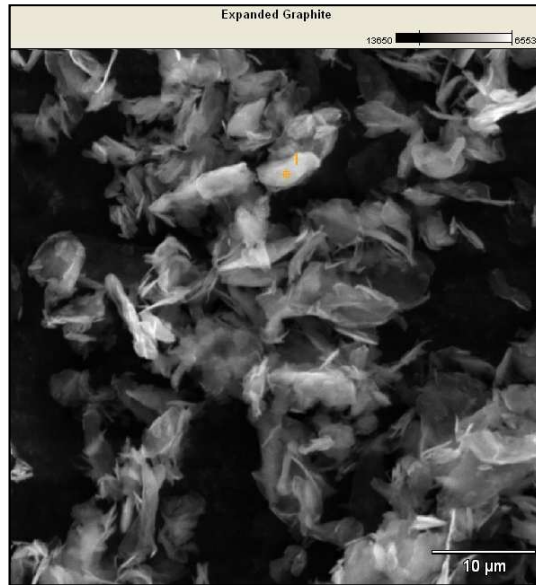


Figure 8.1, SEM Micrograph Virgin Expanded Graphite

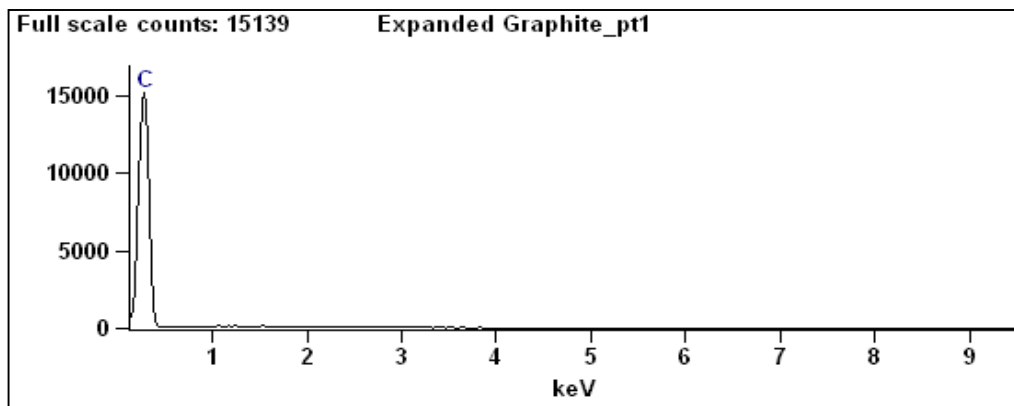


Figure 8.2, EDX Analysis of Virgin Expanded Graphite

Figures 8.3 and 8.4 show the powder structure and the resulting analysis spectrum of the expanded graphite powder after heat treatment. As expected after heat treatment there has been no change to the structure or chemical composition with an identical spectrum to the virgin condition being observed.

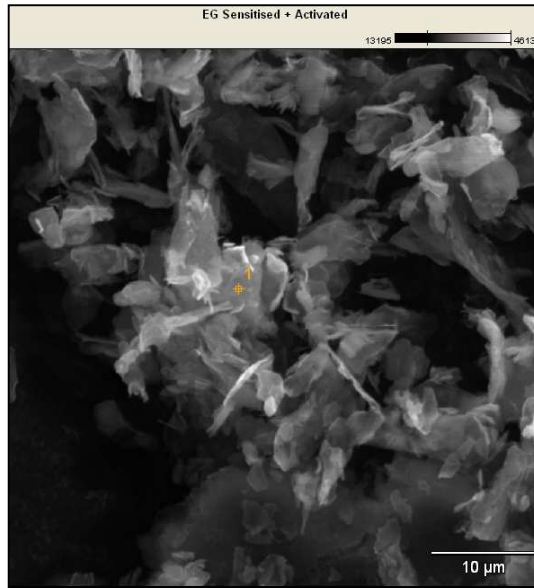


Figure 8.3, SEM Micrograph of Heat Treated Expanded Graphite

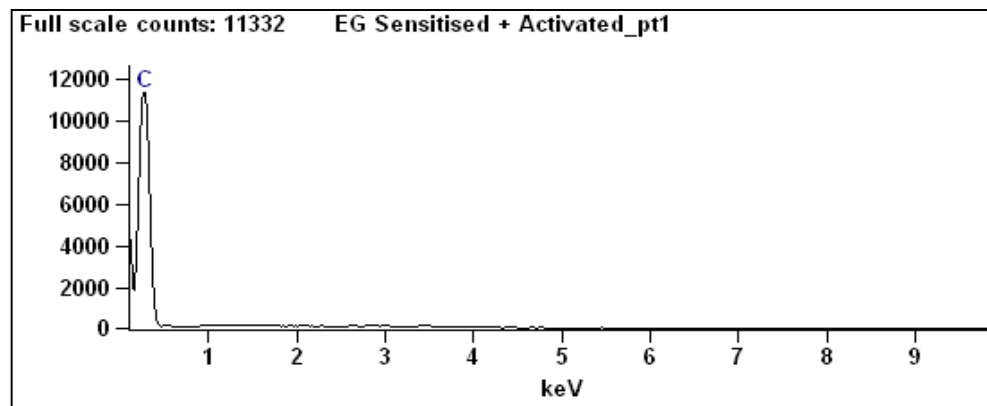


Figure 8.4, EDX Analysis of Heat Treated Expanded Graphite

Figures 8.5 and 8.6 demonstrate the structure and resulting spectrum of the expanded graphite after heat treatment sensitisation and electroless nickel plating bath. It can be clearly seen from the EDXA spectrum that the plating process was unsuccessful with no nickel or phosphorus being detected upon the surface of the expanded graphite.

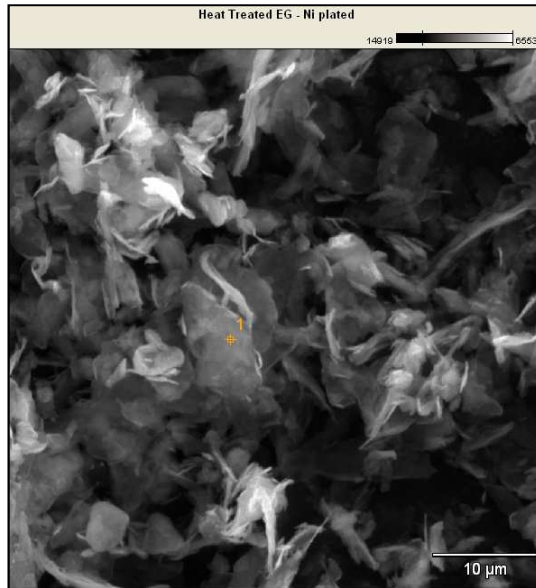


Figure 8.5, SEM Micrograph of Heat Treated Expanded Graphite after Nickel Plating Bath

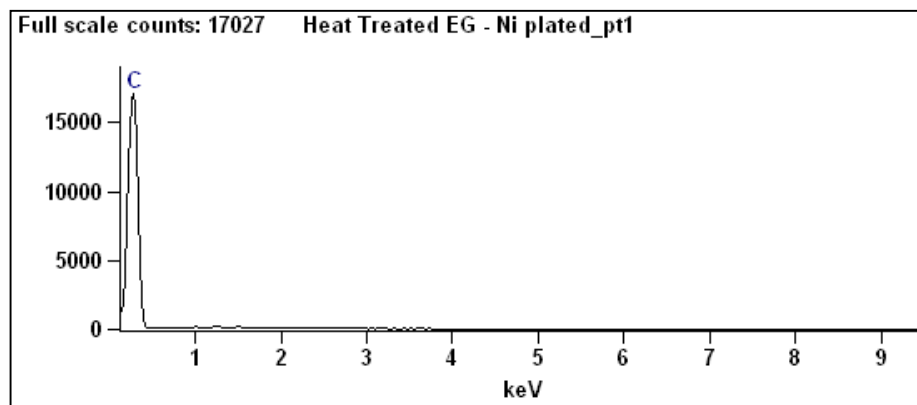


Figure 8.6, EDX Analysis of Heat Treated Expanded Graphite after Nickel Plating Bath

The plating bath stage was repeated with the lengths of plating time increased, at no stage was any plating successfully observed.

Figures 8.7 and 8.8 demonstrate the structure and resulting spectrum of expanded graphite after a full conventional nickel plating process. As can be seen distinct peaks of nickel and phosphorus are both evident in the EDX analysis spectrum. This is clearly indicative of a successful plating procedure. Also it can be seen in the SEM image that

the surface of the expanded graphite particles has become globular in appearance where the nickel has encapsulated the agglomerated particles.

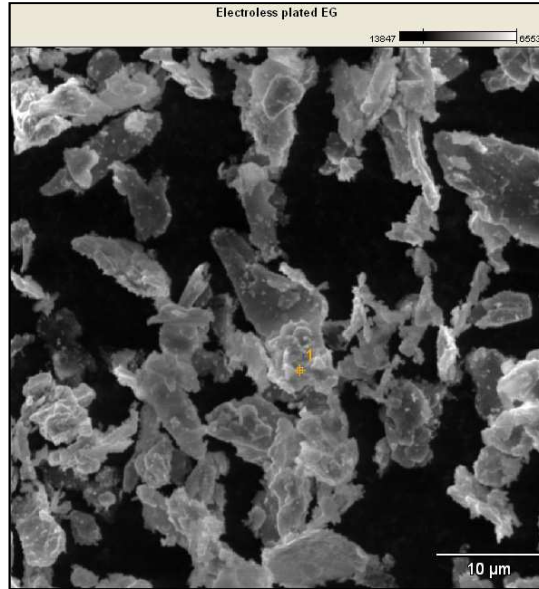


Figure 8.7, SEM Micrograph of Electroless Nickel Plated Expanded Graphite

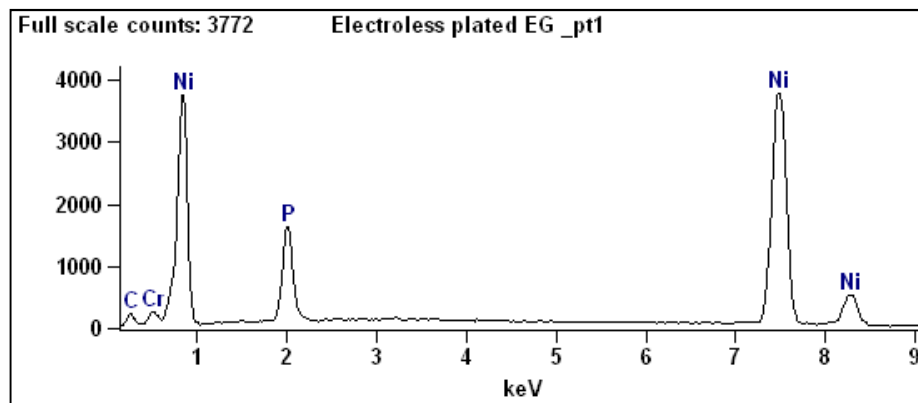


Figure 8.8, Expanded Graphite after Standard Nickel Plating Bath

These results have identified that the heat treatment process followed here has been unsuitable for sensitising and activating expanded graphite for electroless nickel plating. It has also shown that the expanded graphite itself is suitable for plating when catalytically active. The challenge of activating this surface while preserving the

properties that make such an attractive material in the first place remain. However there is definite scope for further research and continued development of such a heat treatment technique.

8.2 Brabender Compounded PMMA-Nickel Compared Against Electroless Nickel Plated PMMA

As discussed in section 3.8, it was theorised that by electroless plating nickel onto PMMA granules and then compression moulding them into plaques, a conductive network within the composite could be produced. The electrical and EMI shielding properties of these plaques produced would be compared with that produced through a more conventional filling and compounded process. Oval cross-sectioned granules of injection moulding grade PMMA (Diakon from Lucite) with approximate dimensions as shown in Figure 8.9 were chosen for both the processes.

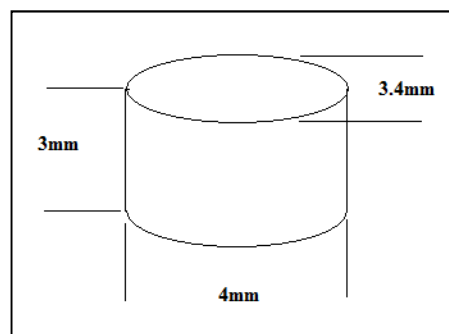


Figure 8.9, PMMA Granule Dimensions

Compounded samples were manufactured in a Brabender Plasti-Corder at increasing intervals of Novamet HCA-1 nickel flake ranging from 10% to 80% by weight. The Brabender process involves hot mixing of the acrylic granules in the chamber where

they are softened before the desired volume of nickel is added to the polymer melt. This mixture is then compounded for another minute at a higher mixing rate. The amalgamated mixture is then removed from the chamber while soft and allowed to cool before being broken down into smaller more manageable fragments suitable for an even distribution within the mould. The plaque mould produces samples 150 mm x 50 mm x 2 mm by pressing them in a twin plate hot press at 20 tonne at 170°C.

The electroless plating process followed the same 4 bath pre-treatment followed by the nickel solution plating bath used previously to plate the expanded graphite, although in this case there was not going to be such filtration issues between sensitisation stages as the granules are sufficiently large and non-agglomerating.

Initially the plating procedure was failing to plate the PMMA and it was clear that the sensitising stage was proving unsuccessful. It is common for sensitisation to discolour the surface of light or transparent substrates with a light brown hue. This was not apparent in this case. It was thought that by coarsening the surface and therefore increasing the surface area, the wettability characteristics would improve and aid the sensitising process. If successful it would also have the benefit of providing the final nickel deposition more opportunity to interlock onto the substrate surface resulting in improved adhesion.

The PMMA granules were subsequently placed inside stainless steel mixing cups lined with 120 grit silicon carbide abrasive paper and rotated within a planetary ball mill. Only the mixing action was required therefore milling balls were not used in the process. A five minute mixing cycle was sufficient to uniformly abrade the surfaces of the

granules and remove the glossy appearance leaving a coarse dulled surface finish. Subsequent sensitising was fully successful. This allowed for batches of PMMA to be plated with increasing bath submersion times. Plating times of 20, 30, 40 and 50 minutes were carried out to compare the effect of increasing nickel thickness.

Initial visual observations indicated that a successful procedure had been achieved although under optical microscopy it could be seen that there were still some occasional uncoated faces on the granules.

A second alternative approach used was to reduce the size of the PMMA granules by passing them through a powdering grinder. This reduced the granule size to approximately 2 mm and resulted in a highly angular granule with an opaque appearance. No further surface roughening was required. Plating was then performed following the exact conditions as undertaken with the larger granules. This resulted in a more homogenous coating. Examination under optical microscopy revealed no observable surfaces remained uncoated.

The nickel plated PMMA granules and powders were compression moulded under identical conditions to the Brabender compounded samples. The resultant plaques exhibited a distribution of thin nickel sheets throughout the matrix of PMMA. The samples produced from the larger PMMA granules exhibited an even distribution of nickel sheets in amongst a matrix of PMMA. It was apparent that the nickel had not completely formed a network as there were transparent regions of PMMA surrounding the isolated nickel sheets throughout the samples. The ground PMMA samples appeared

to be more far more homogenous, although some small but distinct transparent regions of PMMA were still evident in places.

20 mm² samples were cut from each plaque and the densities were measured following the Archimedes method. The same samples were also measured for relative dielectric constant then finally for their EMI attenuation.

It was found that the plaques retained an insulative surface layer after compression moulding. This limited the electrical testing that could be undertaken on the samples as resistivity measurements would not provide relevant results. Provided a conductive network had formed internally within the plaque, any surface layer would not adversely affect the electromagnetic shielding effectiveness.

For comparisons between the samples the relative permittivities were measured. These were made on a Wayne Kerr Precision Component Analyser 6425 with a Wayne Kerr permittivity micrometer jig – D321. Capacitive measurements were taken with the sample in place between the electrodes and then corresponding capacitive measurements taken of the air gap that the sample occupied. The relative permittivity “ ϵ_r ” was then calculated following equation (5).

Table 19 details the results obtained.

The variations in density between the Brabender compounded samples and the electroless plated ones indicate the relative quantities of nickel contained within the

sample. It can be seen that the electroless plated samples all demonstrate lower densities and higher relative permittivity than the Brabender compounded samples.

Table 19 – Density and Dielectric Properties of Plaques Produced

Sample	Density (g/cm³)	Relative Permittivity
Brabender Mixed 10%Wt	1.29	1.16
Brabender Mixed 20%Wt	1.45	1.14
Brabender Mixed 30%Wt	1.59	1.18
Brabender Mixed 40%Wt	1.68	1.26
Brabender Mixed 50%Wt	1.72	1.24
Brabender Mixed 60%Wt	1.71	1.25
Brabender Mixed 70%Wt	1.80	1.27
Brabender Mixed 80%Wt	1.81	1.26
Electroless Plated (Large Granules) 20 min	1.13	1.33
Electroless Plated (Large Granules) 30 min	1.19	1.24
Electroless Plated (Large Granules) 40 min	1.26	1.34
Electroless Plated (Large Granules) 50 min	1.26	1.77
Electroless Plated (Ground Granules) 20 min	1.22	1.43
Electroless Plated (Ground Granules) 30 min	1.23	1.80
Electroless Plated (Ground Granules) 40 min	1.23	1.88
Electroless Plated (Ground Granules) 50 min	1.28	2.79

PMMA is quoted to have a relative permittivity value of 3.7 – 2.6 (50 Hz – 1 MHz) ^[192].

8.3 Shielding Effectiveness

The samples were all tested following the coupled waveguide technique for the shielding effectiveness in the S-Band Range as described. Figure 8.10 indicates that the Brabender filled samples exhibited low levels of shielding effectiveness, approximately 3 dB. This indicates that the maximum loading of 80% (wt%) nickel flake was not sufficient to achieve percolation within these samples. Conversely, the electroless plated samples all showed higher shielding effectiveness which improved markedly as the

plating time was increased. The larger granule sized samples achieved values in the region of 20 dB after 50 minutes of nickel plating prior to moulding (Figure 8.11) and the ground granule sample achieving values in the region of 35 dB (Figure 8.12).

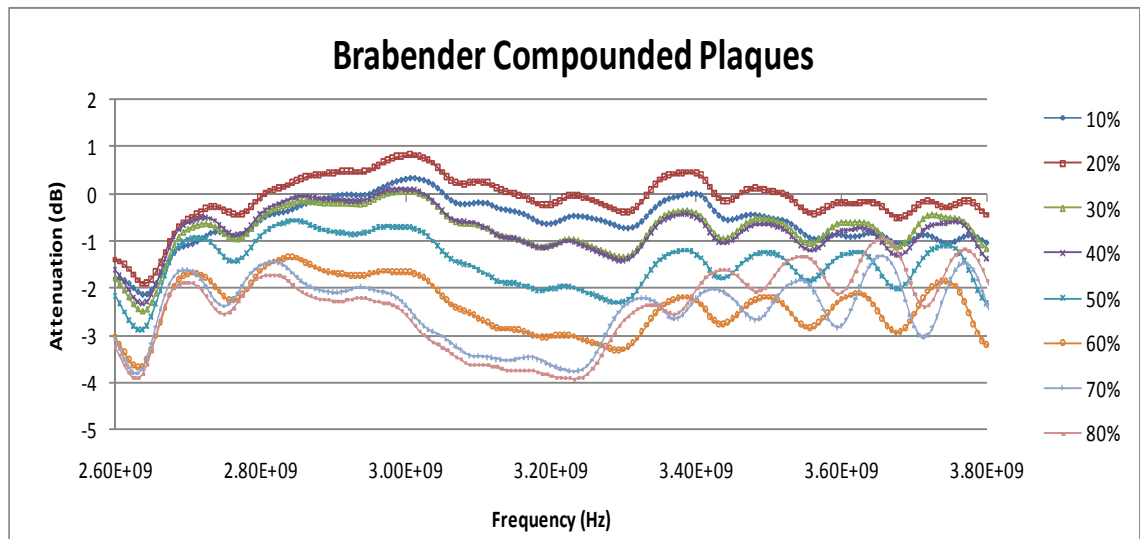


Figure 8.10, S-Band Attenuation Measurements of Brabender Compounded Samples

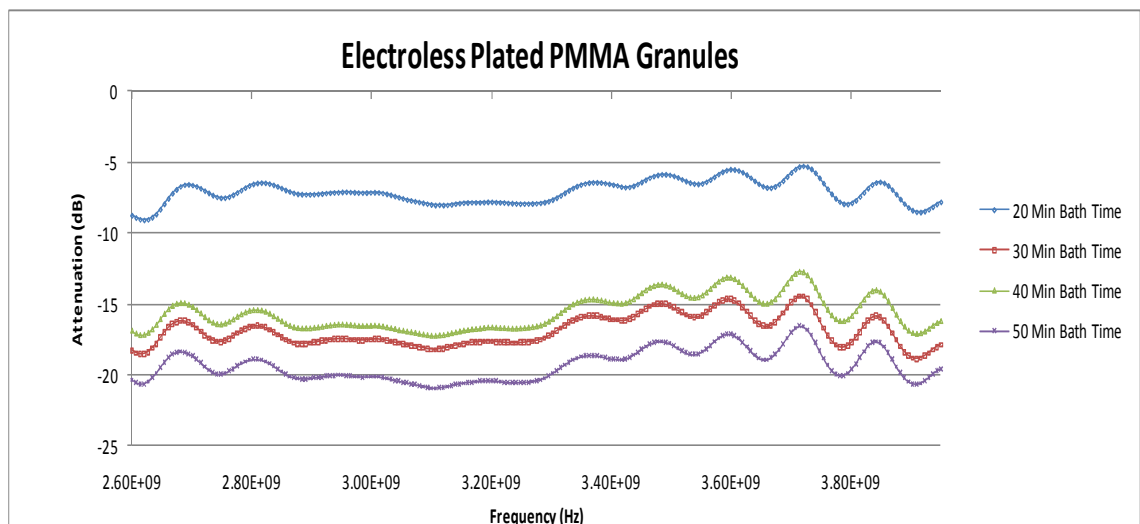


Figure 8.11, S-Band Attenuation of Electroless Nickel Plated PMMA Samples

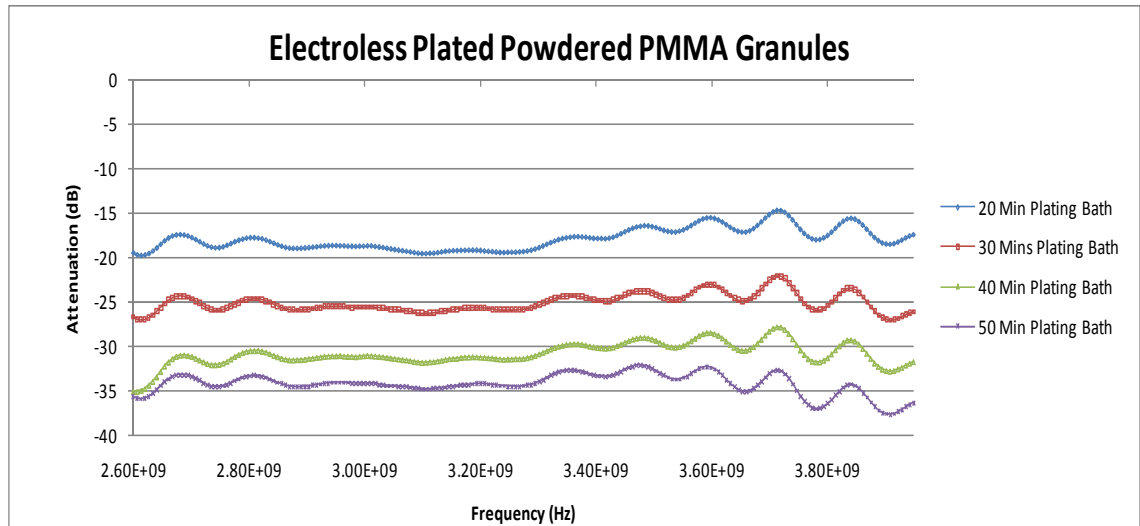


Figure 8.12, S-Band Attenuation of Electroless Nickel Plated Ground PMMA Samples

The density, relative permittivity and shielding effectiveness results of the two compared processes, indicate that superior electromagnetic shielding is achievable at a reduced metallic content. By following the electroless plating process to manufacture the polymer plaques a lower density composite capable of shielding approximately 35 dB was produced. Samples produced via the Brabender compounding process contained notably higher nickel content yet only attenuated around 3 dB.

It has yet to be seen what values of attenuation are achievable through this process. It is evident that the initial granule dimensions and plating time both have an effect on the properties of the final composite. The smaller ground PMMA granules resulted in approximately a 15 dB attenuation improvement over the larger granules. The increased surface area would result in higher nickel content. However as the density measurements indicate this difference was minimal. The large attenuation improvement is therefore more likely to be a result of a more coherent network formation within the plaque.

Further investigations into the dependency of the coating thickness, granule dimensions and moulding parameters would be highly beneficial to determine the values that may ultimately be achievable.

8.4 Comsol Multiphysics Modelling

As previously discussed in section (5.14), a model for simulating the EMI shielding waveguide test has been developed in Comsol Multiphysics. When the filler conductivity is known an estimate for the composite's effective conductivity can be made. It is then possible to generate shielding effectiveness values under different conditions within the software.

The effective media equation used to calculate the composite conductivity is given below;

$$\sigma_{eff} = \sigma_2 \left(\frac{V_2 - V_c}{1 - V_c} \right)^t$$

Where;

σ_{eff} = Effective conductivity S/m

σ_2 = Filler conductivity S/m

V_c = Critical percolation volume fraction

V_2 = Loading volume fraction

t = Critical exponent = 2.0

If it is assumed that the critical percolation occurs at a value of 24% loading, then for nickel ($\sigma = 1.563 \times 10^7$ S/m ^[193]) and graphite ($\sigma = 0.017 \times 10^6$ S/m ^[194]) the calculated effective conductivities are given in Table 20.

Table 20 – Effective Conductivities of Composite Materials

Loading Volume (%)	Effective Conductivity (S/m)	
	Nickel	Graphite
25	2.706×10^3	0.003×10^3
30	9.742×10^4	0.105×10^3
35	3.274×10^5	0.356×10^3
40	6.927×10^5	0.753×10^3
45	1.193×10^6	1.297×10^3
50	1.829×10^6	1.989×10^3
55	2.600×10^6	2.828×10^3

8.4.1 Model Parameters

The model was constructed using the built in RF module with a 3D geometry (Figure 8.13). This module alone would be sufficient for the applications required, although if necessary additional modules could be operational simultaneously such as heat transfer in an electromagnetic system ^[195].

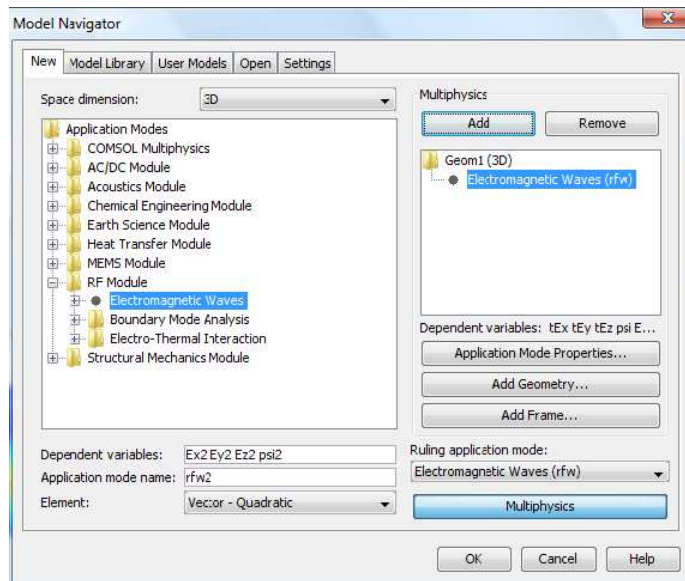


Figure 8.13, Model Navigator

The waveguide was constructed as a single perfect electrical conductor cubic shape and then a section removed at the midpoint. This was then replaced with cross sectional area that would in effect become the material under test. The external boundary conditions highlighted in red have been allocated as perfect magnetic conductors, Figure 8.14.

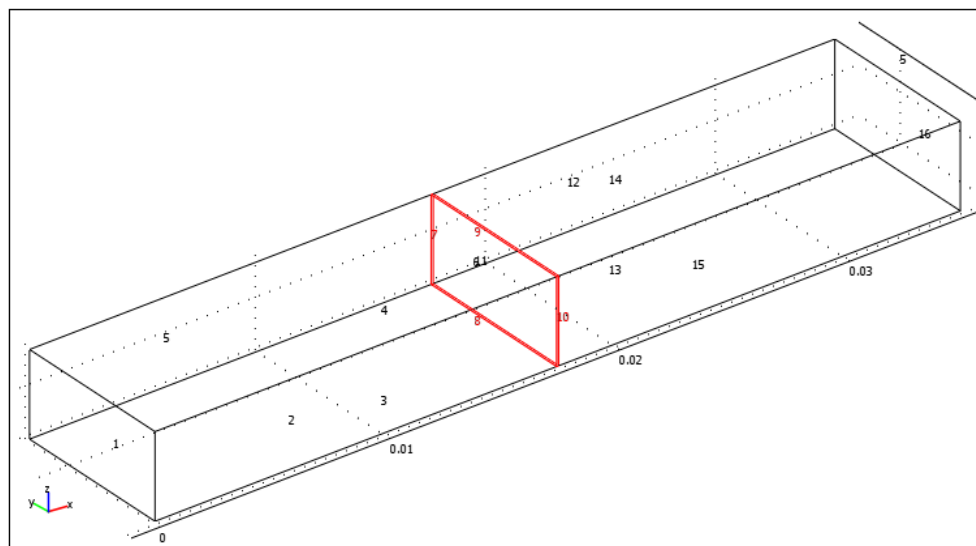


Figure 8.14, Material Boundary Conditions

The two faces at either end were each designated as a transmitting or receiving port. The signal would be generated at port 1 and S_{21} attenuation values would be measured at port 2 (Figure 8.15). It was then required to sweep the required frequencies across the Q-Band range and measure the attenuation across the sample material.

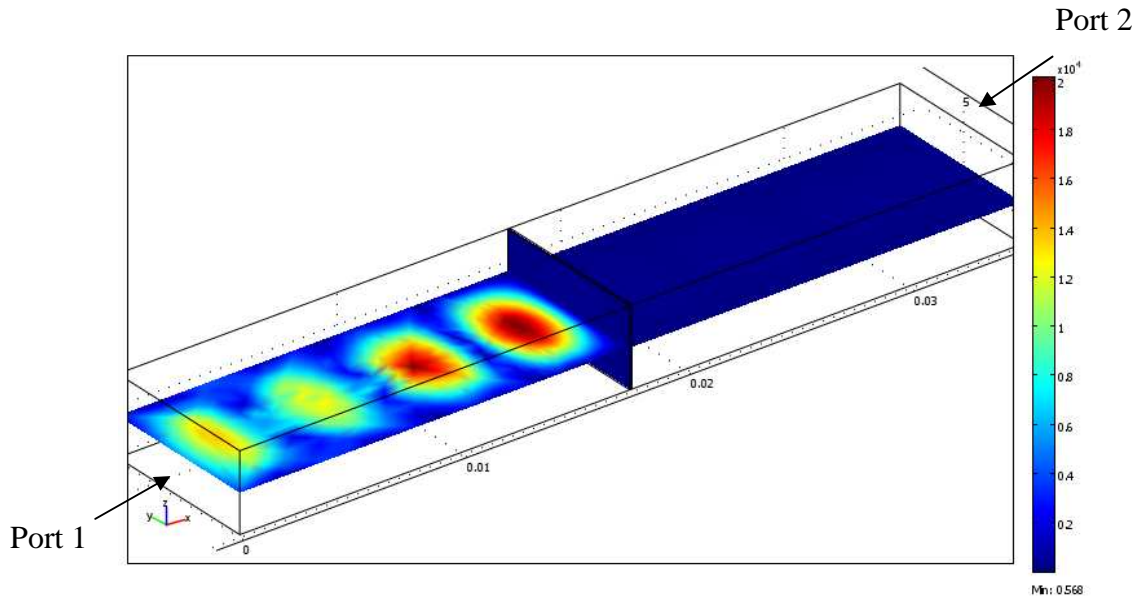


Figure 8.15, Electric Field Strength

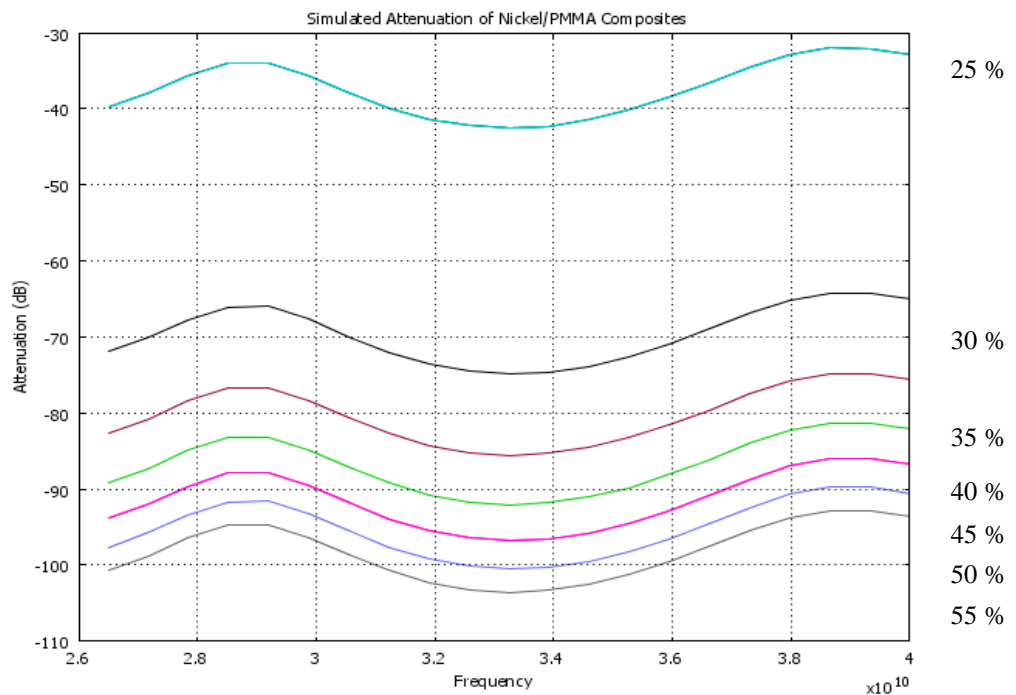


Figure 8.16, Simulated Attenuation Values of Nickel/PMMA Composite

Using the effective conductivity values, the simulated S_{21} attenuations values were generated for ideal nickel and graphite composites (Figure 8.16 and Figure 8.17).

We see that from the nickel simulation results, the upper percolation appears to have been reached between 25% and 30% where a 40 dB increase in attenuation is predicted. It is also indicated that the shielding attenuation would continue to increase incrementally as the loading volume increases. At the limit of the range evaluated here, a value of approximately 100 dB was measured for a 55% volume loading. These values differ from the measured attenuations of nickel/PMMA composites tested in the laboratory where the attenuation generally reached a maximum of approximately 35 - 40 dB.

The attenuation values predicted for graphite composites appear to indicate a similar pattern to the nickel model. As expected the shielding effectiveness is significantly less than for nickel with the 25% simulation only predicting a 2-3 dB shielding effectiveness. This increases to approximately 38 dB for a 55% loading. Once again these values are much greater than measured experimentally where carbon based samples peaked at approximately 4 dB attenuation.

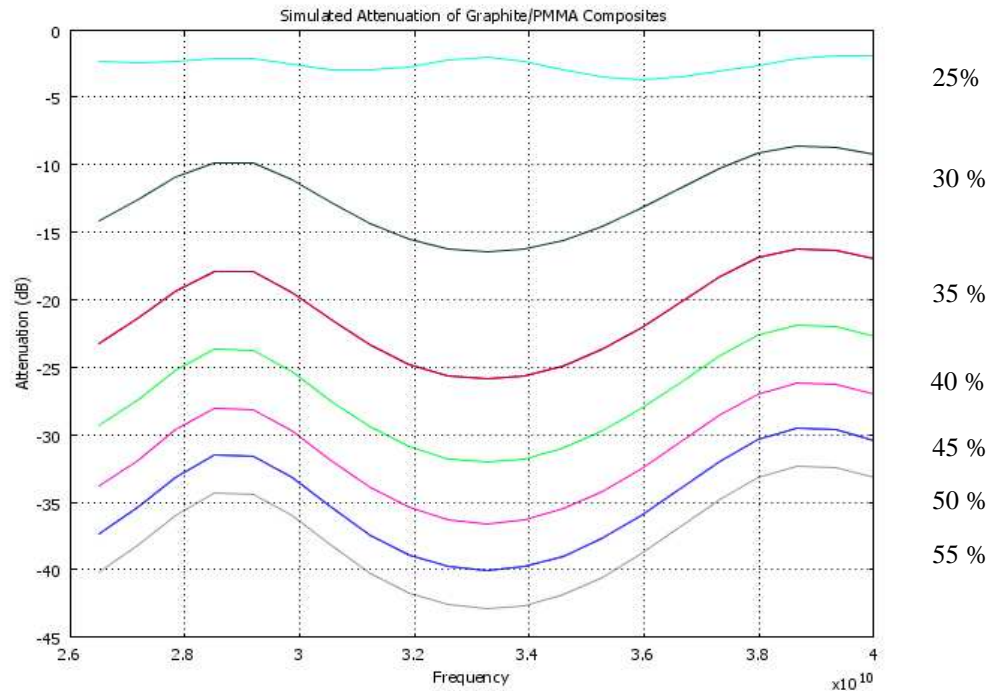


Figure 8.17, Simulated Attenuation Values of Graphite/PMMA Composite

The simulations appear to provide results that follow the expected percolation trends of filled polymer composites. As the loading volume initially increases, a rapid rise in attenuation is observed. The extent of attenuation improvements reduces as the loading volume further increases.

Attenuation values of these magnitudes were not observed in the corresponding experimental data gathered during laboratory testing. This suggests that there are errors within the Effective Media Theory conductivity predictions or within the simulation program itself.

It was however noted that in both simulations the 25% loading results are very similar to the maximum values obtained empirically. As the effective conductivity calculations do not take into account factors such as constriction resistance, a true upper percolation

limit is not observed. It may be that the values calculated nearer the estimated critical percolation correspond more accurately to the upper threshold of composites manufactured. However these connections may just be coincidental. A far more conclusive study would be required to tailor the modelling procedure and gain more accurate results.

9 Conclusion

A successful procedure has been established using standard laboratory equipment and a K-Control coater to prepare and print electrically conductive polymer composite samples. This process produced repeatable and good quality prints of sufficient dimensions that were suitable to be tested via a multitude of different electrical testing methods. These testing procedures were developed and refined throughout the study from reasonably basic surface resistivity and dipole shielding tests to high frequency shielding effectiveness testing on the network analyser. All these tests played a significant role towards achieving the most suitable and productive testing regime. Although some of the materials tested did not produce effective shielding composites, many of the results obtained did compare favourably with comparable commercially available products.

The electroless plating of expanded graphite powders was not fully successful in producing a nickel plated expanded graphite that optimised the expanded structure. The thermal sensitisation processes undertaken proved to be unable to sensitise and activate the graphite surface for electroless plating. The alternative aqueous sensitising process was successful in nickel plating the graphite although it also resulted in an agglomeration of the graphite particles prior to plating. This however also resulted in a loss of many of the desired properties of expanded graphite. All attempts to overcome these setbacks were ultimately unsuccessful.

A successful electroless nickel plating process was utilised in developing a method to manufacture compression moulded plaques of PMMA and nickel. By depositing a thin

coating of nickel onto the surface of PMMA granules followed by a compression moulding process, composite test plaques were able to be produced. These compression moulded plaques were refined by reducing the granule dimensions whilst also improving the adhesion of nickel to them. These materials proved that in comparison to samples produced by a more conventional method of composite production, higher shielding effectiveness at a lower nickel content is achievable.

Simulation of the electromagnetic shielding effectiveness of composite materials in Comsol Multiphysics demonstrated potential to model the waveguide attenuation testing of conductive composite materials. The model was successful in generating attenuation values for given properties of materials. Effective media theory was followed to generate conductivity values of two phase composites. The theoretical values did exhibit a degree of a percolation trend as observed in the attenuation simulations. The effective media model does not reach an upper percolation threshold until the bulk conductivity of the filler is reached. This resulted in higher simulated shielding effectiveness values than were obtained from empirical results measured in the laboratory.

10 Suggestions for Future Work

Development of a non-aqueous sensitisation and activation stage for electroless nickel plating of expanded graphite may assist in produce some novel materials. If a dry sensitisation process can be developed it could possibly eliminate the agglomeration issues encountered in this study. Successful plating would likely produce a lightweight, very high aspect ratio and conductive filler material. This could make for excellent conductive fillers for electromagnetic shielding composites.

The initial results achieved in the PMMA/electroless nickel plaque study demonstrated the potential to reduce the metallic content required for electromagnetic interference shielding of composite materials. Further investigations are required to identify the granule dimensions, coating thickness and processing conditions that would optimise the composite properties. It is possible that reducing the granule dimensions could result in further improvements to the shielding capabilities. It is also likely that through more rigorously tailored processing conditions, compression mouldings could be produced with more control of the polymer flow within the mould. This would potentially reduce the segregated regions where only PMMA was apparent. Such improvements would aid in retaining more of the conductive network that forms as the granules are compressed together. There is scope for a far more detailed investigation in order to optimise the potential of these materials.

11 References

- [1] Schwarz, S. *Electromagnetics for engineers*; Oxford University Press, USA, 1990.
- [2] Kodali, V. *Engineering electromagnetic compatibility: principles, measurements, technologies, and computer models*; Institute of Electrical and Electronics Engineers, 2001.
- [3] Brewer, R.; Fenical, G. *EE Evaluation Engineering* **1998**, 37.
- [4] Chung, D. *Journal of Materials Engineering and Performance* **2000**, 9, 350.
- [5] Montrose, M. *EMC and the printed circuit board: design, theory, and layout made simple*; Wiley-IEEE Press, 1999.
- [6] Gaboian, J. *Analog Applications Journal* **2000**, 4.
- [7] Raper, T.; Knauber, S. *AMD Publication* **1999**, 22507.
- [8] Chung, D. *Carbon* **2001**, 39, 279.
- [9] Kraz, V. *Conformity, January* **2007**, 38.
- [10] Wang, S.; Lee, F.; Chen, D.; Odendaal, W. *Power Electronics, IEEE Transactions on* **2004**, 19, 869.
- [11] Hammond, P. *Electromagnetism for engineers: an introductory course*; Oxford University Press, 1997.
- [12] Faraday, M. *Experimental researches in electricity*, 1839.
- [13] Hecht, E. *Physics*; Brooks/Cole Pub., 1994.
- [14] Texas Instruments *PCB Design Guidelines for Reduced EMI*, 1999.
- [15] Jackson, B.; Bleeks, T. *West Conshohoken, PA, ITEM* **1999**, 125.
- [16] Arnold, R. R. In *Compliance Engineering* 2002.
- [17] GE Plastics *Product Assembly - Shielding Principles and Shielding Effectiveness*.

- [18] Khalifa, O.; Sakr, E. *The Open Corrosion Journal* **2009**, 2, 211.
- [19] Klauk, H. *Organic Electronics: Materials, Manufacturing, and Applications*; John Wiley & Sons, 2007.
- [20] Chung, D. D. L. *Materials for electronic packaging*; Butterworth-Heinemann, 1995.
- [21] Hannafin, J.; Woburn, M. **2002**.
- [22] Blythe, A. R. *Electrical properties of polymers*; Cambridge University Press, 1979.
- [23] Jiles, D. *Introduction to the electronic properties of materials*; CRC, 2001.
- [24] Bohr, N. *Philosophical Magazine Series 6* **1913**, 26, 1.
- [25] Nelson, S. A.; Earth Science Australia.
- [26] Ebbing, D. D. *General Chemistry*; Boston, 1987.
- [27] Delaney, C. *Electronics for the physicist*; Penguin Books Ltd, 1969.
- [28] Voet, A.; Whitten, W.; Cook, F. *Colloid & Polymer Science* **1965**, 201, 39.
- [29] MacDiarmid, A. G. *Reviews of Modern Physics* **2001**, 73, 701.
- [30] Ito, T.; Shirakawa, H.; Ikeda, S. *J. Polym. Sci. Polym. Chem. Ed* **1974**, 12, 11.
- [31] Chiang, C.; Fincher Jr, C.; Park, Y.; Heeger, A.; Shirakawa, H.; Louis, E.; Gau, S.; MacDiarmid, A. G. *Physical Review Letters* **1977**, 39, 1098.
- [32] Heeger, A.; MacDiarmid, A. G.; Shirakawa, H. NobelPrize.org.
- [33] Epstein, A.; Ginder, J.; Zuo, F.; Bigelow, R.; Woo, H. S.; Tanner, D.; Richter, A.; Huang, W. S.; MacDiarmid, A. *Synthetic Metals* **1987**, 18, 303.
- [34] Stejskal, J.; Gilbert, R. *Pure and applied chemistry* **2002**, 74, 857.
- [35] Cao, Y.; Smith, P.; Heeger, A. J. *Synthetic Metals* **1992**, 48, 91.
- [36] Heeger, A. J. *Angew. Chem. Int. Ed* **2001**, 40, 2591.
- [37] Zhang, K.; Zhang, L. L.; Zhao, X.; Wu, J. *Chemistry of materials* **2010**, 22, 1392.

- [38] Basavaraja, C.; Kim, W. J.; Kim, Y. D.; Huh, D. S. *Materials Letters* **2011**.
- [39] Yamamoto, T.; Sanechika, K.; Yamamoto, A. *Journal of Polymer Science: Polymer Letters Edition* **1980**, *18*, 9.
- [40] Lin, J. W. *Journal of Polymer Science: Polymer Chemistry Edition* **1980**, *18*, 2869.
- [41] McCullough, R. D. *Advanced Materials* **1998**, *10*, 93.
- [42] Sugimoto, R.; Takeda, S.; Gu, H.; Yoshino, K. *Chem. Express* **1986**, *1*, 635.
- [43] Karim, M. R.; Lee, C. J.; Lee, M. S. *Journal of Polymer Science Part A: Polymer Chemistry* **2006**, *44*, 5283.
- [44] Groenendaal, B.; Louwet, F.; WO Patent WO/2003/054,052: 2003.
- [45] Liu, C. D.; Hsieh, K. H.
- [46] Eley, D. D. *Organic Semiconducting Polymers* **1968**.
- [47] Friend, R. H. *Conductive Polymers II: From Science to Applications*; RAPRA Technology Ltd, 1993.
- [48] Petty, M.; Bryce, M.; Bloor, D.; Mahmood, M. *An introduction to molecular electronics*; Oxford University Press New York, 1995.
- [49] Weder, C. *Journal of Inorganic and Organometallic Polymers and Materials* **2006**, *16*, 101.
- [50] Newell, J. *Essentials of modern materials science and engineering*; Wiley, 2009.
- [51] Callister, W.; Rethwisch, D. *Materials science and engineering: an introduction*; John Wiley & Sons New York, 1997.
- [52] Jing, X.; Zhao, W.; Lan, L. *Journal of Materials Science Letters* **2000**, *19*, 377.
- [53] Toker, D.; Azulay, D.; Shimoni, N.; Balberg, I.; Millo, O. *Physical review B* **2003**, *68*, 41403.
- [54] Thongruang, W.; Spontak, R.; Balik, C. *Polymer* **2002**, *43*, 3717.

- [55] He, D.; Ekere, N. *Journal of Physics D: Applied Physics* **2004**, *37*, 1848.
- [56] Roldughin, V.; Vysotskii, V. *Progress in Organic Coatings* **2000**, *39*, 81.
- [57] Xue, Q. *European polymer journal* **2004**, *40*, 323.
- [58] Mamunya, Y.; Davydenko, V.; Pissis, P.; Lebedev, E. *European polymer journal* **2002**, *38*, 1887.
- [59] Stauffer, D.; Aharony, A. *Introduction to percolation theory*; Taylor & Francis, 1992.
- [60] Kirkpatrick, S. *Reviews of Modern Physics* **1973**, *45*, 574.
- [61] Abeles, B.; Pinch, H.; Gittleman, J. *Physical Review Letters* **1975**, *35*, 247.
- [62] Sheng, P.; Abeles, B.; Arie, Y. *Physical Review Letters* **1973**, *31*, 44.
- [63] Sheng, P.; Sichel, E.; Gittleman, J. *Physical Review Letters* **1978**, *40*, 1197.
- [64] Hill, R.; Google Patents: 1938.
- [65] Bauer, W.; Google Patents: 1940.
- [66] Brydson, J. *Plastics materials*; Butterworth-Heinemann, 1999.
- [67] Bhattacharya, S.; Chaklader, A. *Polymer-Plastics Technology and Engineering* **1982**, *19*, 21.
- [68] Breuer, O.; Sundararaj, U. *Polymer Composites* **2004**, *25*, 630.
- [69] Gangopadhyay, R.; De, A. *Chemistry of materials* **2000**, *12*, 608.
- [70] Ponomarenko, A.; Shevchenko, V.; Enikolopyan, N. *Filled Polymers I Science and Technology* **1990**, 125.
- [71] Strumpler, R.; Glatz-Reichenbach, J. *Journal of Electroceramics* **1999**, *3*, 329.
- [72] Bloor, D.; Donnelly, K.; Hands, P.; Laughlin, P.; Lussey, D. *Journal of Physics D: Applied Physics* **2005**, *38*, 2851.
- [73] Celzard, A.; Mareche, J.; Furdin, G.; Puricelli, S. *Journal of Physics D: Applied Physics* **2000**, *33*, 3094.

- [74] Zheng, W.; Wong, S. C. *Composites Science and Technology* **2003**, *63*, 225.
- [75] Chen, G.; Weng, W.; Wu, D.; Wu, C. *European polymer journal* **2003**, *39*, 2329.
- [76] Jia, W.; Tchoudakov, R.; Narkis, M.; Siegmann, A. *Polymer Composites* **2005**, *26*, 526.
- [77] Chernysh, I.; Nikitin, Y.; Levental', N. *Powder Metallurgy and Metal Ceramics* **1991**, *30*, 459.
- [78] Celzard, A.; McRae, E.; Mar ché, J.; Furdin, G.; Dufort, M.; Deleuze, C. *Journal of Physics and Chemistry of Solids* **1996**, *57*, 715.
- [79] Voß, S.; Nigmatoulline, V.; Bele, M.; Pejovnik, S.; Besenhard, J. O. *Monatshefte für Chemie/Chemical Monthly* **2001**, *132*, 487.
- [80] Kroto, H. W.; Heath, J. R.; O'Brien, S. C.; Curl, R. F.; Smalley, R. E. *Nature* **1985**, *318*, 162.
- [81] Culotta, L.; Koshland, D. E. *Science* **1991**, *254*, 1706.
- [82] Richard, C. R. *Chemical Engineering* **2009**, *116*, 34.
- [83] Wilson, M. *Nanotechnology: basic science and emerging technologies*; CRC Press, 2002.
- [84] Wolf, E. L. *Nanophysics and nanotechnology*; Wiley Online Library, 2004.
- [85] Iijima, S. *Nature* **1991**, *354*, 56.
- [86] Iijima, S.; Ajayan, P.; Ichihashi, T. *Physical Review Letters* **1992**, *69*, 3100.
- [87] Ajayan, P.; Iijima, S. *Nature* **1992**, *358*, 23.
- [88] Dresselhaus, M. S.; Dresselhaus, G.; Eklund, P.; Jones, D. E. H. *Science of fullerenes and carbon nanotubes*; Academic Press New York, 1996; Vol. 965.
- [89] SHI, X.; LU, G.; Qing, M.; WO Patent WO/2003/064,321: 2003.
- [90] Olk, C. H.; United States Patent 5753088: 1998.

- [91] Journet, C.; Maser, W.; Bernier, P.; Loiseau, A.; Lamy de La Chapelle, M.; Lefrant, S.; Deniard, P.; Lee, R.; Fischer, J. *Nature* **1997**, *388*, 756.
- [92] Qin, L. C.; Zhao, X.; Hirahara, K.; Miyamoto, Y.; Ando, Y.; Iijima, S. *Nature* **2000**, *408*, 50.
- [93] Dunsch, L.; Kuran, P.; Kirbach, U.; Scheller, D. *The Electrochemical Society, Pennington, NJ* **1994**, *94*, 24.
- [94] Demczyk, B.; Wang, Y.; Cumings, J.; Hetman, M.; Han, W.; Zettl, A.; Ritchie, R. *Materials Science and Engineering A* **2002**, *334*, 173.
- [95] Li, F.; Cheng, H.; Bai, S.; Su, G.; Dresselhaus, M. *Applied physics letters* **2000**, *77*, 3161.
- [96] Wong, E. W.; Sheehan, P. E.; Lieber, C. M. *Science* **1997**, *277*, 1971.
- [97] Harris, P. J. F. *Carbon nanotube science and technology*, University of Reading.
- [98] Khare, R.; Bose, S. *Journal of Minerals & Materials Characterization & Engineering* **2005**, *4*, 31.
- [99] Baughman, R. H.; Zakhidov, A. A.; De Heer, W. A. *Science* **2002**, *297*, 787.
- [100] Bianco, A.; Kostarelos, K.; Prato, M. *Current Opinion in Chemical Biology* **2005**, *9*, 674.
- [101] Milne, W.; Teo, K.; Amaratunga, G.; Legagneux, P.; Gangloff, L.; Schnell, J. P.; Semet, V.; Binh, V. T.; Groening, O. *Journal of Materials Chemistry* **2004**, *14*, 933.
- [102] Bianco, A.; Prato, M. *Advanced Materials* **2003**, *15*, 1765.
- [103] Biercuk, M.; Llaguno, M. C.; Radosavljevic, M.; Hyun, J.; Johnson, A. T.; Fischer, J. E. *Applied physics letters* **2002**, *80*, 2767.
- [104] Bauhofer, W.; Kovacs, J. Z. *Composites Science and Technology* **2009**, *69*, 1486.
- [105] Shrivastava, N. K.; Khatua, B. *Carbon* **2011**.

- [106] Jurewicz, I.; Worajittiphon, P.; King, A. A. K.; Sellin, P. J.; Keddie, J. L.; Dalton, A. B. *The Journal of Physical Chemistry B* **2011**.
- [107] Li, Y.; Zhao, L.; Shimizu, H. *Macromolecular Rapid Communications* **2011**.
- [108] Kim, H.; Kim, K.; Lee, C.; Joo, J.; Cho, S.; Yoon, H.; Pejakovi, D.; Yoo, J.; Epstein, A. *Applied physics letters* **2004**, *84*, 589.
- [109] Li, N.; Huang, Y.; Du, F.; He, X.; Lin, X.; Gao, H.; Ma, Y.; Li, F.; Chen, Y.; Eklund, P. C. *Nano letters* **2006**, *6*, 1141.
- [110] Li, Y.; Chen, C.; Zhang, S.; Ni, Y.; Huang, J. *Applied Surface Science* **2008**, *254*, 5766.
- [111] Andre Geim, K. N.; Nobelprize.org: 2010.
- [112] Geim, A. K.; Novoselov, K. S. *Nature materials* **2007**, *6*, 183.
- [113] Geim, A. K. *Science* **2009**, *324*, 1530.
- [114] Mukhopadhyay, P.; Gupta, R. K. **2011**.
- [115] Wang, S.; Zhang, Y.; Abidi, N.; Cabrales, L. *Langmuir* **2009**, *25*, 11078.
- [116] Awasthi, K.; Kumar, R.; Raghubanshi, H.; Awasthi, S.; Pandey, R.; Singh, D.; Yadav, T.; Srivastava, O. *Bulletin of Materials Science* **2011**, *34*, 607.
- [117] Stankovich, S.; Dikin, D. A.; Dommett, G. H. B.; Kohlhaas, K. M.; Zimney, E. J.; Stach, E. A.; Piner, R. D.; Nguyen, S. B. T.; Ruoff, R. S. *Nature* **2006**, *442*, 282.
- [118] Ramanathan, T.; Abdala, A.; Stankovich, S.; Dikin, D.; Herrera-Alonso, M.; Piner, R.; Adamson, D.; Schniepp, H.; Chen, X.; Ruoff, R. *Nature nanotechnology* **2008**, *3*, 327.
- [119] Tien, H. W.; Huang, Y. L.; Yang, S. Y.; Wang, J. Y.; Ma, C. C. M. *Carbon* **2010**.
- [120] He, H.; Tao, N. J. *Encyclopedia of nanoscience and nanotechnology* **2003**, *2*, 755.

- [121] Zhang, D.; Qi, L.; Yang, J.; Ma, J.; Cheng, H.; Huang, a. L. *Chemistry of materials* **2004**, *16*, 872.
- [122] MacNaughton, S.; DeMeo, D. F.; Sonkusale, S.; Vandervelde, T. E. In *Semiconductor Device Research Symposium, 2009. ISDRS '09. International* 2009, p 1.
- [123] Reches, M.; Gazit, E. *Science* **2003**, *300*, 625.
- [124] Gelves, G. A.; Lin, B.; Sundararaj, U.; Haber, J. A. *Advanced Functional Materials* **2006**, *16*, 2423.
- [125] Parker-Chomerics *Conductive Compounds Selectors Guide*, 2011.
- [126] Parker-Chomerics *Cho-Shield 2056 Data Sheet*, 2000.
- [127] Parker-Chomerics *Cho-Shield 2044 Data Sheet*, 2011.
- [128] Parker-Chomerics *Conductive Compounds Cho-Shield Conductive Coatings*, 2000.
- [129] MG-Chemicals *MG Chemicals AppGuide - EMI/RFI Shielding* 2004.
- [130] Creative-Materials *117-48 Pad printable, Electrically Conductive, Modified Silver Epoxy Ink* 1996.
- [131] Ceno Technologies Incorporated 2011.
- [132] Kemtron *Conductive Elastomers: Materials Data*, 2011.
- [133] SSP *SSP547-65 Silicone Sheilding Elastomers: Product Description*, 2009.
- [134] Young, H. D.; Freedman, R. A.; Sears, F. W.; Zemansky, M. W. *Sears and Zemansky's university physics : with modern physics*; 10th ed.; Pearson/Addison Wesley: San Francisco, Calif. ; London, 2000.
- [135] Kraz, V. *Conformity* **2007**, *January*, 38.
- [136] Maxwell, J. C. *Clarendon Press, Oxford* **1892**, *2*, 247.
- [137] Crowell, B. *Light and Matter*; Creative Common Attribution, 1998.

- [138] Ampere, A. M. *Ann. Chemie et Phys.* **1820**, 15, 59.
- [139] Liao, S. Y. *Microwave devices and circuits*; Prentice Hall, 1980.
- [140] Cowdell, R. *Electronic Design News* **1982**, 44.
- [141] Parker Chomerics *Theory of shielding and gasketing - EMI Shielding Theory*, 2000.
- [142] Matthew, N.; Sadiku, O. *Elements of electromagnetics*; Oxford University Press.
- [143] Straus, I.; Conformity: 2001.
- [144] GE-Plastics *Product Assembly - Shielding Principles and Shielding Effectiveness*.
- [145] Luke, S. **2007**.
- [146] Munk, B. *Frequency selective surfaces: theory and design*; Wiley-Interscience, 2000.
- [147] Commission, I. E. *Geneva, Switzerland: CISPR2008* **1997**.
- [148] National Security Agency *Specification for Shielded Enclosures: NSA 73-2A*, 1972.
- [149] Hemming, L. H. *Architectural Electromagnetic Shielding Handbook: A Design and Specification Guide*; Institute of Electrical and Electronics Engineers, 2000.
- [150] Markham, D. *Materials & Design* **1999**, 21, 45.
- [151] Levy, O.; Stroud, D. *Physical review B* **1997**, 56, 8035.
- [152] Kovacik, J. *Scripta Materialia* **1998**, 39.
- [153] Jamnik, J.; Kalnin, J.; Kotomin, E.; Maier, J. *Physical Chemistry Chemical Physics* **2006**, 8, 1310.
- [154] Thommerel, E.; Valmalette, J.; Musso, J.; Villain, S.; Gavarrri, J.; Spada, D. *Materials Science and Engineering A* **2002**, 328, 67.
- [155] Garnett, J. *Philos. Trans. R. Soc. London Ser. A* **1904**, 203, 385.

- [156] Bruggeman, D. *Ann. Phys.(Leipzig)* **1935**, 24, 636.
- [157] Landauer, R. 1978; Vol. 40, p 2.
- [158] Ruppin, R. *Optics Communications* **2000**, 182, 273.
- [159] Karkkainen, K.; Sihvola, A.; Nikoskinen, K. *Geoscience and Remote Sensing, IEEE Transactions on* **2002**, 38, 1303.
- [160] Mackay, T. G.; Lakhtakia, A. *Optics Communications* **2004**, 234, 35.
- [161] Agilent Technologies *RF Network Analysis Basics - A Self Paced Tutorial*, 2003.
- [162] J. K. Hunton, H. C. P.; Reis, a. C. S. *Hewlett-Packard Journal* **1955**, 7, 1.
- [163] Bernd Schinle, J. L. *Basics of Vector Network Analysis*; Rohde&Schwarz UK Ltd., 2005.
- [164] Ramo, S.; Whinnery, J.; Van Duzer, T. **1994**.
- [165] ASTM 2010.
- [166] Robeson, L. *Polymer blends: a comprehensive review*; Hanser Gardner Pubns, 2007.
- [167] Matthews, G. *Polymer mixing technology*; Applied Science New York, 1982.
- [168] Mallory, G.; Hajdu, J.; Electroplaters, A.; Society, S. F.; Knovel *Electroless plating: fundamentals and applications*; AESF, 1990.
- [169] Wurtz, A. *Ann. chim. phys* **1844**, 11, 250.
- [170] Brenner, A.; Riddell, G. 1948, p 156.
- [171] Brown, R.; Brewer, P.; Milton, M. *Journal of Materials Chemistry* **2002**, 12, 2749.
- [172] Sahoo, P.; Das, S. K. *Materials & Design* **2010**.
- [173] Palaniappa, M.; Seshadri, S. *Wear* **2008**, 265, 735.
- [174] Grosjean, A.; Rezrazi, M.; Takadoum, J.; Bercot, P. *Surface and Coatings Technology* **2001**, 137, 92.

- [175] Straffelini, G.; Colombo, D.; Molinari, A. *Wear* **1999**, 236, 179.
- [176] Balaraju, J.; Sankara Narayanan, T.; Seshadri, S. *Journal of applied Electrochemistry* **2003**, 33, 807.
- [177] Parkinson, R. *Nickel Development Institute* **1997**, 37.
- [178] Yoon, J. W.; Park, J. H.; Shur, C. C.; Jung, S. B. *Microelectronic Engineering* **2007**, 84, 2552.
- [179] Grossmann, G.; Zardini, C. *The ELFNET Book on Failure Mechanisms, Testing Methods, and Quality Issues of Lead-Free Solder Interconnects*; Springer, 2011.
- [180] Johal, K.; Roberts, H.; Lamprecht, S.; Wunderlich, C. *Americas* **2005**, 25, 35.
- [181] *ASTM Standard Test Methods for DC Resistance or Conductance of Insulating Materials*, 2007.
- [182] William A. Maryniak, T. U., Maciej A. Noras 2003, p 4.
- [183] Chatagnon, C., Edinburgh Napier University, 2007.
- [184] RTP Company *Surface Resistivity and Applications* 2008.
- [185] Standard, M. *Method of Attenuation Measurements for Enclosures, Electromagnetic Shielding, for Electronic Purposes, US Government Printing Office, Washington, DC, 1956, MIL-STD-285*.
- [186] *ASTM Standard Test Method for Measuring the Electromagnetic Shielding Effectiveness of Planar Materials*, 1999.
- [187] Novamet *HCA-1 Conductive Nickel Flake Data Sheet*, 2006.
- [188] Novamet *525 Conductive Nickel Powder Data Sheet*, 2006.
- [189] Wayne-Kerr *Instruction/ Service Manual for 6425 Precision Component Analyser* Farnell Instruments Limited.
- [190] Panteny, S.; Stevens, R.; Bowen, C. *Ferroelectrics* **2005**, 319, 199.

- [191] Palaniappa, M.; Veera Babu, G.; Balasubramanian, K. *Materials Science and Engineering: A* **2007**, *471*, 165.
- [192] ASM International *Characterization and failure analysis of plastics*; ASM International, 2003.
- [193] www.matweb.com *Nickel Data Sheet*.
- [194] www.matweb.com *Graphite Data Sheet*.
- [195] Multiphysics, C. *Comsol Multiphysics Minicourse*, 2006.

12 Appendix A – Institute of Circuit Technology Publication

EMI Shielding Properties of Polymer Composites

The Journal of the Institute of Circuit Technology

October 2008 vol.1 no.4

EMI Shielding Properties of Polymer Composites

Jonathan Smuga

Research Student,
Napier University

Introduction

Shielding from radiated electromagnetic interference is a constantly growing issue with the increase and miniaturisation of electronic devices. Often these devices require shielding from the external EM environment or from internally generated sources such as self generated waves or from adjacent circuits. Considering this EMI issue while designing of a PCB will aid the overall efficiency of the process as it is a common scenario that "decisions on the RFI enclosures are left until the end of the design process creating a situation that makes their addition more difficult to accommodate. As a result, the enclosures may interfere mechanically with other areas of the design." (Warner, 2008). Considering available shielding options at the design stage will help to control the cost, manufacture and weight issues while also potentially expanding the options available for the desired application.

Shielding methods

The majority of unwanted EM emissions are the result of voltages and currents travelling within circuitry, where voltages generate electric fields and the currents generate magnetic fields. Good design and grounding can reduce the levels of these emissions but often it is necessary to provide a barrier shield. Just as conductive materials will emit radiation they also reflect and absorb it converting it back to voltages and currents.

Board level enclosures are one of the standard methods of shielding within PCBs and circuitry, they are housings that surround the component providing it with a conductive cage to shield and reduce the levels of emissions entering or being transmitted from the device. Enclosure design is varied but in general they take the form of a conductive blanket known as a "shadow shield" or a five sided box that encapsu-

lated the desired components, they can be multi cavity and have accessibility for maintenance via hinged flaps. Commonly these are thin metallic sheets that could be stamped, folded or machined to shape, the manufacturing process followed will depend on the volume required and the stage of development reached. Metallic shields perform well when manufactured and installed correctly but there is a risk that further processing of the board can result in apertures being created, if these are of similar length to any wavelengths involved, they can act as an antenna for localised emissions.

Polymer enclosures are a viable option in terms of cost weight and manufacturability but with most commodity plastics being excellent insulators they are essentially invisible to EM waves. Therefore to utilise polymers they have to include a conduction mechanism, this could be in the form of metallisation, doping, inherent conduction or conductively filled polymers.

Metallised plastic housings involve depositing a very thin layer of metal onto a moulded plastic enclosure providing a continuous conductive path that can provide high EM attenuation levels. Possible metallisation processes include :-

a) **Electroless plating** – A chemical reduction process that requires various stages of baths to sensitise and activate the surface of the material before finally being submerged in a solution rich in metal ions that are deposited uniformly over the all active surfaces. This provides a two layer shield as both internal and external surfaces are coated resulting in a potential shielding effectiveness in the range of 90dB (Bastenbeck, 2008). Although a good method of providing shielding this requires large amounts of chemicals and can have slow deposition rates.

b) **Vacuum metallisation** – Various vacuum plating processes are feasible, these include evaporation coating where a metal is vaporised then deposited onto the substrate surface and sputtering where by the introduction of a current and inert gas within the vacuum chamber creates a plasma which releases metal atoms from a target material which are then deposited throughout the chamber. These processes are rela-

tively simple and provide good quality coatings but are limited by the chamber dimensions and are both line of sight processes making complex substrates more difficult to coat. They can achieve shielding in the region of 50-70dB (Gerke, 1990) depending on the frequency and thickness of the coating, at lower frequency the coating must be thicker to compensate for the skin effect.

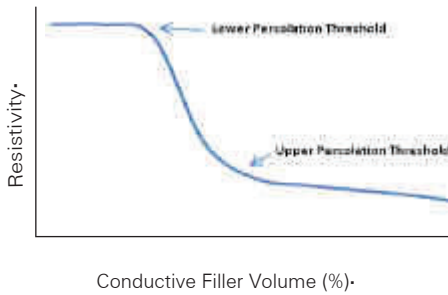
Inherently conductive Polymers

Polymers that are conductive as a property of their structure are known as inherently conductive polymers (ICP), they can be synthesised for a specific structure or to contain dopants to allow electron transfer. One solution can be achieved through modification to the polymer structure to allow the transfer of electrons along a chain structure known as a conjugated chain polymer. These involve chemically unsaturated polymers that have a backbone chain structure of alternating single and double bonded carbon atoms. This structure allows for each carbon atom to only be bonded with one other kind of atom this leaves one electron free from each carbon atom and allows for electron transport within. Although ICP's are potentially ideal for these applications often their high crystallinity and insolubility have limited their use, although more recent developments have shown more promise.

Conductively filled polymer

Conductive polymer composite are manufactured by filling an insulative matrix with conductive fillers, the matrix gradually becomes less resistive as the volume of filler increases. This trend continues until the filler volume reaches a level where the resistance rapidly drops known as percolation threshold, this resistance drop continues until a limit is reached and the reduction in resistance slows down again. At this stage conductive networks have been formed and once percolation has been reached the addition of further fillers is unlikely to give any significant improvement to the conductivity but maybe likely to have a detrimental impact on the mechanical properties of the composite.

Typical Percolation Curve



Percolation threshold values are varied dependant on filler and matrix properties and with the filler usually the heaviest and most costly aspect to a composite, reduction in the percolation threshold value will reduce amounts of filler required. Common fillers include metallic or carbon powders, flakes or fibres and also ICP particles dispersed into a non conducting matrix are being researched.

Polymer composite manufacture

Samples were manufactured in a matrix of poly(methyl methacrylate) PMMA resin and using commercially available filler materials such as nickels, graphite's and silver coated glass. These are then printed following a simple hand mixing and automated printing process. Hand mixing is preferred to mechanical or ultrasonic mixing as the more dispersed the particles the more likely they are to be isolated within the insulative matrix and therefore less likely to form the desired conductive networks. The samples are then printed on a K-control coater, where a wire wound bar is drawn down the substrate giving a uniform coating at controlled thicknesses, then cured inside an oven at 80°C.

Filler Materials

The range of filler materials tested covers the commonly used types of conductive particles used for these types of applications they are;

Expanded Graphite

Expanded graphite is a form of graphite powder that has been chemically and heat treated to increase its volume giving a very low density conductive powder,

measured at 0.098 g/cm³ It is formed by taking natural flake graphite and treating it with acids then rapidly heating it to temperatures in the region of 1000⁰ C (Figure 1). This process expands the weaker interlayer van der Waals bonds which then allow the individual layers to collapse and support their surroundings allowing for the expansion to remain after cooling. This process can expand the graphite to between 100-300% of its volume therefore should allow for low percolation values and lightweight composites.

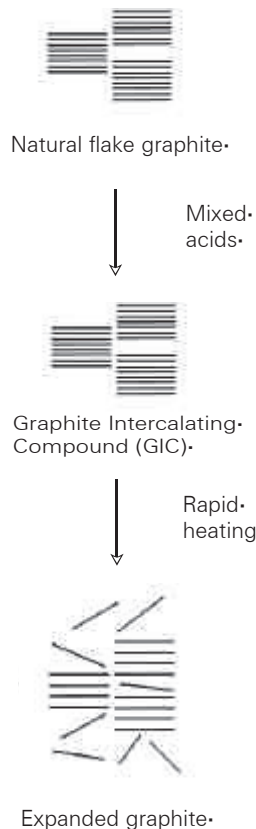
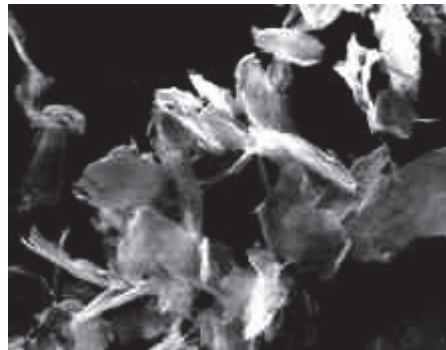
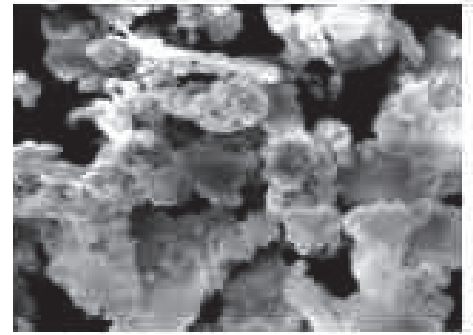
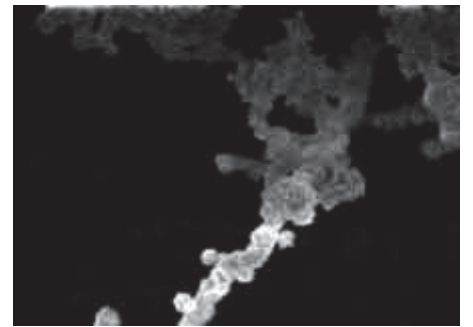


Fig 1. Formation of Expanded Graphite (Zheng)



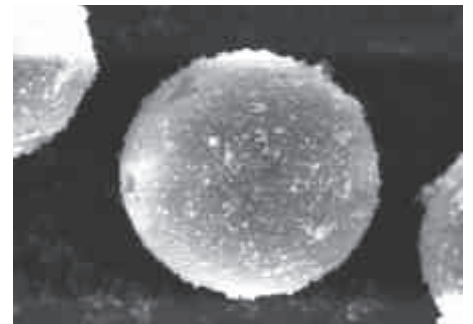
Flake Nickel

Flake nickel is a powder with a high aspect ratio of close to 20 to 1 allowing maximum area of contact between the particles and therefore reducing the contact resistance.



Filamentary Nickel

Filamentary nickel is a fine powder that has been produced through heat treated nickel carbonyl giving filamentary, type particles that should form networks more easily within the matrix.



Silver Coated Glass

Silver coated glass spheres have the advantage of combining the lightweight glass core with the excellent electrical properties of the silver coating. Silver is one of the most conductive materials and also has a conductive oxide therefore degradation of these materials isn't as drastic as with other metallic powders,

copper for example can require an acidic additive to inhibit this effect

Resistivity Measurements

Surface resistivity is a material property describing the electrical resistance of a set area of the materials surface, it is measured following the parallel plate electrode configuration described in the standard ASTM D257, and this involves measuring the resistance between two parallel copper electrodes over a known square area. The potential applications for conductive materials are predominantly determined by the level of resistivity achieved, as can be seen in figure 2 materials that are less resistive than plastics are capable of dissipating static charges and materials close to the resistivity of metals have far greater shielding properties.

Attenuation Measurements

Attenuation measurements were taken on a Rohde & Schwarz ZVA network analyser using a waveguide with a range 2.6GHz - 3.95GHz. Samples of the printed materials were placed in between the two halves of the waveguide and the through transmission attenuation due to the coating material was measured. Calibration was performed with a blank polyester sheet substrate therefore the attenuations evaluated were of the coatings only.

Results

As can be seen in figure 3, all materials followed the classical percolation behaviour with the resistivities dropping rapidly between 35-45% with the exception of the silver coated glass which occurred slightly higher at about 50-55%. The raised level may be due to the spherical nature of the particles having less contact area available, although when percolation occurred the resistivity dropped dramatically. The expanded graphite shows the limitations of carbon based fillers, with graphite being inherently more resistive even after percolation it was far higher than the other materials. Both the nickel samples followed almost identical curves reaching ohmic levels after about 40% volume.

The attenuation measurements shown in figure 4 were measured from the point of each materials up-

per percolation threshold and shows a significant increase in shielding effectiveness with the silver coated glass sample although readings were taken at 55% volume it was

measured to have a similar resistivity as the nickel samples yet achieved around a 20dB increase in shielding. The expanded graphite sample provided very little shielding and is only

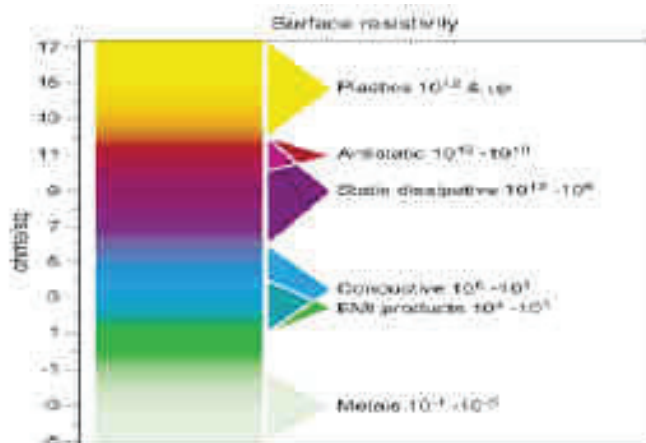


Fig.2 Surface Resistivity Applications (RTP Company)

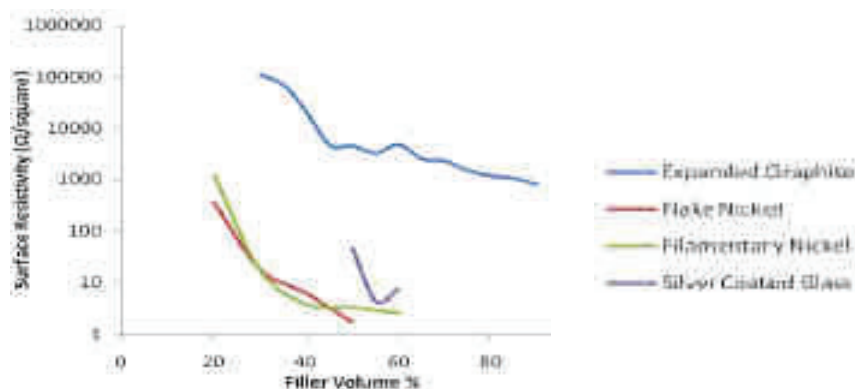


Fig.3 Resistivity Measurements

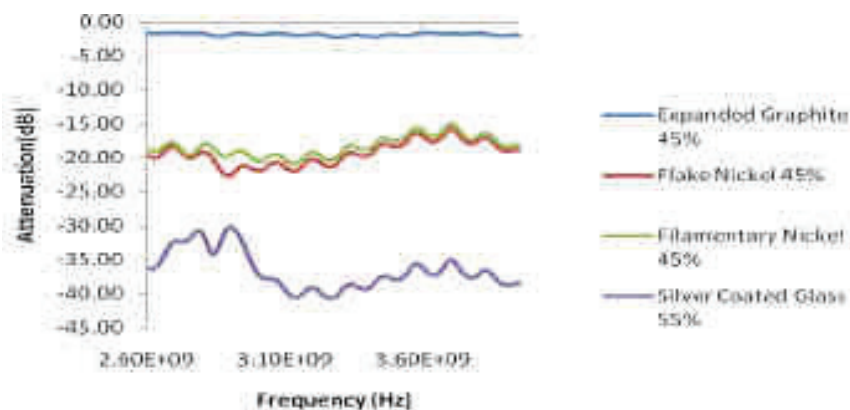


Fig.4 Attenuation Measurements

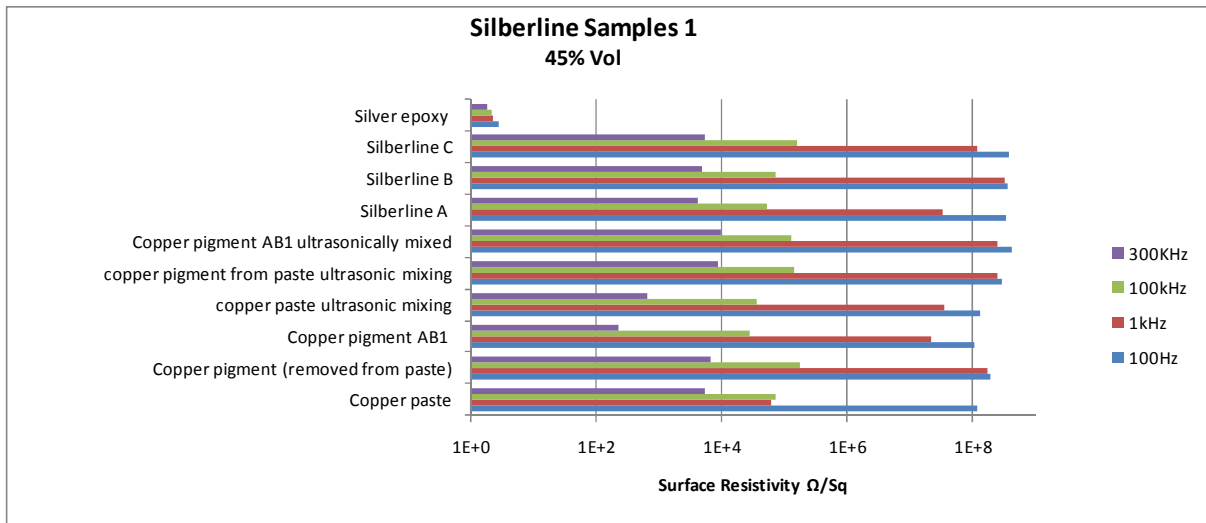
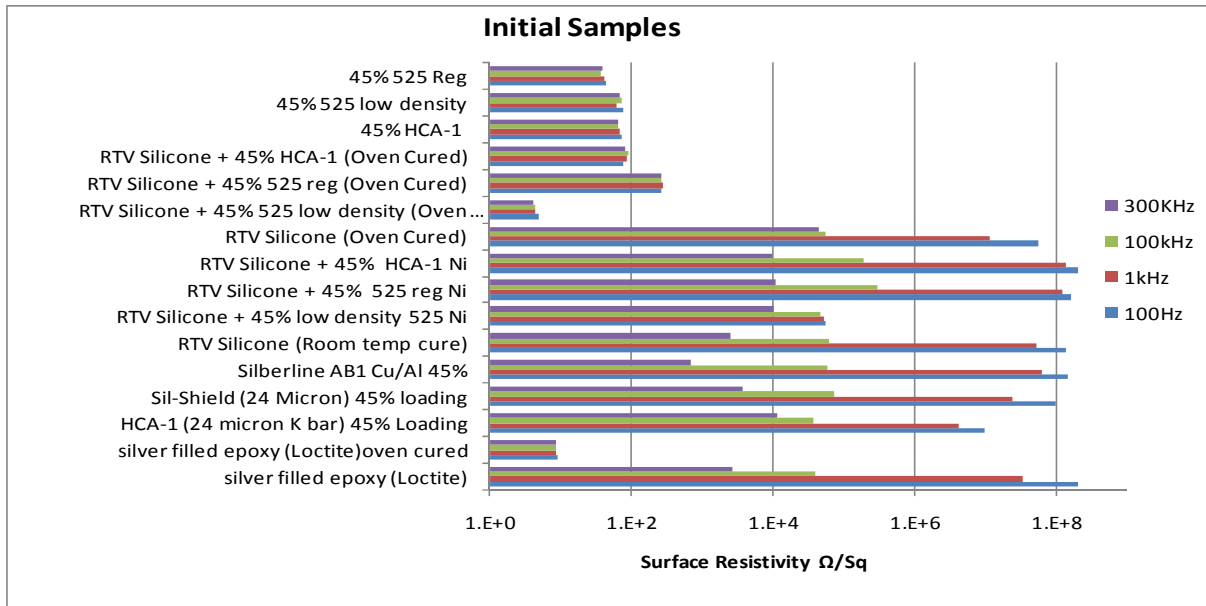
Conclusion

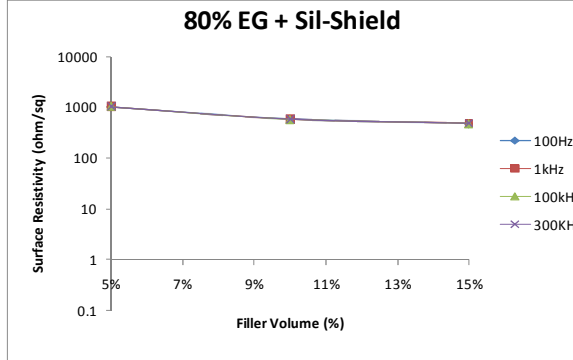
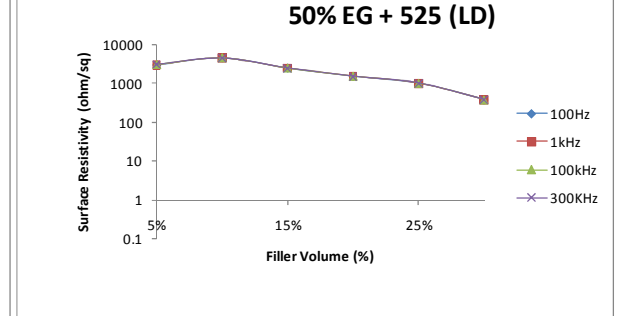
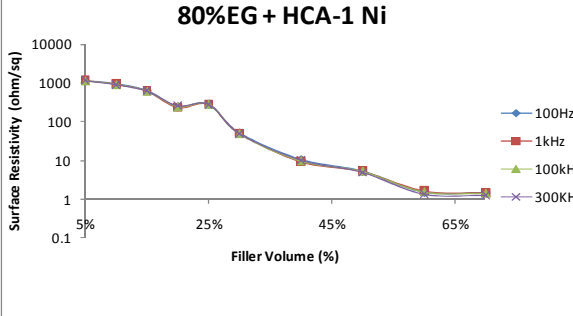
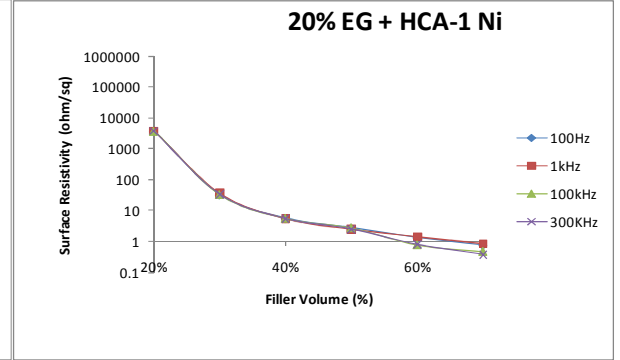
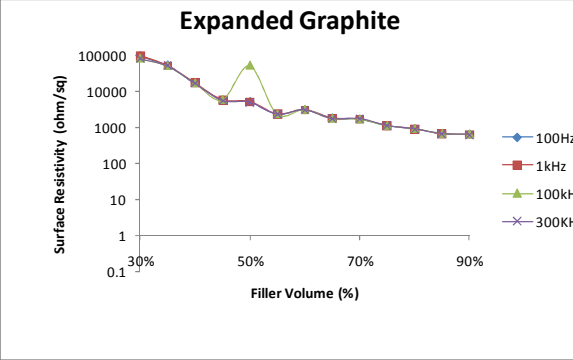
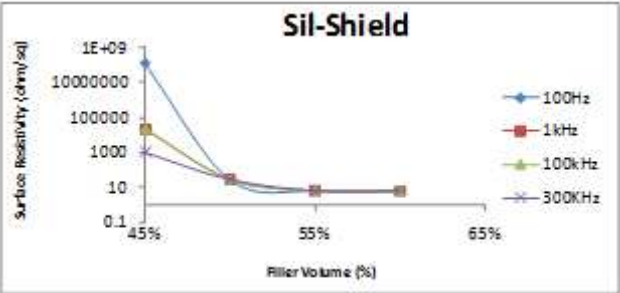
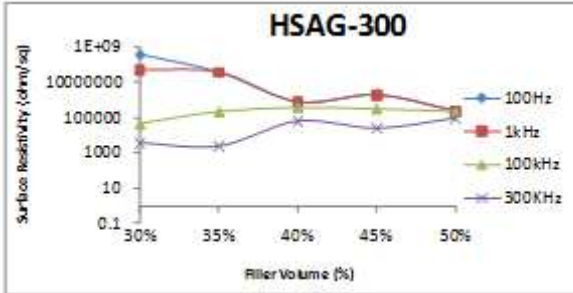
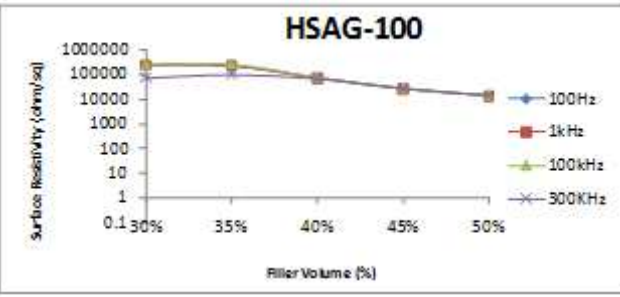
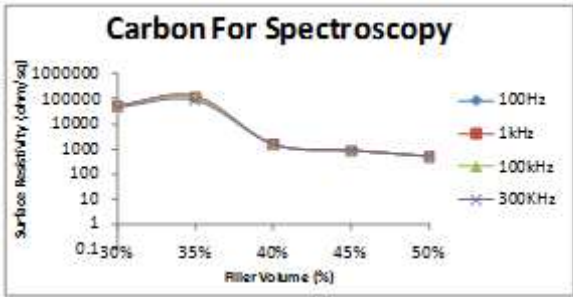
Although conductive polymer composites can be beneficial in terms of cost, ease of manufacture and weight saving benefits the limitations of the shielding effectiveness restrict their potential applications. Efforts will continue to be directed towards developing these materials with a goal of increasing the conductivity and shielding effectiveness while keeping the metal content to a minimum.

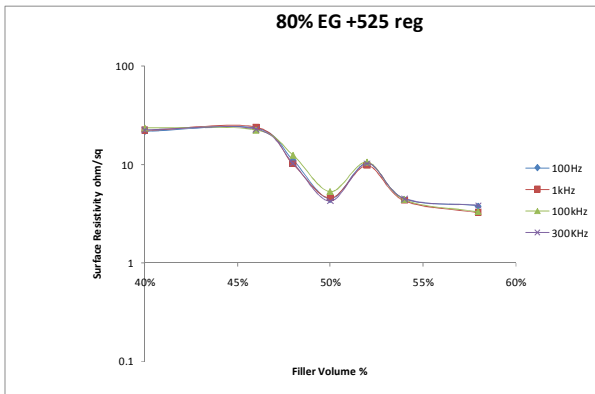
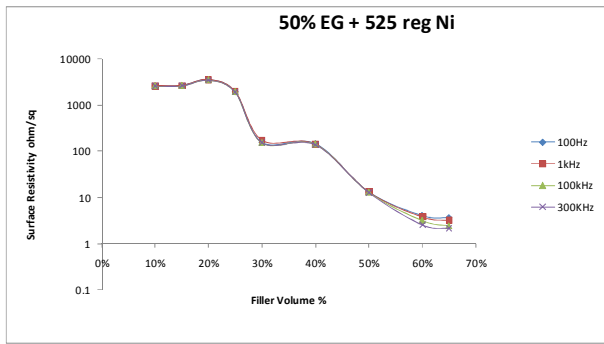
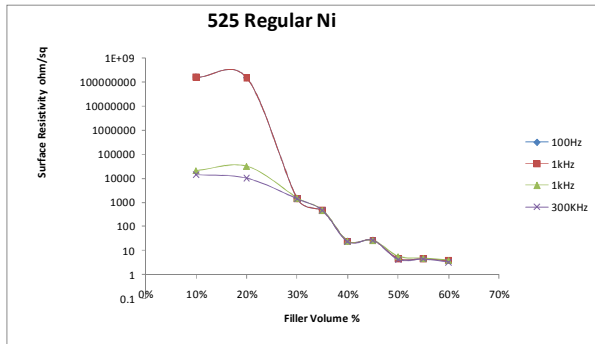
- 1 Bastenbeck, E. (2007). EMI Shielding Design Guide. Cookson Electronics.
- 2 RTP Company (2008) Gerke, D. (1990). Vacuum Deposition Shielding Effectiveness Tests.
- 3 Warner, A. (2008). PCB Board Level Enclosures: A Vital Design Element. Interference Technology.
- 4 Zheng, W. a. (2003). Electrical conductivity and dielectric properties of PMMA/expanded graphite composites. Polymer Composites Science and Technology .

13 Appendix B – Resistivity Measurements

Resistivity Measurements





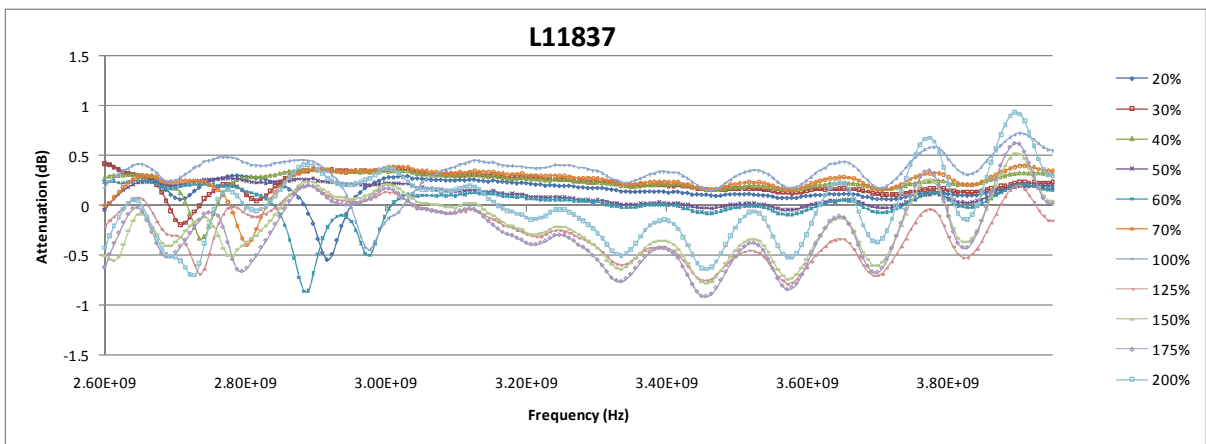
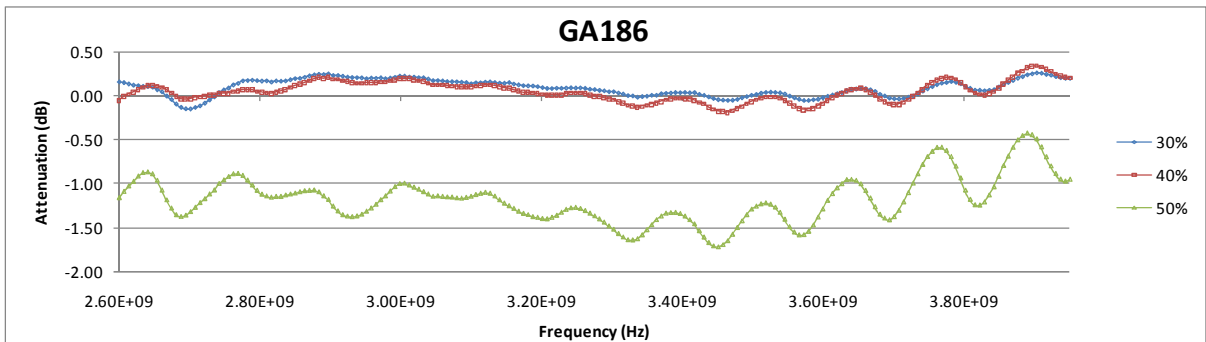
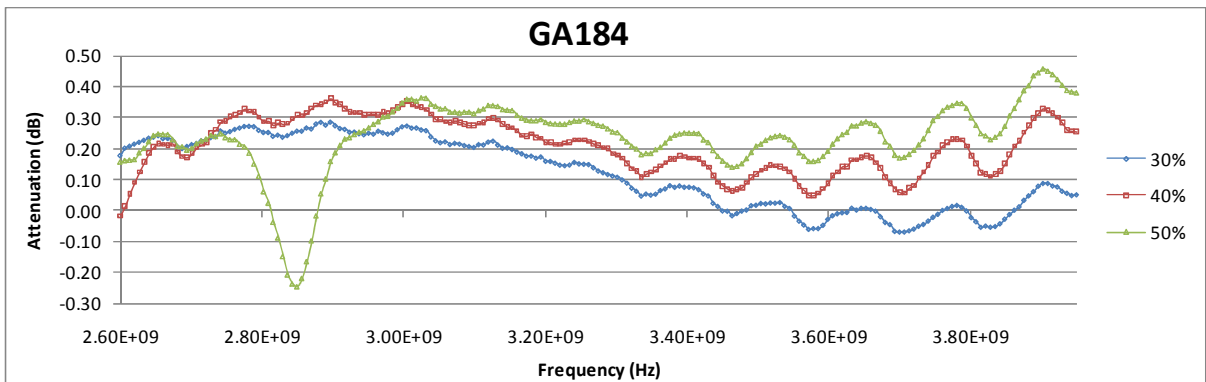
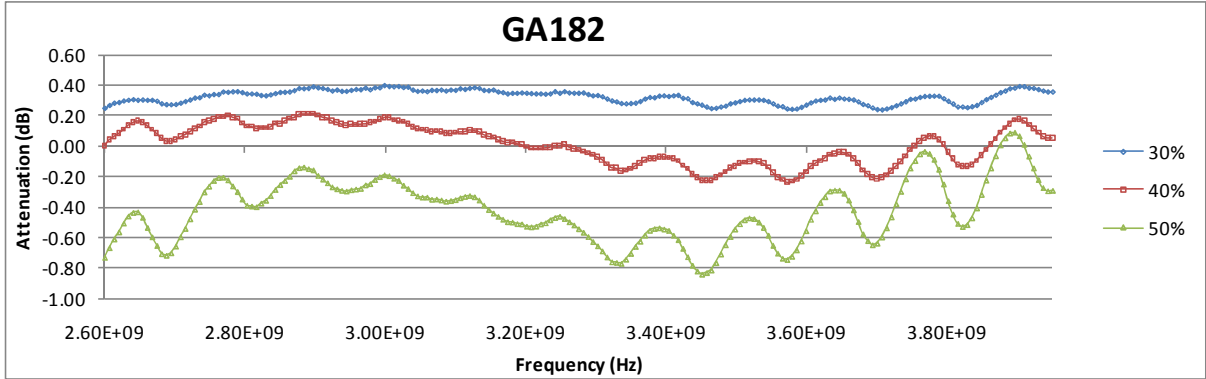


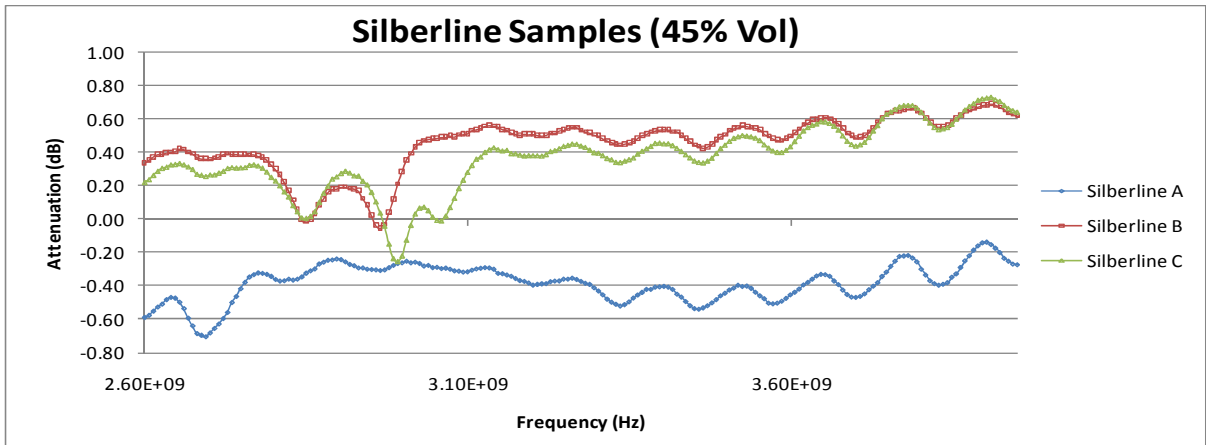
14 Appendix C – Waveguide EMI Measurements

Waveguide EMI Shielding Results

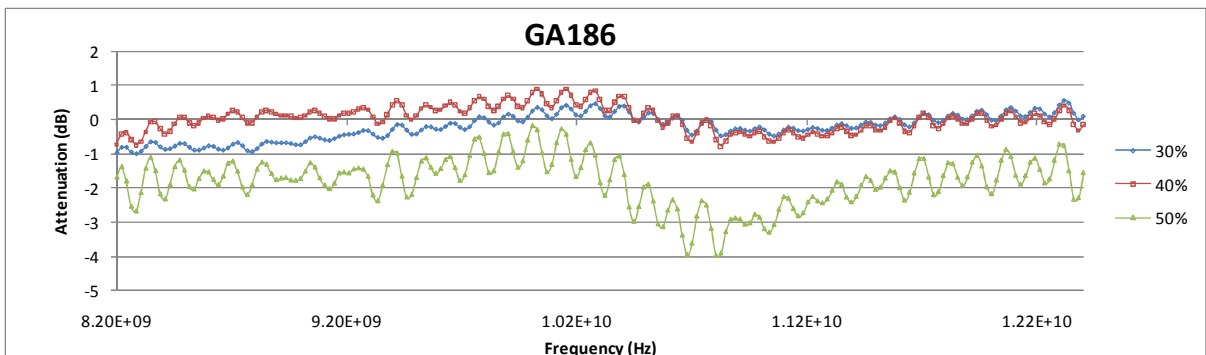
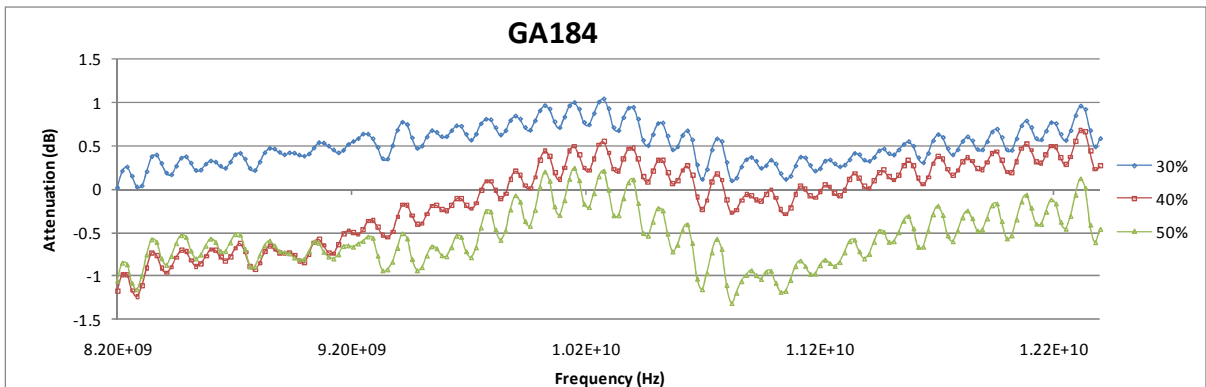
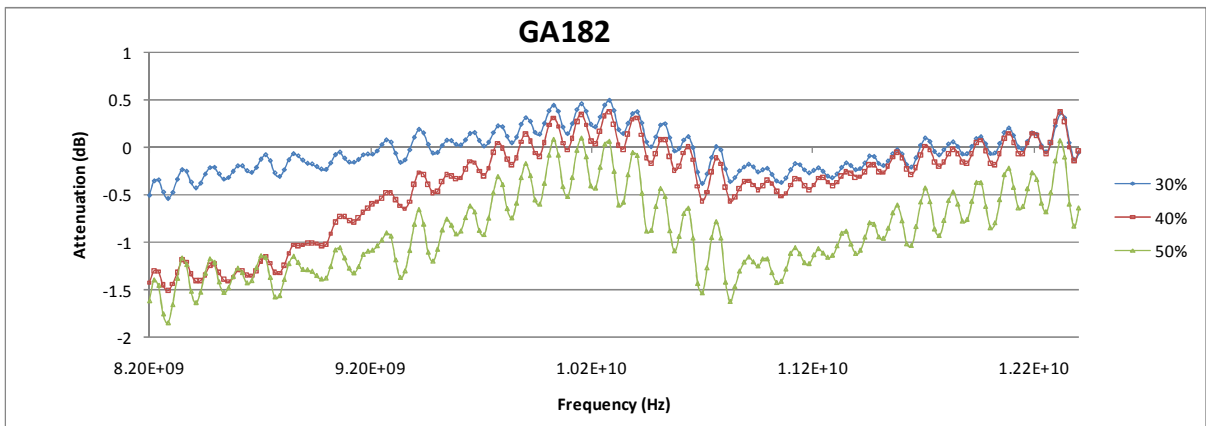
Silberline Samples

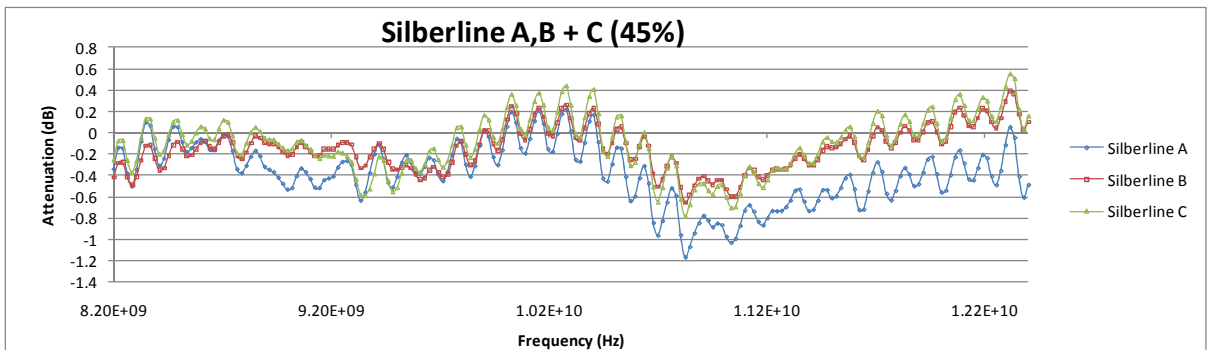
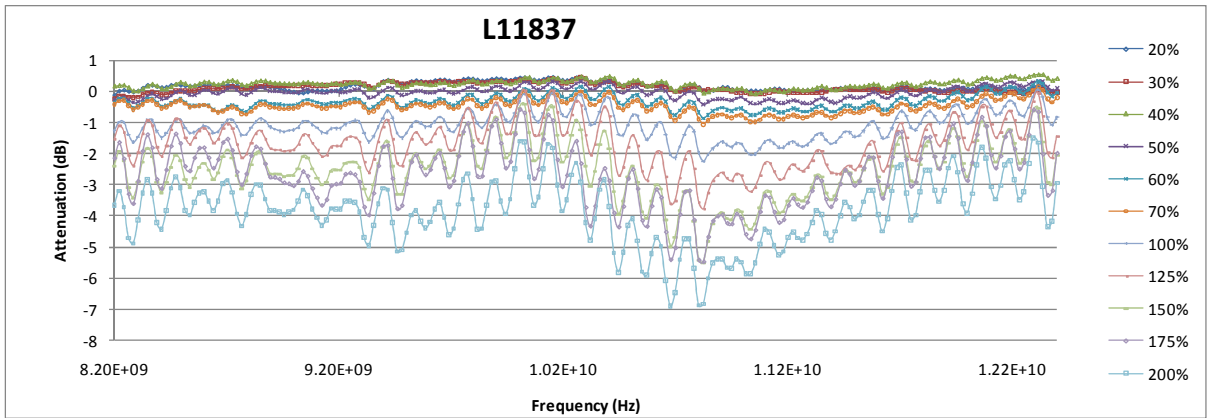
S-band



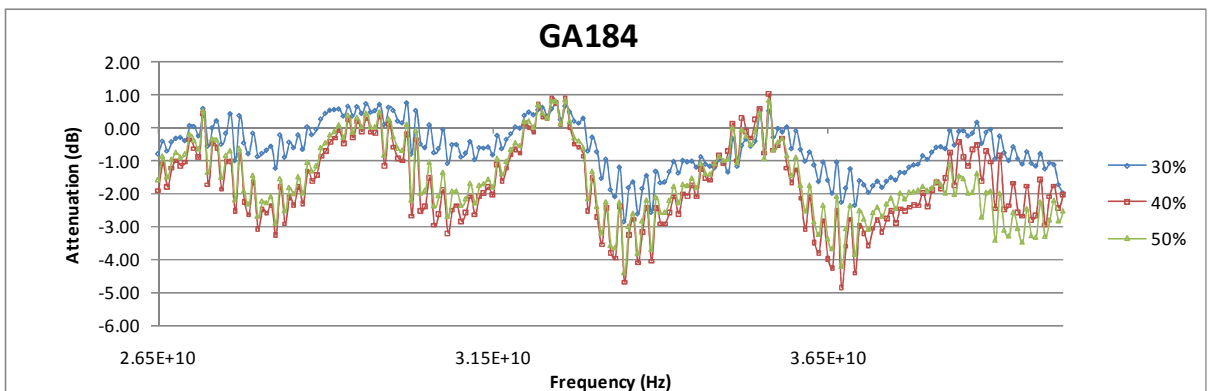
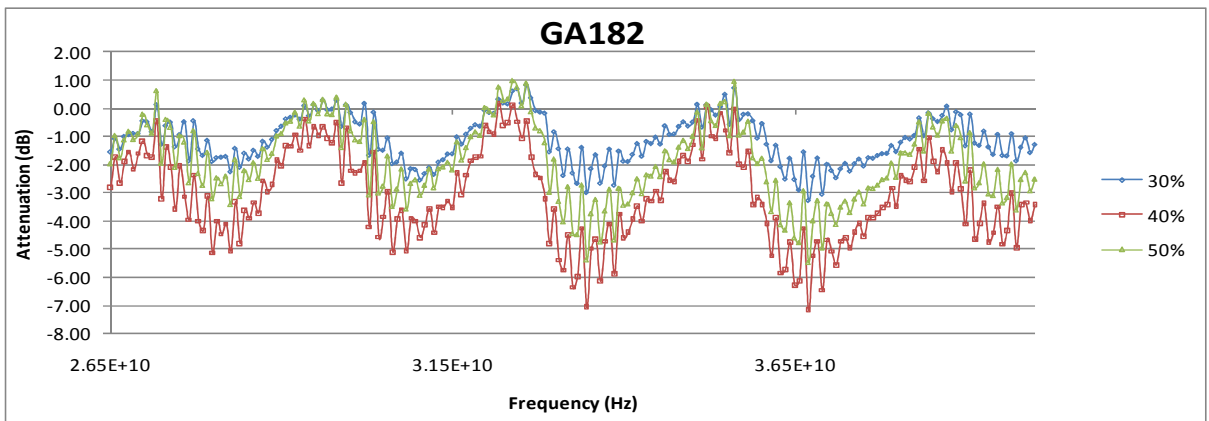


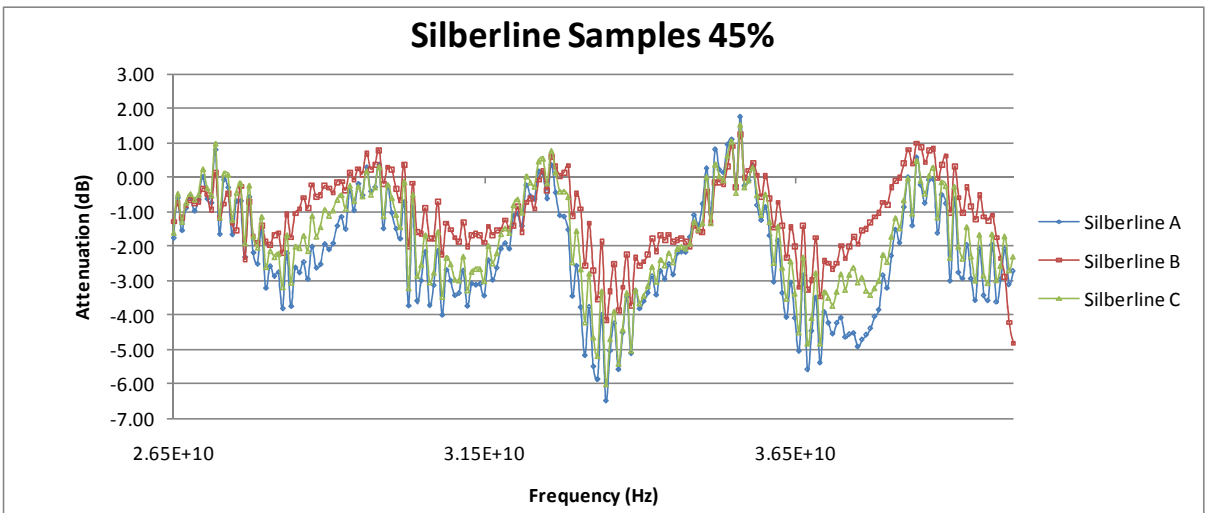
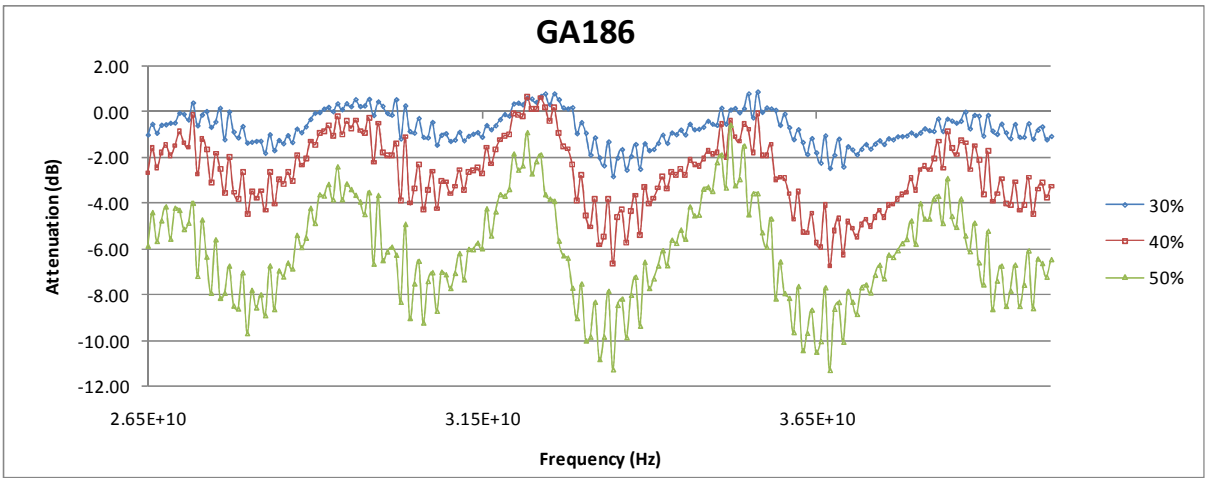
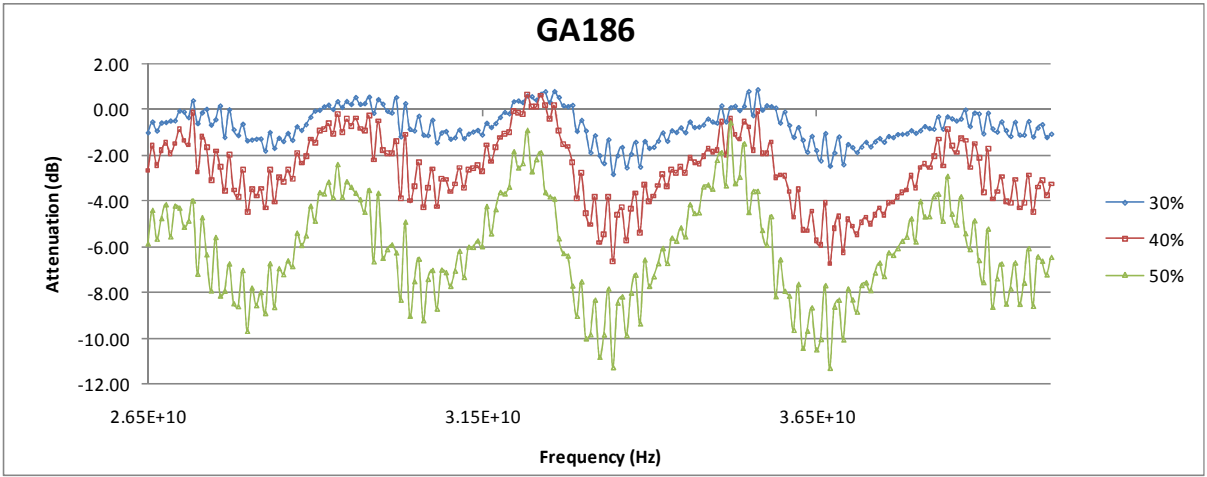
X-Band





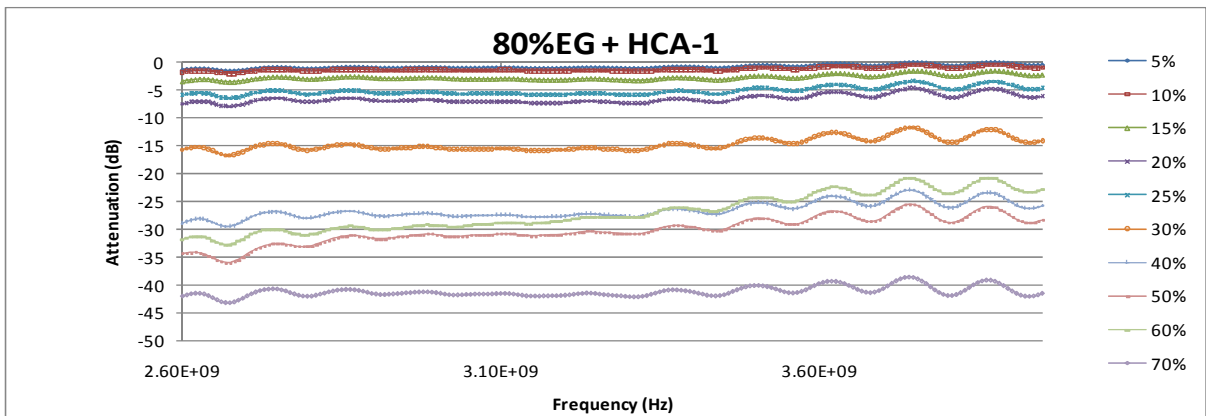
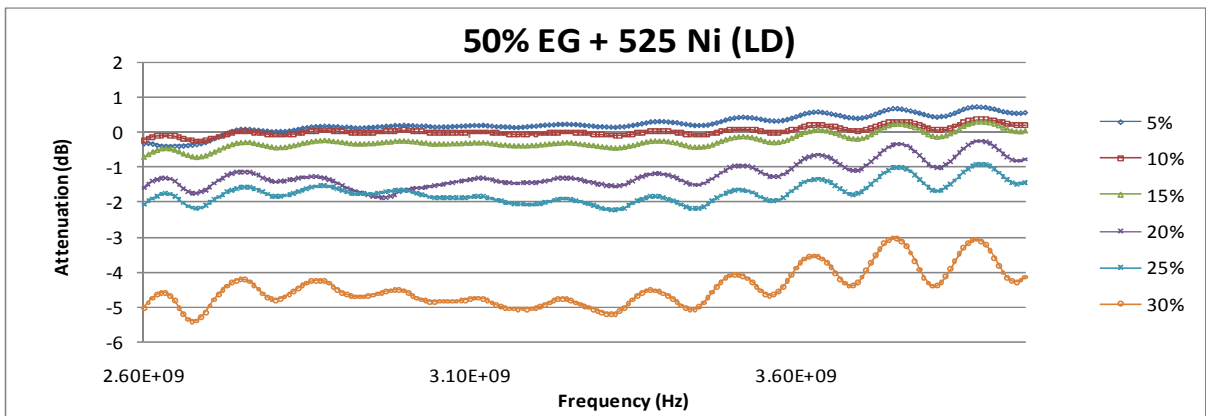
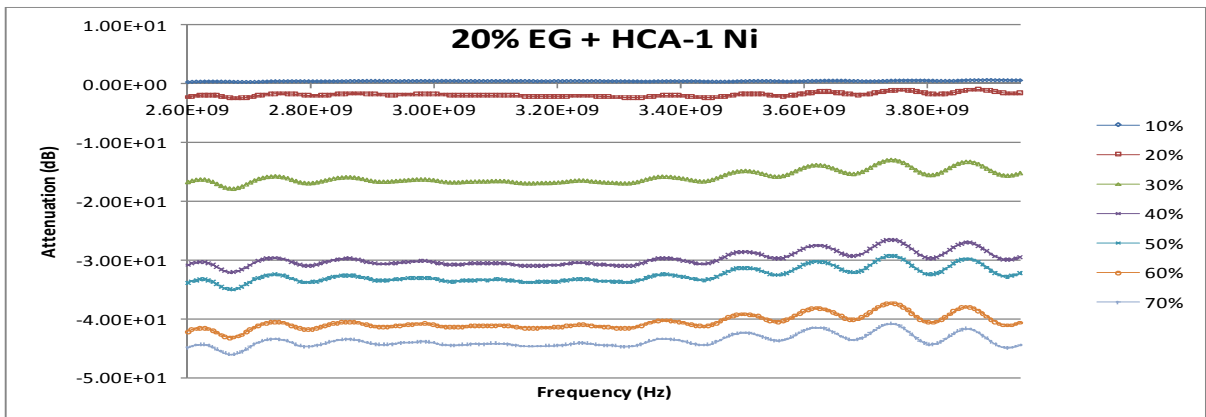
Q-Band

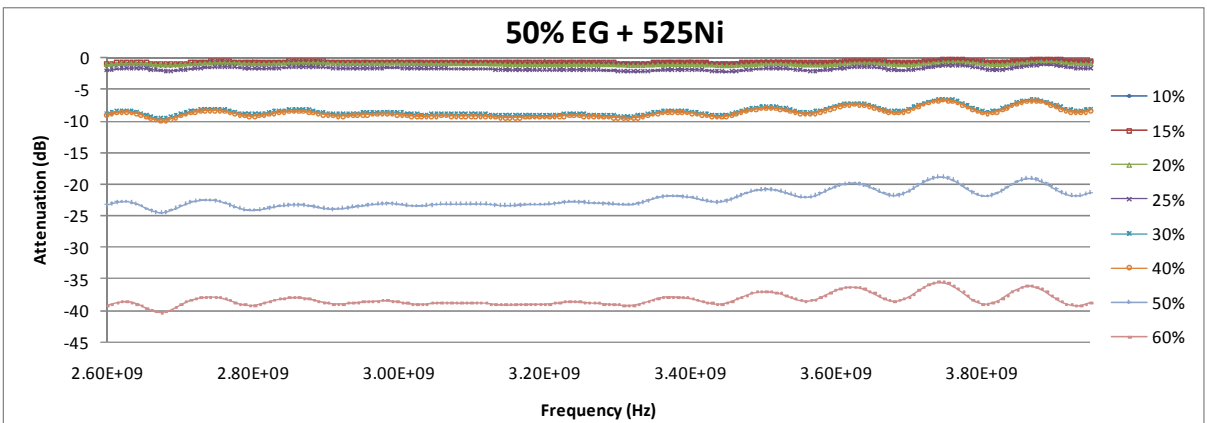
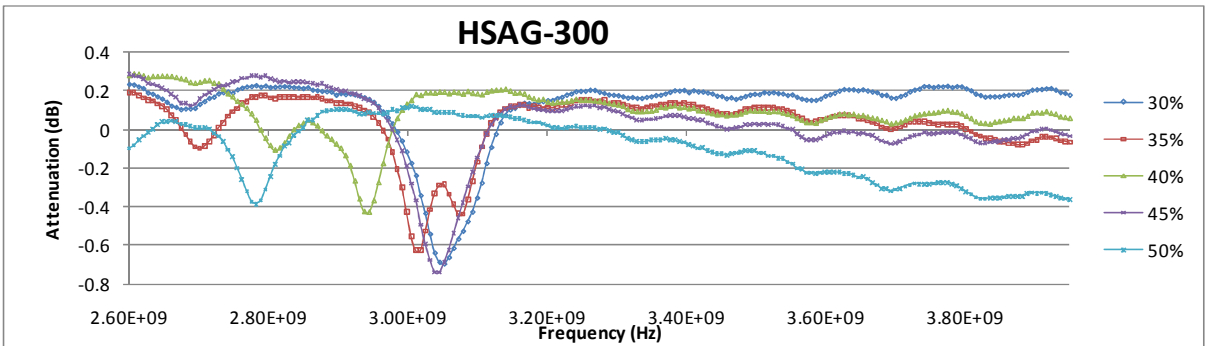
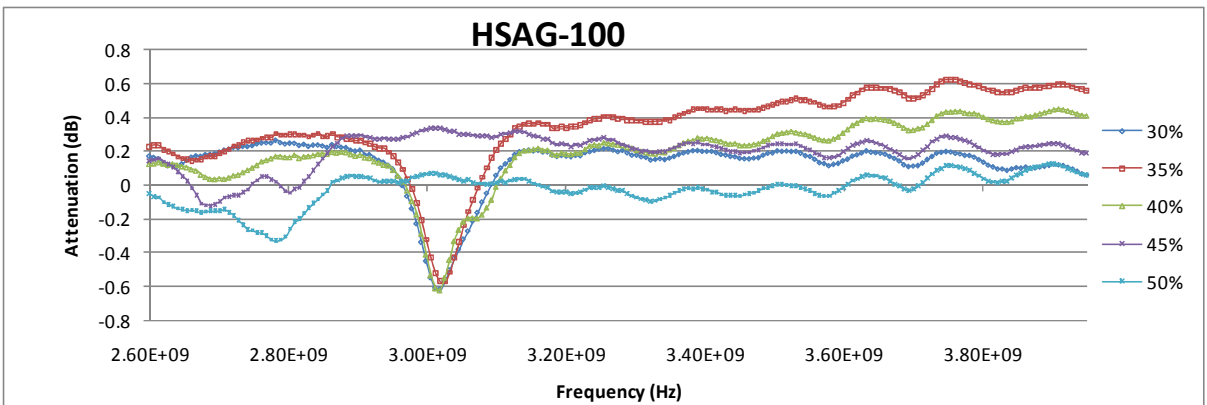
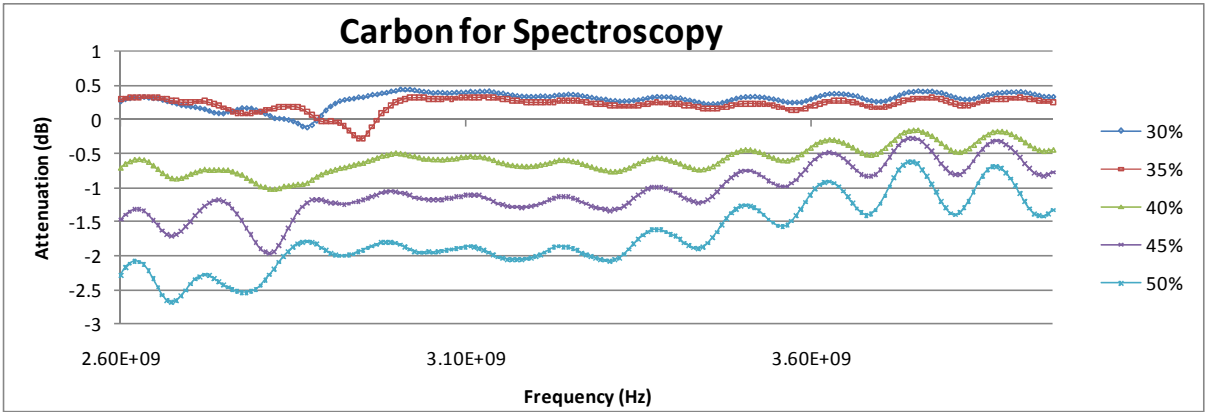


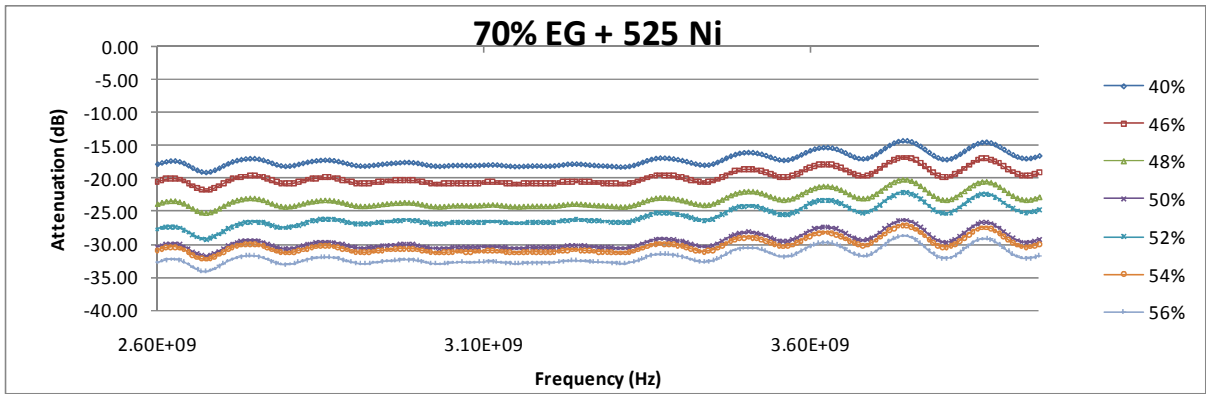


Carbon/Nickel Samples

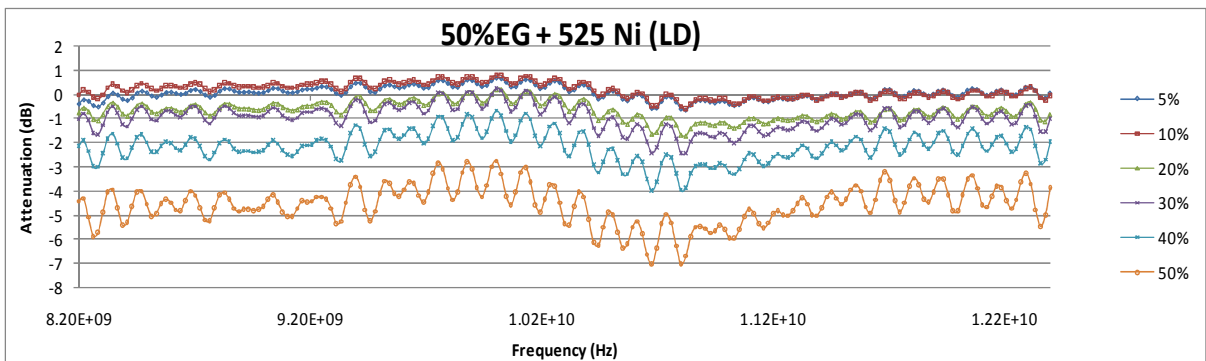
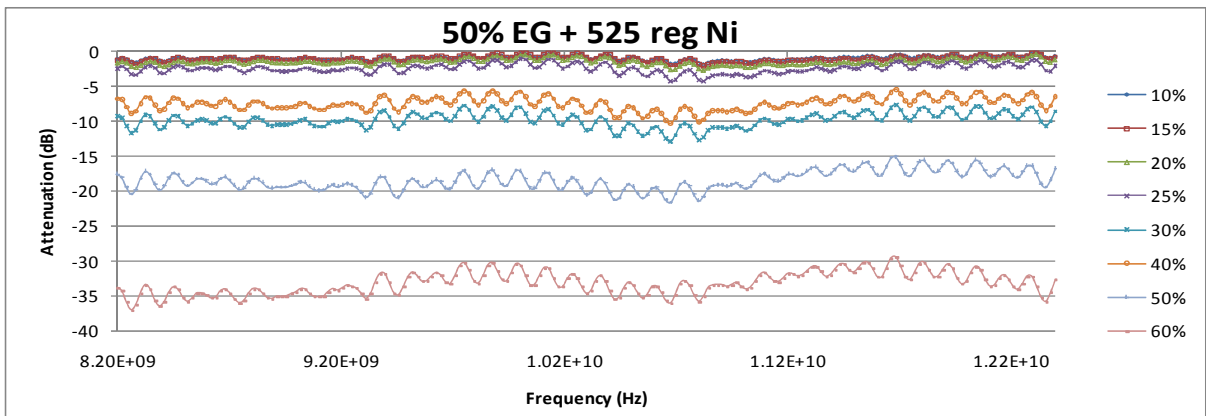
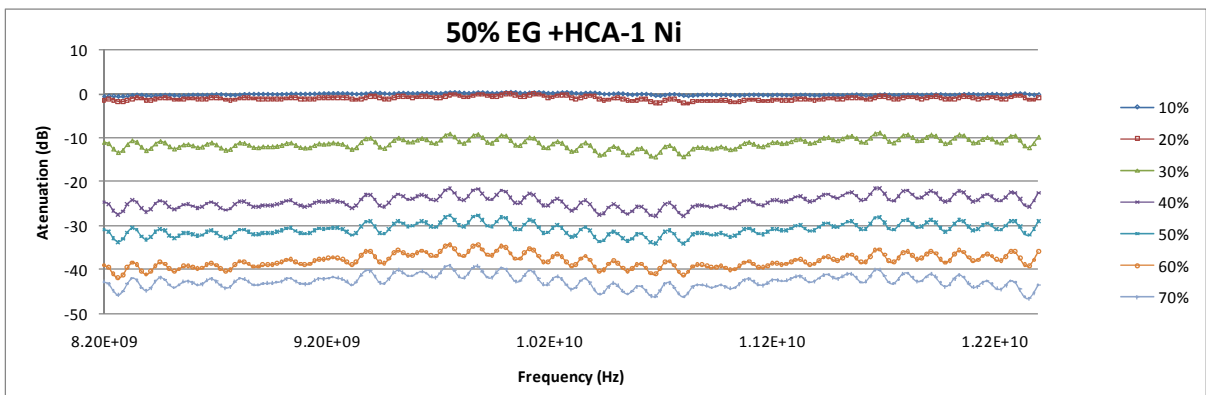
S-Band

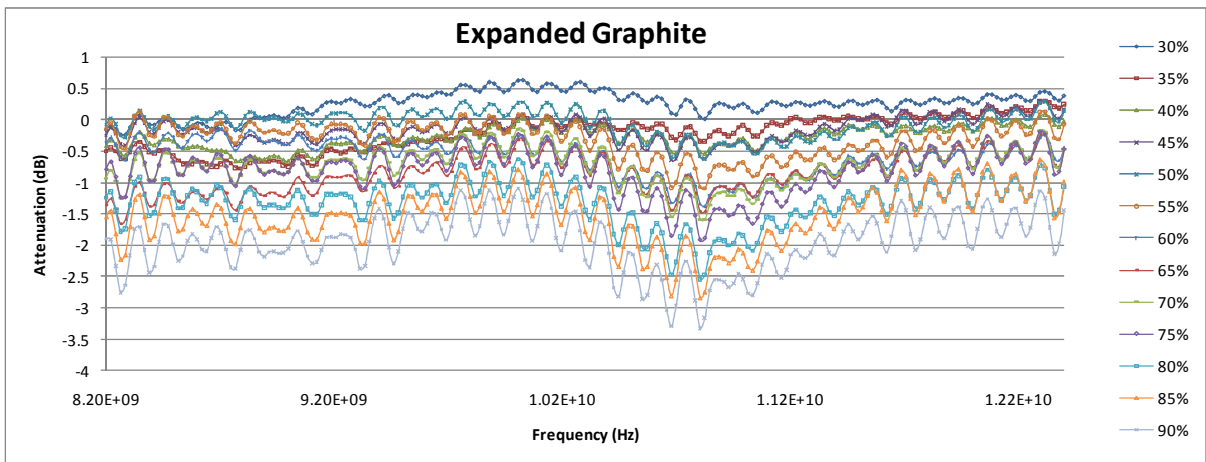
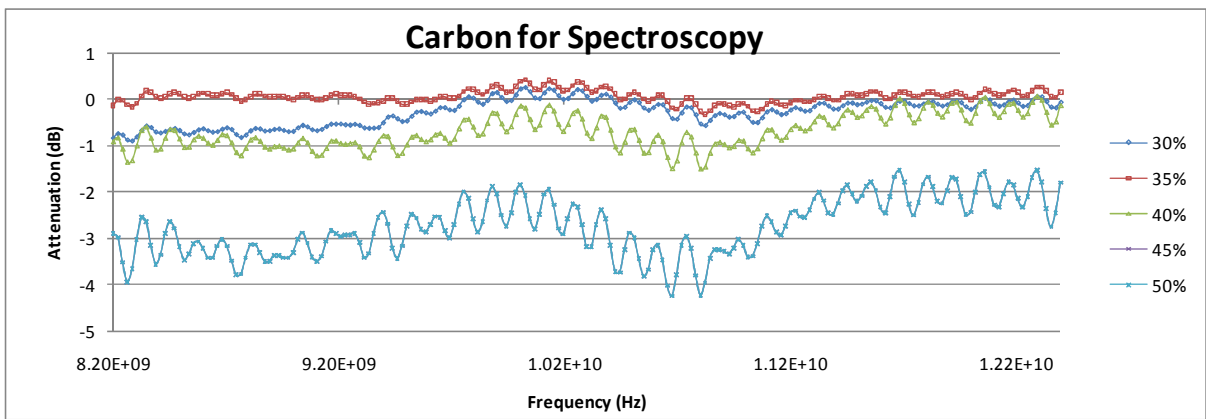
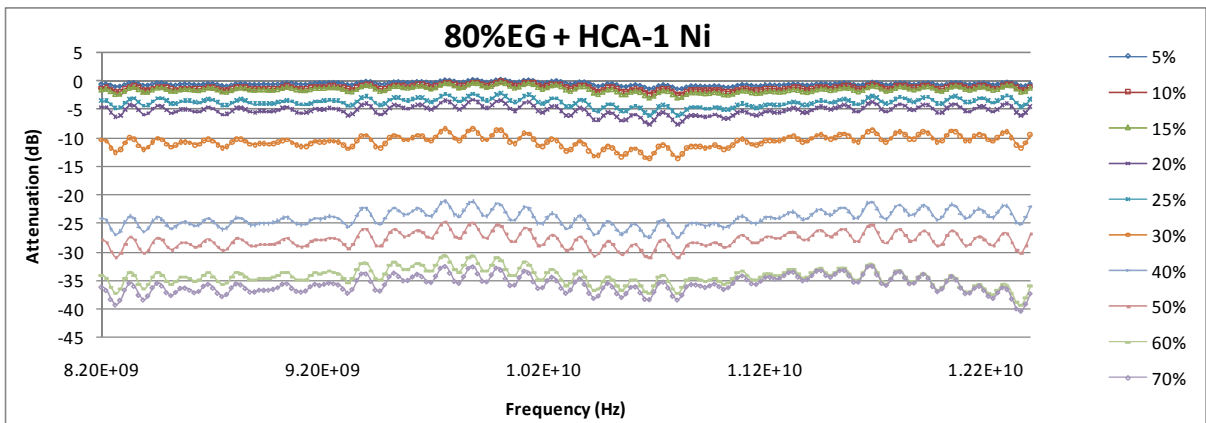
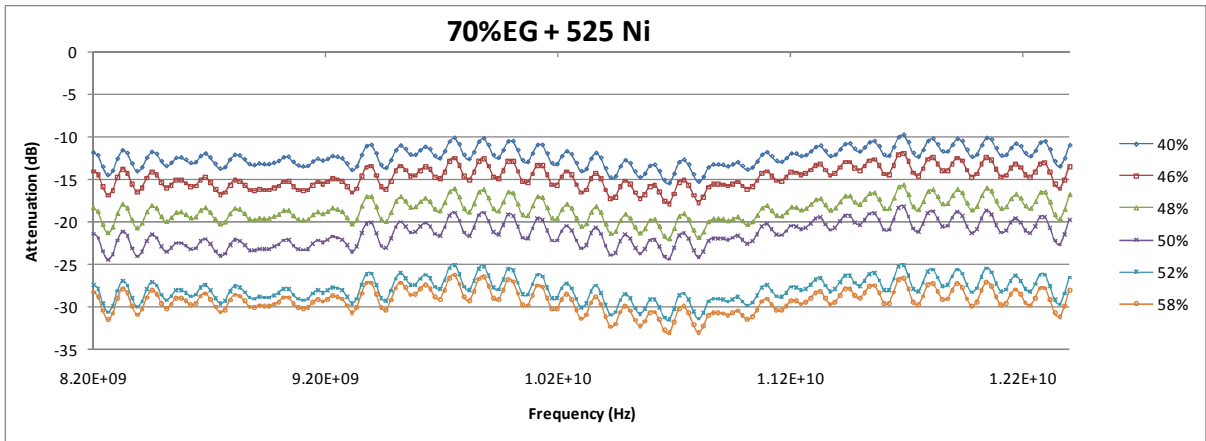


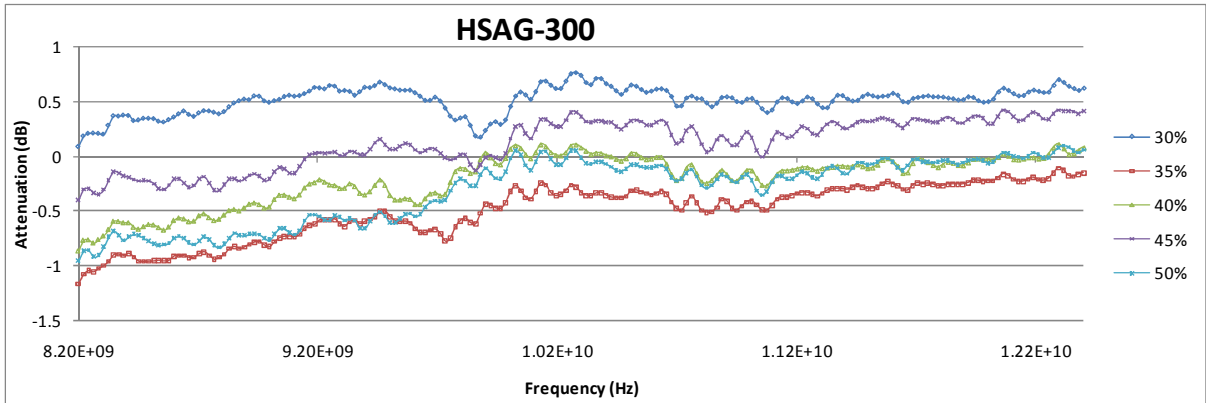
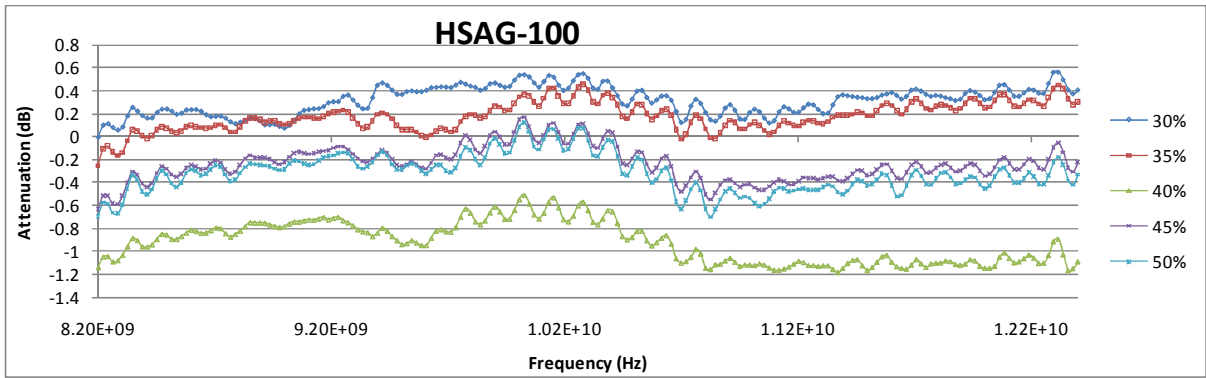




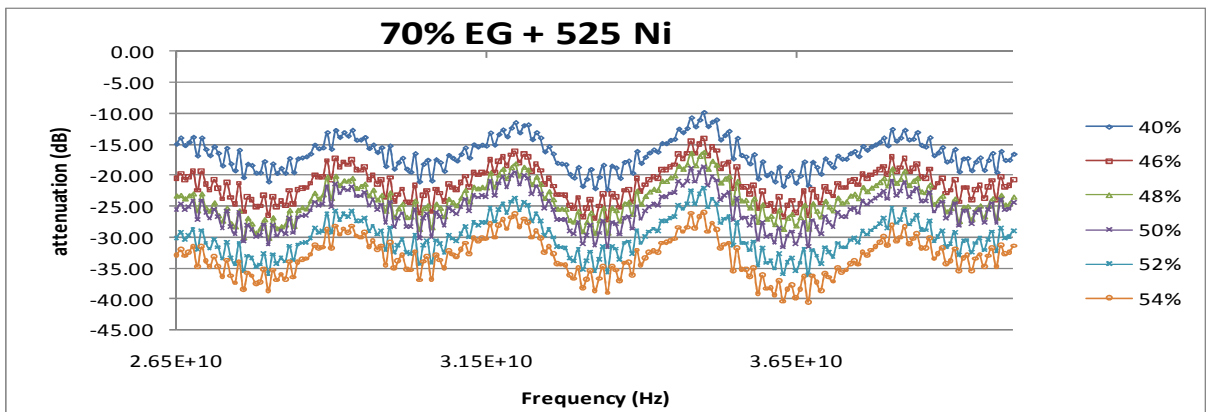
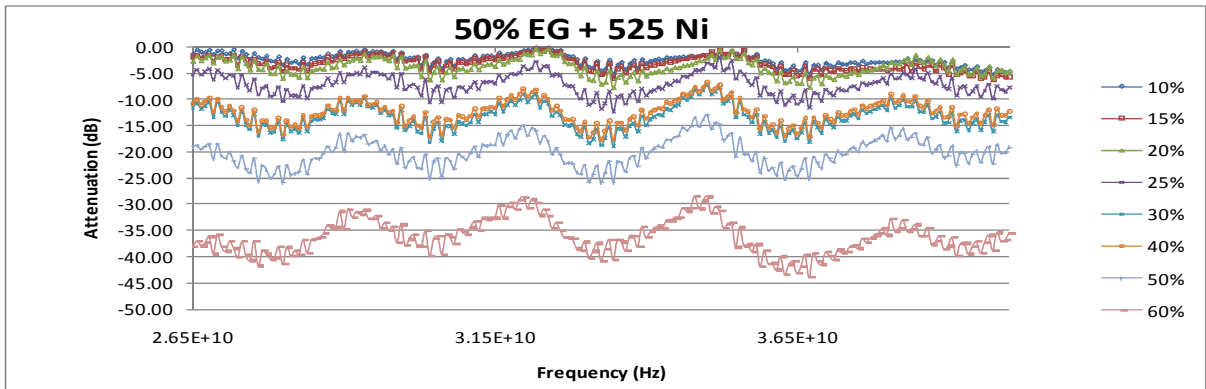
X-Band

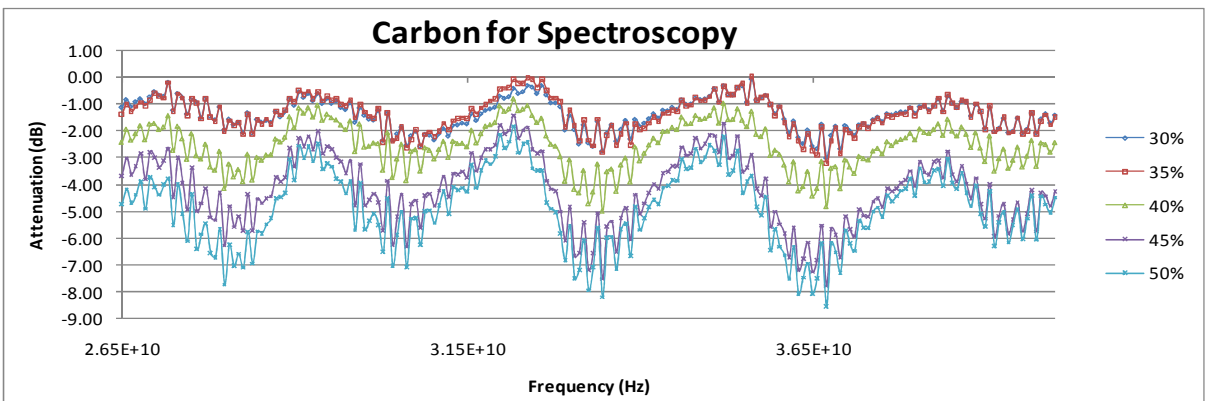
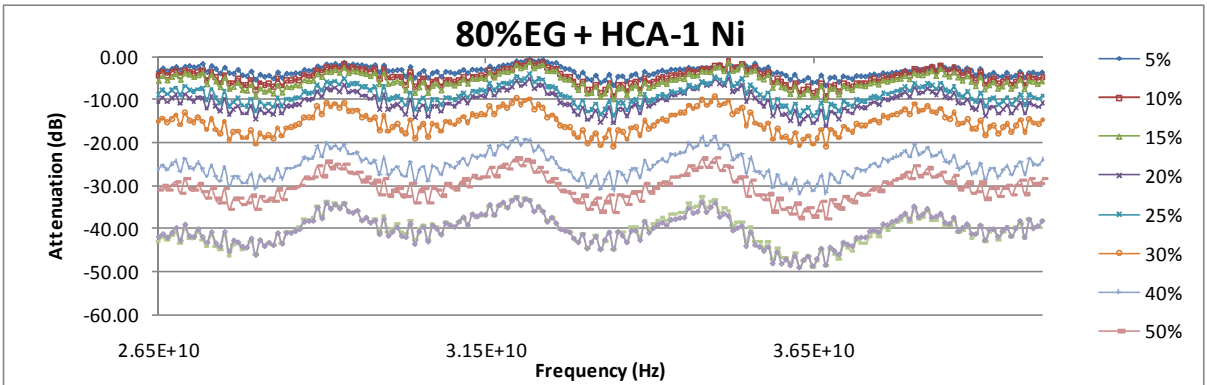
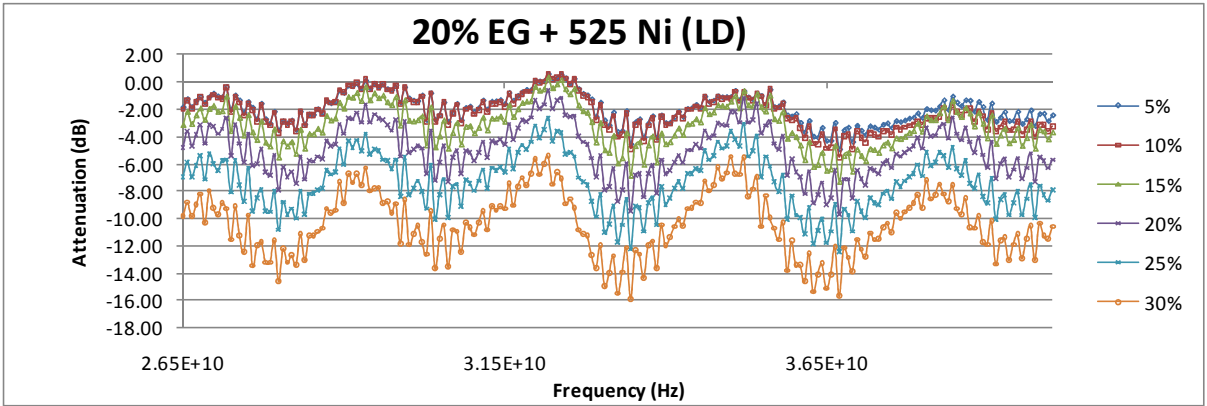
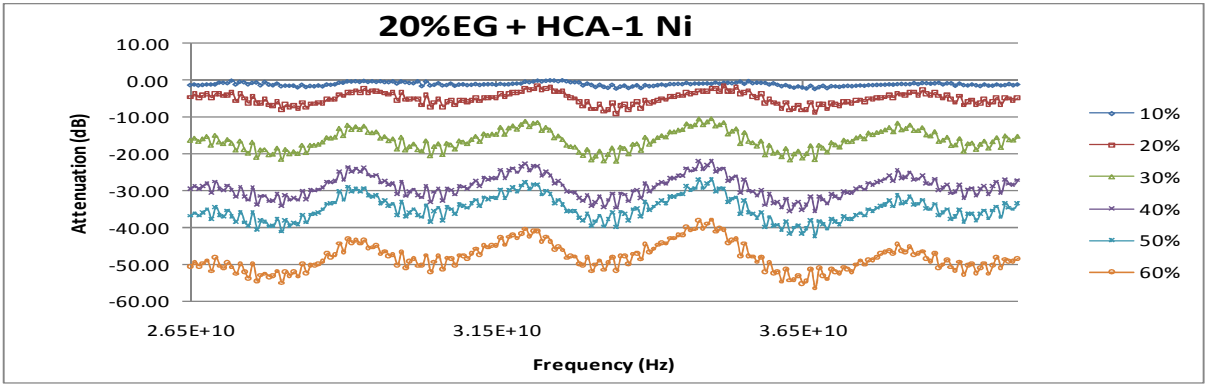


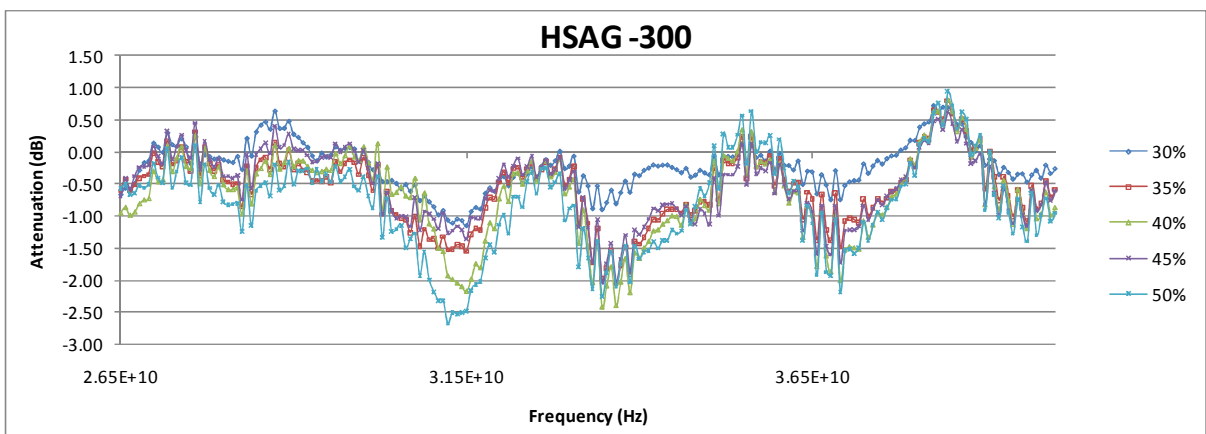
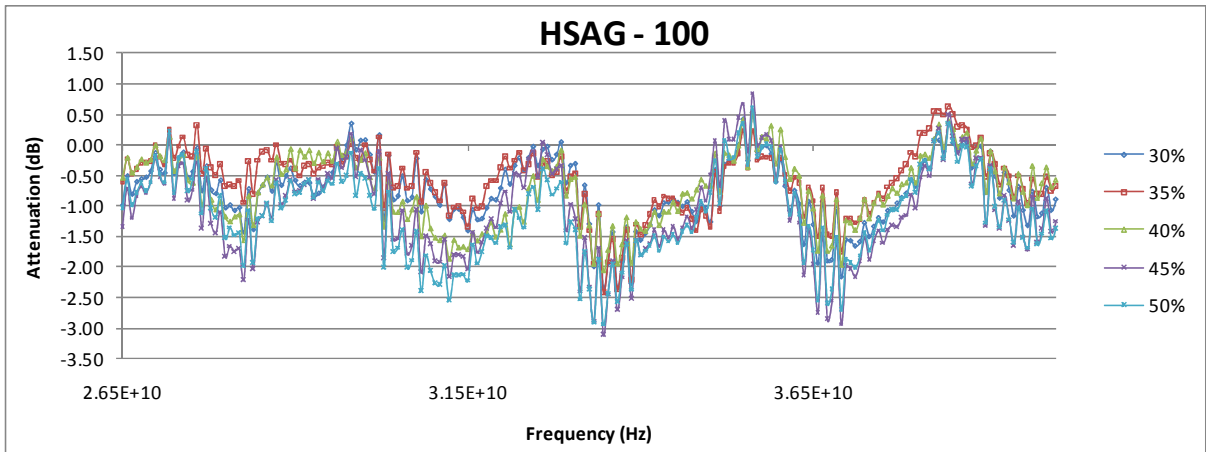




Q-Band

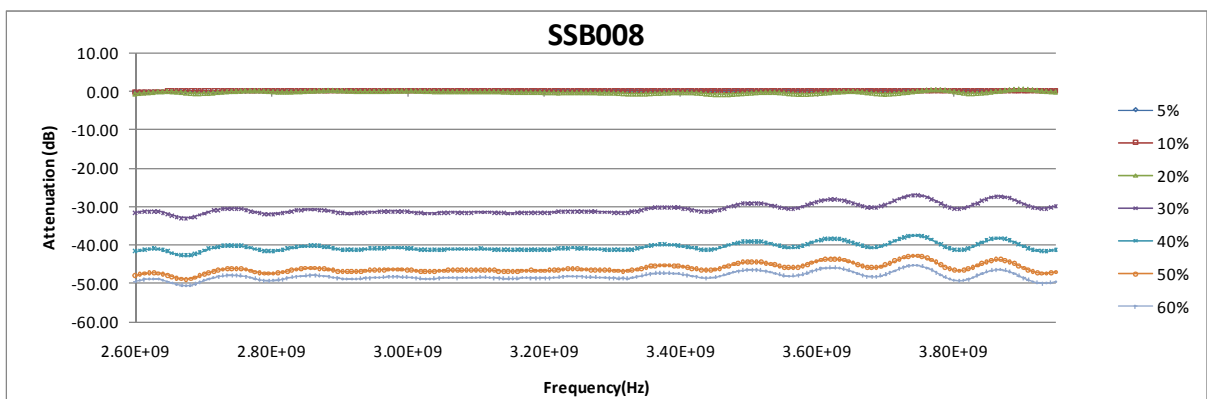
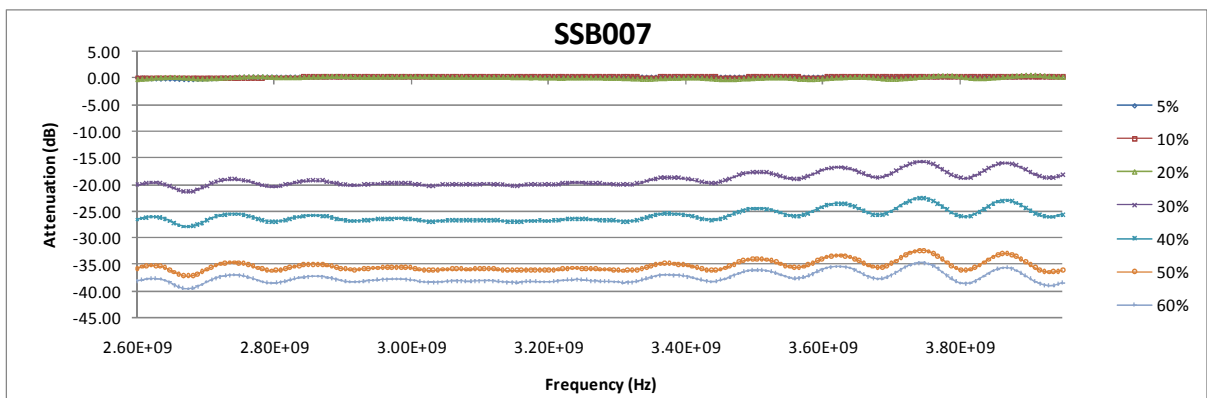
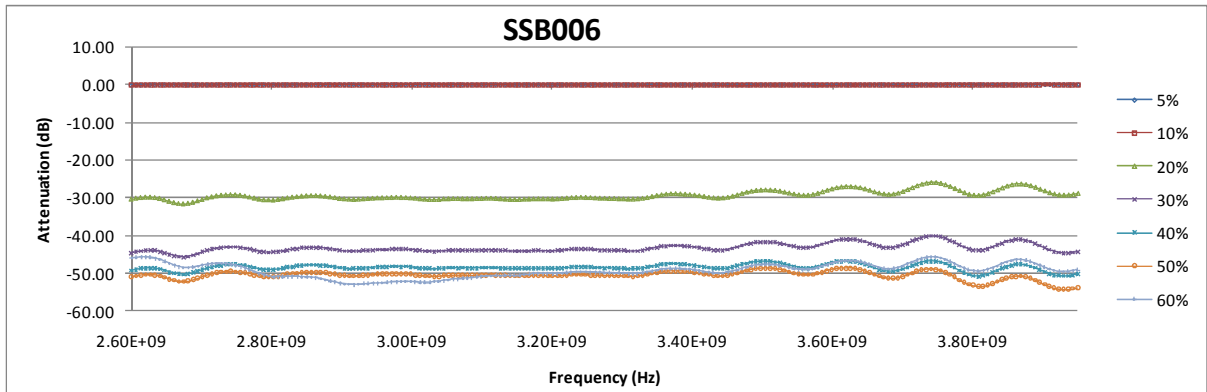


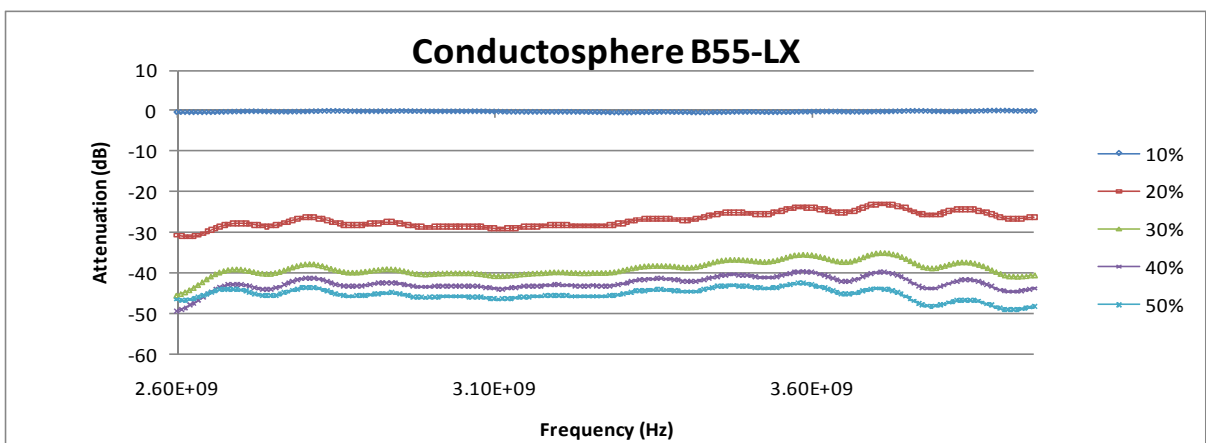
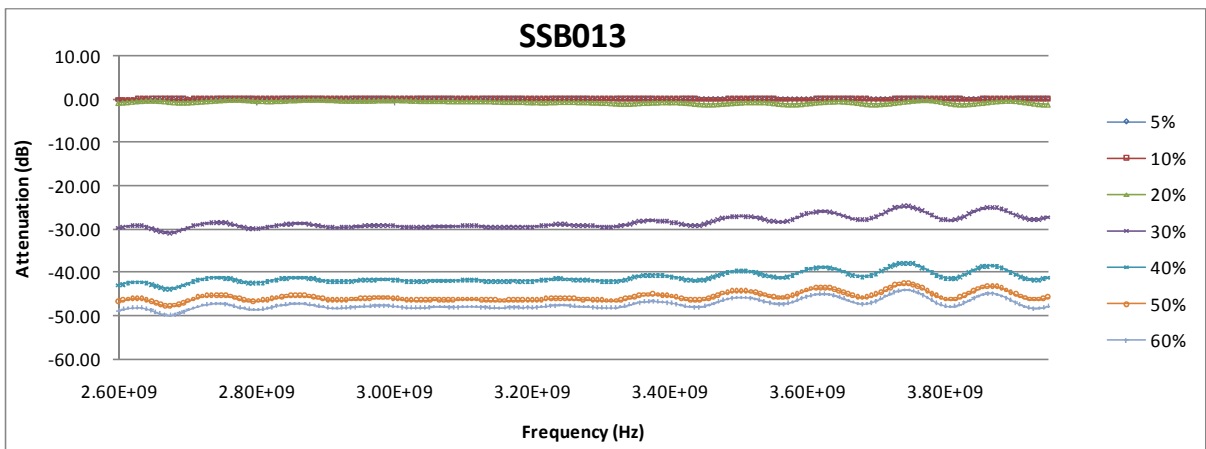
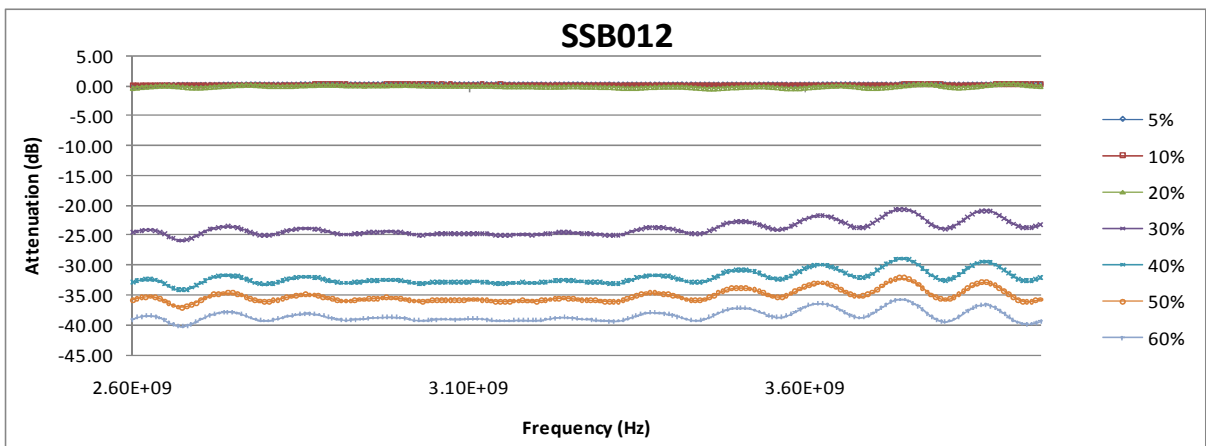
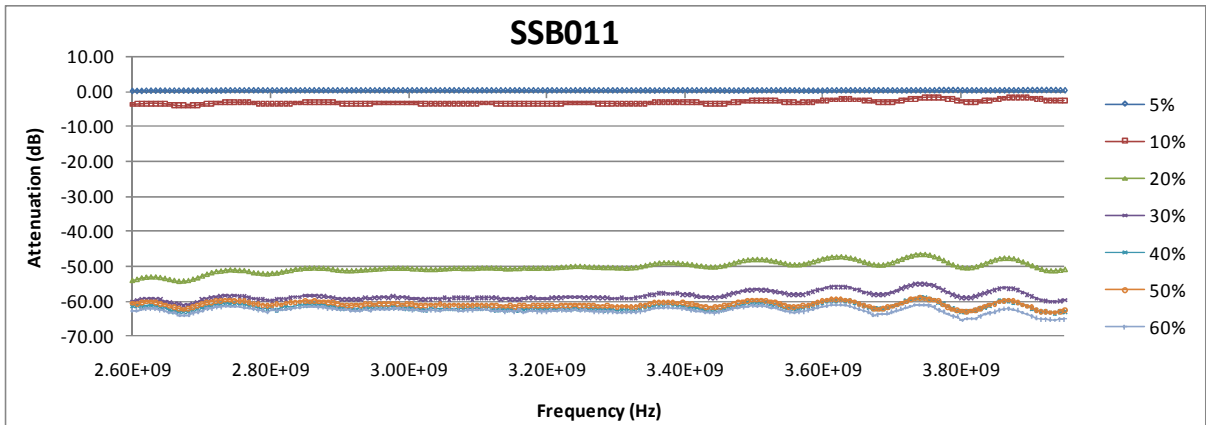


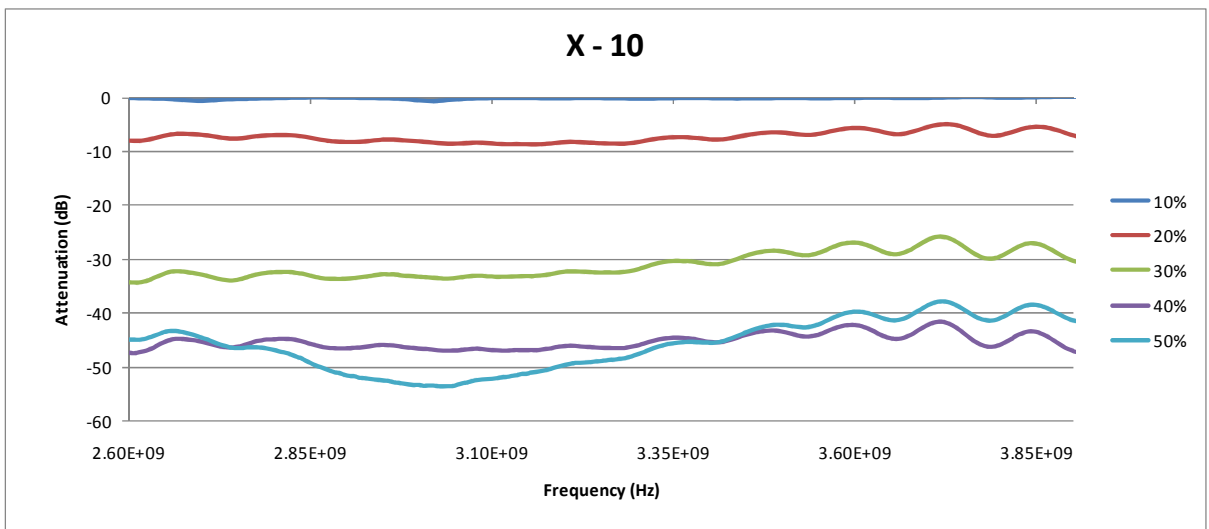
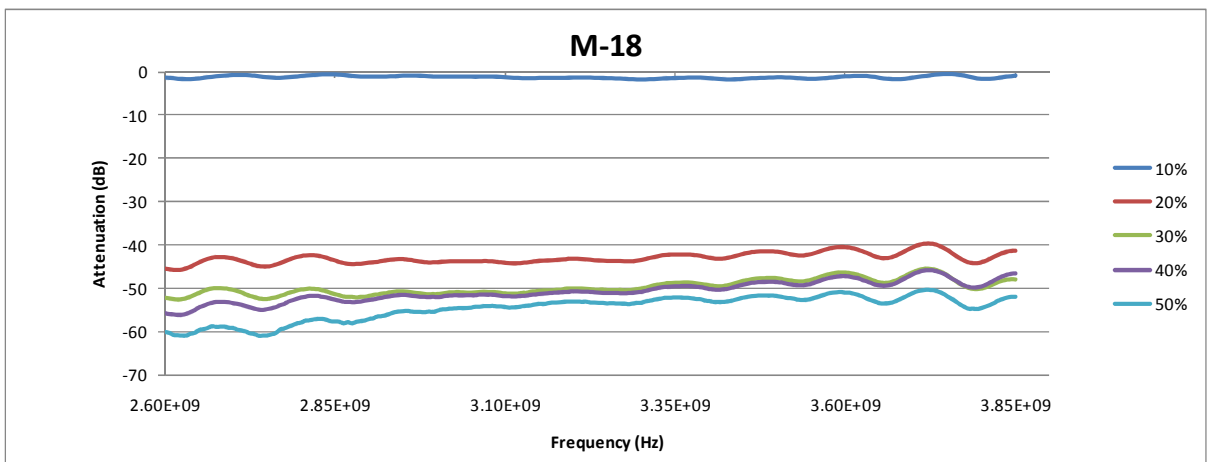
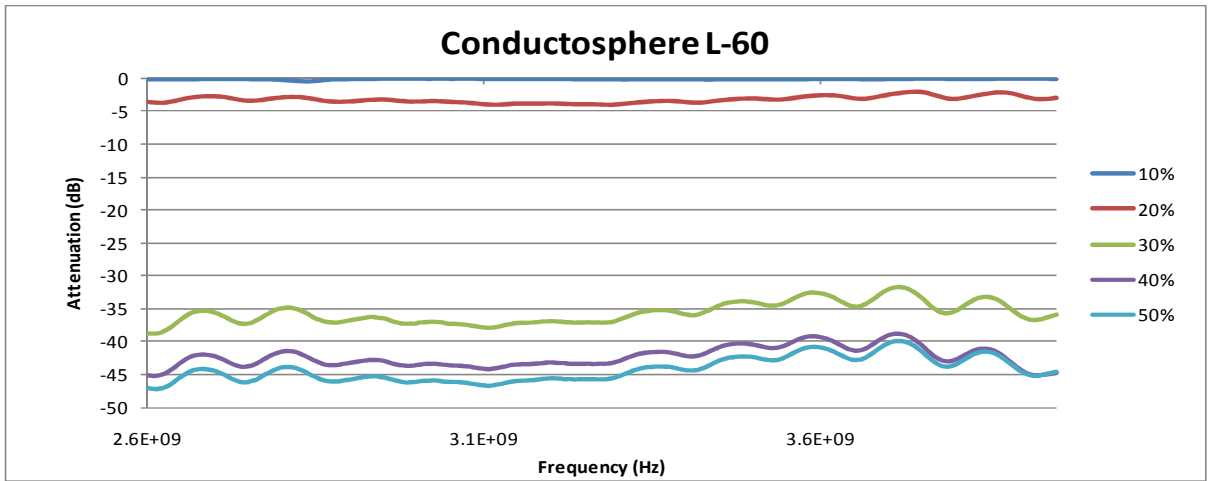


Microsphere

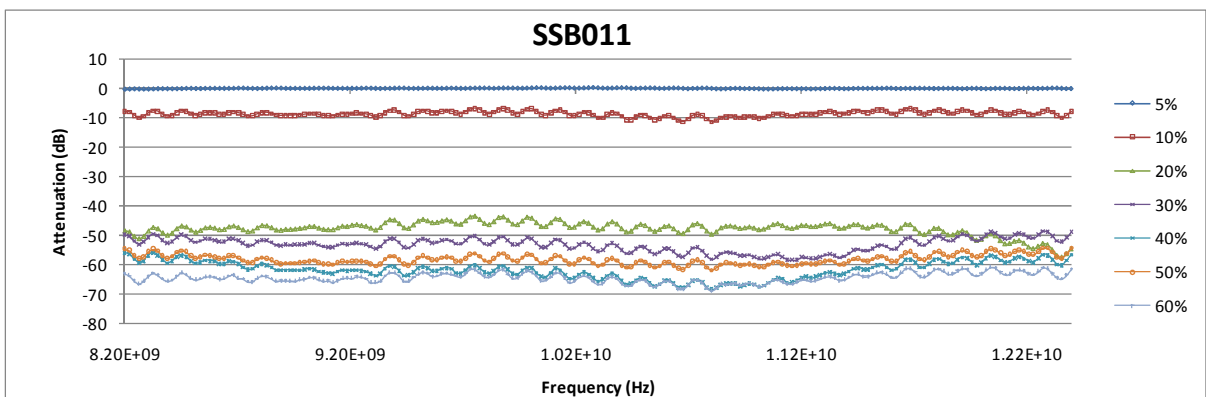
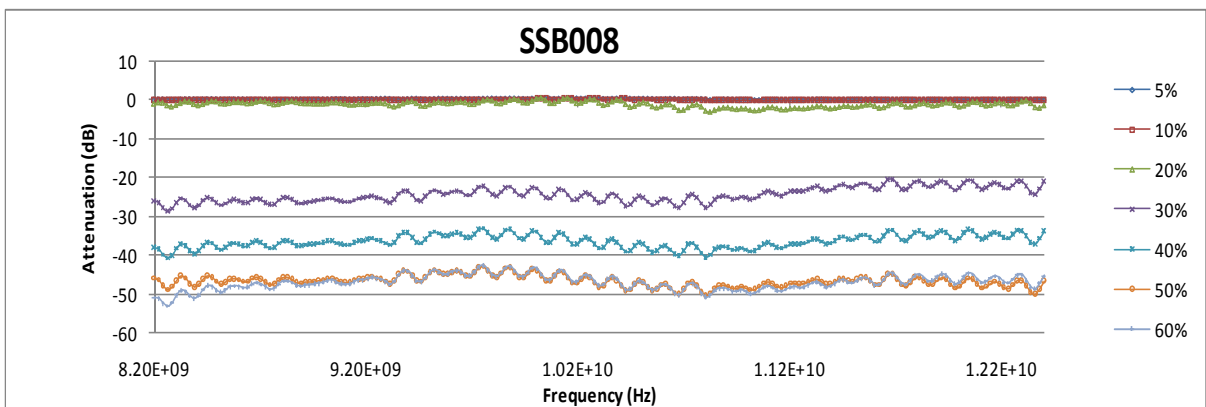
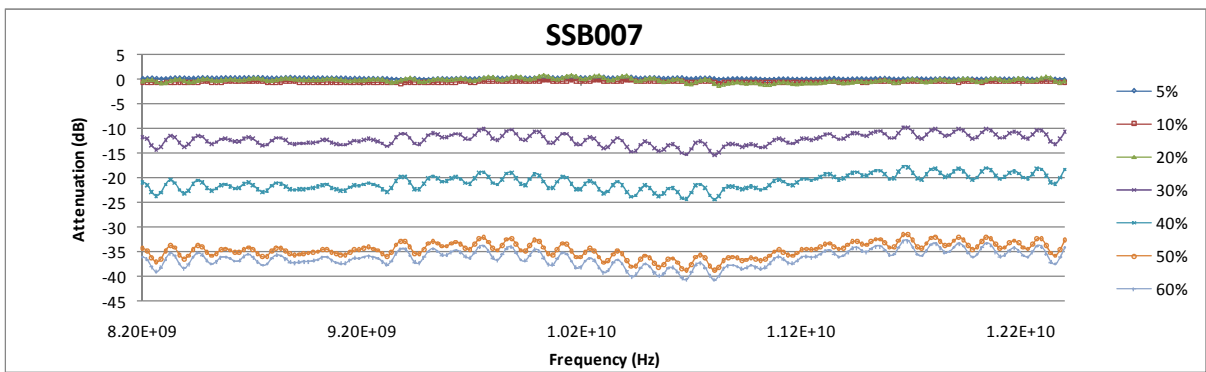
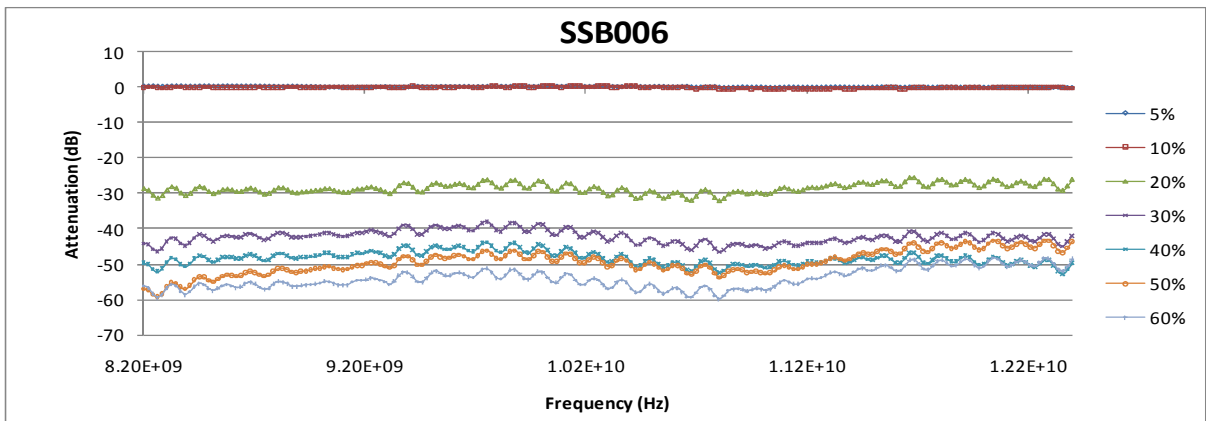
S-Band

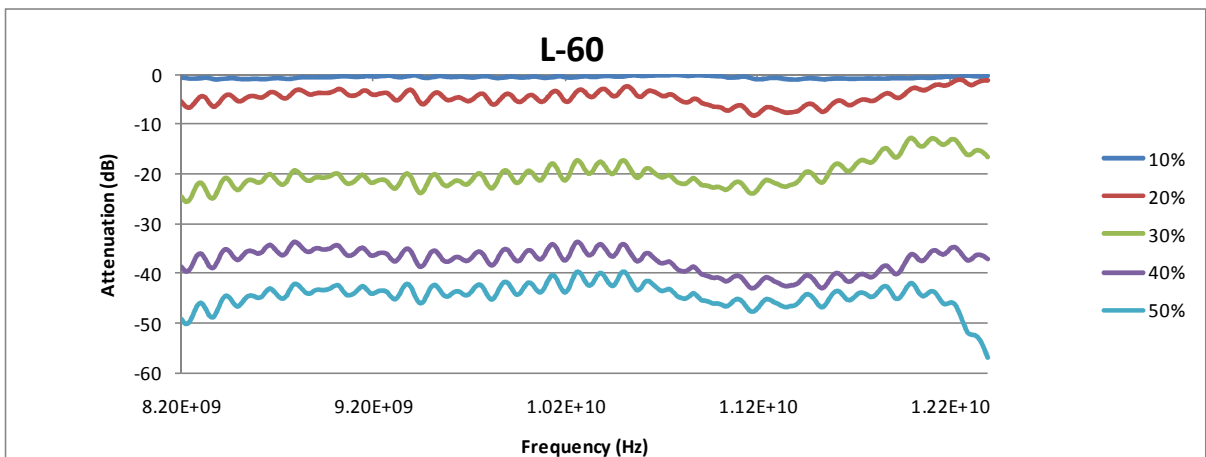
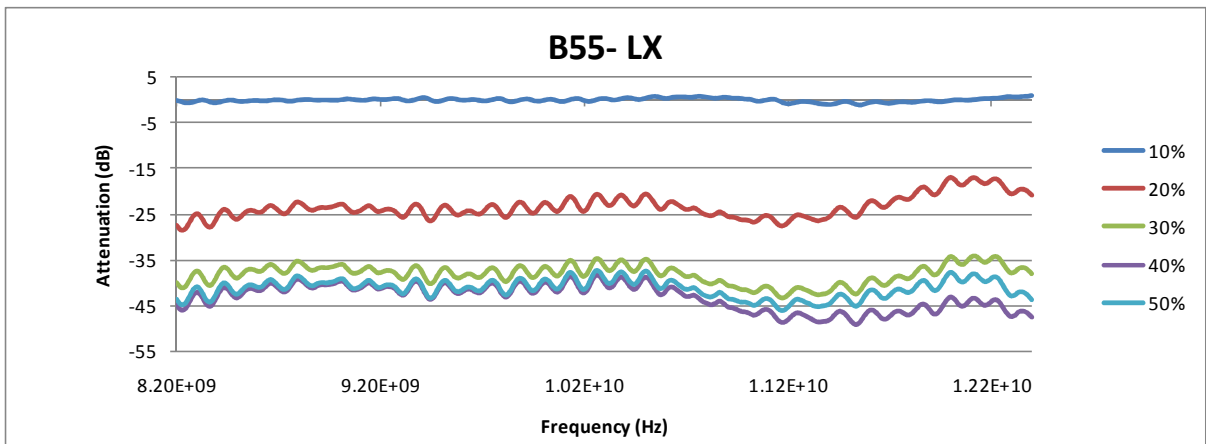
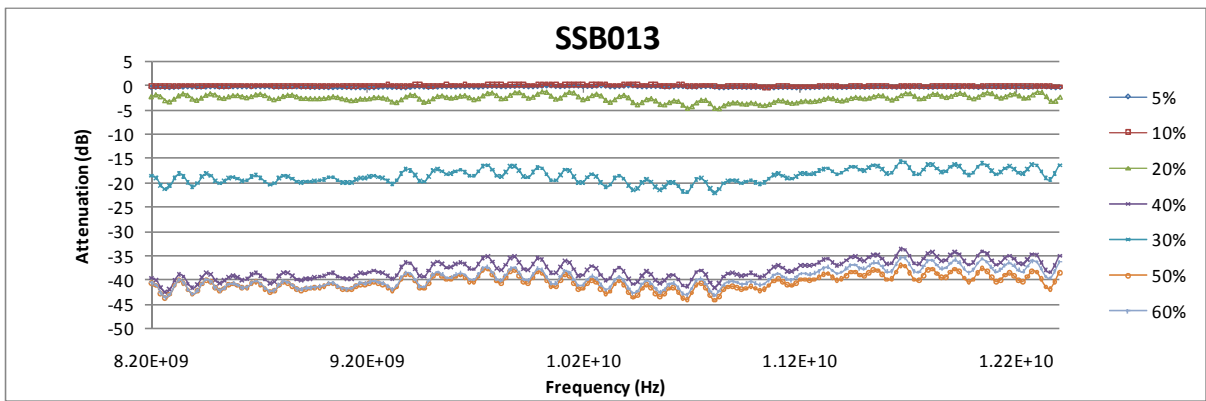
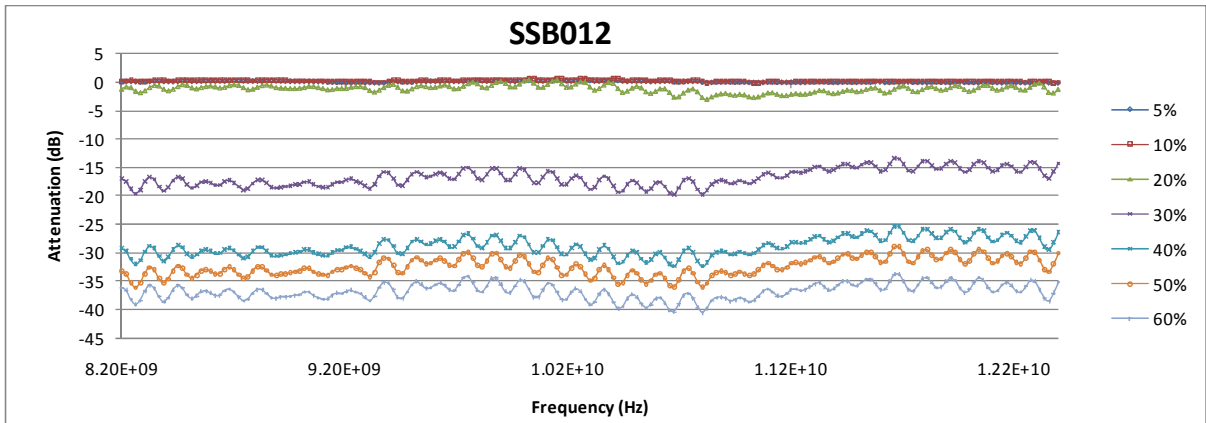


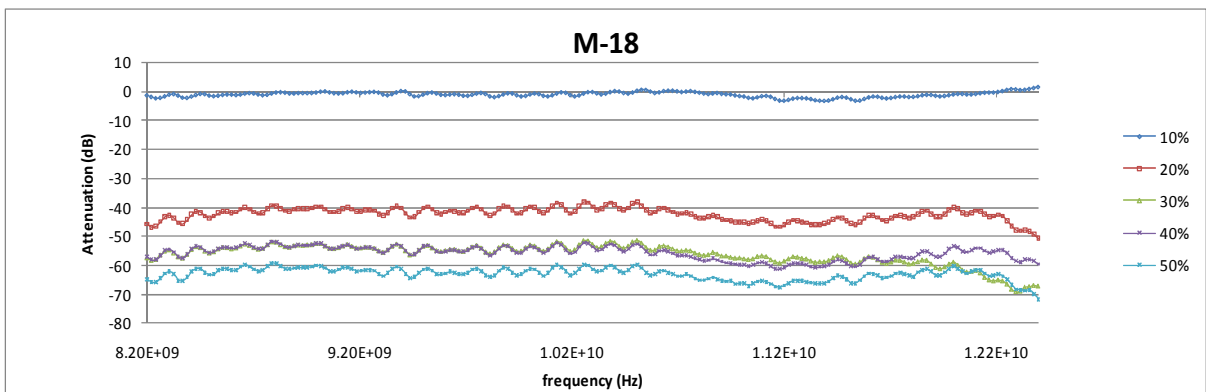
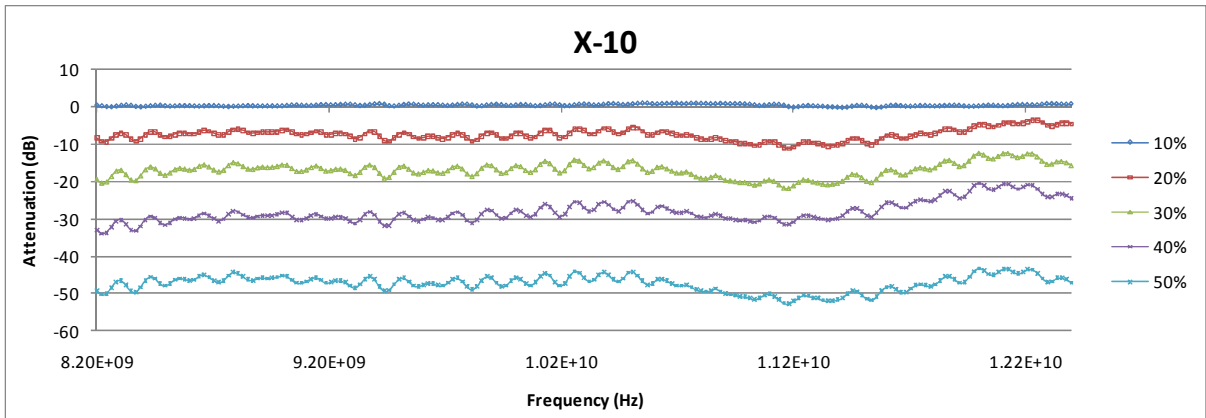




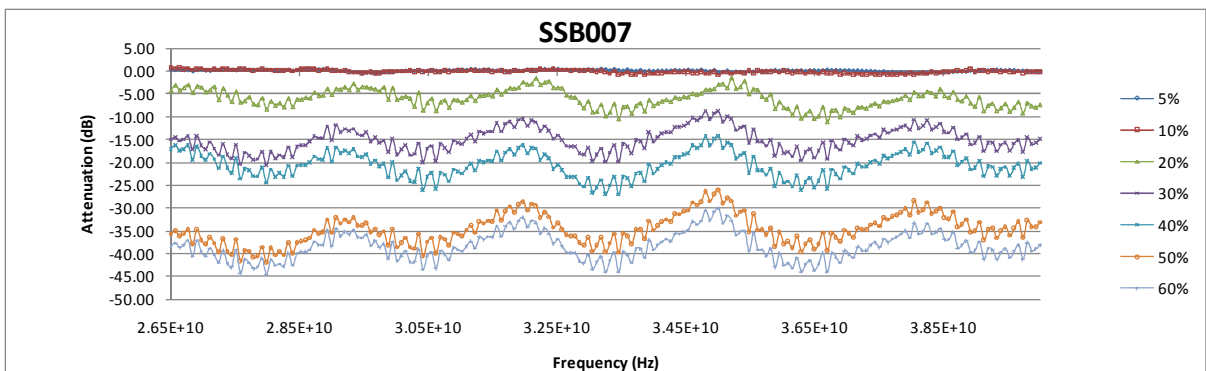
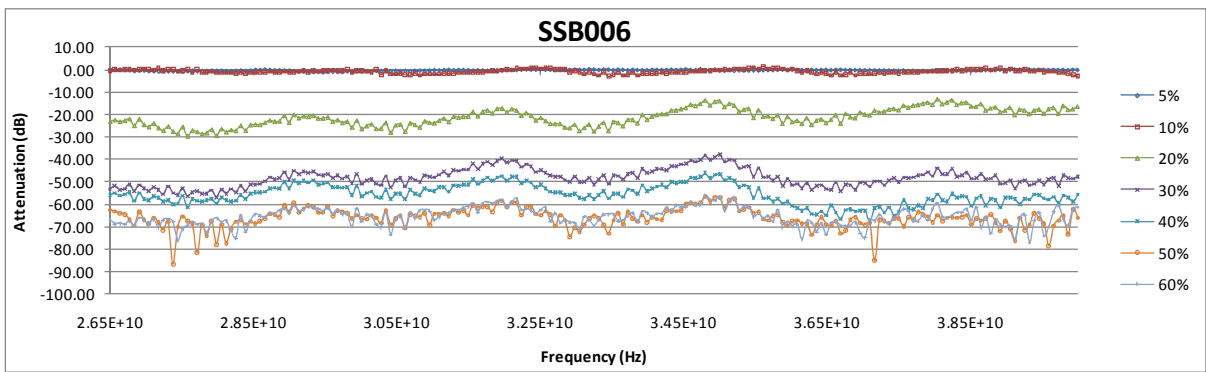
X-Band

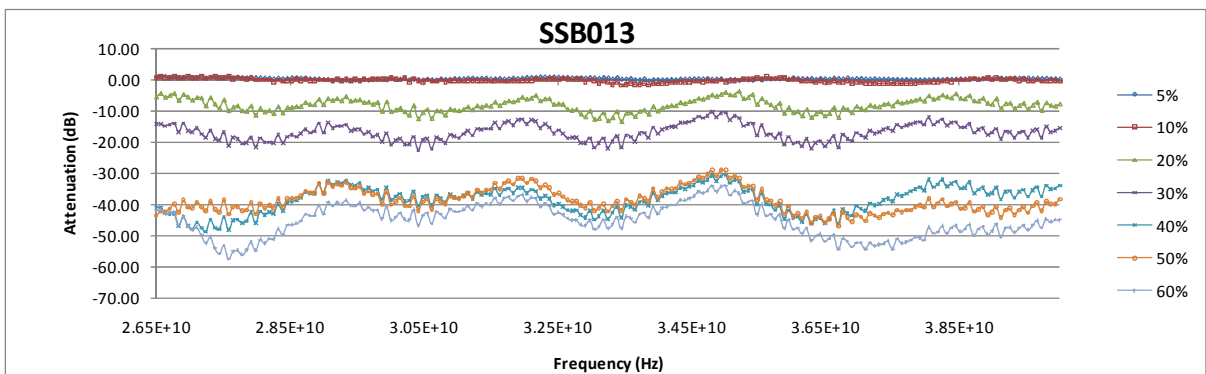
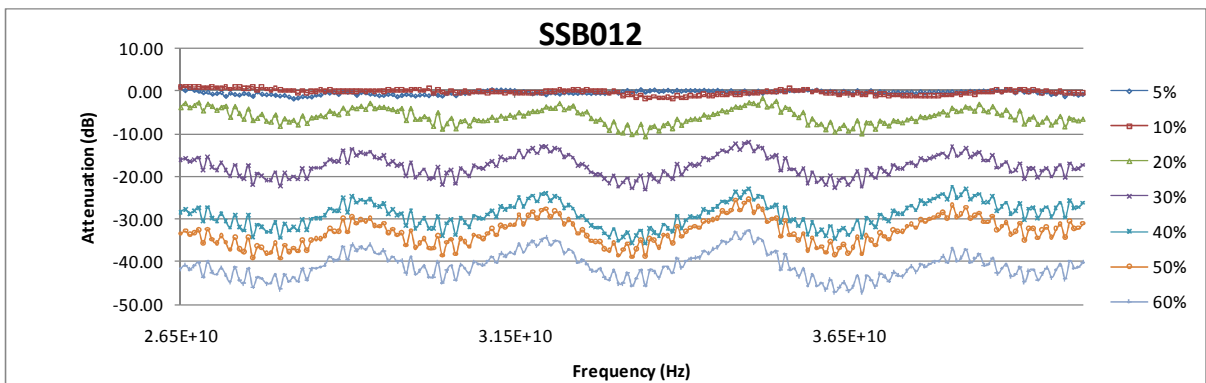
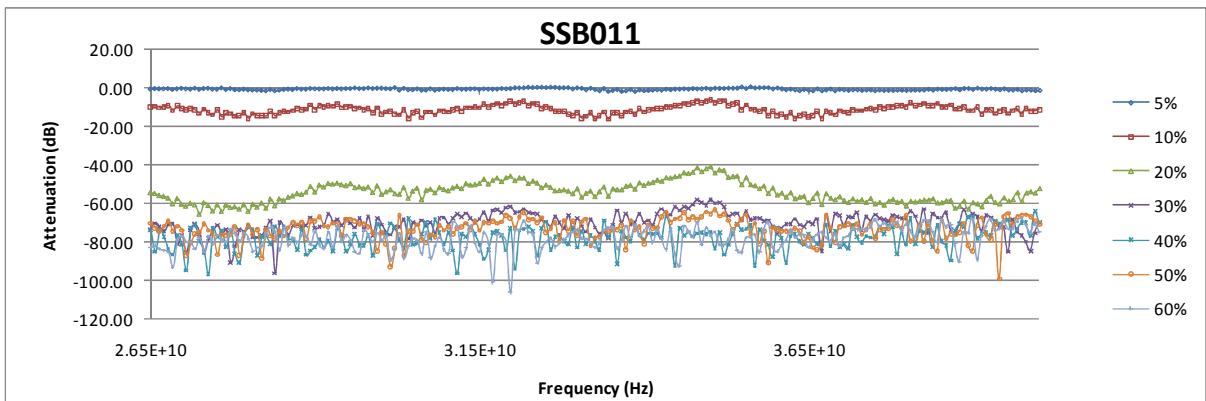
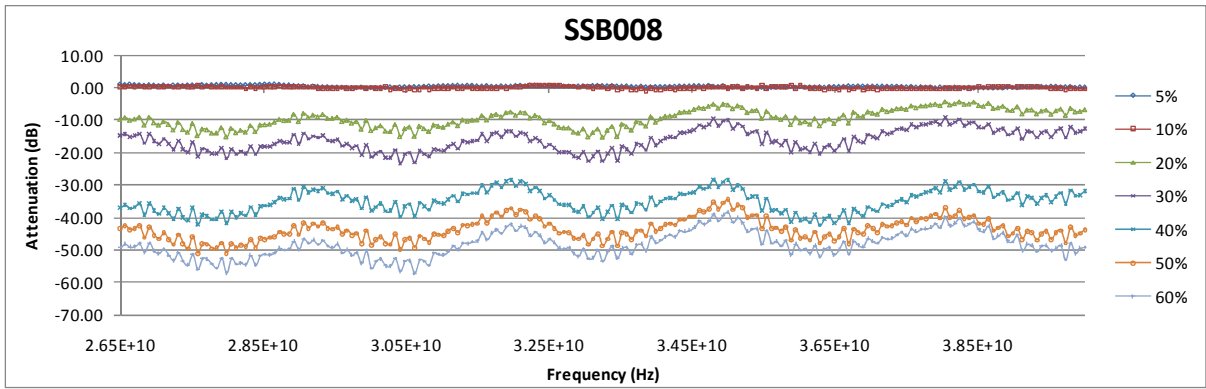


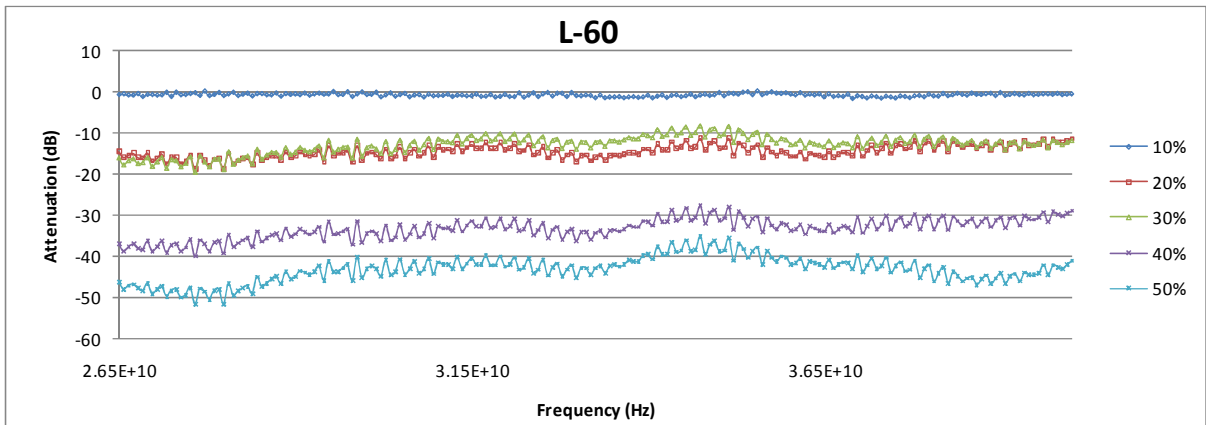
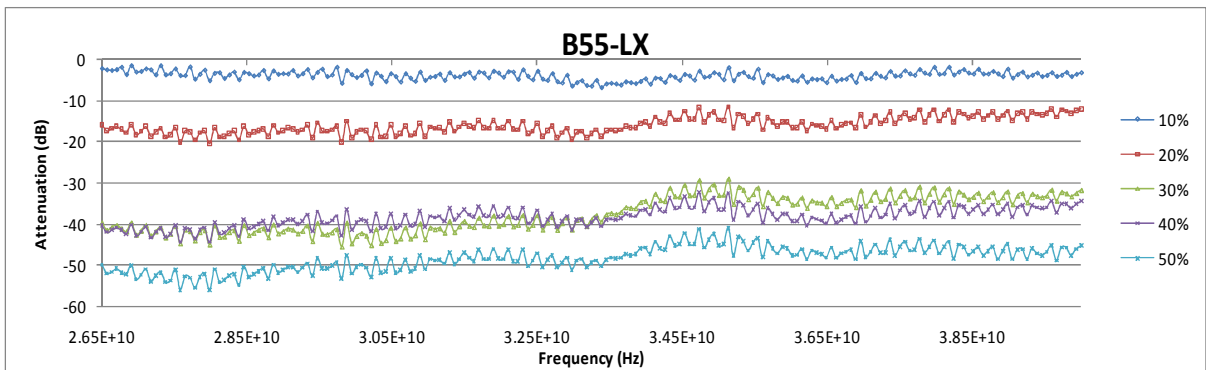
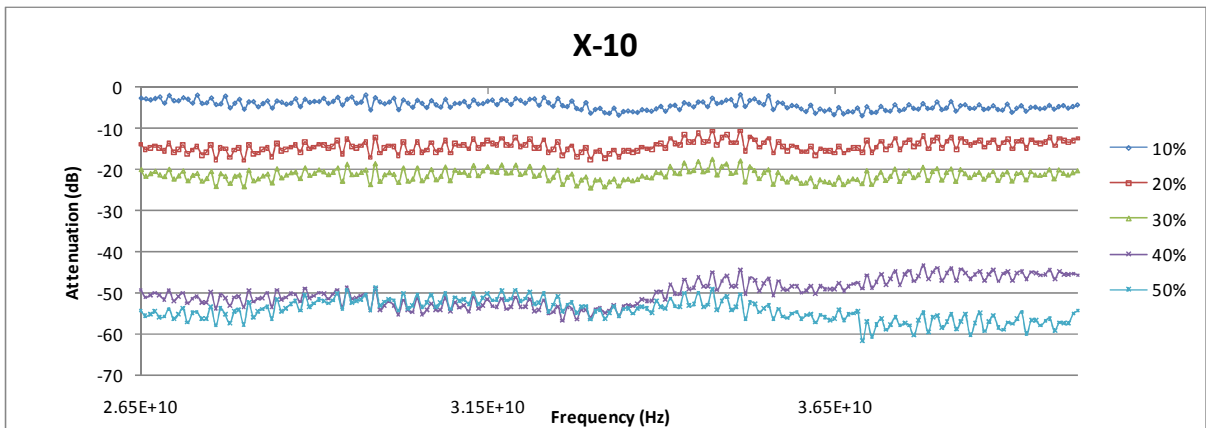
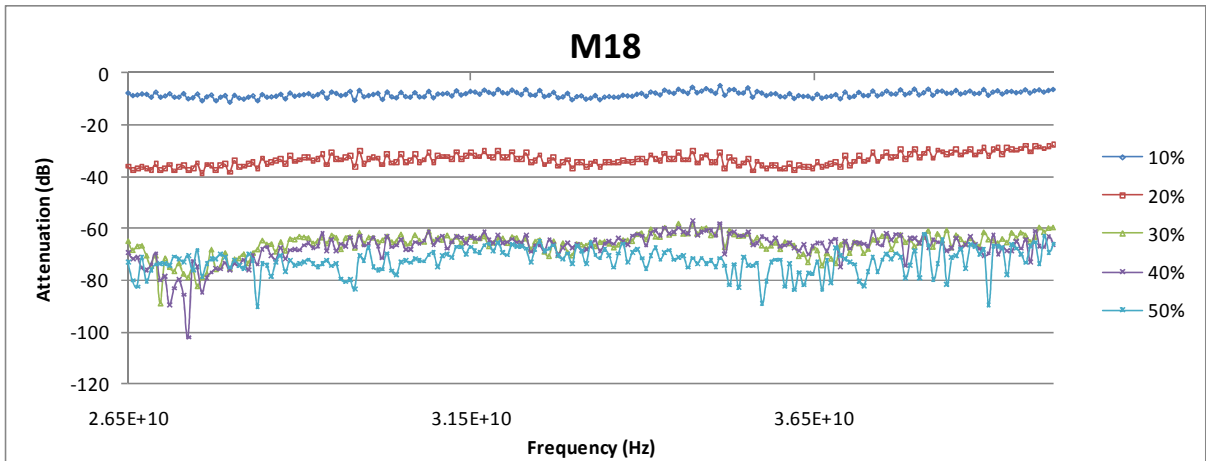




Q-Band

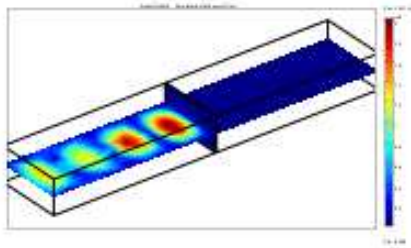






15 Appendix D – Comsol Multiphysics Model Report

Comsol Multiphysics Model Report



1. Table of Contents

- Title - COMSOL Model Report
- Table of Contents
- Model Properties
- Geometry
- Geom1
- Geom2
- Materials/Coefficients Library
- Solver Settings
- Postprocessing
- Variables

2. Model Properties

Property	Value
Model name	
Author	
Company	
Department	
Reference	
URL	
Saved date	Mar 8, 2010 5:54:46 PM
Creation date	Mar 3, 2010 11:29:05 AM
COMSOL version	COMSOL 3.5.0.494

File name: C:\Users\JRS-1\Documents\PhD\Comsol Models for thesis\Q-Band without SMA.mph

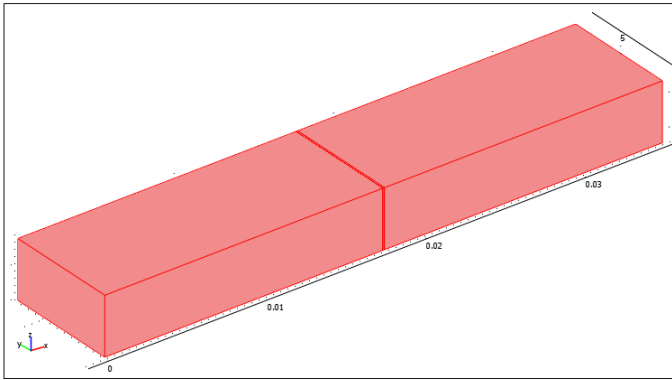
Application modes and modules used in this model:

- Geom1 (3D)
 - Electromagnetic Waves (RF Module)
- Geom2 (2D)

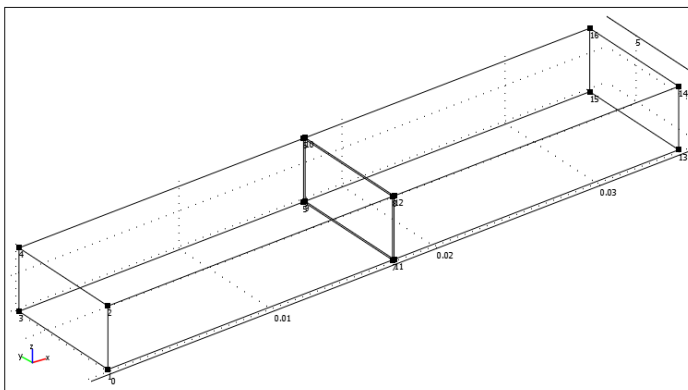
3. Geometry

Number of geometries: 2

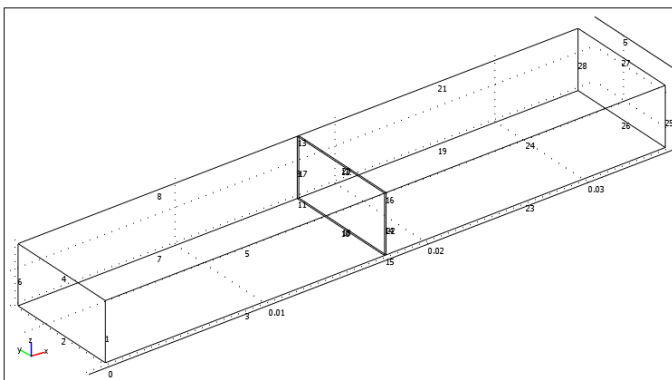
3.1. Geom1



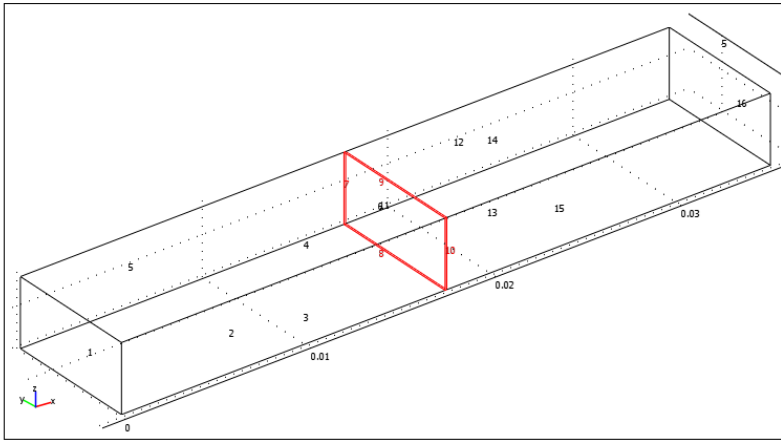
3.1.1. Point mode



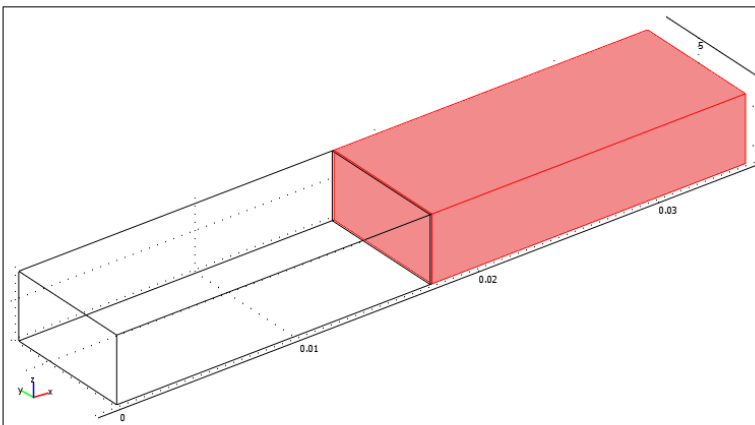
3.1.2. Edge mode



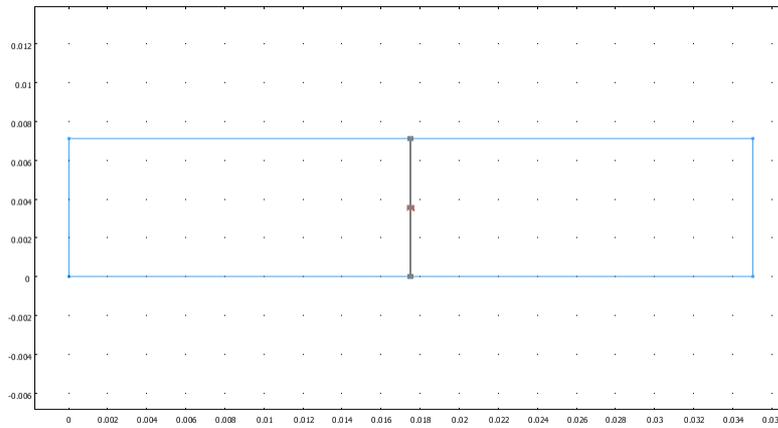
3.1.3. Boundary mode



3.1.4. Subdomain mode



3.2. Geom2



4. Geom1

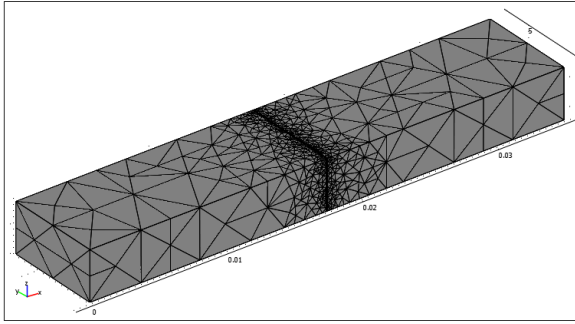
Space dimensions: 3D

Independent variables: x, y, z

4.1. Mesh

4.1.1. Mesh Statistics

Number of degrees of freedom	252302
Number of mesh points	7475
Number of elements	38859
Tetrahedral	38859
Prism	0
Hexahedral	0
Number of boundary elements	5784
Triangular	5784
Quadrilateral	0
Number of edge elements	324
Number of vertex elements	16
Minimum element quality	0.181
Element volume ratio	0



4.2. Application Mode: Electromagnetic Waves (rfw)

Application mode type: Electromagnetic Waves (RF Module)

Application mode name: rfw

4.2.1. Scalar Variables

Name	Variable	Value	Unit	Description
epsilon0	epsilon0_rfw	8.854187817e-12	F/m	Permittivity of vacuum
mu0	mu0_rfw	4*pi*1e-7	H/m	Permeability of vacuum
nu	nu_rfw	Freq	Hz	Frequency
E0ix	E0ix_rfw	exp(-j*k0_rfw*z)	V/m	Incident electric field, x component
E0iy	E0iy_rfw	0	V/m	Incident electric field, y component
E0iz	E0iz_rfw	0	V/m	Incident electric field, z component
psi0	psi0_rfw	psi0_guess_rfw	V/m^2	Gauge fixing variable scaling

4.2.2. Application Mode Properties

Property	Value
Default element type	Vector - Quadratic
Analysis type	Harmonic propagation
Solve for	Electric field
Specify wave using	Frequency
Specify eigenvalues using	Eigenfrequency
Divergence condition	Off
Frame	Frame (ref)
Weak constraints	Off
Constraint type	Ideal

4.2.3. Variables

Dependent variables: Ex, Ey, Ez, Hx, Hy, Hz, Ax, Ay, Az, scEx, scEy, scEz, scHx, scHy, scHz, psi

Shape functions: shcurl(2,{'Ex','Ey','Ez'}), shlag(2,'psi')

Interior boundaries not active

4.2.4. Boundary Settings

Boundary	2-5, 12-15	1	16
----------	------------	---	----

Type		Perfect electric conductor	Port	Port
Port number (portnr)	1	1	1	2
inport		0	1	0
modespec		User defined	Rectangular	Rectangular
Boundary		7-10		
Type		Perfect magnetic conductor		
Port number (portnr)	1	1		
inport		0		
modespec		User defined		

4.2.5. Subdomain Settings

Subdomain		1, 3	2
Electric conductivity (sigma)	S/m	{0,0,0;0,0,0;0,0,0}	{2705,0,0;0,2705,0;0,0,2705}

5. Geom2

Space dimensions: 2D

Independent variables: x, y, z

6. Materials/Coefficients Library

6.1. Nickel

Parameter	Value
Heat capacity at constant pressure (C)	C_solid_1(T[1/K])[J/(kg*K)]
Instantaneous coefficient of thermal expansion (CTE)	CTE(T[1/K])[1/K]
Young's modulus (E)	E(T[1/K])[Pa]
Molar heat capacity (HC)	HC_solid_1(T[1/K])[J/(mol*K)]
Yield stress level (Sys)	Sys_solid_40_reduction_in_area_by_cold_drawing_2(T[1/K])[Pa]
Tensile strength (Syt)	Syt_solid_40_reduction_in_area_by_cold_drawing_2(T[1/K])[Pa]
Thermal diffusivity (TD)	TD(T[1/K])[m^2/s]
Vapor pressure (VP)	VP_solid_1(T[1/K])[Pa]
Thermal expansion coeff. (alpha)	alpha_solid_1(T[1/K])[1/K]+(Tempref-293[K])/(T-Tempref)*(alpha_solid_1(T[1/K])[1/K]-alpha_solid_1(Tempref[1/K])[1/K])
Linear expansion (dL)	dL_solid_1(T[1/K])-dL_solid_1(Tempref[1/K])
Elongation (elong)	elong_solid_40_reduction_in_area_by_cold_drawing_2(T[1/K])
Surface emissivity (epsilon)	epsilon(T[1/K])
Dynamic viscosity (eta)	eta(T[1/K])[Pa*s]
Thermal conductivity (k)	k_solid_1(T[1/K])[W/(m*K)]
Initial bulk modulus (hyperelastic material) (kappa)	kappa(T[1/K])[Pa]
Initial shear modulus (hyperelastic material) (mu)	mu(T[1/K])[Pa]
Poisson's ratio (nu)	nu(T[1/K])
Electric resistivity (res)	res(T[1/K])[ohm*m]
Density (rho)	rho_solid_1(T[1/K])[kg/m^3]
Electric conductivity	sigma(T[1/K])[S/m]

(sigma)

6.1.1. Piecewise Analytic Functions

6.1.1.1. Function: dL_solid_1(T)

Type: Polynomial

x_{start}	x_{end}	$f(x)$
81.0	1173.0	0 -0.002789643 1 7.14274E-6 2 4.576494E-9 3 1.933928E-11 4 -2.795727E-14 5 1.089338E-17

6.1.1.2. Function: dL_liquid_2(T)

Type: Polynomial

x_{start}	x_{end}	$f(x)$
1728.0	2370.0	0 -0.04761756 1 2.394001E-5 2 2.092851E-9

6.1.1.3. Function: CTE(T)

Type: Polynomial

x_{start}	x_{end}	$f(x)$
50.0	350.0	0 -5.87011E-6 1 1.938799E-7 2 -8.26993E-10 3 1.664025E-12 4 -1.249417E-15
350.0	635.0	0 3.858532E-6 1 5.641275E-8 2 -1.218844E-10 3 1.07478E-13
635.0	650.0	0 7.005974E-4 1 -2.020734E-6 2 1.489546E-9
650.0	800.0	0 4.61122E-5 1 -7.991209E-8 2 5.274725E-11

6.1.1.4. Function: k_solid_1(T)

Type: Polynomial

x_{start}	x_{end}	$f(x)$
0.0	18.0	1 214.0436 2 2.199849 3 -0.4089829 4 -0.02700268 5 0.001304208
18.0	30.0	0 -5208.712 1 1431.939 2 -103.9216 3 3.410781 4 -0.05321568 5 3.189215E-4
30.0	90.0	0 3817.001 1 -161.048 2 2.761625 3 -0.02121476 4 6.040699E-5
90.0	223.0	0 700.7063 1 -11.21132 2 0.08276592 3 -2.776075E-4 4 3.493035E-7
223.0	630.0	0 185.3755 1 -0.6437058 2 0.00164864 3 -2.193597E-6 4 1.131921E-9
630.0	1500.0	0 50.42098 1 0.02143115

6.1.1.5. Function: k_liquid_2(T)

Type: Polynomial

x_{start}	x_{end}	$f(x)$
1723.0	3000.0	0 5.62102 1 0.03270527 2 -2.541548E-6

6.1.1.6. Function: E(T)

Type: Polynomial

x_{start}	x_{end}	$f(x)$
0.0	773.0	0 2.198604E11 1 -4.976173E7 2 -6940.452

773.0	1323.0	0	3.675636E11	1	-5.264939E8	2	511021.8	3	-191.9755
--------------	--------	---	-------------	---	-------------	---	----------	---	-----------

6.1.1.7. Function: res(T)

Type: Polynomial

X_{start}	X_{end}	f(x)							
100.0	633.0	0	-3.610912E-8	1	5.575728E-10	2	-1.189788E-12	3	1.811005E-15
633.0	800.0	0	5.696199E-8	1	4.544983E-10	2	-1.128754E-13		

6.1.1.8. Function: epsilon(T)

Type: Polynomial

X_{start}	X_{end}	f(x)							
245.0	1093.0	0	0.05021919	1	2.137239E-4	2	-2.976342E-7	3	1.846619E-10

6.1.1.9. Function: Syt_solid_annealed_1(T)

Type: Polynomial

X_{start}	X_{end}	f(x)									
77.0	644.0	0	7.215399E8	1	-2463963.0	2	5666.31	3	-5.387338	4	0.001198245
644.0	1088.0	0	6.106184E8	1	-477284.4	2	-235.4998	3	0.1737128		

6.1.1.10. Function: Syt_solid_40_reduction_in_area_by_cold_drawing_2(T)

Type: Polynomial

X_{start}	X_{end}	f(x)									
293.0	922.0	0	4.1792E8	1	1573711.0	2	-5397.305	3	6.871309	4	-0.003530385
922.0	1200.0	0	1.17785E9	1	-1804915.0	2	707.427				

6.1.1.11. Function: elong_solid_annealed_1(T)

Type: Polynomial

X_{start}	X_{end}	f(x)									
77.0	1088.0	0	80.39804	1	-0.134346	2	1.823587E-4	3	-1.545278E-8	4	-3.859654E-11

6.1.1.12. Function: elong_solid_40_reduction_in_area_by_cold_drawing_2(T)

Type: Polynomial

X_{start}	X_{end}	f(x)									
296.0	811.0	0	28.22172	1	-0.04478956	2	4.523716E-5				
811.0	1088.0	0	-3976.9	1	11.81486	2	-0.01155191	3	3.776914E-6		

6.1.1.13. Function: alpha_solid_1(T)

Type: Polynomial

X_{start}	X_{end}	f(x)									
81.0	500.0	0	7.24503E-6	1	4.503271E-8	2	-1.564717E-10	3	2.721998E-13	4	-1.695788E-16

500.0	1173.0	0	4.931202E-6	1	3.05557E-8	2	-2.958128E-11	3	1.004274E-14
--------------	--------	---	-------------	---	------------	---	---------------	---	--------------

6.1.1.14. Function: alpha_liquid_2(T)

Type: Polynomial

X_start	X_end	f(x)
1728.0	2370.0	0 2.830799E-5 1 1.414267E-9 2 1.535536E-13

6.1.1.15. Function: C_solid_1(T)

Type: Polynomial

X_start	X_end	f(x)
100.0	599.0	0 -90.38582 1 4.504691 2 -0.01467413 3 2.223124E-5 4 -1.187679E-8
599.0	631.0	0 -29261.06 1 162.9617 2 -0.2972179 3 1.809085E-4
631.0	700.0	0 8011.774 1 -20.08609 2 0.01341446
700.0	1728.0	0 572.5331 1 -0.2122174 2 2.399215E-4 3 -5.186512E-8

6.1.1.16. Function: C_liquid_2(T)

Type: Polynomial

X_start	X_end	f(x)
1546.0	3184.0	0 715.5025

6.1.1.17. Function: C_gas_3(T)

Type: Polynomial

X_start	X_end	f(x)
293.0	1000.0	0 431.5461 1 -0.4547117 2 0.001818506 3 -2.770237E-6 4 1.881568E-9 5 -4.834294E-13
1000.0	2000.0	0 377.8208 1 0.1640738 2 -1.806734E-4 3 7.23499E-8 4 -1.037917E-11

6.1.1.18. Function: HC_solid_1(T)

Type: Polynomial

X_start	X_end	f(x)
100.0	599.0	0 -5.305647 1 0.2644255 2 -8.613714E-4 3 1.304974E-6 4 -6.971678E-10
599.0	631.0	0 -1717.624 1 9.565854 2 -0.01744669 3 1.061933E-5
631.0	700.0	0 470.2912 1 -1.179054 2 7.874292E-4
700.0	1728.0	0 32.82242 1 -0.01014919 2 1.190822E-5 3 -2.385652E-9

6.1.1.19. Function: HC_liquid_2(T)

Type: Polynomial

X_start	X_end	f(x)
1546.0	3184.0	0 42.0

6.1.1.20. Function: HC_gas_3(T)

Type: Polynomial

x_{start}	x_{end}	$f(x)$
293.0	1000.0	0 25.33175 1 -0.02669158 2 1.067463E-4 3 -1.626129E-7 4 1.104481E-10 5 -2.837731E-14
1000.0	2000.0	0 22.17808 1 0.009631137 2 -1.060553E-5 3 4.24694E-9 4 -6.092569E-13

6.1.1.21. Function: mu(T)

Type: Polynomial

x_{start}	x_{end}	$f(x)$
293.0	773.0	0 8.483201E10 1 -1.654608E7 2 -5055.849

6.1.1.22. Function: sigma(T)

Type: General

x_{start}	x_{end}	$f(x)$
100.0	633.0	1/(1.811005E-15*T^3-1.189788E-12*T^2+5.575728E-10*T-3.610912E-08)
633.0	800.0	1/(-1.128754E-13*T^2+4.544983E-10*T+5.696199E-08)

6.1.1.23. Function: Sys_solid_annealed_1(T)

Type: Polynomial

x_{start}	x_{end}	$f(x)$
77.0	1088.0	0 1.42427E8 1 -320861.9 2 678.0062 3 -0.7322205 4 2.658365E-4

6.1.1.24. Function: Sys_solid_40_reduction_in_area_by_cold_drawing_2(T)

Type: Polynomial

x_{start}	x_{end}	$f(x)$
293.0	422.0	0 4.667454E8 1 679245.1 2 -1328.707
422.0	922.0	0 -1.288517E8 1 6279729.0 2 -19629.06 3 24.67331 4 -0.01144651
922.0	1200.0	0 3.689946E8 1 -540737.3 2 201.0582

6.1.1.25. Function: rho_solid_1(T)

Type: Polynomial

x_{start}	x_{end}	$f(x)$
81.0	1173.0	0 8969.428 1 -0.1034728 2 -5.582955E-4 3 4.097446E-7 4 -1.117427E-10

6.1.1.26. Function: rho_liquid_2(T)

Type: Polynomial

x_{start}	x_{end}	$f(x)$
1728.0	2370.0	0 9120.08 1 -0.735

6.1.1.27. Function: TD(T)

Type: Polynomial

x_{start}	x_{end}	$f(x)$
-------------	-----------	--------

1723.0	1923.0	0	0.01461563	1	-3.267521E-5	2	2.740722E-8	3	-1.021654E-11	4	1.42831E-15
---------------	--------	---	------------	---	--------------	---	-------------	---	---------------	---	-------------

6.1.1.28. Function: VP_solid_1(T)

Type: General

X_start	X_end	f(x)
293.0	1728.0	$(\exp((-2.260600e+004/T-8.717000e-001*\log_{10}(T)+1.343781e+001)*\log(10.0)))*1.333200e+002$

6.1.1.29. Function: VP_liquid_2(T)

Type: General

X_start	X_end	f(x)
1728.0	2150.0	$(\exp((-2.076500e+004/T+9.546810e+000)*\log(10.0)))*1.333200e+002$

6.1.1.30. Function: nu(T)

Type: Polynomial

X_start	X_end	f(x)
293.0	773.0	0 0.2970106 1 -4.70622E-5 2 3.902138E-8

6.1.1.31. Function: kappa(T)

Type: Polynomial

X_start	X_end	f(x)
293.0	773.0	0 1.789167E11 1 -7.188841E7 2 22477.8

6.1.1.32. Function: eta(T)

Type: Polynomial

X_start	X_end	f(x)
1667.0	1930.0	0 0.04103066 1 -3.475375E-5 2 7.940521E-9

7. Solver Settings

Solve using a script: off

Analysis type	Harmonic_propagation
Auto select solver	On
Solver	Parametric
Solution form	Automatic
Symmetric	auto
Adaptive mesh refinement	Off
Optimization/Sensitivity	Off
Plot while solving	Off

7.1. Direct (SPOOLES)

Solver type: Linear system solver

Parameter	Value
Pivot threshold	0.1
Preordering algorithm	Nested dissection

7.2. Stationary

Parameter	Value
Linearity	Automatic
Relative tolerance	1.0E-6
Maximum number of iterations	25
Manual tuning of damping parameters	Off
Highly nonlinear problem	Off
Initial damping factor	1.0
Minimum damping factor	1.0E-4
Restriction for step size update	10.0

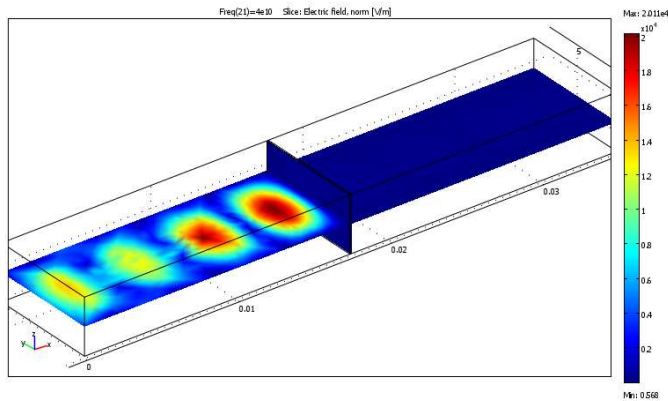
7.3. Parametric

Parameter	Value
Parameter name	Freq
Parameter values	linspace(26.5e9,40e9,21)
Predictor	Linear
Manual tuning of parameter step size	Off
Initial step size	0.0
Minimum step size	0.0
Maximum step size	0.0

7.4. Advanced

Parameter	Value
Constraint handling method	Elimination
Null-space function	Automatic
Automatic assembly block size	On
Assembly block size	1000
Use Hermitian transpose of constraint matrix and in symmetry detection	Off
Use complex functions with real input	On
Stop if error due to undefined operation	On
Store solution on file	Off
Type of scaling	Automatic
Manual scaling	
Row equilibration	On
Manual control of reassembly	Off
Load constant	On
Constraint constant	On
Mass constant	On
Damping (mass) constant	On
Jacobian constant	On
Constraint Jacobian constant	On

8. Postprocessing



9. Variables

9.1. Boundary

Name	Description	Unit	Expression
Eix_rfw	Incident electric field	V/m	$E0ix_rfw * \exp(j * \text{phase})$
Eiy_rfw	Incident electric field	V/m	$E0iy_rfw * \exp(j * \text{phase})$
Eiz_rfw	Incident electric field	V/m	$E0iz_rfw * \exp(j * \text{phase})$
tHx	Tangential magnetic field, x component	A/m	$Hx - (nx_rfw * Hx + ny_rfw * Hy + nz_rfw * Hz) * nx_rfw$
tHy	Tangential magnetic field, y component	A/m	$Hy - (nx_rfw * Hx + ny_rfw * Hy + nz_rfw * Hz) * ny_rfw$
tHz	Tangential magnetic field, z component	A/m	$Hz - (nx_rfw * Hx + ny_rfw * Hy + nz_rfw * Hz) * nz_rfw$
dVolbnd_rfw	Area integration contribution	1	1
epsilon_rbndinvxx_rfw	Inverse complex relative permittivity, xx component	1	$1/\text{epsilon_rbnd_rfw}$
epsilon_rbndinvxy_rfw	Inverse complex relative permittivity, xy component	1	0
epsilon_rbndinvxz_rfw	Inverse complex relative permittivity, xz component	1	0
epsilon_rbndinvyx_rfw	Inverse complex relative permittivity, yx component	1	0
epsilon_rbndinvyy_rfw	Inverse complex relative permittivity, yy component	1	$1/\text{epsilon_rbnd_rfw}$

	relative permittivity, yy component			
epsilonrbndinvyz_rfw	Inverse complex relative permittivity, yz component	1	0	
	relative permittivity, yz component			
epsilonrbndinvzx_rfw	Inverse complex relative permittivity, zx component	1	0	
	relative permittivity, zx component			
epsilonrbndinvzy_rfw	Inverse complex relative permittivity, zy component	1	0	
	relative permittivity, zy component			
epsilonrbndinvzz_rfw	Inverse complex relative permittivity, zz component	1		1/epsilonrbnd_rfw
	relative permittivity, zz component			
murbndinvxx_rfw	Inverse relative permeability, xx component	1		1/murbnd_rfw
	relative permeability, xx component			
murbndinvxy_rfw	Inverse relative permeability, xy component	1	0	
	relative permeability, xy component			
murbndinvxz_rfw	Inverse relative permeability, xz component	1	0	
	relative permeability, xz component			
murbndinvyx_rfw	Inverse relative permeability, yx component	1	0	
	relative permeability, yx component			
murbndinvyy_rfw	Inverse relative permeability, yy component	1		1/murbnd_rfw
	relative permeability, yy component			
murbndinvyz_rfw	Inverse relative permeability, yz component	1	0	
	relative permeability, yz component			
murbndinvzx_rfw	Inverse relative permeability, zx component	1	0	
	relative permeability, zx component			
murbndinvzy_rfw	Inverse relative permeability, zy component	1	0	
	relative permeability, zy component			
murbndinvzz_rfw	Inverse relative permeability, zz component	1		1/murbnd_rfw
	relative permeability, zz component			
Jsx_rfw	Surface current density, x component	A/m		$un_y * (Hz_down - Hz_up) - un_z * (Hy_down - Hy_up)$
Jsy_rfw	Surface current density, y component	A/m		$un_z * (Hx_down - Hx_up) - un_x * (Hz_down - Hz_up)$
Jsz_rfw	Surface current density, z component	A/m		$un_x * (Hy_down - Hy_up) - un_y * (Hx_down - Hx_up)$
nPoav_rfw	Power outflow, time average	W/m ²	$nx_rfw * Poxav_rfw + ny_rfw * Poyav_rfw + nz_rfw * Pozav_rfw$	
normJs_rfw	Surface current density, norm	A/m		$\sqrt{abs(Jsx_rfw)^2 + abs(Jsy_rfw)^2 + abs(Jsz_rfw)^2}$
normtE_rfw	Tangential	V/m		$\sqrt{abs(tEx)^2 + abs(tEy)^2 + abs(tEz)^2}$

	electric field, norm			
normtH_rfw	Tangential magnetic field, norm	A/m		$\sqrt{\text{abs}(tHx)^2 + \text{abs}(tHy)^2 + \text{abs}(tHz)^2}$
Qsav_rfw	Surface resistive heating, time average	W/m ²		$0.5 * \text{real}(Jsx_rfw * \text{conj}(tEx) + Jsx_rfw * \text{conj}(tEy) + Jsx_rfw * \text{conj}(tEz))$
Z_TE_rfw	Wave impedance, TE waves	ohm		$\omega_rfw * \mu_rfw / \beta_rfw$
Z_TM_rfw	Wave impedance, TM waves	ohm		$\beta_rfw / (\omega_rfw * \epsilon_rfw)$
Z_TEM_rfw	Wave impedance, TEM waves	ohm		$\sqrt{\mu_rfw / \epsilon_rfw}$
Pin_port_rfw	Port power level for the inport	1	1	
wport_rfw	Width of port	m		
hport_rfw	Height of port	m		
ahx_rfw	Voltage reference direction, x component	1		
ahy_rfw	Voltage reference direction, y component	1		
ahz_rfw	Voltage reference direction, z component	1		

9.2. Subdomain

9.2.1. Subdomain 1, 3

Name	Description	Unit	Expression
dr_guess_rfw	Width in radial direction default guess	m	0
R0_guess_rfw	Inner radius default guess	m	0
SRcoord_rfw	PML radial coordinate		
Sx_rfw	PML x coordinate	m	x
Sdx_guess_rfw	Width in x direction default guess	m	0
rCylx_rfw	PML r cylindrical vector, x component	m	
Sy_rfw	PML y coordinate	m	y
Sdy_guess_rfw	Width in y	m	0

rCylz_rfw	direction default guess PML r cylindrical vector, z component	m	
Sz_rfw	PML z coordinate	m	z
Sdz_guess_rfw	Width in z direction default guess	m	0
rCylz_rfw	PML r cylindrical vector, z component	m	
detJ_rfw	PML transformation matrix determinant	1	1
Jxx_rfw	PML transformation matrix, element xx	1	1
invJxx_rfw	PML inverse transformation matrix, element xx	1	1
Jxy_rfw	PML transformation matrix, element xy	1	0
invJxy_rfw	PML inverse transformation matrix, element xy	1	0
Jxz_rfw	PML transformation matrix, element xz	1	0
invJxz_rfw	PML inverse transformation matrix, element xz	1	0
Jyx_rfw	PML transformation matrix, element yx	1	0
invJyx_rfw	PML inverse transformation matrix, element yx	1	0
Jyy_rfw	PML transformation matrix, element yy	1	1
invJyy_rfw	PML inverse transformation matrix, element yy	1	1
Jyz_rfw	PML	1	0

invJyz_rfw	transformation matrix, element yz PML inverse transformation matrix, element yz	1	0
Jzx_rfw	transformation matrix, element yz PML	1	0
invJzx_rfw	transformation matrix, element zx PML inverse transformation matrix, element zx	1	0
Jzy_rfw	transformation matrix, element zy PML	1	0
invJzy_rfw	transformation matrix, element zy PML inverse transformation matrix, element zy	1	0
Jzz_rfw	transformation matrix, element zz PML	1	1
invJzz_rfw	transformation matrix, element zz PML inverse transformation matrix, element zz	1	1
k_rfw	Wave number	1/m	$k0_rfw * \sqrt{\text{mur_rfw} * (\text{epsilon}_r_rfw + \text{sigma}_r_rfw / (j\omega_rfw * \text{epsilon}_0_rfw))}$
dVol_rfw	Volume integration contribution	1	detJ_rfw
c_rfw	Phase velocity	m/s	$c0_rfw / \sqrt{\text{epsilon}_r_rfw * \text{mur_rfw}}$
Z_wave_rfw	Wave impedance	ohm	$c_rfw * \mu0_rfw * \text{mur_rfw}$
delta_rfw	Skin depth	m	$1 / \text{real}(\sqrt{j * \omega_rfw * \mu0_rfw * \text{mur_rfw} * (\text{sigma}_r_rfw + j * \omega_rfw * \text{epsilon}_0_rfw * \text{epsilon}_r_rfw)})$
Eix_rfw	Incident electric field	V/m	$E0ix_rfw * \exp(j * \text{phase})$
Eiy_rfw	Incident electric field	V/m	$E0iy_rfw * \exp(j * \text{phase})$
Eiz_rfw	Incident electric field	V/m	$E0iz_rfw * \exp(j * \text{phase})$
epsilon_rinvxx_rfw	Inverse complex relative permittivity, xx component	1	1/epsilon_r_rfw
epsilon_rinvxy_rfw	Inverse complex relative permittivity, xy component	1	0
epsilon_rinvxz_rfw	Inverse complex relative	1	0

epsilon_rinvyx_rfw	permittivity, xz component Inverse complex relative permittivity,	1	0
epsilon_rinvyy_rfw	permittivity, yx component Inverse complex relative permittivity,	1	1/epsilon_rfw
epsilon_rinvyz_rfw	permittivity, yy component Inverse complex relative permittivity,	1	0
epsilon_rinvzx_rfw	permittivity, yz component Inverse complex relative permittivity,	1	0
epsilon_rinvzy_rfw	permittivity, zx component Inverse complex relative permittivity,	1	0
epsilon_rinvzz_rfw	permittivity, zy component Inverse complex relative permittivity,	1	1/epsilon_rfw
mu_rinvxx_rfw	permeability, zz component Inverse relative permeability,	1	1/mu_rfw
mu_rinvxy_rfw	permeability, xx component Inverse relative permeability,	1	0
mu_rinvxz_rfw	permeability, xy component Inverse relative permeability,	1	0
mu_rinvyx_rfw	permeability, xz component Inverse relative permeability,	1	0
mu_rinvyy_rfw	permeability, yx component Inverse relative permeability,	1	1/mu_rfw
mu_rinvyz_rfw	permeability, yy component Inverse relative permeability,	1	0
mu_rinvzx_rfw	permeability, yz component Inverse relative permeability,	1	0
	permeability, zx component		

murinvzy_rfw	Inverse relative permeability, zy component	1	0
murinvzz_rfw	Inverse relative permeability, zz component	1	1/mur_rfw
epsilon_rfw	Permittivity	F/m	epsilon0_rfw * epsilon0_rfw
epsilonxx_rfw	Permittivity, xx component	F/m	epsilon0_rfw * epsilon0_rfw
epsilonxy_rfw	Permittivity, xy component	F/m	epsilon0_rfw * epsilon0_rfw
epsilonxz_rfw	Permittivity, xz component	F/m	epsilon0_rfw * epsilon0_rfw
epsilonyx_rfw	Permittivity, yx component	F/m	epsilon0_rfw * epsilon0_rfw
epsilonyy_rfw	Permittivity, yy component	F/m	epsilon0_rfw * epsilon0_rfw
epsilonyz_rfw	Permittivity, yz component	F/m	epsilon0_rfw * epsilon0_rfw
epsilonzx_rfw	Permittivity, zx component	F/m	epsilon0_rfw * epsilon0_rfw
epsilonzy_rfw	Permittivity, zy component	F/m	epsilon0_rfw * epsilon0_rfw
epsilonzz_rfw	Permittivity, zz component	F/m	epsilon0_rfw * epsilon0_rfw
mu_rfw	Permeability	H/m	mu0_rfw * mu0_rfw
muxx_rfw	Permeability, xx component	H/m	mu0_rfw * mu0_rfw
muxy_rfw	Permeability, xy component	H/m	mu0_rfw * mu0_rfw
muxz_rfw	Permeability, xz component	H/m	mu0_rfw * mu0_rfw
muyx_rfw	Permeability, yx component	H/m	mu0_rfw * mu0_rfw
muyy_rfw	Permeability, yy component	H/m	mu0_rfw * mu0_rfw
muyz_rfw	Permeability, yz component	H/m	mu0_rfw * mu0_rfw
muzx_rfw	Permeability, zx component	H/m	mu0_rfw * mu0_rfw
muzy_rfw	Permeability, zy component	H/m	mu0_rfw * mu0_rfw
muzz_rfw	Permeability, zz component	H/m	mu0_rfw * mu0_rfw
scHx	Scattered magnetic field	A/m	murinvxx_rfw * scBx_rfw/mu0_rfw
scHy	Scattered magnetic field	A/m	murinvyy_rfw * scBy_rfw/mu0_rfw
scHz	Scattered magnetic field	A/m	murinvzz_rfw * scBz_rfw/mu0_rfw
Qmav_rfw	Magnetic hysteresis losses	W/m ³	real(-0.5 * j * omega_rfw * (Bx_rfw * conj(Hx)+By_rfw * conj(Hy)+Bz_rfw * conj(Hz)))
curlEx_rfw	Curl of electric field, x component	V/m ²	EzyEyz
depEx_rfw	Electric field test variable,	V/m	Ex

Dx_rfw	x component Electric displacement,	C/m ²	$\epsilon_{xx_rfw} * E_x$
scDx_rfw	x component Scattered electric displacement,	C/m ²	$\epsilon_{xx_rfw} * scE_x$
Jdx_rfw	x component Displacement current density,	A/m ²	$j\omega_{rfw} * D_{x_rfw}$
Jix_rfw	Induced current density, x component	A/m ²	0
Gfx_rfw	Gauge fixed field, x component	V/m	$D_{x_rfw}/\epsilon_{0_rfw}$
jwHx_rfw	Magnetic field, x component, times $j\omega$	A/(m*s)	$(\mu_{rx_rfw} * j\omega B_{x_rfw} + \mu_{ry_rfw} * j\omega B_{y_rfw} + \mu_{rz_rfw} * j\omega B_{z_rfw})/\mu_{0_rfw}$
Hx	Magnetic field, x component	A/m	$j\omega H_{x_rfw}/\omega_{rfw}$
scEx	Scattered electric field, x component	V/m	$E_x - E_{ix_rfw}$
jwBx_rfw	Magnetic flux density, x component, times $j\omega$	V/m ²	$-\text{curl}E_{x_rfw}$
Bx_rfw	Magnetic flux density, x component	T	$j\omega B_{x_rfw}/\omega_{rfw}$
scBx_rfw	Scattered magnetic flux density, x component	T	$-(\text{diff}(scE_z, y) - \text{diff}(scE_y, z))/\omega_{rfw}$
curlEy_rfw	Curl of electric field, y component	V/m ²	$E_x z - E_z x$
depEy_rfw	Electric field test variable, y component	V/m	E_y
Dy_rfw	Electric displacement, y component	C/m ²	$\epsilon_{yy_rfw} * E_y$
scDy_rfw	Scattered electric displacement, y component	C/m ²	$\epsilon_{yy_rfw} * scE_y$
Jdy_rfw	Displacement current density, y component	A/m ²	$j\omega_{rfw} * D_{y_rfw}$
Jiy_rfw	Induced current density, y component	A/m ²	0

Gfy_rfw	component Gauge fixed field, y	V/m	Dy_rfw/epsilon0_rfw
jwHy_rfw	component Magnetic field, y	A/(m*s)	(murinvyx_rfw * jwBx_rfw+murinvyy_rfw * jwBy_rfw+murinvyz_rfw * jwBz_rfw)/mu0_rfw
Hy	component, times jω Magnetic field, y	A/m	jwHy_rfw/jomega_rfw
scEy	component Scattered electric field, y component	V/m	Ey-Eiy_rfw
jwBy_rfw	Magnetic flux density, y component, times jω	V/m^2	-curlEy_rfw
By_rfw	Magnetic flux density, y component	T	jwBy_rfw/jomega_rfw
scBy_rfw	Scattered magnetic flux density, y component	T	-(diff(scEx,z)-diff(scEz,x))/jomega_rfw
curlEz_rfw	Curl of electric field, z component	V/m^2	EyxExy
depEz_rfw	Electric field test variable, z component	V/m	Ez
Dz_rfw	Electric displacement, z component	C/m^2	epsilonzz_rfw * Ez
scDz_rfw	Scattered electric displacement, z component	C/m^2	epsilonzz_rfw * scEz
Jdz_rfw	Displacement current density, z component	A/m^2	jomega_rfw * Dz_rfw
Jiz_rfw	Induced current density, z component	A/m^2	0
Gfz_rfw	Gauge fixed field, z component	V/m	Dz_rfw/epsilon0_rfw
jwHz_rfw	Magnetic field, z component, times jω	A/(m*s)	(murinvzx_rfw * jwBx_rfw+murinvzy_rfw * jwBy_rfw+murinvzz_rfw * jwBz_rfw)/mu0_rfw
Hz	Magnetic field, z component	A/m	jwHz_rfw/jomega_rfw
scEz	Scattered electric field, z component	V/m	Ez-Eiz_rfw
jwBz_rfw	Magnetic flux density, z component	V/m^2	-curlEz_rfw

Bz_rfw	density, z component, times j ω Magnetic flux density, z component	T	$j\omega Bz_rfw/j\omega_{rfw}$
scBz_rfw	Scattered magnetic flux density, z component	T	$-(diff(scEy,x)-diff(scEx,y))/j\omega_{rfw}$
normE_rfw	Electric field, norm	V/m	$\sqrt{abs(Ex)^2+abs(Ey)^2+abs(Ez)^2}$
normD_rfw	Electric displacement, norm	C/m ²	$\sqrt{abs(Dx_rfw)^2+abs(Dy_rfw)^2+abs(Dz_rfw)^2}$
normB_rfw	Magnetic flux density, norm	T	$\sqrt{abs(Bx_rfw)^2+abs(By_rfw)^2+abs(Bz_rfw)^2}$
normH_rfw	Magnetic field, norm	A/m	$\sqrt{abs(Hx)^2+abs(Hy)^2+abs(Hz)^2}$
normPoav_rfw	Power flow, time average, norm	W/m ²	$\sqrt{abs(Poxav_rfw)^2+abs(Poyav_rfw)^2+abs(Pozav_rfw)^2}$
normscE_rfw	Scattered electric field, norm	V/m	$\sqrt{abs(scEx)^2+abs(scEy)^2+abs(scEz)^2}$
normscD_rfw	Scattered electric displacement, norm	C/m ²	$\sqrt{abs(scDx_rfw)^2+abs(scDy_rfw)^2+abs(scDz_rfw)^2}$
normscB_rfw	Scattered magnetic flux density, norm	T	$\sqrt{abs(scBx_rfw)^2+abs(scBy_rfw)^2+abs(scBz_rfw)^2}$
normscH_rfw	Scattered magnetic field, norm	A/m	$\sqrt{abs(scHx)^2+abs(scHy)^2+abs(scHz)^2}$
Wmav_rfw	Magnetic energy density, time average	J/m ³	$0.25 * \text{real}(Hx * \text{conj}(Bx_rfw)+Hy * \text{conj}(By_rfw)+Hz * \text{conj}(Bz_rfw))$
Weav_rfw	Electric energy density, time average	J/m ³	$0.25 * \text{real}(Ex * \text{conj}(Dx_rfw)+Ey * \text{conj}(Dy_rfw)+Ez * \text{conj}(Dz_rfw))$
Wav_rfw	Total energy density, time average	J/m ³	$Wmav_rfw+Weav_rfw$
Qav_rfw	Resistive heating, time average	W/m ³	$0.5 * \text{real}(Jix_rfw * \text{conj}(Ex)-j * \text{real}(\omega_{rfw}) * Ex * \text{conj}(Dx_rfw)+Jiy_rfw * \text{conj}(Ey)-j * \text{real}(\omega_{rfw}) * Ey * \text{conj}(Dy_rfw)+Jiz_rfw * \text{conj}(Ez)-j * \text{real}(\omega_{rfw}) * Ez * \text{conj}(Dz_rfw))$
Poxav_rfw	Power flow, time average, x component	W/m ²	$0.5 * \text{real}(Ey * \text{conj}(Hz)-Ez * \text{conj}(Hy))$
Poyav_rfw	Power flow, time average, y component	W/m ²	$0.5 * \text{real}(Ez * \text{conj}(Hx)-Ex * \text{conj}(Hz))$
Pozav_rfw	Power flow, time average, z component	W/m ²	$0.5 * \text{real}(Ex * \text{conj}(Hy)-Ey * \text{conj}(Hx))$

9.2.2. Subdomain 2

Name	Description	Unit	Expression
dr_guess_rfw	Width in radial direction default guess	m	0
R0_guess_rfw	Inner radius default guess	m	0
SRcoord_rfw	PML radial coordinate		
Sx_rfw	PML x coordinate	m	x
Sdx_guess_rfw	Width in x direction default guess	m	0
rCylx_rfw	PML r cylindrical vector, x component	m	
Sy_rfw	PML y coordinate	m	y
Sdy_guess_rfw	Width in y direction default guess	m	0
rCyly_rfw	PML r cylindrical vector, y component	m	
Sz_rfw	PML z coordinate	m	z
Sdz_guess_rfw	Width in z direction default guess	m	0
rCylz_rfw	PML r cylindrical vector, z component	m	
detJ_rfw	PML transformation matrix determinant	1	1
Jxx_rfw	PML transformation matrix, element xx	1	1
invJxx_rfw	PML inverse transformation matrix, element xx	1	1
Jxy_rfw	PML transformation matrix, element xy	1	0
invJxy_rfw	PML inverse transformation matrix, element xy	1	0
Jxz_rfw	PML transformation matrix, element xz	1	0

invJxz_rfw	n matrix, element xz PML inverse transformatio	1	0
Jyx_rfw	n matrix, element xz PML transformatio	1	0
invJyx_rfw	n matrix, element yx PML inverse transformatio	1	0
Jyy_rfw	n matrix, element yx PML transformatio	1	1
invJyy_rfw	n matrix, element yy PML inverse transformatio	1	1
Jyz_rfw	n matrix, element yy PML transformatio	1	0
invJyz_rfw	n matrix, element yz PML inverse transformatio	1	0
Jzx_rfw	n matrix, element yz PML transformatio	1	0
invJzx_rfw	n matrix, element zx PML inverse transformatio	1	0
Jzy_rfw	n matrix, element zx PML transformatio	1	0
invJzy_rfw	n matrix, element zy PML inverse transformatio	1	0
Jzz_rfw	n matrix, element zy PML transformatio	1	1
invJzz_rfw	n matrix, element zz PML inverse transformatio	1	1
k_rfw	Wave number	1/m	$k0_rfw * \sqrt{\text{mur_rfw} * (\text{epsilon}_r_rfw + \text{sigma}_rfw / (\text{jomega_rfw} * \text{epsilon}_0_rfw))}$
dVol_rfw	Volume integration contribution	1	detJ_rfw
c_rfw	Phase velocity	m/s	$c0_rfw / \sqrt{\text{epsilon}_r_rfw * \text{mur_rfw}}$

Z_wave_rfw	Wave impedance	ohm	$c_rfw * \mu 0_rfw * \mu r_rfw$
delta_rfw	Skin depth	m	$1/\text{real}(\text{sqrt}(j * \omega_rfw * \mu 0_rfw * \mu r_rfw * (\sigma_rfw + j * \omega_rfw * \epsilon 0_rfw * \epsilon r_rfw))))$
Eix_rfw	Incident electric field	V/m	$E0ix_rfw * \exp(j * \text{phase})$
Eiy_rfw	Incident electric field	V/m	$E0iy_rfw * \exp(j * \text{phase})$
Eiz_rfw	Incident electric field	V/m	$E0iz_rfw * \exp(j * \text{phase})$
epsilon_rinvxx_rfw	Inverse complex relative permittivity, xx component	1	$1/(\epsilon r_rfw + \sigma_rfw / (j * \omega_rfw * \epsilon 0_rfw))$
epsilon_rinvxy_rfw	Inverse complex relative permittivity, xy component	1	0
epsilon_rinvxz_rfw	Inverse complex relative permittivity, xz component	1	0
epsilon_rinvyx_rfw	Inverse complex relative permittivity, yx component	1	0
epsilon_rinvyy_rfw	Inverse complex relative permittivity, yy component	1	$1/(\epsilon r_rfw + \sigma_rfw / (j * \omega_rfw * \epsilon 0_rfw))$
epsilon_rinvyz_rfw	Inverse complex relative permittivity, yz component	1	0
epsilon_rinvzx_rfw	Inverse complex relative permittivity, zx component	1	0
epsilon_rinvzy_rfw	Inverse complex relative permittivity, zy component	1	0
epsilon_rinvzz_rfw	Inverse complex relative permittivity, zz component	1	$1/(\epsilon r_rfw + \sigma_rfw / (j * \omega_rfw * \epsilon 0_rfw))$
mu_rinvxx_rfw	Inverse relative permeability, xx component	1	$1/\mu r_rfw$
mu_rinvxy_rfw	Inverse relative permeability, xy component	1	0

	relative permeability, xy component		
murinvxz_rfw	Inverse relative permeability, xz component	1	0
murinvyx_rfw	Inverse relative permeability, yx component	1	0
murinvyy_rfw	Inverse relative permeability, yy component	1	1/mur_rfw
murinvyz_rfw	Inverse relative permeability, yz component	1	0
murinvzx_rfw	Inverse relative permeability, zx component	1	0
murinvzy_rfw	Inverse relative permeability, zy component	1	0
murinvzz_rfw	Inverse relative permeability, zz component	1	1/mur_rfw
epsilon_rfw	Permittivity	F/m	epsilon0_rfw * epsilon0r_rfw
epsilonxx_rfw	Permittivity, xx component	F/m	epsilon0_rfw * epsilon0rxx_rfw
epsilonxy_rfw	Permittivity, xy component	F/m	epsilon0_rfw * epsilon0rxy_rfw
epsilonxz_rfw	Permittivity, xz component	F/m	epsilon0_rfw * epsilon0rxz_rfw
epsilonyx_rfw	Permittivity, yx component	F/m	epsilon0_rfw * epsilon0ryx_rfw
epsilonyy_rfw	Permittivity, yy component	F/m	epsilon0_rfw * epsilon0ryy_rfw
epsilonyz_rfw	Permittivity, yz component	F/m	epsilon0_rfw * epsilon0ryz_rfw
epsilonzx_rfw	Permittivity, zx component	F/m	epsilon0_rfw * epsilon0rzx_rfw
epsilonzy_rfw	Permittivity, zy component	F/m	epsilon0_rfw * epsilon0rzy_rfw
epsilonzz_rfw	Permittivity, zz component	F/m	epsilon0_rfw * epsilon0rzz_rfw
mu_rfw	Permeability	H/m	mu0_rfw * mu0r_rfw
muxx_rfw	Permeability, xx component	H/m	mu0_rfw * mu0rxx_rfw
muxy_rfw	Permeability, xy component	H/m	mu0_rfw * mu0rxy_rfw
muxz_rfw	Permeability, xz component	H/m	mu0_rfw * mu0rxz_rfw
muyx_rfw	Permeability, yx component	H/m	mu0_rfw * mu0ryx_rfw
muyy_rfw	Permeability, yy component	H/m	mu0_rfw * mu0ryy_rfw

muyz_rfw	yy component Permeability,	H/m	$\mu_0_rfw * \text{muryz_rfw}$
muzx_rfw	yz component Permeability,	H/m	$\mu_0_rfw * \text{murzx_rfw}$
muzy_rfw	zx component Permeability,	H/m	$\mu_0_rfw * \text{murzy_rfw}$
muzz_rfw	zy component Permeability,	H/m	$\mu_0_rfw * \text{murzz_rfw}$
scHx	zz component Scattered magnetic field	A/m	$\text{murinvxx_rfw} * \text{scBx_rfw}/\mu_0_rfw$
scHy	Scattered magnetic field	A/m	$\text{murinvyy_rfw} * \text{scBy_rfw}/\mu_0_rfw$
scHz	Scattered magnetic field	A/m	$\text{murinvzz_rfw} * \text{scBz_rfw}/\mu_0_rfw$
Qmav_rfw	Magnetic hysteresis losses	W/m ³	$\text{real}(-0.5 * j * \omega_rfw * (\text{Bx_rfw} * \text{conj}(\text{Hx}) + \text{By_rfw} * \text{conj}(\text{Hy}) + \text{Bz_rfw} * \text{conj}(\text{Hz})))$
curlEx_rfw	Curl of electric field,	V/m ²	EzyEyz
depEx_rfw	x component Electric field test variable,	V/m	Ex
Dx_rfw	x component Electric displacement,	C/m ²	$\text{epsilonxx_rfw} * \text{Ex}$
scDx_rfw	x component Scattered electric displacement,	C/m ²	$\text{epsilonxx_rfw} * \text{scEx}$
Jdx_rfw	x component Displacement current density,	A/m ²	$\text{jomega_rfw} * \text{Dx_rfw}$
Jix_rfw	Induced current density, x component	A/m ²	$\text{sigmaxx_rfw} * \text{Ex}$
Gfx_rfw	Gauge fixed field, x component	V/m	$\text{Dx_rfw}/\text{epsilon0_rfw}$
jwHx_rfw	Magnetic field, x component, times j ω	A/(m*s)	$(\text{murinvxx_rfw} * \text{jwBx_rfw} + \text{murinvxy_rfw} * \text{jwBy_rfw} + \text{murinvxz_rfw} * \text{jwBz_rfw})/\mu_0_rfw$
Hx	Magnetic field, x component	A/m	$\text{jwHx_rfw}/\text{jomega_rfw}$
scEx	Scattered electric field, x component	V/m	$\text{Ex} - \text{Eix_rfw}$
jwBx_rfw	Magnetic flux density, x component, times j ω	V/m ²	$-\text{curlEx_rfw}$
Bx_rfw	Magnetic flux density, x component	T	$\text{jwBx_rfw}/\text{jomega_rfw}$
scBx_rfw	Scattered	T	$-(\text{diff}(\text{scEz}, y) - \text{diff}(\text{scEy}, z))/\text{jomega_rfw}$

	magnetic flux density, x component		
curlEy_rfw	Curl of electric field, y component	V/m ²	ExzEzx
depEy_rfw	Electric field test variable, y component	V/m	Ey
Dy_rfw	Electric displacement, y component	C/m ²	epsilonyy_rfw * Ey
scDy_rfw	Scattered electric displacement, y component	C/m ²	epsilonyy_rfw * scEy
Jdy_rfw	Displacement current density, y component	A/m ²	jomega_rfw * Dy_rfw
Jiy_rfw	Induced current density, y component	A/m ²	sigmayy_rfw * Ey
Gfy_rfw	Gauge fixed field, y component	V/m	Dy_rfw/epsilon0_rfw
jwHy_rfw	Magnetic field, y component, times j ω	A/(m*s)	(murinvyx_rfw * jwBx_rfw+murinvyy_rfw * jwBy_rfw+murinvyz_rfw * jwBz_rfw)/mu0_rfw
Hy	Magnetic field, y component	A/m	jwHy_rfw/jomega_rfw
scEy	Scattered electric field, y component	V/m	Ey-Eiy_rfw
jwBy_rfw	Magnetic flux density, y component, times j ω	V/m ²	-curlEy_rfw
By_rfw	Magnetic flux density, y component	T	jwBy_rfw/jomega_rfw
scBy_rfw	Scattered magnetic flux density, y component	T	-(diff(scEx,z)-diff(scEz,x))/jomega_rfw
curlEz_rfw	Curl of electric field, z component	V/m ²	EyxExy
depEz_rfw	Electric field test variable, z component	V/m	Ez
Dz_rfw	Electric displacement, z component	C/m ²	epsilonzz_rfw * Ez
scDz_rfw	Scattered electric displacement,	C/m ²	epsilonzz_rfw * scEz

Jdz_rfw	z component Displacement current density, z component	A/m ²	jomega_rfw * Dz_rfw
Jiz_rfw	Induced current density, z component	A/m ²	sigmazz_rfw * Ez
Gfz_rfw	Gauge fixed field, z component	V/m	Dz_rfw/epsilon0_rfw
jwHz_rfw	Magnetic field, z component, times jω	A/(m*s)	(murinvzx_rfw * jwBx_rfw+murinvzy_rfw * jwBy_rfw+murinvzz_rfw * jwBz_rfw)/mu0_rfw
Hz	Magnetic field, z component	A/m	jwHz_rfw/jomega_rfw
scEz	Scattered electric field, z component	V/m	Ez-Eiz_rfw
jwBz_rfw	Magnetic flux density, z component, times jω	V/m ²	-curlEz_rfw
Bz_rfw	Magnetic flux density, z component	T	jwBz_rfw/jomega_rfw
scBz_rfw	Scattered magnetic flux density, z component	T	-(diff(scEy,x)-diff(scEx,y))/jomega_rfw
normE_rfw	Electric field, norm	V/m	sqrt(abs(Ex)^2+abs(Ey)^2+abs(Ez)^2)
normD_rfw	Electric displacement, norm	C/m ²	sqrt(abs(Dx_rfw)^2+abs(Dy_rfw)^2+abs(Dz_rfw)^2)
normB_rfw	Magnetic flux density, norm	T	sqrt(abs(Bx_rfw)^2+abs(By_rfw)^2+abs(Bz_rfw)^2)
normH_rfw	Magnetic field, norm	A/m	sqrt(abs(Hx)^2+abs(Hy)^2+abs(Hz)^2)
normPoav_rfw	Power flow, time average, norm	W/m ²	sqrt(abs(Poxav_rfw)^2+abs(Poyav_rfw)^2+abs(Pozav_rfw)^2)
normscE_rfw	Scattered electric field, norm	V/m	sqrt(abs(scEx)^2+abs(scEy)^2+abs(scEz)^2)
normscD_rfw	Scattered electric displacement, norm	C/m ²	sqrt(abs(scDx_rfw)^2+abs(scDy_rfw)^2+abs(scDz_rfw)^2)
normscB_rfw	Scattered magnetic flux density, norm	T	sqrt(abs(scBx_rfw)^2+abs(scBy_rfw)^2+abs(scBz_rfw)^2)
normscH_rfw	Scattered magnetic field, norm	A/m	sqrt(abs(scHx)^2+abs(scHy)^2+abs(scHz)^2)
Wmav_rfw	Magnetic energy	J/m ³	0.25 * real(Hx * conj(Bx_rfw)+Hy * conj(By_rfw)+Hz * conj(Bz_rfw))

Weav_rfw	density, time average Electric energy density, time average	J/m ³	$0.25 * \text{real}(E_x * \text{conj}(D_x_{\text{rfw}}) + E_y * \text{conj}(D_y_{\text{rfw}}) + E_z * \text{conj}(D_z_{\text{rfw}}))$
Wav_rfw	Total energy density, time average	J/m ³	$W_{\text{mav_rfw}} + W_{\text{eav_rfw}}$
Qav_rfw	Resistive heating, time average	W/m ³	$0.5 * \text{real}(J_{ix_rfw} * \text{conj}(E_x) - j * \text{real}(\omega_{\text{rfw}}) * E_x * \text{conj}(D_x_{\text{rfw}}) + J_{iy_rfw} * \text{conj}(E_y) - j * \text{real}(\omega_{\text{rfw}}) * E_y * \text{conj}(D_y_{\text{rfw}}) + J_{iz_rfw} * \text{conj}(E_z) - j * \text{real}(\omega_{\text{rfw}}) * E_z * \text{conj}(D_z_{\text{rfw}}))$
Poxav_rfw	Power flow, time average, x component	W/m ²	$0.5 * \text{real}(E_y * \text{conj}(H_z) - E_z * \text{conj}(H_y))$
Poyav_rfw	Power flow, time average, y component	W/m ²	$0.5 * \text{real}(E_z * \text{conj}(H_x) - E_x * \text{conj}(H_z))$
Pozav_rfw	Power flow, time average, z component	W/m ²	$0.5 * \text{real}(E_x * \text{conj}(H_y) - E_y * \text{conj}(H_x))$
